Why and how is silk spun?
Integrating rheology with advanced spectroscopic techniques

Thesis Abstract

Maxime Boulet-Audet

Merton College Department of Zoology
Trinity 2013 University of Oxford

This thesis investigates the mechanisms behind natural silk spinning by integrating rheology, spectroscopy and small angle scattering to better understand this process and to guide our efforts towards mimicking Nature's ways of producing high performance fibres.

As a result of natural selection, arthropods such as spiders and moths have evolved the ability to excrete silk proteins in a highly controlled manner. Spun from liquid feedstocks, silk fibres are used *ex vivo* to build structures with mechanical properties currently unmatched by industrial filaments. As yet, relatively little attention has been directed to the investigation of spinning under biologically relevant conditions. To better understand how and why silk is spun, this thesis bridges the gap between liquid silk flow properties and structure development.

To directly connect the two, I have developed and deployed novel experimental platforms that combine infrared spectroscopy and small angle scattering with rheology. This approach has clarified long-standing ambiguities on the structural root of silk's apparently complex flow properties. Small angle scattering revealed the length scales involved in the flow induced solidification under a range of spinning conditions. Moreover, infrared spectroscopy offered a unique perspective into silk's formation process immediately after excretion.

In a similar manner to the post-extrusion tuning of the properties of partly solidified spider silk filaments, this thesis has revealed that silkworm silk fibres are far from completely formed once excreted. One might describe the filaments of mulberry silkworm as seeded molten polymers that form its hydrogen bonding network and crystallises slowly on site. Consequently, it enlightens that post-spinning conditions are equally paramount for silkworm silk, giving an explanation for the relatively poorer mechanical properties. The comparison of silks from a range of species, allowed this hypothesis to be extended to wild silkworm silk. My insights into spinning had the fortuitous repercussion of facilitating silk fibre solubilisation leading to the development of better artificial silk feedstocks flowing like native silks. With these findings, I believe we are now in an improved position to conceive artificial fibres with properties rivalling those of Nature.

Why and how is silk spun?
Integrating rheology with advanced spectroscopic techniques

A thesis submitted in partial fulfilment for the degree of Doctor of Philosophy

Submitted by

Maxime Boulet-Audet

Supervised by

Professor Fritz Vollrath

Dr Chris Holland

Dr Ann Terry

Oxford Silk Group

Department of Zoology

University of Oxford

Merton College

Trinity 2013

In dedication to my colleagues, friends and family which made my DPhil the most fulfilling experience of my life thus far.

I, Maxime Boulet-Audet, declare that this thesis titled *'Why and how is silk spun? Integrating rheology with advanced spectroscopic techniques'* and the work presented in it are my own.

I confirm that:

- This work was done wholly or mainly while in candidature for a research degree at this University.
- Where any part of this thesis has previously been submitted for a degree or any other qualification at this University or any other institution, this has been clearly stated.
- Where I have consulted the published work of others, this is always clearly attributed.
- Where I have quoted from the work of others, the source is always given. With the exception of such quotations, this thesis is entirely my own work.
- I have acknowledged all main sources of help.
- Where the thesis is based on work done by myself jointly with others, I have made clear exactly what was done by others and what I have contributed myself.

Maxime Boulet-Audet

Signed:_____

Date:_____

Acknowledgements

I would like to thank my supervisor, Prof. Fritz Vollrath, for assigning me this exciting and important project from which many career opportunities will emerge. I would also like to especially acknowledge Dr Chris Holland for his devoted support and guidance as well for introducing me to the field of biology and rheology. Thanks to Dr Ann Terry for opening the field of scattering to me and for being indispensable on beamline experiments.

Prof. David Porter played a crucial role in incorporating my conclusions into a larger framework and taught me to be critical of the work in the field. I would also like to thank Dr Fujia Chen for revealing to me the diversity of silk, providing me with wild cocoons, insightful discussions on cocoon morphology and much appreciated moral support when needed. I want to thank also Dr Imke Greving who has been most helpful in analysing the data obtained from scattering experiments. I would also like to express my gratitude to Dr Tom Gheysens for his assistance with the reconstitution process and for transmitting his contagious passion for silk research. In addition I would like to acknowledge Beth Mortimer and Dr Juan Guan, who has been a real delight in helping me with the thesis writing process and for baking all those cakes. I would also like to extend my gratitude to Nicholas Hawkins and Alex Greenhalgh for organising my stag do party and for taking great care of the lab and instruments. Thanks for Gunnar Thalwitz, Miguel Astudillo for the fascinating silk economics talks.

I wish to express my gratitude to Merton College that facilitated the transition from my home country. I would also like to thank Prof. Tim Guilford for being my college advisor over the course of my degree. For their direct vital financial support, I would like to acknowledge the Natural Sciences and Engineering Research Council of Canada (NSERC) and the Engineering and Physical Science Research Council of the United-Kingdom (EPSRC). I would also like to acknowledge the support of the American Air Force Office of Scientific Research and the European commission for sponsoring our research. Finally, I would like to extend my acknowledgements to my examiners, Prof. Christian Pellerin and Dr Robert Jacobs who kindly accepted to examine my work and helped improving this thesis as a result.

Publications

Boulet-Audet, M., Terry A.E., Vollrath, F. and C. Holland
Silk protein aggregation kinetics revealed by Rheo-IR
Acta Biomaterialia, 2013. 10(2): p. 776–784.

Boulet-Audet, M., Vollrath, F. and Holland, C.
Rheo-attenuated total reflectance infrared spectroscopy: a new tool to study biopolymers.
Physical Chemistry Chemical Physics, 2011. 13(9): p. 3979-3984.
(Full text in appendices)

Kingdon, J., Agwanda, B., Kinnaird, M., O'Brien, T., Holland, C., Gheysens, T., Boulet-Audet, M. and Vollrath, F.
A poisonous surprise under the coat of the African crested rat
Proceedings of the Royal Society B-Biological Sciences, 2011. 279(1729): p. 675-680.

In preparation

Boulet-Audet, M., Terry, A.E., Greving, I., Gheysens, T., Portale, G., Bras, W., Vollrath, F. and Holland, C.
Silk spinning studied by small angle scattering
2013.

Boulet-Audet, M., Vollrath, F. and Holland, C.
The chemical diversity of silk revealed by infrared spectroscopy

Boulet-Audet, M., Gheysens, T., Vollrath, F. and C. Holland, C.
Interrupting silk's processing

Table of contents

ACKNOWLEDGEMENTS I
PUBLICATIONS I
TABLE OF CONTENTS II
LIST OF FIGURES VI
LIST OF TABLES XII
LIST OF ABBREVIATIONS AND SYMBOLS XIII
PROTEIN RELATED GLOSSARY XVI
CHAPTER 1 INTRODUCTION 1
1.1 ABSTRACT 1
1.2 WHERE DOES SILK COME FROM? 2
1.3 WHAT MAKES SILK DESIRABLE? 3
1.4 SYNTHETIC SILK ANALOGUES 5
1.5 BIOENGINEERED ARTIFICIAL SILKS 6
1.6 ARTIFICIAL SILK FROM COCOONS 6
1.7 WHAT IS SILK MADE OF? 8
1.8 WHAT ARE THE TYPES OF SILKS? 10
1.9 WHAT DOES INFRARED SPECTROSCOPY TELL US ABOUT SILK? 12
1.10 WHAT DOES SMALL ANGLE SCATTERING TELL US ABOUT SILK? 13
1.11 WHAT DOES RHEOLOGY TELL US ABOUT SILK? 16
1.12 HOW IS SILK SPUN? 20
1.13 DEFINING THE SCOPE OF THE PROJECT 23
1.14 THESIS SUMMARY 23
CHAPTER 2 THEORY AND EXPERIMENTAL METHODS 26
2.1 LIQUID SILK SAMPLE PREPARATION 26
2.1.1 Native feedstock preparation 26
2.1.2 Silk fibroin reconstitution 29
2.2 RHEOLOGY 30
2.2.1 Rheology instrumentation 30
2.2.2 Sample loading for rheology measurements 32
2.2.3 Shear flow 34
2.2.4 Oscillatory measurements 39
2.2.5 Extensional flow 42
2.3 INFRARED SPECTROSCOPY 43
2.3.1 Infrared spectroscopy instrumentation 43
2.3.2 Infrared absorption 45
2.3.3 Attenuated Total Reflection (ATR) 46
2.3.4 Coupling a shear cell with an infrared spectrometer 48
2.3.5 Coupling infrared spectrometer with a rheometer 48
2.3.6 2D correlation 50
2.3.7 Principal Component Analysis (PCA) and Linear Discriminant Analysis (LDA) 51
2.3.8 Self-Modelling Curve Resolution (MCR) 52
2.4 SMALL ANGLE SCATTERING (SAS) 54
2.4.1 Small Angle Scattering (SAS) theory 55
2.4.2 Small Angle X-ray Scattering (SAXS) instrumentation 62
2.4.3 Scattering data analysis 63

2.4.4 Small Angle Neutron Scattering (SANS) instrumentation 63
CHAPTER 3 SHEAR-INDUCED AGGREGATION STUDIED BY TIME RESOLVED INFRARED SPECTROSCOPY 65
3.1 ABSTRACT 65
3.2 INTRODUCTION 66
3.3 MATERIALS AND METHODS 68
3.3.1 Reconstituted silk fibroin (RSF) 68
3.3.2 Spectral acquisition 68
3.3.3 Dry weight quantification 69
3.3.4 Experimental setup 70
3.4 RESULTS AND DISCUSSION 71
3.4.1 Silk shear-induced conversion kinetic 71
3.4.2 2D correlation analysis 74
3.4.3 Conformation analysis 77
3.4.4 The effect of concentration 78
3.4.5 Polarisation rotation measurements 79
3.5 CONCLUSIONS 82
CHAPTER 4 NATIVE SILK CONVERSION KINETICS STUDIED BY SMALL ANGLE SCATTERING 83
4.1 ABSTRACT 83
4.2 INTRODUCTION 84
4.3 EXPERIMENTAL METHOD 87
4.3.1 Native silk preparation 87
4.3.2 Small Angle X-ray Scattering (SAXS) beamline 87
4.3.3 Small Angle Neutron Scattering (SANS) beamline 88
4.3.4 In situ X-ray scattering platform 89
4.3.5 Ex situ shear method 90
4.3.6 Visual imaging data collection and analysis 92
4.3.7 SAXS data collection and analysis 93
4.3.8 SANS data collection and analysis 94
4.4 RESULTS AND DISCUSSIONS 95
4.4.1 Comparing neutron and X-ray scattering 95
4.4.2 Orientation under shear 98
4.5 CONCLUSIONS 111
CHAPTER 5 SILK PROTEIN AGGREGATION KINETICS REVEALED BY RHEO-IR 114
5.1 ABSTRACT 114
5.2 INTRODUCTION 115
5.3 MATERIALS AND METHODS 117
5.3.1 Reconstituted Silk Feedstock (RSF) 117
5.3.2 Native Silk Feedstock (NSF) 118
5.3.3 Rheo-IR experimental platform 118
5.3.4 Experimental procedure 121
5.4 RESULTS AND DISCUSSION 123
5.4.1 Oscillatory test 123
5.4.2 Static infrared spectroscopy 125
5.4.3 Coupling rheology and infrared spectroscopy 128
5.4.4 Effect of the polarisation 134
5.4.5 Self-Modelling Curve Resolution (MCR) 135
5.5 CONCLUSIONS 139

CHAPTER 6 INTERRUPTING SILK'S PROCESSING 141
6.1 ABSTRACT 141
6.2 INTRODUCTION 142
6.3 METHOD 146
6.3.1 Controlled In situ spinning experimental setup 146
6.3.2 UV-vis-NIR measurements 147
6.3.3 Native silk preparation 148
6.3.4 High fidelity reconstituted silk feedstock preparation 148
6.3.5 Rheology and infrared measurements 148
6.4 RESULTS AND DISCUSSION 148
6.4.1 Silk curing infrared spectra 148
6.4.2 Effect of humidity upon silk secretion 151
6.4.3 Effect of humidity of dried fresh silk fibres 153
6.4.4 Wild silk curing 155
6.4.5 Silk in situ solubilisation 160
6.4.6 Controlled spinning reconstituted silk flow properties comparison 161
6.4.7 Compared silk shear sensitivity 164
6.5 CONCLUSIONS 166
CHAPTER 7 THE CHEMICAL DIVERSITY OF SILK REVEALED BY INFRARED SPECTROSCOPY 168
7.1 ABSTRACT 169
7.2 INTRODUCTION 169
7.3 EXPERIMENTAL METHOD 173
7.3.1 Native silk feedstock preparation 173
7.3.2 Silk cocoon preparation 174
7.3.3 Spectral acquisition and treatment 174
7.3.4 Multivariate analysis 176
7.4 RESULTS AND DISCUSSION 177
7.4.1 Native feedstock spectral features 177
7.4.2 Silk cocoons spectral features 182
7.4.3 Comparison of species chemical composition 185
7.4.4 Silk species classification 190
7.5 CONCLUSIONS 199
CHAPTER 8 SUMMARY, IMPACT AND FUTURE DIRECTIONS 202
8.1 THESIS SUMMARY 203
8.2 HOW IS SILK SPUN? 204
8.3 WHY IS SILK SPUN? 207
8.4 THESIS IMPACT 211
Partially formed silk makes better artificial silk feedstocks 213
8.5 FUTURE DIRECTIONS 214
REFERENCES
APPENDICES ..... M
APPENDIX 1 SILKWORM REARING ..... M
Bombyx mori\Bombycidae\Lepidoptera\Insecta\Arthropoda ..... M
Actias luna\Saturniini\Saturniidae\ Lepidoptera\Insecta\Arthropoda ..... N
Antheraea yamamai\Saturniini\Saturniidae\Lepidoptera\Insecta\Arthropoda ..... O
Attacus atlas\Attacini\Saturniidae\Lepidoptera\Insecta\Arthropoda ..... P
Saturnia pavonia\Saturniini\Saturniidae\Lepidoptera\Insecta\Arthropoda ..... Q
APPENDIX 2 SPECTROSCOPY SUPPLEMENTARY MATERIAL ..... S

Wild silk shear induced denaturation ..... *S*
Dry weight fraction quantification by partial least squares ..... *T*
Infrared peak integration ..... *V*
Water intake reversibility ..... *W*
Sericin content in silkworm glands ..... *X*
Polarisation calibration ..... *Z*
Infrared and rheology data coupling with rheology data ..... *AA*
APPENDIX 3 RHEOLOGY SUPPLEMENTARY MATERIAL CC
Viscosity calibration for the Rheo-IR platform ..... *CC*
Linear viscoelastic limit validation ..... *DD*
Instrumental limit of oscillatory tests ..... *EE*
Rheology for ex situ SAXS ..... *FF*
APPENDIX 4 SAXS SUPPLEMENTARY MATERIAL ..... GG
SAXS Comparing reconstituted to native silk fibroin ..... *GG*
SAXS Pixel validation ..... *HH*
SAXS Absolute Intensity calibration ..... *JJ*
SAXS Small Q range calibration ..... *KK*
SAXS Frame validation ..... *LL*
SAXS Radiation damage ..... *MM*
SAXS Cell scanning ..... *NN*
APPENDIX 5 THESIS FINDING SUMMARY ..... QQ
APPENDIX 6 LO-FI RSF PROTOCOL ..... TT
APPENDIX 7 HI-FI RSF PROTOCOL ..... WW
APPENDIX 8 PUBLISHED MANUSCRIPTS ..... ZZ

List of figures

Figure 1.1 *Bombyx mori* complete life cycle, adapted from Lim et al.[Lim1990] 2
Figure 1.2 Stress as a function of strain for some natural and synthetic fibres, drawn by Chris Holland and adapted from Wynne et al.[Wynne1997] 4
Figure 1.3 Stress-strain curves for some natural and synthetic materials, reproduced from Vollrath et al.[Vollrath2011; Vollrath2013b] 7
Figure 1.4 a) Peptide bond dihedral angles around the carbon α. b) Ramachandran dihedral angles plot.[Ramachandran1963] c) Anti-parallel β-sheet strand. d) α-helix secondary structure..... 8
Figure 1.5 Three main types of silk. 11
Figure 1.6 Main peptide bond vibration modes. The main vibration of the amide I mode is given by yellow arrows whilst the green arrows show the direction of the amide II mode. 12
Figure 1.7 Length scale R probed by elastic scattering techniques..... 14
Figure 1.8 Elastic and viscous components of a viscoelastic bouncing ball..... 16
Figure 1.9 a) schematic of the shear deformation. b) Stress dependency on shear rate for characteristic fluid. c) Viscosity-shear rate relation for the main fluid with different behaviour. 17
Figure 1.10 Oscillatory strain and stress measured for a liquid and a solid like sample. 18
Figure 1.11 a) Schematic of the *Bombyx mori* silkworm. b) Spinning duct c) Schematics of silk's multi-scale hierarchical structure ending with the string of beads model.[Porter2009] 20
Figure 2.1 a) Solubilisation platform comprising the temperature controlled bath and the dialysis bag. b) Temperature controlled automatic dialysis system with the resistivity meter used for process monitoring. 30
Figure 2.2 Schematics of a single axis TA Ares G2 rotational rheometer with lines pointing at the most important components. The rotating components are shown in red whilst the fix parts are shown in grey. 31
Figure 2.3 a) Transport of a *Bombyx mori* silk gland to the ATR accessory. b) Deposition of the posterior part of the gland on the ATR sensor. c) Pulling-out of the gland's epithelium using forceps. d) Discarding of the epithelium. e) Lowering of cone by the rheometer at 0.1 mm/s. f) Overflowing of the native silk feedstock at set gap (30 µm). 32
Figure 2.4 a) Distribution of a RSF droplet from the dialysis bag nozzle. b) Pouring of a RSF drop on the ATR accessory or geometry bottom plate. c) Spreading of the RSF droplet over the ATR sensor of the bottom plate. 33
Figure 2.5 Carreau-Yasuda fit of a representative native silk feedstock viscosity test ($R2 >$ 0.99). 38
Figure 2.6 Infrared beam path of modern Fourier transform infrared spectrometer (Thermo Nicolet 6700). 44
Figure 2.7 Attenuated total reflection schematic. The green arrow represents an incident beam below the critical angle θ_c which is reflected and refracted. The red arrow represents a light beam above θc reflected internally and producing an evanescent wave. 47

Figure 2.8 a) Coupling of a purpose built shear cell with a Smart Orbit ATR assessor (Thermo, Madison, USA). b) Cone and plate geometry with the laboratory referential coordinate system. 48
Figure 2.9 Coupling of the rheometer and the infrared spectrometer with laboratory referential. 49
Figure 2.10 Matrices involved in the deconvolution of dynamic spectra 53
Figure 2.11 Schematic of the scattering vector for a typical small angle scattering experiment. 55
Figure 2.12 Visual representation of the Distance vector R, autocorrelation function γR and distance probability function pR 57
Figure 2.13 Small angle X-ray scattering data analysis MATLAB programming flow chart. 63
Figure 3.1 Graphical abstract of "Rheo-attenuated total reflection infrared spectroscopy: a new tool to study biopolymers" published in Physical Chemistry Chemical Physics.[Boulet-Audet2011] 66
Figure 3.2 Experimental setup used for the Shear-IR measurements with the polarisation vector relative to the laboratory coordinate system. 70
Figure 3.3 Difference spectra of a 68±3 % RSF sample under 5 s^{-1} shear rate as a function of time. 71
Figure 3.4 Difference spectra at the beginning of the growth (blue curve) and after the gelation divided by a factor of 10 (red curve). 72
Figure 3.5 Difference absorbance and centre of gravity of the major bands of a 68±3 % RSF sample under 5 s^{-1} shear rate as a function of time 73
Figure 3.6 a) Synchronous spectrum generated from the RSF shear-induced conversion presented in Figure 3.3. The orange squares represent the band rising synchronously whilst the purple box indicates components decreasing synchronously. The color scale ranges from -1.4E^{-4} (deep blue) to +1.4E^{-4} (bright red). b) Asynchronous spectrum. The red squares represent the pair of components with $v1$ before $v2$ whilst the blue square represent the component pairs where changes in $v1$ occur after $v2$. The color scale ranges from -9.4E^{-6} (deep blue) to +9.5E^{-6} (bright red). c) 2D Correlation selection and temporal rules. 75
Figure 3.7 ATR FTIR spectra before, after 2000 sec of shearing at 5 s^{-1}, after MeOH vapour treatment and their difference. 77
Figure 3.8 Strain (time * shear rate) at the growth point as a function of the dry weight fraction (concentration). The critical RSF concentration is marked as C_β and the native concentration of natural silk is marked as C_{native}. 78
Figure 3.9 Dichroic ratio of the 1512, 1547, 1512, 1617 and 1642 cm^{-1} components dichroic ratio as a function of time for a 60 ± 3 % RSF sample. 80
Figure 3.10 Schematics of the sheets' orientation relative to the setup referential. 81
Figure 4.1 Chapter 4 graphical abstract 84
Figure 4.2 Schematic of the shear cell SAXS platform for *in situ* measurements showing the shear cell as well as the velocity gradient and vorticity vector. The scattered beam is detected by the small angle detector several meters back. 89
Figure 4.3 a) Schematic of the Rheology followed by SAXS or SANS platform for spontaneous conversion studies. b) Sequence used for scanning the cell used multiple x-ray scattering patterns. 91
Figure 4.4 a) Small angle neutron scattering curves for unsheared native silk (blue curve) and 65000 seconds after shearing native silk at ~30 s^{-1} (green curve). The difference between sheared and unsheared (grey line) is fitted with a power

function from 0.003 to 0.05 A^{-1}. b) Small angle X-ray scattering curves for unsheared native silk (blue curve) and 45000 seconds after shearing native silk at ~30 s^{-1} (green curve). The difference between the two (grey line) is fitted with a power function from 0.007 to 0.05 A^{-1}. The error bars are calculated from the standard deviation of the azimuthal bins. The higher intensity above 0.09 $Å^{-1}$ for SANS compared to SAXS could be due to the incoherent scattering background 95
Figure 4.5 a) Scattering intensity at q = 0.01 $Å^{-1}$ (dashed line) as a function of the azimuthal angle for native silk for a 50 ms exposure before shear. b) After 1 second at 100 s^{-1}. The dashed line is the result of the fit Legendre polynomial function fit. ... 98
Figure 4.6 a) Second order parameter $<P_2>$ difference and b) fourth order parameter $<P_4>$ difference as a function of time and q for a native silk sample sheared at 100 s^{-1} for 1 second. 100
Figure 4.7 Second order parameter $P2$ as a function of time for native silk sheared at 1, 5, 10, and 100 s^{-1} integrated from q = 0.01 to 0.02 $Å^{-1}$. 101
Figure 4.8 a) Representative visual image 1000 seconds after shear and 45000 seconds after shearing native silk. b) Map of the isotropic scattering intensity $Iiso$ between 0.01 and 0.02 $Å^{-1}$. c) Map of the calculated $< P2 >$ between 0.01 and 0.02 $Å^{-1}$. 103
Figure 4.9 Brightness level of the visual images as a function of the local shear rate after shearing native silk for 10 seconds. The grey curves represent the sigmoid fit of the brightness level distribution. The double vertical bars show the inflexion point $\gamma 1/2$ and the single vertical bars represent the onset of the curve ($\gamma 1/2 - w$). 105
Figure 4.10 a) Integrated isotropic scattering intensity $Iiso$ between 0.01 and 0.02$Å$ as function of time as well as the shear rate for a representative sheared native silk sample. b) $Iiso$ as a function of time for a shear of 70 s^{-1}, yellow box. The $Iiso$ represents the average of each shear rate radial bin and the error bars their associated standard deviation. c) $Iiso$ as a function of the shear rate of after 45000 seconds, pink box. d) 2d sigmoid function parameters with 95% confidence bounds in bracket, R^2 = 0.98. 108
Figure 5.1 Graphical abstract of "Silk protein aggregation kinetics revealed by Rheo-IR" submitted in Acta Biomaterialia. 115
Figure 5.2 a) Schematics of the Rheo-IR setup consisting of a rheometer mounted onto the infrared spectrometer equipped with an attenuated total reflection accessory. The bottom plate of the geometry is the spectrometer's ATR accessory made of a tungsten carbide disk with an embedded diamond prism. b) Cross-sectional view of the Rheo-IR geometry with the laboratory coordinate system and the polarisation vectors. c) Top view of the flow field in relation to the laboratory coordinate system and the polarisation vectors. 119
Figure 5.3 Storage modulus G' (red lines) and loss modulus G'' (blue lines) as a function of the angular frequency for a representative native (green circles) and reconstituted (orange diamonds) silkworm feedstock (22 ± 3 % w/w). 123
Figure 5.4 a) Native silk feedstock spectrum before shearing (blue line with arrows for p polarisation and red line with circles for s polarisation), reconstituted silk feedstock before shearing (yellow line with squares for p polarisation and brown line with hexagons for s polarisation). b) Difference between after and before the slow exponential shear ramp profile for native silk feedstock and reconstituted silk feedstock with assigned components. *Miyazawa1961; Moore1976;*

Venyaminov1990; Yoshimizu1990; Muller1993; Goormaghtigh1994a; Sonoyama1997; Sonoyama2000; Garside2005; Lv2005; Taddei2005; Teramoto2005; Jeong2006; Boulet-Audet2008 The p polarisation difference spectra were multiplied by 0.5 for comparison. The flow direction vector relative to the laboratory coordinate system is represented on top left corner. 125
Figure 5.5 Viscosity, first normal force, amide I and II centre of gravity shift as a function of the shear rate and time for NSF and RSF for two exponential shear ramps (slow ramp a and b , fast ramp c and d). The black crosses represent the end of the shearing after the exponential shear ramp or once the 250 kPa threshold was reached. The unspun silk molecules are represented by yellow cartoons with its outer hydration shell represented by a blue outline and the converted fibroin illustrated as dark green string of beads..... 129
Figure 5.6 Amide I and II band shift as a function of time under low and high shear rates for native silk fibroin samples using p and s polarisation. The shear rate transient experiment is analogous to the experiment performed in section Chapter 4. 135
Figure 5.7 Evolving Factor Analysis (EFA) initial estimate of the concentration profile (eigenvalue threshold = 1) 136
Figure 5.8 a) Four components MCR-ALS deconvolved concentration profile. b) Pure spectra for native silk sheared under an exponential shear ramp. 137
Figure 6.1 Chapter 6 graphical abstract..... 142
Figure 6.2 a) Schematics of the experimental setup for the *in situ* study of silk's post-spinning by ATR-IR with a *Bombyx mori* silkworm b) Photo of a silk thread spun directly onto the ATR sensor under controlled environmental conditions. 146
Figure 6.3 Infrared spectra between of *Bombyx mori* native hydrated unconverted (lime), unconverted dried (brown) and hydrated converted (purple) silk as well as the difference between them (blue and black curves). The blue arrows represent the direction of the amide I and II band shift caused by dehydration (reverse for hydration process) whilst black arrows point the direction of the conversion induced shift (irreversible process)..... 149
Figure 6.4 Centre of gravity of the amide I and II band as a function of time after secretion for a single *Bombyx mori* fibre spun at 1% relative humidity at ~5 L/min (light curves) and 95% relative humidity at 50 mL/min (dark curves). The dashed lines represent the fitting results of exponential functions. 152
Figure 6.5 a) Rehydration kinetics of few dry spun fibres under a linear humidity increase ramp (1 to 95% RH), infrared spectra and centre of gravity of the amide bands for *Bombyx mori*. b) *Saturnia pavonia.* 154
Figure 6.6 a) *Saturnia pavonia* cocoons UV-vis spectra of a dry spun silk cocoon disk before (grey) and 8000 seconds (brown) after expose to humidity. The difference is shown in red b) Difference spectrum as a function of time. 156
Figure 6.7 a) Arbitrary unit Infrared spectrum of dry and wet spun *Saturnia Pavonia* cocoons (n =30). The absorbance was normalised to the integrated area between 1800 and 900 cm^{-1}..... 157
Figure 6.8 Arbitrary unit infrared spectra of dried dope from *Attacus atlas* from the middle division of the silk gland. The absorbance was normalised to the integrated area between 1800 and 900 cm^{-1}. 159
Figure 6.9 a) Dry spun silk before solubilisation b) After solubilisation c) ATR-IR spectra before (black) and after (red) adding LiBr. d) Amide II band area of dry spun silk fibres under LiBr 9M at 25°C. 160
Figure 6.10 a) Native silk feedstock average storage and loss modulus b) High fidelity reconstituted silk feedstock at 22 ± 3 %. The red lines represent the storage

modulus G'' whilst the blue line is the loss modulus G''. The error bars represent the standard deviation of the sample probed. 162
Figure 6.11 a) Native silk average viscosity (green curves) and normal force (magenta curves) for native under an exponential shear ramp. b) High Fidelity Reconstituted Silk Feedstock. The error bars represent the standard variation of the different tests. 163
Figure 6.12 Native Silk Feedstock (NSF) and High Fidelity Reconstituted Silk Feedstock (Hi-Fi RSF) amide bands centre of gravity of under an exponential shear ramp from 0 to 150 s^{-1}. 165
Figure 7.1 Graphical abstract for the "The chemical diversity of silk revealed by infrared spectroscopy" authors: Boulet-Audet, M. Vollrath, F. and Holland, C. manuscript in preparation for submission in Biomacromolecules. 169
Figure 7.2 Summary of higher-level relationships of the superfamily related to species studies adapted from Regier et al.[Regier2008a] The number in bracket represents the number of species measured in the superfamily. 172
Figure 7.3 Infrared spectra of unspun native silk feedstock from domesticated silkworm silk (*Bombyx mori*), wild silkworm silk (*Attacus atlas, Antheraea yamamai, Actias luna, Saturnia pavonia*) and spider (*Nephila edulis* major ampulate). The 1700 to 1500 cm^{-1} region is not shown since no important difference between species were observed. 178
Figure 7.4 a) Infrared spectra of key species innermost layer and sericin spectrum. b) Outermost layer spectra. 183
Figure 7.5 a) Relative area of a band assigned to calcium oxalate (740-800 cm^{-1}). b) Relative area of peak associated with $(A)_n$ β-sheets (931-983 cm^{-1}). c) Relative area of a $(AG)_n$ β-sheets assigned band (984-1006 cm^{-1}). d) Relative area of a band associated with tannins band (1094-1135 cm^{-1}) d) Relative area of a sericin marker band (1384-1403 cm^{-1}). The outermost layer is presented by brown bars and innermost layer is represented by green bars. The error bars represent the standard deviation of the different observation. A value of 1 represent the higher area measured amongst all the observations. 186
Figure 7.6 Ultrametric tree generated from the infrared of native feedstock main canonical functions. 191
Figure 7.7 First and second canonical function of the cocoon spectra contributing to 62% of species discrimination. 192
Figure 7.8 Ultrametric tree generated from the hierarchical clustering analysis of cocoon infrared spectra main canonical functions. Species with with Euclidean distance smaller than 525 were regrouped together. 194
Figure 7.9 a) Cladogram generated from the phylogenetic analysis of Regier et al.[Regier2002; Regier2005; Regier2008a; Regier2008b; Chen2012c] b) Ultrametric tree generated from infrared spectra cocoons main canonical functions. 198
Figure 8.1 A graphical summary representing the techniques used and the types of silk measured for the thesis work. The lower part lists the attributes of deposition and ejection as well as the compromise achieved by spinning. The deposited example is a *Gazella* grown keratin horn and a gastropod shell whilst the ejected example is an *Onychophora* (red velvet worm) and a *Scytodes fusca* (spitting spider). 210
Figure A.1 a) *Bombyx mori* (white) silk gland. b) *Bombyx mori* yellow strain worm. c) *Bombyx mori* yellow strain moth emerging from its cocoon. The coin showed on the picture had a diameter of 18 mm. ..... M

Figure A.2 Aerial photography of the parks surrounding the University of Oxford. The locations of the trees from which leaves were collected are marked by arrows. .....N
Figure A.3 a) *Actias luna* last instar worm. b) *Actias luna last* silk glands. c) *Actias luna* cocoon. The coin showed on the pictures had a diameter of 18 mm. .....O
Figure A.4 a) *Antheraea yamamai* second instar worm. b) *Antheraea yamamai* moulting. c) *Antheraea yamamai* final instar worm. d) *Antheraea yamamai* silk gland. The coin showed on the pictures had a diameter of 18 mm. ..... P
Figure A.5 a) *Attacus atlas* second instar worm. b) *Attacus atlas* final instar worm next to the ATR accessory of the infrared spectrometer. c) *Attacus atlas* silk glands. The coin showed on the picture had a diameter of 18 mm. .....Q
Figure A.6 a) *Saturnia pavonia* second instar worm. b) *Saturnia pavonia* final instar worm. c) *Saturnia pavonia* silk glands. d) *Saturnia pavonia* tanned cocoon. The coin showed on the pictures had a diameter of 18 mm..... R
Figure A.7 Infrared spectra before and after shear-induced denaturation of *Bombyx mori* (red curves)and *Attacus atlas* (blue) along with their corresponding difference spectrum. ..... S
Figure A.8 Partial Least squares (PLS) calibration curve for the dry weight quantification based on 4 factors. .....U
Figure A.9 Low frequency infrared band of *Bombyx mori* and *Antheraea Pernyi* with integrated bands. A linear baseline between the regions boundaries was subtracted from the integrated area. V
Figure A.10 a) Rehydration kinetics of few *Bombyx mori* dry-spun fibres under a humidity cyclic ramp, centre of gravity of the amide bands b) Rehydration kinetics of few 2 days old dry-spun fibres under a linear humidity increase ramp, centre of gravity of the amide bands. .....W
Figure A.11 a) infrared spectra of silk solution casted films on the ATR accessory as a function of the position (dark green posterior, light green anterior part). b) Absorbance ratio of the 1010-1145 region between the silk dope and a sericin extract. ..... Y
Figure A.12 Integrated absorbance between 4000 and 2600 cm^{-1} of the water O-H stretching modes as a function of the angle of the polariser. ..... Z
Figure A.13 Rheo-IR calibration curve comprising 39 independent measurements of calibration oils of 0.026, 0.101, 1 and 10 Pa·s provided by Malvern Instruments. CC
Figure A.14 a) Amplitude sweep from 1 to 50 Pa at 6.28 Rad/s for native silk feedstock b) Amplitude sweep Amplitude sweep from 1 to 100 Pa at 62.8 Rad/s for native silk feedstock..... DD
Figure A.15 Storage modulus G' for a range of silk feedstock collected using the Bolhin Gemini Nano Rheometer in the Rheo-IR platform with a strain γ of 0.002. ..... EE
Figure A.16 First normal force as a function of the accumulated strain..... EE
Figure A.17 a) average storage modulus G' (red lines) and loss modulus G'' (blue lines) as a function of the angular frequency for silkworm feedstock. b) Viscosity and first normal force as a function of time for a representative sample sheared at 1 s^{-1} for 300 s and 10 s at 100 s^{-1} .....FF
Figure A.18 a) Scattering curves for native silk and reconstituted silk, b) Guinier plot for native and reconstituted silk..... HH
Figure A.19 Detector mask from a typical scattering pattern obtained using a 1M Pilatus detector for native silk fibroin. II

Figure A.20 Uncorrected Eltex intensity left pane (top pane), uncorrected water intensity (bottom pane) ..... JJ
Figure A.21 a) I(q) as a function of the azimuthal angle and q for rat tail hydrated collagen, b) I(q) at 140 degrees for hydrated collagen with helix lattice order labels. ..... KK
Figure A.22 Transmission for a native silk sheared at 1s^{-1} for 300 seconds and corresponding scattering pattern near the beam. The scattering was measured for 1 second every 4 seconds. Rejected time frames outside the 2 σ interval are presented in red. ..... MM
Figure A.23 $I(q)$ of static native silk as a function of time under constant X-ray exposure. NN
Figure A.24 a) Transmission of an empty cell as a function of the horizontal position, b) Cell mapping scattering acquisition sequence. ..... OO
Figure A.25 Schematic of the Hi-Fi RSF process. ..... YY

List of tables

Table 1.1 Most relevant literature cited in this thesis. Highlighted in blue are the thesis contribution areas. NSF is the acronym for native silk feedstock whilst RSF stands for reconstituted silk feedstock. 22
Table 2.1 Metadata collected during the rearing of some wild silkworm species. The coin showed on the pictures presented had a diameter of 18 mm. 27
Table 2.2 Fundamental rheological quantities calculated for a cone and plate as well as parallel plate geometries. σ strands for stress and γ for the shear rate. Ω is the angular velocity and $\theta 0$ is the cone's angle. 35
Table 3.1 Assignment of the main fibroin bands 73
Table 7.1 Assignment of the main bands present in silk between 1700 and 1315 cm^{-1}. (δ is bending, υ is stretching, w is wagging, r is for rocking, * is for "strongest for") 179
Table 7.2 Assignment of the main bands present in silk between 1308 and 779 cm^{-1}. δ represents bending, υ is for stretching and r for rocking). 180
Table 8.1 Summary of the chapter's contribution to the final conclusions. See Appendix 5 for a complete list. 203
Table A.1 List of macros written for task automation, data acquisition, data analysis and data visualisation. ..... BB
Table A.2 The main findings from Chapter 3 and 4 with their associated observation and interpretation. $Iiso$ is the isotropic scattering intensity. RSF is the abbreviation for reconstituted silk feedstock ..... QQ
Table A.3 The main findings from Chapter 5 with their associated observation and interpretation. NSF is the abbreviation for native silk feedstock. γi represents the instability shear rate whilst GN is the plateau modulus and $\eta 0$ is the zero shear viscosity. MCR-ALS is the abbreviation of self-Modelling Curve Resolution Alternating Least Square. ..... RR
Table A.4 The main findings from Chapter 6 and 7 with their associated observation and interpretation. RSF stands for reconstituted silk feedstock whilst Hi-Fi stands for High Fidelity. RH stands for relative humidity. IR is the abbreviation for infrared ..... SS

List of abbreviations and symbols

Generic

ψ, φ	*dihedral angles*
AA	*Amino Acid, residue*
Ala	*alanine*
amm	*Anterior part of middle piece of middle division*
CCD	*Charge Coupling Dispositive*
DLS	*Dynamic Light Scattering*
DW	*Dry weight*
Gly	*glycine*
HPLC	*High Pressure Liquid Chromatography*
LCD	*Liquid Crystal Dispositive*
MaG	*Major ampulate Gland*
MaSp1	*Major ampulate Spidroin 1*
MaSp2	*Major ampulate Spidroin two*
MiG	*Minor ampulate Gland*
min	*minutes*
MiSp1	*Minor ampulate Spidroin 1*
MiSp2	*Minor ampulate Spidroin 2*
M_w	*Molecular Weight*
MWCO	*Molecular weight cut-off*
NSF	*Native Silk Feedstock*
p	*Posterior piece of the silkworm gland*
Pa	*Pascal (N/m²)*
pm	*Middle division posterior piece of the silkworm gland*
pmm	*Posterior part of middle piece of middle division*
PPII	*Polyproline two helix*
Recon	*Reconstituted*
RH	*Relative Humidity*
RSF	*Reconstituted Silk Feedstock*
s	*Seconds*
SD	*Standard Deviation*
SE	*Standard Error*
t	*Time (seconds)*
W/V	*Weight on Volume fraction*
W/W	*Weight on Weight fraction*
N	*Newton (kg*m*s^{-2})*
n	*Number of observations*

Infrared spectroscopy

ω	*Angular frequency of the incident wave or angular velocity*
λ	*Light wavelength (nm or Å)*
$\langle E_x^2 \rangle \langle E_y^2 \rangle \langle E_z^2 \rangle$	*Squared average amplitude of the evanescent wave electric field*
$\langle P_2 \rangle$	*Second order parameter*
$A_{\parallel}$	*Absorbance parallel to the reference axis*
$A_{\perp}$	*Absorbance perpendicular to the reference axis*

A_P ..... *p-polarised absorbance*
A_S ..... *s-polarised absorbance*
C^T ..... *Concentration profiles matrix for all components T*
G^* ..... *Complex modulus (Pa or N*m^{-2} or kg*m^{-1}*s^{-2})*
G_0 ..... *Zero modulus, G' extrapolated at 0 Hz (Pa)*
G_N ..... *Plateau modulus, G' at minimum tan δ (Pa)*
M_x, M_y, M_z ..... *Vibration mode component along the lab's coordinates x, y and z*
R^{ATR} ..... *Attenuated total reflection dichroic ratio dichroic ratio (A_P /A_S)*
R_P, R_S ..... *p and s polarised reflectance*
R^T ..... *Transmission dichroic ratio ($A_{\parallel}/A_{\perp}$)*
S^T ..... *Pure spectra matrix for all components T*
k_x, k_y, k_z ..... *Extinction coefficient along the lab's coordinates x, y and z*
n_1, n_2 ..... *First and second medium refractive index*
n_∞ ..... *Refractive index in the visible range*
n_{air} ..... *air refractive index*
$n_{crystal}$ ..... *ATR crystal refractive index*
n_x, n_y, n_z ..... *Refractive index along the x, y and z axes*
θ_B ..... *Brewster angle*
θ_c ..... *Total internal reflection critical angle*
θ_{pol} ..... *Angle between the electric field and the vibration mode*
θ_r ..... *Reflected light angle*
θ_t ..... *Transmitted light angle*
$\bar{\nu}$ ..... *Vacuum light frequency*
c ..... *Sample concentration*
FFT ..... *Fast Fourier Transform*
A ..... *Absorbance*
AD ..... *Anomalous Dispersion*
ATR ..... *Attenuated Total Reflection*
$CP\ 1/10$ ..... *Cone and Plate: 1 degree, 10 mm of diameter*
$DRIFT$ ..... *Diffuse Reflection Infrared Fourier Transform*
E ..... *Electric field*
$FTIR$ ..... *Fourier Transform Infrared*
G' ..... *Elastic modulus or storage modulus (Pa)*
G'' ..... *Viscous modulus or loss modulus (Pa)*
KKT ..... *Kramers-Krönig Transform*
M ..... *Transition moment*
MCT ..... *Mercury Cadmium Telluride*
T ..... *Number of pure spectra/concentration profiles*
d ..... *Film total thickness*
l ..... *Beam path length*
z ..... *Film normal axis*
ε ..... *Molar absorptivity*
θ ..... *Incidence angle or polariser angle or tilt angle*
ν ..... *Stretching vibration mode or vibration frequency*
υ ..... *Velocity of the moving mirror*
$\psi\ (\nu_1, \nu_2)$ ..... *Asynchronous 2D spectrum*
$\phi\ (\nu_1, \nu_2)$ ..... *Synchronous 2D spectrum*

Rheology

$\dot{\gamma}_c$	*Critical shear rate for triggering crystallisation (second^{-1})*
$\dot{\gamma}_i$	*Shear rate instability point triggering conformation conversion*
$\dot{\gamma}_p$	*Critical shear rate for shear thinning passed the LVR (second^{-1})*
$\dot{\gamma}_\tau$	*Shear rate at relaxation time (onset of shear thinning)*
T_r	*Trouton ratio*
$\hat{f}()$	*Fourier transform*
$\dot{\gamma}$	*Shear rate (second^{-1})*
η_0	*Zero shear viscosity (Pa·s)*
η_e	*Elastic viscosity (Pa·s)*
τ_p	*Relaxation time*
h	*Geometry gap (m)*
CP	*Cone and plate*
LVE	*Linear Viscoelastic Elastic*
PP	*Parallel plate*
T	*Torque or Couple ($N * m$)*
a	*Rate of transmission of the Carreau-Yasuda constitutive model*
n	*Power-law exponent characteristic of the shear thinning rate*
$v(r)$	*Velocity profile*
w	*Energy density (Pa, W/m^3)*
w	*Specific work (MPa or MJ/m^3)*
Ω	*Angular velocity (radian / second)*
γ	*Strain (unit less ratio)*
δ	*Phase angle*
η	*Viscosity (Pa·s)*
μ	*Newtonian viscosity, scalar constant (Pa·s)*
σ	*Shear stress (Pa)*
τ	*Relaxation time (second)*
φ	*Azimuthal angle*
χ	*Extensional viscosity*
ω	*Angular frequency (Hz or s^{-1})*

Scattering

λ	*Light wavelength (nm or Å)*
$\vec{k}_i$	*Incident radiation vector*
$\vec{k}_s$	*Scattered radiation vector*
D_{max}	*Maximum dimension of a particle*
I_0	*Isotropic scattering intensity (orientation independent)*
N_A	*Avogadro number (6.022*10^{23} mol^{-1})*
$\bar{R}$	*Perfect gas constant (8.314 L*kPa*K^{-1}*mol^{-1})*
V_R	*Sample volume*
$b_i(\vec{q})$	*Scattering length of the electrons*
c_s	*Spring constant*
n_e	*Number of electrons in the volume V_r*
r_e	*Scattering length of one electron (2.8179*10^{-15})*
t_0	*Half process time*
$\bar{\nu}$	*Vacuum light wavelength*
ρ_0	*Density*
2θ	*Diffraction angle*

$Å$	*Ångstrom (10^{-10} m)*
b	*Scattering length*
c	*Concentration*
I	*Scattering intensity*
SAXS	*Small Angle X-ray Scattering*
SLD	*Scattering Length Density*
WAXS	*Wide Angle X-ray Scattering*
Z	*Atomic number*
φ	*Azimuthal angle*
A	*Scattering amplitude*
S	*Wave vector ($2\theta/\lambda$)*
T	*Temperature*
d	*Distance*
$f(\vec{q})$	*Atom's form factor*
n	*Degree of the Legendre polynomial*
q	*Wave vector*
μ	*Mass on the number of electron per mole* $(M_w/(m * N_A^{-1}))$
ψ	*Electronic partial specific volume*

Protein related glossary

Aggregation	*Caused by denaturation, this phenomenon occurs when protein mis-fold and clump together leading to precipitation of the aggregate.*
Attenuator	*Device or material designed to reducing beam intensity or particle speed.*
Conformation	*A protein's mixture of secondary structures.*
Conversion	*Process under which the protein changes its conformation.*
Crystallisation	*Formation of ordered domains in the protein.*
Denaturation	*Loss of tightly bonded water locking the protein secondary structure by inhibiting the dihedral angle rotation.*
Primary structure	*The characteristic sequence of residues or amino acids forming a protein.*
Recombinant	*Process under which genetically modified organisms express bioengineered proteins.*
Reconstituted	*Process under which solid proteins are liquefied.*
Regenerated	*Process under which the protein are restored from their denaturated state back into their initial native structure. Note that "regenerated" is often used instead of "reconstituted"* in the literature .
Secondary structure	*The local three-dimensional structure adopted by a polypeptide chain once folded including sheets, helices, or turns.*

Chapter 1

Introduction

This chapter contextualises the work performed to answer my thesis' two overarching questions: "Why and how silk is spun?" It describes where silk comes from and what is already known about its structure and processing. I will then introduce the techniques used and place them within the context of relevant previous work in this area before briefly summarizing the thesis' content.

1.1 Abstract

Evolution has created a multitude of natural materials with a wide range of properties, from the abundant cellulose, which gives strength to tree trunks, to the extensible rubber derived from latex. Natural selection has also driven arthropods to grow a hardened sclerotic exoskeleton for protection,[Brunet1967] as well as secreting silk proteins as construction materials. These silks have many functions, from predation to dispersal, reproduction and protection.[Craig1997] The spinning process under which silk is formed can generate fibres that outperform the toughness of any man-made material.[Gosline1984; Gosline1999] Unlike synthetic fibres, silk is spun using only water at ambient pressure. Distantly related animals are capable of spinning threads, including silkworms,[Machida1926] spiders,[Vollrath2001] bees[Sutherland2011] and even marine amphipods.[Kronenberger2011] Even though these animals evolved independently, their silks are similar in many respects,[Holland2006] suggesting these evolutionary pathways converged towards the optimal solution for spinning high performance threads on-demand, using only proteins. Can *Homo sapiens* become the first non-arthropod species to achieve a

similar feat? To date, artificial silk spinning has resulted only in fibres with poorer strength and toughness than their natural counterpart. The distinct flow properties of artificial silk feedstock stressed the need to mimic the natural feedstock's rheology before attempting to spin it. However, the structural causes underlying the feedstock flow behaviour were poorly understood. To fill this gap in our knowledge we integrated rheology with advanced spectroscopic techniques to shed light onto silk spinning.

1.2 Where does silk come from?

Once worth its weight in gold for merchants along the ancient silk road,[Gordon2004] silk is still praised by weavers around the world for its gloss, long fibres, dyeability and soft feel. For thousands of years[Good2009] silk's production method was a secret jealously kept by Asian countries, until silkworm eggs were smuggled into occidental countries. As an agricultural product, silk is sustainable.[Pauli2010] Most of the world's production comes from the common white mulberry silkworm, *Bombyx mori.* To feed to larvae, mulberry trees were planted around the world.

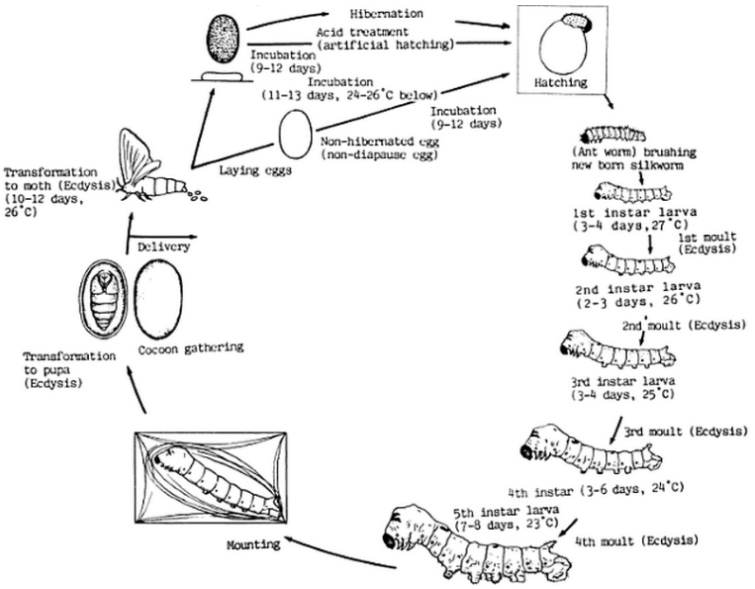


Figure 1.1 *Bombyx mori* complete life cycle, adapted from Lim et al.[Lim1990]

As shown in Figure 1.1, larva will grow 50 000 fold before reaching their last instar, having eaten more than 10 times their weight in food. At the time of pupation, silkworms will start to spin their cocoon from a single strand of silk 1200 to 1600 meters long.[Cao2009] The cocoon's purpose is to protect the larva from the environment and predation during metamorphosis into an adult moth. In nature once pupation is complete, the moth will excrete an enzyme used to pierce a hole in the cocoon to emerge and mate.[Lim1990] Each fertilised female will lay around four hundred eggs to restart the life cycle. Because sericulture is highly labour intensive, decades of research have been invested in the development of artificial analogue fibres which could replicate silk's desirable combination of lustre, softness and strength.

1.3 What makes silk desirable?

Silk threads were amongst the first solid materials found to disobey Hooke's law ($F = kx$). Wilhelm Weber discovered in 1835 that they were not perfectly elastic but also deformed in an irreversible plastic fashion. This dual behaviour confers spider silk the ability to absorb more mechanical energy than any other material of the same mass.[Gosline1999]

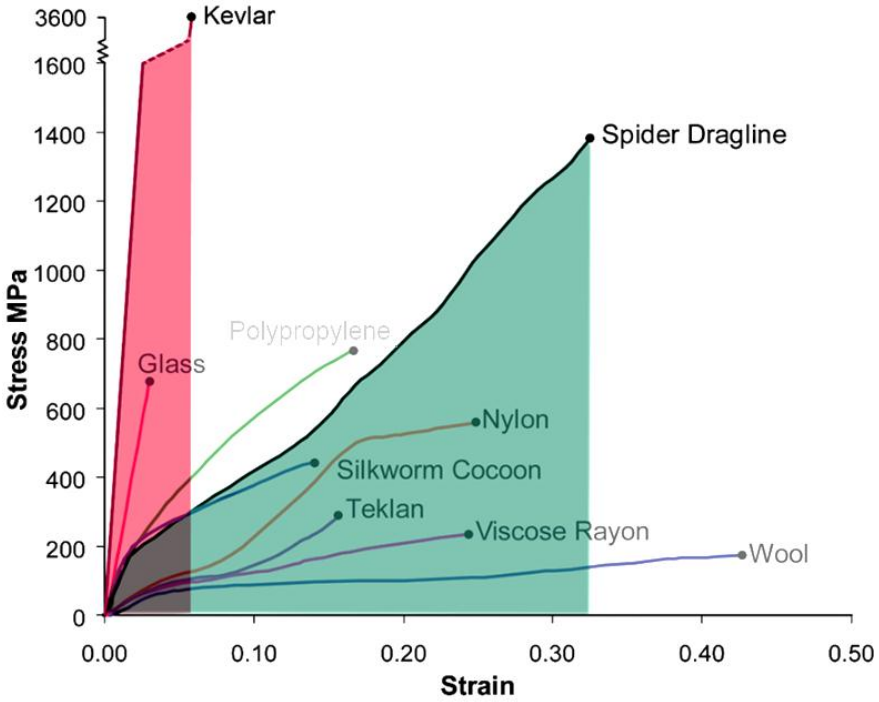


Figure 1.2 Stress as a function of strain for some natural and synthetic fibres, drawn by Chris Holland and adapted from Wynne et al.[Wynne1997]

Figure 1.2 shows the stress-strain tensile properties of natural spider and silkworm silk compared to other common manmade and natural fibres. Although artificial filaments can be made stiffer or more extensible, they are not yet as good for both properties simultaneously, as they do not strain harden and so have lower toughness (area under the curve).[Zhou2009; Elices2011; Humenik2011] Thus, spider silk has a higher toughness to weight ratio than any other natural or manmade fibre.[Wynne1997]

In addition, silk is an antigen free animal protein which can be implanted into the human body.[Altman2003] Some wild silkworm species such as *Antheraea myllita* possess amino acid patterns (such as RGD) known to promote cell adhesion and thus enhance biocompatibility.[Minoura1995] Consequently, silk has numerous biomedical applications.[Altman2003] For thousands of years silk fibres have been used as suture threads along with other natural materials like cotton and animal gut.[Halsted1913] Because of the wax coating normally added, silk suture threads are defined by the U.S. Pharmacopeia (USP) as non-absorbable, but silk

devices can be designed to degrade at controlled rates inside the human body.[Omenetto2010] In addition, silk does not necessarily need to be a fibre and can be shaped into any form for other applications. Resolubilised silk can be turned into drug delivery systems,[Wenk2008] vaccine stabilisation matrices,[Zhang2012b] nerve regeneration guides,[Cunha2011] reversible electro activated adhesives,[Leisk2010] ligament replacements[Fan2009] or even bone repair scaffoldings.[Meechaisue2007] In addition to its biocompatibility and tenacity, silk fibroin can be made transparent to visible light for bio-optics applications such as fibre optics or as substrates for implantable electronics.[Omenetto2010; Kaplan2012; Sun2013]

1.4 Synthetic silk analogues

Because of its desirable combination of properties, decades of scientific research have been devoted to producing artificial analogues. Among the first attempts to make artificial silk was nitro-cellulose, which managed to give cotton the lustre of silk but had the alarming tendency to ignite violently when brought close to a flame.[Le Couteur2003] Interestingly, one can use silk's fire retardation properties to differentiate between natural and artificial fibres.[Economy1977] Further efforts toward mimicking silk have given us valuable artificial textile fibres such as nylon, which revolutionised women's fashion[Le Couteur2003] and Kevlar® (polyaramide), saving lives as ballistic protection (i.e. bullet proof vests).[Greenwoo1974] Despite their very different physical and engineering properties,[Gosline1999] these two artificial polymers share the same main types of amide chemical bonds with natural silk. Although modern engineering polymers present a range of interesting properties, efforts have been directed towards biological methods to make artificial silk as a true analogue could only be made of protein, a biopolymer.

1.5 Bioengineered artificial silks

An alternative to chemical methods to produce artificial silk is to use genetically modified organisms. These bioengineered silks are produced using recombinant DNA technology to express proteins in a variety of organisms such as yeasts,[Fahnestock1997] bacteria,[Xia2010] insect cells,[Huemmerich2004] tobacco plants,[Scheller2001] or even goats.[Lazaris2002] Although it allows the control of the protein's primary sequence, the purification of those proteins is challenging and poor yields are the norm. Despite matching native protein sizes,[Xia2010] the material's resulting mechanical properties do not match its natural counterpart (see Figure 1.3). The astronomical cost of these techniques is another obstruction to large scale production. Notwithstanding, this approach was chosen by some biotechnology firms such as Nexia Biotechnologies ltd., AmSilk® and Spiber technologies® which prefer the precise sequence control over low cost.

1.6 Artificial silk from cocoons

The most cost effective method to liquid silk feedstocks is to tap into the diverse pool of the animals which have evolved to produce large amounts of silk for use at a specific time of their life cycle, silkmoths. Spiders produce silk during their entire life, but only in minute amounts and it is painstaking to harvest by forced reeling. The thousands of silk types[Regier2008b] produced by wild silkworms have a broad range of composition and morphology,[Chen2012c] some silkworms even produce silks very similar to spider filaments (see Chapter 7). Using strong chaotropic agents such as a concentrated lithium bromide solution, silk fibres can be solubilised into artificial silk feedstock. From this liquid, artificial silk fibres can be spun again or cast into any other shape. Each year, more than 500,000 tonnes of raw silk cocoons are produced worldwide.[Tomita2011] Considering that a portion of this

production consists of double cocoons and short fibres that are not reelable, thousands of tons could be potentially redirected to artificial silk production through liquefaction. The only limitation is the fixed amino acid block sequence of the biopolymer, which is dictated by the genes of the animal producing the silk. Fortunately, post-treatment chemical decoration can still be used to alter silk's structure. Non domesticated species' silk, with varying properties can thus present properties more suitable for certain applications. This cheaper and scalable technology was chosen by Orthox Ltd. and Oxford Biomaterials Ltd. to produce their silk biomedical devices.

Numerous attempts have been made to spin fibres from these artificial silk feedstocks using various techniques. However this has been with limited success as they could not achieve both strength and extensibility simulatenously.[*Elices2011Matsumoto1996, Seidel2000, Lazaris2002, Yao2002, Shao2003 Zuo2006*]

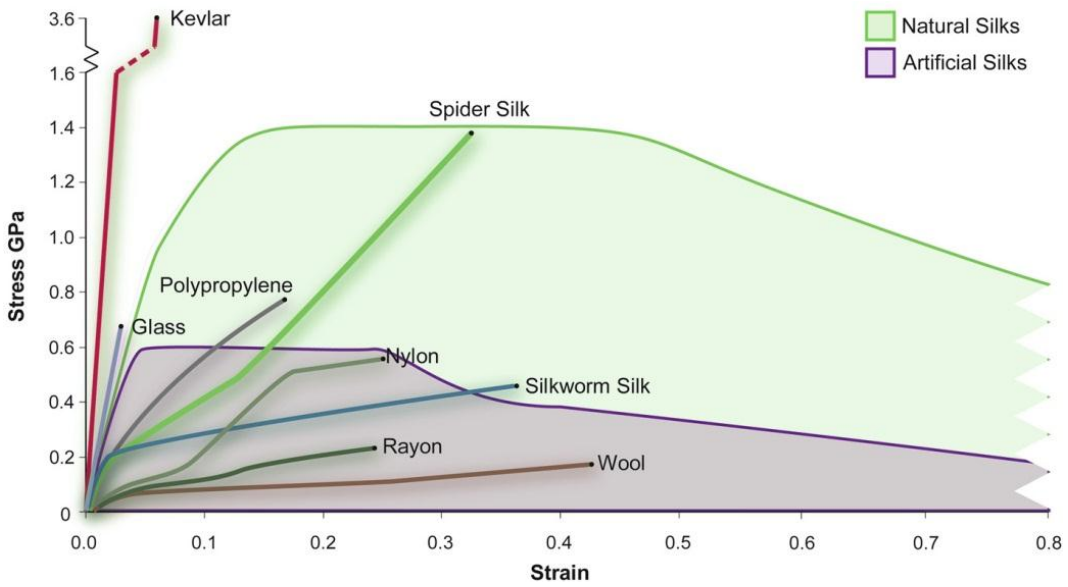


Figure 1.3 Stress-strain curves for some natural and synthetic materials, reproduced from Vollrath et al.[*Vollrath2011; Vollrath2013b*]

Figure 1.3 shows the stress-strain domain which natural silk can achieve (green) and the mechanical property domain achieved by artificially spun fibres. The chief goal of silk

biomimicry is thus to extend the domain of artificial silks' tensile properties to match their natural counterparts. Because of our lack of a coherent understanding of the molecular mechanism underlying the spinning process, true silk fibre analogues with comparable properties are yet to be spun artificially. Even with carefully controlled processing conditions, this feat will be impossible if the starting feedstock does not have the potential to produce such fibres. This is why we must first have a coherent understanding of the molecular components in the precursor feedstock.

1.7 What is silk made of?

Silk is mostly comprised of high molecular weight fibroin proteins consisting of long chains of amino acids assembled at the point of synthesis in the silk gland cells.[Akai1983] Each amino acid is linked to another by a peptide bond to form the protein's primary structure.

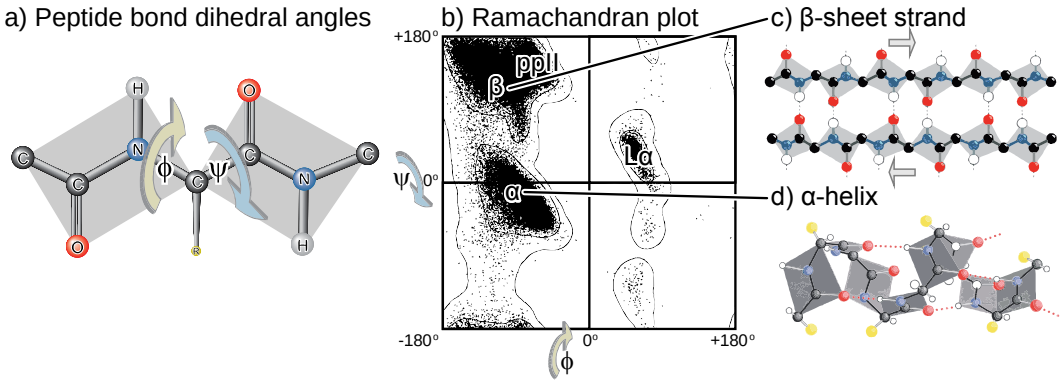


Figure 1.4 a) Peptide bond dihedral angles around the carbon α. b) Ramachandran dihedral angles plot.[Ramachandran1963] c) Anti-parallel β-sheet strand. d) α-helix secondary structure.

As represented by the grey rectangles on Figure 1.4a, it is commonly assumed that the amide plane is fixed because of the resonance in the molecular bond between the oxygen, nitrogen and carbon atoms. By mixing their orbitals, these atoms form an amide functional group with planar sp^2 hybridation at a 120° bond angle.[Pauling1951] This hybridisation greatly reduces the protein's degrees of freedom as the atoms included in the amide plane are

assumed to keep the same relative position. Therefore, it leaves only two possible rotations around the N−Cα and Cα−C=O, defined as the dihedral angles ϕ and ψ respectively. The knowledge of the dihedral angle values theoretically allows the localisation of atoms to determine the three-dimensional secondary structure.[Ramachandran1963] Unfortunately, the knowledge of primary structure does not provide ϕ and ψ as they are dependent on the chemical environment (H bonds, hydrophobic interactions, van der Waals forces, etc). As shown in Figure 1.4b, the different possible angles adopted by proteins can be illustrated as a Ramachandran plot showing the combinations of ϕ and ψ observed for the different conformations of known protein structures obtained by X-ray crystallography. Figure 1.4c shows the model of an anti-parallel β-sheet strand as found in spun silk.[Marsh1955b] β-sheet hydrogen bonds (dashed lines) are formed with another protein chain (intermolecular). Helices, sheets, turns, and unordered structures can be found in large proteins, but absolute prediction from the primary amino acid sequence is currently not possible. On the other hand, Figure 1.4d shows the model of an α-helix, which may also be present in certain silks.[Dong1991] In contrast to β-sheets, α-helices form intramolecular hydrogen bonds at every loop constituted of 3.6 amino acids. Certain residues are more likely to generate certain secondary structures. For example, alanine predominantly forms a helical structure whilst proline residues tend to create disordered structures due to its smaller number of degrees of freedom.[Eker2003] Strongly bound water molecules are known to hold the secondary structure in place and could have the effect of unlocking the dihedral angles when the protein is denatured.[Porter2012; Porter2013] The folding of these secondary structures in space defines the tertiary structure, giving the protein domains. Furthermore, the macromolecular assembly of these domains is named the quaternary structure. Proteins with a round overall shape will be described as globular whilst elongated proteins like silk, keratin, collagen and elastin are referred to as fibrous proteins.

Beyond an individual protein, fibrous proteins like silk form long strings or filaments on the nanometre scale. Fibrous proteins are generally inert and insoluble, and are mainly used for structural tissues or storage.[Huggins1943; Coulombe2002] Their amino acid sequence is often repetitive and with only a few different amino acids. Proteins such as collagen and elastin, for example, are secreted by the organism's cells in order to form the extra-cellular assembly or matrix of many organisms.[Reiser1992] Another fibrous protein, keratin, is present in many animals, forming unordered nanoscale filaments conferring stiffness to nails, claws, skin and feathers.[Coulombe2002] Biosynthesis not only controls the sequence, but the three dimensional structure of the proteins as well,[Baltimore1977; Buchner2004] allowing the slow formation of complex self-assembled composite structures. The precision with which living organisms control their protein's organisational level can explain the extraordinary diversity of structures formed by fibrous proteins.[O'Brien1998] If fibrous proteins can be clearly identified, what distinguishes silks as distinct from all these other proteins?

1.8 What are the types of silks?

To lift potential ambiguities as to which proteins qualify as silks, I used Catherine L. Craig's definition of silk for this thesis.

"Silks are fibrous proteins containing highly repetitive sequences of amino acids and are stored in the animal as a liquid and configure into fibers when sheared or spun at secretion" [Craig1997]

Amongst fibrous proteins, silk proteins can be categorised based on their distinctive pre-programmed sequence to assemble into three different types of structures once spun.

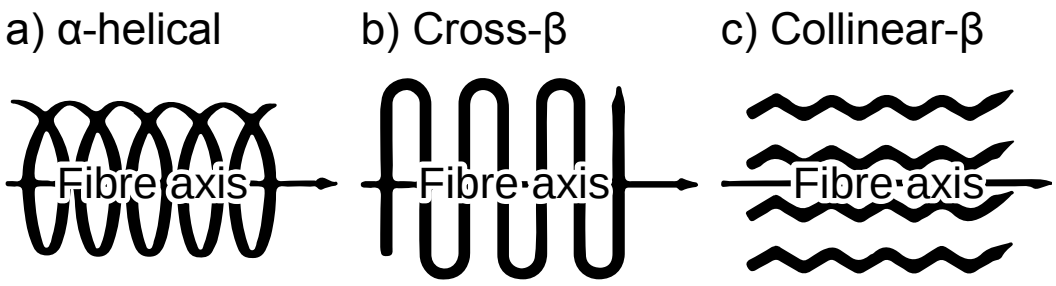


Figure 1.5 Three main types of silk.

The wide diversity of silk is encompassed by three classes with different secondary structure compositions (conformations): the α silk, the cross β silk[Geddes1968] and the common collinear β silk.[Craig1997] α silks mainly consist of helix structures similar to the one presented in Figure 1.4d and are produced by a few arthropods such as the honey bee.[Hepburn1979] The cross β silk is not reported to be produced by any spiders or Lepidoptera,[Craig1997] and is secreted by a few insects like the green lacewing fly *Chrysopa flava.*[Geddes1968] It is made primarily of β-sheets stacked perpendicular to the fibre axis in a structure comparable to amyloid fibrils.[Sigurdsson2012] When stretched, α and cross β silks sometimes have the remarkable property of converting to collinear β silks, which exhibit anti-parallel β-sheets along the fibre axis.[Marsh1955a; Simmons1996; Asakura2002b] Spiders (in their dragline fibres) and silkworms both produce collinear β silks.[Warwicker1960a] In most silkworm and spider silks the β-sheets are made of repetitive polyalanine $(A)_n$ segments, but *Bombyx mori* has poly(alanine-glycine) $(AG)_n$ blocks instead[Lucas1956] (see Chapter 7). For these animals, the main silk fibroins are very large, 390kDa for *Bombyx mori*[Shimura1976; Mita1994] and 270 to 326 kDa for the major ampullate silk of *Nephila*.[Lombardi1990; Jackson1995] Analytical techniques such as spectroscopy and scattering are required to classify these silks based on markers indicative of their secondary structures.[Marsh1955a; Warwicker1960a; Grubb1997; Riekel1999; van Beek2000; Sirichaisit2003] Since infrared spectroscopy is highly sensitive to protein conformation, it has proven particularly useful for the characterisation of silk proteins since the 1950s.[Kratky1950; Marsh1955a]

1.9 What does infrared spectroscopy tell us about silk?

Infrared spectroscopy is based on the principle that light in the µm wavelength range can excite molecular vibrations.[Mališek1971; Silverstein1981] If the infrared light's frequency matches the quantum vibration level gap, the molecules can absorb the radiation and be promoted to an excited state. For a vibration mode to be active in infrared spectroscopy and give rise to an absorption band, the relative movement of the atoms must be associated with a variation of the dipolar momentum in time below and beyond the terahertz regime.

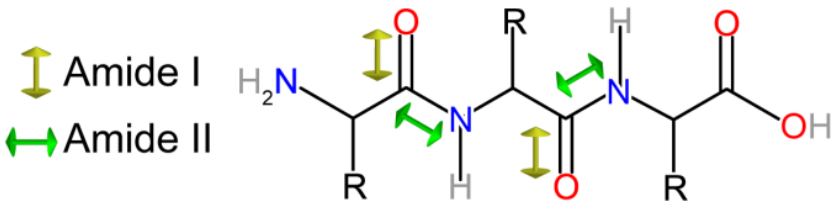


Figure 1.6 Main peptide bond vibration modes. The main vibration of the amide I mode is given by yellow arrows whilst the green arrows show the direction of the amide II mode.

For proteins, the most important mid-infrared vibration modes are associated with the peptide bond O=C-N. As shown in Figure 1.6, the amide I band corresponds mostly to the carbonyl stretching C=O with a preferential orientation perpendicular to the chain axis, whilst the amide II band is associated mainly with the C-N stretching aligned along the polypeptide chain.[Moore1976] The frequencies at which these modes will vibrate will be dependent on the strength of the neighbouring bonds which can be affected by the secondary structure and the hydrogen bonding network. Hence by measuring these frequencies, infrared spectroscopy provides valuable information on the protein conformation and molecular orientation. First used in the 1960s,[Iizuka1968] infrared spectroscopy has been extensively employed to study silk in all its form factors, including

liquid, film, scaffolding and fibre.[Yoshimizu1990; Chen2001a; Um2001; Garside2005; Chen2007; Yuan2010; Ling2011] Spectra can even be collected from a single silk fibre. These studies revealed the important difference in protein conformation before and after spinning. Using chemical or thermal sources of stress, many infrared spectroscopy studies looked at the conversion kinetics.[Chen2001b; Kweon2001; Mo2006] Unfortunately, few studies attempted to induce conversion using stresses involved *in vivo,* whilst probing with infrared light.[Chen2002a]

Infrared spectroscopy does not however provide information on length scales much larger than interatomic distance (Angstrom scale). To cover length scales in the nanometre range, small angle scattering techniques are a worthwhile complementary set of tools to characterise silk's properties.

1.10 What does small angle scattering tell us about silk?

In contrast to spectroscopy, which relies on an inelastic phenomenon based on an energy transfer between radiation and matter, small angle scattering (SAS) measures mostly radiation which is elastically scattered. SAS can provide information about the size, shape and orientation of particles over a large range of length scales.[Glatter1982] The SAS technique encompasses small angle neutron (SANS), X-ray (SAXS), and light scattering (Static SLS and Dynamic DLS). Although they are governed by a similar set of laws (Guinier,[Guinier1955] Zimm,[Zimm1945] Kratky[Kratky1949] and Porod[Porod1951; Porod1952]), these three techniques are complementary as they can probe different structures and length scales.

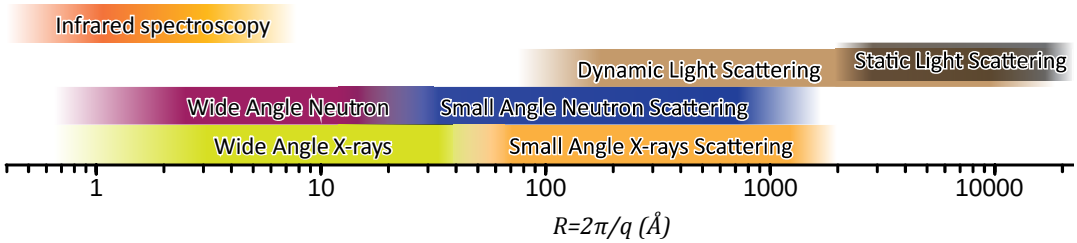


Figure 1.7 Length scale R probed by elastic scattering techniques.

X-ray scattering

As shown in Figure 1.7, X-rays can thus probe structures from hundreds of nanometres in size down to atomic distances. X-ray scattering was the first analytical technique used to study silk fibre, revealing its semi-crystalline nature.[Marsh1955a] Since then, X-rays have been used to study numerous types of silks in all its forms.[Shen1998; Takahashi1999; Asakura2002a; Gupta2009; Nagarkar2010] X-rays are sensitive to the electronic density difference within the sample. Since the number of electrons per atom increases linearly with the atomic number, heavier elements scatter much more than lighter ones. Although X-ray scattering is a single technique, it is commonly divided at around R = 50 Å between small (SAXS) and wide angle scattering or diffraction (WAXS). Although the contrast between water and protein molecules is relatively weak, the Scattering Length Density (SLD) can be measured by small angle X-ray scattering (SAXS) to study silk in solution, in order to identify the protein's structure in the liquid feedstock.[Martel2008b] However, the greater energies and brilliance involved with X-ray synchrotron sources together with poor thermal conductivity make heat damage an important consideration for biological samples.[Teixeira2008; Jacques2010]

Neutron scattering

The range of length scales covered by small and wide angle neutron scattering is comparable to X-rays. The difference comes instead from the fact that neutrons scatter from the atomic nuclei instead of from the surrounding electronic cloud. This has important repercussions. Unlike electromagnetic radiation which has an energy $E = hc/\lambda$ related to

Planck's constant h,[Planck1901] the speed of light c, and the wavelength λ, a neutron has a finite mass of $m = 1.674$ x10^{-27} kg. Consequently, the energy of a neutron is its kinetic energy, given by $E = mv^2/2$, where v is the velocity. Using the concept of de Broglie waves, it is possible to relate the kinetic energy to wavelength using: $E = h^2/2m\lambda^2$.[Broglie1973] As a result, neutrons are several orders of magnitude less energetic than photons of equivalent wavelength, for instance 0.0818 eV instead of 12500 eV at λ = 1 Å. Neutrons are thus generally considered to be a non-damaging probe, useful in studying biological materials.[Teixeira2008; Jacques2010] Another interesting feature of neutrons is the contrast offered by different isotopes of the same elements. Even though isotopes have the same atomic number, the SLD of their nucleus can be drastically different.[Sköld1986] Whereas hydrogen and deuterium have similar X-ray SLD due to their close Rydberg constants, their neutron SLD difference is large, allowing contrast matching experiments. These common experiments can resolve complex mixtures through the chemical substitution of H and D in different parts of a sample molecule or in the solvent in order to generate new SLD contrast.[Sköld1986] Unfortunately, the advantages of neutrons as a probe come at the price of flux as even the brightest sources are more than 10 orders of magnitude dimmer than the latest synchrotron X-ray beams. Neutron scattering has proved particularly useful in characterising silk fibre precursor in static diluted solutions, giving size and shape of the protein.[Greving2010] However, no study has ever focused on monitoring silk's structural response to biologically relevant stress, such as flow.

Silk's nanoscale structure in the feedstock is responsible for the macroscopic mechanical properties of the liquid under flow. To coherently understand the impact of the nanoscale structure on the feedstock, direct measurement of the flow properties is required.

1.11 What does rheology tell us about silk?

Similar to silk feedstocks, polymer melts act both like solids and liquids, as they have an elastic component (stress dependent of strain) and a viscous component (stress independent of strain). The field of non-Newtonian rheology focuses on describing these hybrid viscoelastic materials.[Utracki1982] To determine the material's response to flow, we measure the stress σ (resistance to deformation) whilst applying a strain γ (deformation) at a given rate $\dot{\gamma}$. A simple way to describe the viscoelastic behaviour of a material is to drop it on the ground from a given height and measure the bounce.

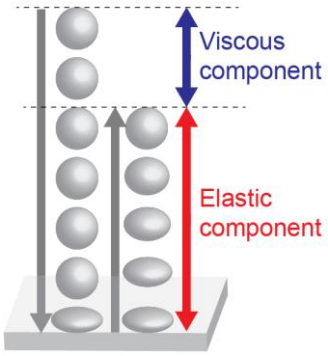


Figure 1.8 Elastic and viscous components of a viscoelastic bouncing ball.

As shown in Figure 1.8, the ratio of the elastic to the viscous component is proportional to height of the rebound compared to the height of the fall. Numerous biological materials behave this way, including silk feedstocks.[Holland2006; Moriya2009] Rheological properties can be determined in three main ways: constant shear (viscosity test), dynamic shear (oscillation test) and extensional flow (including capillary flow test).

Constant shear

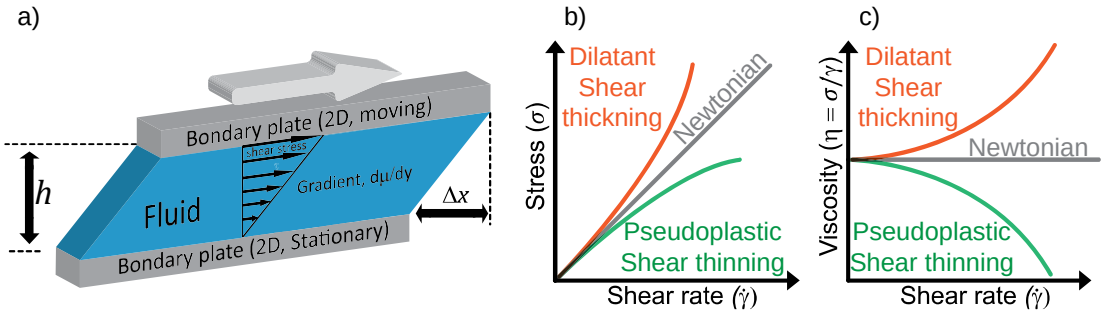


Figure 1.9 a) schematic of the shear deformation. b) Stress dependency on shear rate for characteristic fluid. c) Viscosity-shear rate relation for the main fluid with different behaviour.

Shown on Figure 1.9a, the simplest geometry for flow properties measurements is two horizontal parallel plates. Displacing one of the plates parallel relative to the other will deform the tested material resulting in a shear stress gradient from the fixed plate to the moving plate along the normal direction. As a result, the local stress will be maximum at the moving plate boundary and null at the fixed plate. As illustrated in Figure 1.9b, the strain (γ) applied is given by the dimensionless ratio of the transverse displacement to the distance between the two plates ($\Delta x/h$). The shear rate ($\dot{\gamma}$) corresponds to the derivative of the strain applied with respect to time ($\dot{\gamma} = d\gamma/dt$). The required force to move the geometry is then directly related to the sample's resistance to flow (σ). Some materials like water will flow much more easily than others such as honey. The ease with which a material flows, its viscosity, is proportional to the material's internal friction during deformation.[Ferry1980] For constant shear tests, the viscosity (η) is simply the quotient of the stress on the shear rate as $\eta(\dot{\gamma}) = \sigma/\dot{\gamma}$. Viscosity can vary by many orders of magnitude depending on the material. For instance at 1 atmosphere, the viscosity of air is just $1.8*10^{-5}$ Pa·s, water is $1*10^{-3}$ Pa·s whilst tar barely flows with $\eta = 2.3*10^{8}$ Pa·s. For these materials, the stress is directly proportional to the shear rate ($\sigma \propto \dot{\gamma}$) resulting in a rate independent viscosity (grey line on Figure 1.9c). These materials are classified as Newtonian fluids if they satisfy Newton's liquid law ($\sigma = \eta\dot{\gamma}$). However, many samples show non-Newtonian behaviour with a non-

linear response of the stress to the shear rate, as drawn on the right panel of Figure 1.9. The viscosity can either increase (shear thickening, orange curve) as do corn starch suspensions, or decrease (shear thinning, green curve) like molasses.

Dynamic shear experiments

Stress can be varied periodically to test the mechanism occurring at very short time scales and deconvolve the elastic from the viscous components of viscoelastic materials without damaging the sample. The oscillatory test consists of a sinusoidal strain applied to the sample at a given angular frequency, as $\gamma(t) = \gamma_0 sin(\omega t)$ with a strain γ_0, below the linear viscoelastic limit such that no plastic flow occurs.

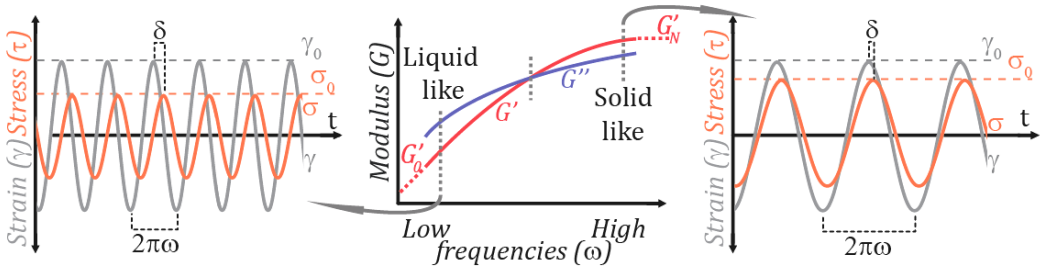


Figure 1.10 Oscillatory strain and stress measured for a liquid and a solid like sample.

Figure 1.10 shows the strain γ and the stress σ for a typical oscillatory test. The stress should also be a periodic wave, but with a phase difference δ, as the material will take a certain time to respond to the deformation $\sigma(t) = \sigma_0 sin(\omega t + \delta)$. This phase angle (δ) indicates the fluid's behaviour: $\delta = 0$, in-phase, for Hookean solid (purely elastic) or $\delta = \pi/2$, out-of-phase, for a Newtonian liquid (purely viscous). A viscoelastic fluid will have a phase angle between these two extremes.

The main advantage of the oscillatory test is its ability to deconvolve the elastic (storage) modulus G' and the viscous (loss) modulus G'' of a viscoelastic fluid like silk feedstocks. The storage modulus G' (Pa) can be calculated by the in-phase projection of the stress on strain amplitude $G' = (\sigma_0/\gamma_0)cos(\delta)$, where σ_0 is the stress amplitude (Pa) and γ_0 is the strain

amplitude (dimensionless). The storage modulus G' (red curve) is representative of the material's ability to store mechanical energy, analogous to the height at which a ball bounces back as presented in Figure 1.8. On the other hand, the loss modulus G'' is given by the out-of-phase projection $G'' = (\sigma_0/\gamma_0)sin(\delta)$. The loss modulus (blue curve) is a measure of the sample's capacity to dissipate energy, equivalent to the bounce height difference of Figure 1.8.

Independent of the absolute value of the moduli, the moduli ratio is directly related to the phase angle δ using $G''/G' = tan(\delta)$. The measured stress σ is a function of both moduli given by $\sigma = \gamma_0\big(G'cos\,(\omega t + \delta) - G''sin\,(\omega t + \delta)\big)$, represented by the orange curve on Figure 1.10. Hence, fitting the stress response to a strain using this equation allows the deconvolution of $G'$and G'' which would have been impossible through a constant shear test.

For non-Newtonian materials like native silk feedstocks both moduli can vary as a function of frequency, making the material behave differently depending on the frequency of the oscillation.[Terry2004; Moriya2009] At high frequencies, materials will typically respond more like a solid as they will have less time to relax, whilst at low frequencies they are more likely to behave like liquids with a higher G'', as they will have more time to relax. Using these oscillatory experiments, it was possible to identify for native silk feedstock the points at which G'becomes equal to G'', which is also indicative of silk's relaxation time.[Kojic2006; Holland2007]

Extensional flow

Extensional flow provides high deformation rates which can effectively align macromolecules along the deformation direction.[Petrie2006] Although biologically relevant,[Knight2000] pure extensional flow is challenging to measure for silk as its water solvent

can evaporate quickly during tests. Nevertheless, the extensional viscosity of silk feedstocks has been measured.[Kojic2006] Due to instrument availability and challenges associated with extensional flow, only constant and dynamic shear experiment were performed to study liquid silk in this thesis. However, silk's extensional flow still represents a mostly uncharted field of silk's flow properties. Although indirectly, this macroscopic material properties measurement can inform us on the behaviour of the underlying molecular structures, such as entanglement, alignment or rearrangement.[Ferry1980] Rheology has therefore played a key role in understanding silk feedstock's flow behaviour during processing and therefore how silk is spun.

1.12 How is silk spun?

Because its molecular structure can be difficult to discriminate from that of other fibrous proteins, silk is often defined based on its formation mechanism instead of its composition. Under such a definition, silks are the materials formed by pultrusion spinning.[Vollrath2009] Based on what spectroscopy, scattering and rheology tell us, we can hypothesise how silk is spun. Because of the large amount of silk produced by *Bombyx mori,* a silkworm, the spinning process of this species is commonly used a model.

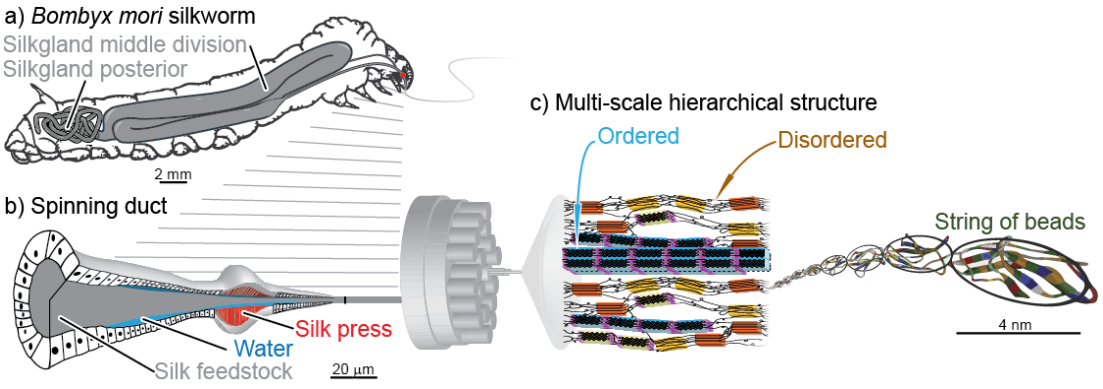


Figure 1.11 a) Schematic of the *Bombyx mori* silkworm. b) Spinning duct c) Schematics of silk's multi-scale hierarchical structure ending with the string of beads model.[Porter2009]

Figure 1.11a illustrates that once secreted by cells, silk proteins are stored in large silk glands (up to 30% of the worm's mass)[Tashiro1968; Brunet1974] at high concentration (>20 % by weight).[Tashiro1968] From the secretion point, the protein's main chains are oriented perpendicular to the gland's wall;[Vollrath2001] with hexagonal packing in spiders.[Knight1999a] For silkworm liquid silk, solution scattering suggests that the fibroin molecules are elongated.[Martel2008b; Greving2010] As shown on Figure 1.11b, the silk feedstock is then directed to the tapered spinning duct, providing a constant shear stress.[Asakura2007] As the non-Newtonian silk feedstock is flowing through the narrowing duct its viscosity decreases, making it flow more easily.[Knight2000; Holland2006] Simultaneously, the silk feedstock undergoes a pH drop and changes in metallic ion concentrations.[Magoshi1994; Knight2001] At some point before or after the silk press (or draw down taper for spiders, shown in red), the dope goes through a stress-induced phase transition from liquid, to weak gel, to solid.[Knight2000; Holland2006] For the duct of spiders, *in situ* Raman spectroscopy suggests that some conformational changes occur before the draw down taper (choking point), but that the molecular orientation only starts after the taper.[Lefèvre2008] The equivalent structure for *Bombyx mori* is the silk press. Birefringence measurements suggest it is the point where most of the molecular changes occur.[Kataoka1977; Asakura2007] If paralysed, the worm cannot use its silk press muscles to apply stress on the silk, resulting in fibres with different mechanical properties, suggesting a dynamically controlled process.[Mortimer2013]

Once the duct stops narrowing, silk is submitted to extensional forces to align the protein molecules and drive the changes in the secondary structure.[Asakura2007] Once outside the animal, silk filaments can be stretched further to increase alignment by post-drawing, which is known to modulate fibre properties.[Shao2002; Liu2005; Chen2006] For forced reeled spider silk, crystallinity was found to be higher when probing further from the spinneret

exit.[Riekel2001] The relevant literature concerning silk's structure, morphology and flow properties is summarised in Table 1.1.

Technique	Stress	System	Sample type	Reference
X-ray + rheology	Shear	*B. mori*	Liquid RSF	Chapter 4 and [Rössle2004]
X-ray scattering		*B. mori*	NSF fibres	*Warwicker1956; Warwicker1960b; Warwicker1960a*
	Extensional flow	*B. mori*	Liquid RSF	*Martel2008b*
		N. clavipes	NSF fibres	*Riekel2001*
Neutron scattering		*B. mori*	RSF & NSF	*Greving2010*
Birefringence		*B. mori*	Liquid NSF	*Kataoka1977*
Nuclear magnetic resonance (NMR)	Shear	*B. mori*	Liquid RSF	*Ohgo2008*
				Ishida1990
			Liquid NSF	*Asakura1985; van Beek2000*
Infrared spectroscopy	Shear	*B. mori*	Liquid RSF	Chapter 3 and [Boulet-Audet2011]
	Chemical		RSF films	*Yoshimizu1990; Chen2001a; Um2001; Chen2007; Yuan2010*
	Shear		RSF films	*Mo2009a*
			Liquid RSF	*Hu2006a*
			NSF fibres	Chapter 6 and Chapter 7 *Garside2005; Boulet-Audet2008; Ling2011*
			Liquid NSF	*Boulet-Audet2010*
Rheology + IR	Shear	*B. mori*	NSF & RSF	Chapter 6 *Boulet-Audet2013*
Rheology	Shear	*B. mori*	Liquid RSF	*Chen2001a; Ochi2002b; Hossain2003c; Xu2005*
			Liquid NSF	*Hossain2000; Kobayashi2001; Ochi2002a; Terry2004; Holland2006; Kojic2006; Moriya2008a; Holland2012c*
			NSF & RSF	*Holland2007*
		Wild silks	Liquid NSF	*Holland2012a*
		A. diadematus	Liquid RSF	*Rammensee2006*
		N. edulis	Liquid NSF	*Chen2002b*
	Extensional flow	*B. mori*	Liquid NSF	*Kojic2006*
Raman spectroscopy	Tensile	*B. mori*	NSF fibres	*Pellerin2005*
				Lefevre2009; Lefèvre2011
	Ext. flow		Liquid RSF	*Martel2008b*
			RSF films	*Pellerin2005*
	Tensile	*S. cynthia*	NSF films	*Rousseau2006*
		N. clavipes	Liquid NSF	*Lefèvre2011*

Table 1.1 Most relevant literature cited in this thesis. Highlighted in blue are the thesis contribution areas. NSF is the acronym for native silk feedstock whilst RSF stands for reconstituted silk feedstock.

1.13 Defining the scope of the project

As explained in the previous sections, the exact location of the onset of the molecular alignment and the protein conformational change is still unclear. Although we expect spinning to be a highly controlled process,[Dicko2006; Porter2009] the relative contribution and time scales involved for each source of stress still needs to be quantified. Until we acquire a coherent understanding of the exact stress combinations for obtaining the required structure in the resulting material, we have little chance of coherently understanding Nature's solution for producing these high performance fibres.

Thesis aim

We believe this gap in our knowledge resides mainly in the poorly understood link between silk's structure and mechanical function, examinations of which have to date relied mostly on circumstantial evidence. To address this incoherence, this thesis aims to directly link silk's structure to its flow properties. Practically, I have integrated infrared spectroscopy and small angle scattering into novel rheo-optic platforms. This permitted the probing of silk's molecular structure and flow properties whilst it is performing its function. As an outcome, we identified the structural and rheological sequence of events in silk processing and put it in silk's biological context. Finally, we combined new insights generated from this work in linking structure and properties of silk to discuss the biological functions of silks to answer the question "*Why is silk spun?*"

1.14 Thesis summary

This thesis is divided into 8 chapters, followed by 8 appendices. The work is not presented in exact chronological order as the work of Chapter 5 took place mostly before that of

Chapter 4. A brief summary of each chapter is given below, but more detailed abstracts can be found at the beginning of each chapter.

Chapter 2 Theory and experimental method

This chapter introduces the development of the experimental methods used as the basis for the individual analytical techniques we employed (rheology, spectroscopy and scattering). It details sample preparation and the precautions required to measuring samples accurately. It will also discuss the theoretical framework required to understand the results presented in the core chapters.

Chapter 3 Shear-induced aggregation studied by time resolved infrared spectroscopy

In Chapter 3 we integrated infrared spectroscopy with a shearing cell by using attenuated total reflection to study the structure development of *Bombyx mori* reconstituted silk feedstocks under flow. We show that the shear induced protein conformation conversion and the molecular orientation can be followed *in situ* as can changes in the local concentration.

Chapter 4 Native silk conversion kinetic studied by small angle scattering

Probing larger length scales than infrared spectroscopy, this chapter studied native silk's conversion *in situ* through small angle scattering whilst taking rheological measurements. In addition, we monitored the spontaneous conversion process for various stress histories to evaluate the critical shear rate and the aggregation kinetics of native silk feedstocks.

Chapter 5 Silk protein aggregation kinetics revealed by Rheo-IR

To directly relate the flow properties to silk's molecular structure, we developed a novel rheo-optic platform consisting of a rheometer coupled with an infrared spectrometer, and compared native to reconstituted silk feedstocks. This study revealed which structural

changes occur during the different phases of silk's shear processing, as well as highlighting the difference between artificial and natural silks.

Chapter 6 Preventing silk from being completely spun

To study the post-processing of silk, we designed a new controlled-environment infrared spectroscopy cell allowing the monitoring of silk spinning in controlled conditions to probe fibres immediately after secretion. This study allowed the monitoring of silk's conformation and water content under a range of environmental conditions. The rheological properties of feedstocks prepared from fibres spun under controlled conditions are compared to those of uncontrolled feedstocks and native silk.

Chapter 7 The chemical diversity of silk revealed by infrared spectroscopy

To explore the variability offered by the biodiversity of silks and evaluate the use of infrared spectroscopy as a phylogenetically informative technique, we discuss the results from a multivariable analysis of silks obtained from diverse species. The data is then put into a wider biological context to explain the link between phylogeny and a silkmoth's cocoon composition.

Chapter 8 Summary and impact

This findings revealed in this thesis are summarised and associated with the overarching conclusions. I propose my perspective on "*How silk is spun?*" before answering the question *"Why is silk spun?"* I then discuss the implications of the contributions of this thesis within a scientific and economic context.

Chapter 2

Theory and experimental methods

This chapter describes the theoretical and experimental framework used in this thesis. It covers sample preparation from the silkworm rearing to the dissection and the reconstitution of the fibres. This chapter also discuss the analytical techniques used to study these samples.

2.1 Liquid silk sample preparation

2.1.1 Native feedstock preparation

2.1.1.1 Silkworm rearing

Since native silk feedstock can only be obtained through the dissection of silkworms, mature larvae had to be procured. Fortunately, domesticated *Bombyx mori* silkworms are commonly reared all around the world and can be easily sourced. Hence most of the experiments presented were performed using the domesticated species. In contrast, wild silks are much less common and cannot be purchased directly. Therefore, we had to rear wild species in-house from eggs and feed them with leaves from locally available plants (see Figure A.2 of Appendix 1, page N). Due to the availability of certain foliage in the south of England, wild silkworms could only be reared during summer. To cover a range of Saturniidae species across the Attacini and the Saturniini tribes, we reared *Actias luna*, *Antheraea yamamai*, *Attacus atlas* and *Saturnia pavonia*. A detailed description of rearing wild silkmoths is available in Appendix 1 whilst the most important metadata collected during the rearing of these species are listed in Table 2.1.

Phylum	*Arthropoda*	*Arthropoda*	*Arthropoda*	*Arthropoda*	*Arthropoda*
Class	*Insecta*	*Insecta*	*Insecta*	*Insecta*	*Insecta*
Order	*Lepidoptera*	*Lepidoptera*	*Lepidoptera*	*Lepidoptera*	*Lepidoptera*
Family	*Bombycidae*	*Saturniidae*	*Saturniidae*	*Saturniidae*	*Saturniidae*
Tribe		*Saturniini*	*Saturniini*	*Attacini*	*Saturniini*
Genus	***Bombyx***	***Actias***	***Antheraea***	***Attacus***	***Saturnia***
Species	***mori***	***luna***	***yamamai***	***atlas***	***pavonia***
Mature larvae					
Silk cocoon					
Eggs hatched		20	19	22	19
Hatching date		2012-07-15	2012-04-10	2012-08-03	2012-06-23
Host plant	White mulberry (*Morus alba*)	Walnut (*Juglans regia*)	Hawthorn (*Crataegus monogyna*)	Privet (*Ligustrum vulgare*)	Hawthorn (*Crataegus monogyna*)
First spinning date		2012-08-17 (33 days)	2012-05-12 (32 days)	2012-09-07 (35 days)	2012-08-01 (39 days)
Worms spinning	>300	20 (100%)	3 (16%)	14 (64%)	19 (100%)
Mass	2.1 ± 0.4 g	3.1 ± 0.6 g	4.8 ± 0.8 g	14 ± 5 g	3.0 ± 0.7 g

Table 2.1 Metadata collected during the rearing of some wild silkworm species. The coin showed on the pictures presented had a diameter of 18 mm.

2.1.1.2 *Bombyx mori* full dissection on interchangeable plates

Fresh native silk feedstock can only be extracted from live silkworm glands. As the shear cell used for *in situ* SAXS and SANS measurements required 220 µL of sample to fill the parallel plate geometry, complete dissection of silkworm glands were necessary. As the basis of his sample preparation, Dr Chris Holland developed a full dissection technique using the entire gland, which was later washed to remove its water soluble sericin coating.[Terry2004; Holland2006; Holland2007; Moriya2009] Without anaesthetic, worms were cut open and the glands extracted within 5 minutes. Then the silk glands were transferred into a petri dish filled with

demineralised water (type II) to remove the epithelium with forceps under a microscope. Great care was taken to prevent damage to the silk dope inside the silk gland. The peeled glands were then transferred into another petri dish filled with water to remove the water soluble sericin coating. Constant gentle levelled shaking was required to prevent the glands from sticking to the bottom which can make loading more difficult and prevent the complete washing of the sericin bottom layer. The demineralised water was changed to remove solubilised sericin every 15 minutes, 3 changes of water being needed to remove most of the sericin. The sericin removal could be verified by infrared spectroscopy base on serine markers with a detection limit around 1 % w/w (see Figure A.11 of Appendix 2, page Y). The timings of each step were diligently recorded to ensure consistency of dissections. It took 52 ± 2 minutes (time ± standard deviation) to complete all these steps (n = 129). Afterwards, the samples were then loaded onto the bottom half of each interchangeable cell. The bottom part was then sealed with wet cotton wool to prevent sample dehydration and stored at 4 ± 1°C for at least 12 hours for homogenisation. For rheological measurements the bottom half cell was then coupled with its complementary top half.

Although it provides high yield, sample consistency requires careful sample preparation and the washing step inevitably dilutes samples slightly (~17-19 % DW). Because Rheo-IR did not require a large sample volume, a more consistent and simple washing-free rapid native silk preparation method was developed for the purpose of these experiments.

2.1.1.3 Washing-free rapid native silk preparation

A method for the rapid preparation of native silk proteins was developed to avoid the washing steps used in section 2.1.1.2. Last (5^{th}) instar spinning *Bombyx mori* silkworms were dissected to extract their silk glands. Silkworms are invertebrate arthropods and all experiments performed for this thesis complied with the Animals (Scientific Procedures) Act

1986 of the United-Kingdom.[GB1986] Glands were rinsed for a few seconds and then submerged in type II demineralised water at 22 ± 2 °C. Since the sericin coating starts between the median part of the middle division (pmm) and the middle division of the posterior part (pm),[Machida1926; Akai1983] glands were cut between the pmm and pm section (position 15 and 16 on Figure A.11b of Appendix 2, page Y). A small fraction (10 ± 5 μL) of the gland's content was expelled for 60 seconds by the osmotic pressure gradient between the dope and demineralised water (type II).

A single silk gland was lifted out of the water with forceps and blotted on tissue paper to remove superficial excess water. After gently pulling off the epithelium, the sample could be used directly without any further processing. A small fraction of the posterior section provided enough liquid silk to completely fill the Rheo-IR cone and plate geometry.

2.1.2 Silk fibroin reconstitution

Our silk reconstitution method is mostly based on well-established procedures.[Holland2007; Rockwood2011] However, we prepared two grades of reconstituted silk feedstocks (RSF) made from mainly fibroin filaments. The Low Fidelity Reconstituted Silk Feedstock (Lo-Fi RSF) was prepared from aged (> 5 year old) *Bombyx mori* silkworm cocoons stored at ambient temperature and humidity. For this procedure, they were degummed in a 0.1% $NaHCO_3$ solution at 70 ± 1 °C for 3 hours. In contrast, the High Fidelity Reconstituted Silk Feedstock (Hi-Fi RSF) was made using fresh dry spun cocoons and degummed to remove the sericin using only demineralised water at room temperature (25 °C). The degumming was also assisted by mechanical blending to reduce the fibre length. Both RSF grades, degummed and cut silk fibres were subsequently dried in a custom made tumble drier at room temperature.

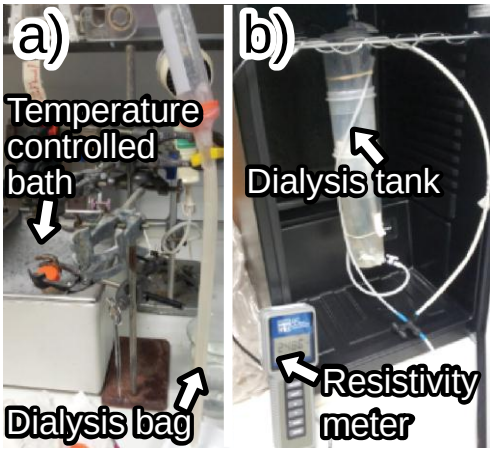


Figure 2.1 a) Solubilisation platform comprising the temperature controlled bath and the dialysis bag. b) Temperature controlled automatic dialysis system with the resistivity meter used for process monitoring.

To prepare RSF, 250 mg of silk fibres were solubilised per millilitre of 9M lithium bromide (LiBr). As shown in Figure 2.1a, the solution's temperature was maintained at 70 ± 1 °C using a temperature controlled bath. Silk was kept at this temperature for 20 minutes for Lo-Fi RSF, but only 5 minutes for Hi-Fi RSF. As shown on Figure 2.1a, the solubilised fibres were then transferred into a dialysis bag (VISKING® molecular weight cut off 12-14 kDa) fitted with a plugged nozzle. To remove the LiBr, the silk solutions were dialysed against demineralized water type II (ρ > 1 MΩcm) changed every two hours automatically over 48 hours at 7 °C using the system presented in Figure 2.1b. After the dialysis, the bags were hung at 4 °C under air flow to increase protein concentration.

2.2 Rheology

2.2.1 Rheology instrumentation

Rheology is the study of the flow, usually liquids but also soft solids which typically exhibit plastic deformation in addition to their elastic response. Hence, instruments called rheometers have been designed to measure this force response to calculate materials' flow properties such as viscosity η and modulus G. Rheometers can be classified either as

extensional, capillary, linear shear or rotational. For this thesis, a commercial rotational rheometer was used for testing silk feedstocks as they provide shear stress and allow easy control of environmental conditions. The first rotational rheometers originally had two rotating plates driven by co-axial shafts, one inducing strain and the other measuring the torque stress (strain controlled instrument). However, most modern instruments can do both from a single rotating axis.

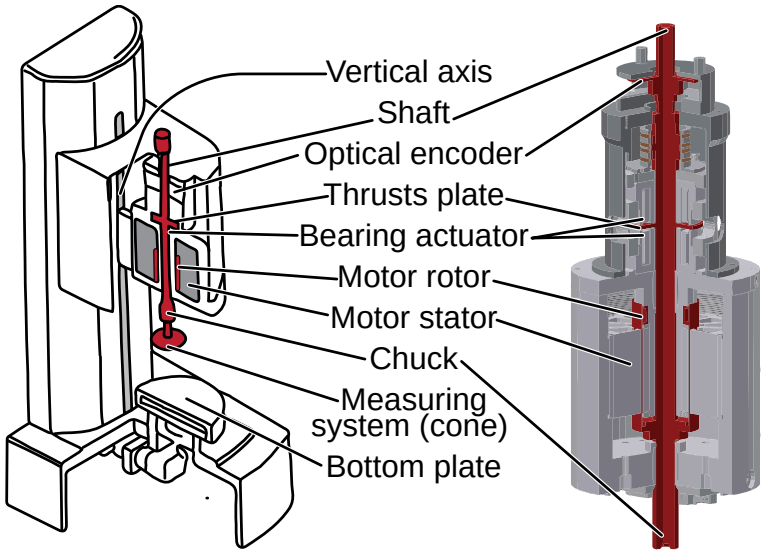


Figure 2.2 Schematics of a single axis TA Ares G2 rotational rheometer with lines pointing at the most important components. The rotating components are shown in red whilst the fix parts are shown in grey.

Figure 2.2 shows the main components of a typical single axis stress controlled rheometer. The measuring geometry of a rheometer typically consists of a fixed bottom plate with an interchangeable rotating upper plate/cone called the tool or measuring geometry. The bottom plate is commonly a temperature controlled and easily interchangeable flat metal plate, but can vary in diameter and material depending on the geometry system selected. To ensure the coaxiality of the measuring system with the shaft, the tool is normally clamped using a chuck with symmetrical jaws. To apply the stress or strain, the shaft is driven by a precise electric motor comprising of a rotor and stator. The torque (stress) applied is calculated from the power required to drive the motor and can vary from 10^{-8} Nm

to 10^{-1} Nm. To measure the strain applied, the angular position is measured by an optical encoder with an accuracy around 10^{-8} radians. The vertical position of the shaft is maintained by the thrust bearing comprising of plate and actuator. To minimise friction, the thrust bearing is either electromagnetic (patented by TA instruments[Doe2006]) or an air bearing system. The rotating shaft cannot move vertically within the bearing case, but the whole assembly can move on a vertical axis rail to set the gap between the measuring tool and the bottom plate, with an accuracy better than 1 µm.

2.2.2 Sample loading for rheology measurements

Native silk feedstock loading

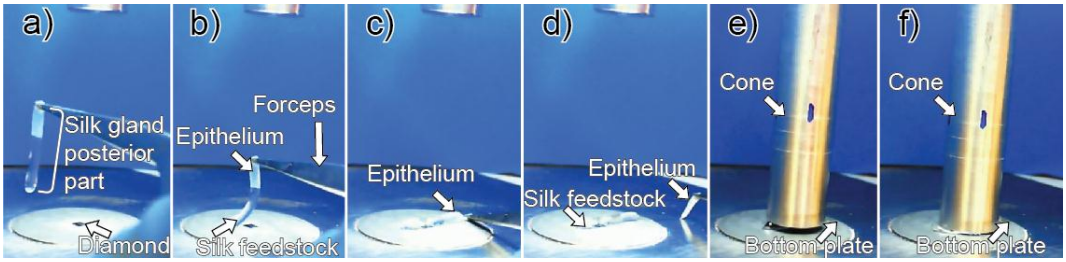


Figure 2.3 a) Transport of a *Bombyx mori* silk gland to the ATR accessory. b) Deposition of the posterior part of the gland on the ATR sensor. c) Pulling-out of the gland's epithelium using forceps. d) Discarding of the epithelium. e) Lowering of cone by the rheometer at 0.1 mm/s. f) Overflowing of the native silk feedstock at set gap (30 µm).

As native silk is highly shear sensitive, careful sample loading is of paramount importance to ensure measurement reproducibility.[Holland2006] Figure 2.3a shows how the posterior section of the middle part of a *Bombyx mori* silk gland is transported with forceps. The clear part is the feedstock ejected by osmosis whilst the turbid portion is still inside the epithelium. The gland is then gently laid onto the bottom plate (Figure 2.3b). Few seconds are given to allow the dope to settle and stick to the bottom plate before the epithelium was slowly removed with the tweezers leaving only the clear feedstock on the bottom plate (Figure 2.3c and d). Figure 2.3e to f show the lowering of the measuring system. After the death of the animal, less than 5 minutes were necessary to have the sample loaded. By using this

technique, the average protein concentration measured by infrared spectroscopy was 21 ± 3 w/w% (n = 21), which is similar to the often reported value of 25% DW for native silk feedstocks.[Zhou2005; Holland2006; Moriya2008a]

Reconstructed silk feedstock loading

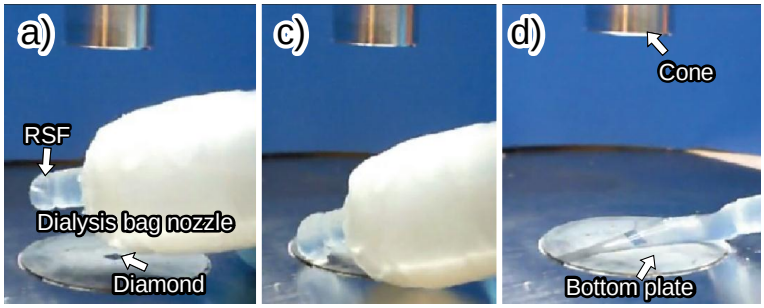


Figure 2.4 a) Distribution of a RSF droplet from the dialysis bag nozzle. b) Pouring of a RSF drop on the ATR accessory or geometry bottom plate. c) Spreading of the RSF droplet over the ATR sensor of the bottom plate.

To measure RSF using Rheo-IR, a droplet of RSF was dispensed from the nozzle of the dialysis bag onto the ATR accessory to cover the diamond sensor as shown on Figure 2.4. To prevent air bubbles in the measured RSF, aliquots were collected from the bottom of the dialysis bag which was always kept upright. The cone was then lowered to gap height at 0.1 mm/s before trimming off the excess RSF with a spatula. The detailed Lo-Fi RSF is given in Appendix 6 whilst the Hi-Fi protocol is given in Appendix 7.

For both native and reconstituted silk feedstock measurements, sample dehydration was prevented by sealing the geometry with an environmental cuff containing wet tissues. This method was found preferable to the method of using a sealing layer of non-miscible oil as infrared spectroscopy revealed that the oil and silk dope can still mix under shear regardless of their different solvent affinities.

2.2.3 Shear flow

Newtonian linear rheology

To obey Newton's law, a material stress must be directly proportional to the strain applied over the range of strain measured ($\sigma \propto \gamma$). Therefore, the viscosity of a Newtonian fluid becomes independent of the rate as illustrated by the grey curve on Figure 1.9c. As schematised on Figure 1.9a, shear flow occurs when the different layers across a material are flowing parallel relative to one another. Rotational rheometers are specifically designed to apply shear and precisely measure the torque $\mathcal{T}$ required to make a sample flow at given angular velocity Ω. Knowing the geometry of the sample and the measuring system it is possible to calculate the shear rate $\dot{\gamma}$ using Ω and the stress σ using $\mathcal{T}$. Therefore it becomes possible to calculate the viscosity by dividing the stress by the shear rate ($\eta = \sigma/\dot{\gamma}$). The viscosity is a key rheological parameter as it informs on the degree of internal friction in the sample. For macromolecules in solution like silk feedstocks, the viscosity is indicative of the chain entanglement degree in the system.[Ferry1980] Amongst the most common geometries, the two shear flow geometries used for this thesis were the cone and plate for Chapter 3, Chapter 5 and Chapter 6 as well as parallel plates in Chapter 5.

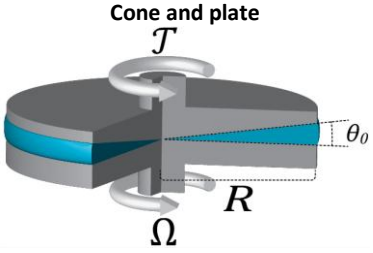
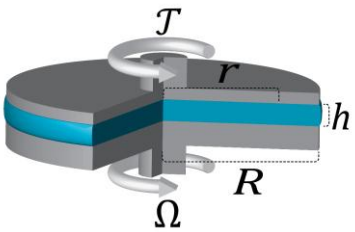
	Cone and plate	Parallel plates
		
Reference chapter	Chapter 3, Chapter 5 and Chapter 6	Chapter 5
Volume	Equation 2.1 $V = \frac{2}{3}\pi R^3 \tan(\theta_0)$	Equation 2.2 $V = 2\pi Rh$
Shear rate	Equation 2.3 $\dot{\gamma} = \Omega/\theta_0$	Equation 2.4 $\dot{\gamma}(r) = r\Omega/h$
Shear stress	Equation 2.5 $\sigma = 3\mathcal{T}/2\pi R$	Equation 2.6 $\sigma\left(\dot{\gamma}_R\right) = \frac{\mathcal{T}}{2\pi R^3}\left(3 + \frac{d\ln\mathcal{T}}{d\ln\dot{\gamma}_R}\right)$ Equation 2.7 If $\sigma \propto \dot{\gamma}^n$ then $\sigma\left(\dot{\gamma}_R\right) = \frac{\mathcal{T}}{2\pi R^3}(3+n)$
Viscosity	Equation 2.8 $\eta = \frac{3\mathcal{T}\theta_0}{2\pi R^3\Omega}$	Equation 2.9 $\eta\left(\dot{\gamma}_R\right) = \frac{3\mathcal{T}}{2\pi R^3\dot{\gamma}_R}\left(1 + \frac{1}{3}\frac{d\ln\mathcal{T}}{d\ln\dot{\gamma}_R}\right)$ Equation 2.10 If $\sigma \propto \dot{\gamma}^n$ then $\eta = \frac{3\mathcal{T}}{2\pi R^3\dot{\gamma}_R}\left(1 + \frac{1}{3}n\right)$
Normal thrust	Equation 2.11 $F\left(\dot{\gamma}\right) = \frac{\pi R^2}{2}N_1\left(\dot{\gamma}\right)$	Equation 2.12 $(N_1 - N_2)\vert_{\dot{\gamma}_R} = \frac{2F}{\pi R^2}\left(1 + \frac{1}{2}\frac{ln\,F}{ln\,\dot{\gamma}_R}\right)$
Normal thrusts difference	Equation 2.13 $\Delta F = 3\pi\rho\Omega^2R^4/40$	

Table 2.2 Fundamental rheological quantities calculated for a cone and plate as well as parallel plate geometries. σ strands for stress and $\dot{\gamma}$ for the shear rate. Ω is the angular velocity and θ_0 is the cone's angle.

As shown in Table 2.2, a cone and plate geometry offers a distinctive advantage; the shear rate is theoretically the same everywhere in the sample if the angle of the cone θ_0 is small enough (1 to 4°). For these reasons, the cone and plate geometry was used for combination with ATR-IR.

Illustrated in Table 2.2, the bottom plate rotates to generate the angular velocity Ω and the top plate measures the resulting stress as torque $\mathcal{T}$. Most rheometers are however capable of both inducing Ω and measuring $\mathcal{T}$ from the top plate in a fast feedback loop where the stress can be adjusted to obtain the desired position dynamically.

For a cone and plate geometry, the tip of the cone is often truncated to prevent contact between the cone and the plate which can cause friction.[Barnes1989] The sample volume required for a cone and plate assembly is only 2/3 of parallel plate system with equivalent gap at the rim. The shear rate $\dot{\gamma}$ (s^{-1}) is independent of the liquid's properties and is given simply by $\dot{\gamma} = \Omega / \theta_0$, where Ω is the angular velocity (rad/s) and θ_0 is the angle between the cone and the plate. The shear stress σ can be calculated using $\sigma = 3\mathcal{T}/2\pi R$, where R is the geometry's radius. The viscosity η can then be calculated by dividing the stress by the shear rate using Equation 2.8.

Parallel plates are simple geometries comprised of two flat disks separated by a gap h. Because of the parallel interfaces, they are well suited for rheo-optic measurements where the radiation passes through the cell or for samples that cannot be easily shaped to fit a cone and plate geometry. For visible light, neutrons or X-ray, a normal angle of incidence can prevent refraction events. Another advantage of this geometry is its ability to accommodate experimental needs by adjusting the sample volume and beam path by changing h. However, wall and edge effects can become important for small gaps.[Jabbarzadeh2000]

The parallel plates have the same gap h across the geometry resulting in a shear rate dependent on the distance from the centre, given by $\dot{\gamma}(r) = r\,\Omega/h$. Therefore if the rate varies across the cell, the local stress response will vary accordingly. Hence, for non-

Newtonian fluids, with a viscosity function dependent on the rate, the viscosity will also vary across the cell. By measuring the torque $\mathcal{T}$ for the range of shear rates, the differential Equation 2.6 can be extended to give the relationship of the viscosity to the shear rate sustained at the rim of the parallel plate geometry. Ideally many angular velocities need to be measured to determine the full viscosity function $\eta(\dot{\gamma})$ using Equation 2.9.

Knowing the viscosity as a function of shear rates it is also possible to calculate the energy dissipated $P(\dot{\gamma})$ using $P = \eta\dot{\gamma}^2$. Consequently, the specific work w (energy density) can be calculated by integrating the dissipated energy over a time period.[Janeschitz-Kriegl2003]

$$w = \int_0^{t_s} \eta(\dot{\gamma}(t))\,\dot{\gamma}^2(t)\mathrm{d}t \qquad \text{Equation 2.14}$$

Non-Newtonian flow

Materials should obey Newton's law at infinitely small strains giving the zero shear viscosity η_0. However, when finite strains or strain rate are applied, several materials will diverge from this approximation. As result, non-Newtonian fluids like native silk feedstocks will show a rate dependent viscosity passed this plateau. This additional level of complexity complicates the mathematical framework required to calculate rheological properties. Fortunately at high rates, the viscosity is often proportional to the power of the shear rate $\sigma \propto \dot{\gamma}^n$, where n is the fractional power law coefficient. n = 1 for Newtonian fluids, $n < 1$ for shear thinning fluids whilst it is $n > 1$ for shear thickening materials. If a material obeys the power law, the Equation 2.6 and Equation 2.8 can be integrated to calculate exactly the rate dependent stress and viscosity for all rates using a single torque value.

The rate at which non-Newtonian the materials stop exhibiting a constant viscosity and start to obey the power law can vary greatly. This point is described as the linear regime whilst thereafter it is described as the non-linear regime. The assumptions surrounding

linear viscoelastic theory is thus essential to know the separating linear viscoelastic (LVE) limit. Occurring at a rate $\dot{\gamma}_P$, the LVE limit corresponds to the reciprocal of the material's relaxation time τ_P. A well-established method to calculate these quantities is the Carreau-Yasuda model of Equation 2.15.

$$\eta = \eta_0(1 + (\dot{\gamma}\tau_P)^a)^{(n-1)/a}$$

Equation 2.15

Fitting the viscosity function of a non-Newtonian material gives the rate at which the sample transits from a plateau viscosity using regime η_0 to a power law regime of index n with a transition coefficient a.[Yasuda1981] The reciprocal of this transition rate thus corresponds to the relaxation time of the sample.

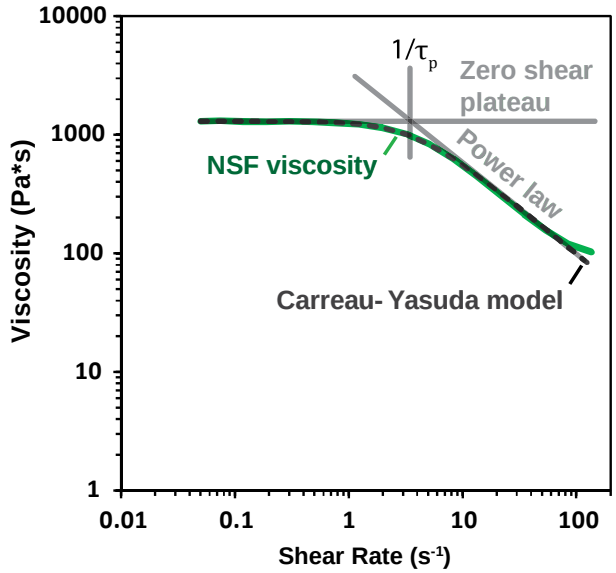


Figure 2.5 Carreau-Yasuda fit of a representative native silk feedstock viscosity test (R^2 > 0.99).

Figure 2.5 shows the Carreau-Yasuda fit for a typical native silk feedstock with a relaxation time $\tau_p = 1/\dot{\gamma}_P$ of 0.5 s at the inflexion point before shear thinning.

Normal stress difference

Non-Newtonian materials can sometimes give a normal stress difference when they possess a rubber-like solid component outside the liquid viscoelastic domain. The elastic

recoverable strain induced during the deformation results in a normal thrust.[Porter1993] The time dependent deformation for viscoelastic liquid/solid is a combination of elastic and viscous effects. In addition to $\mathcal{T}$, rheometers can often measure this normal thrust force (given in Newton) using their force transducer on the thrust plate (see Figure 2.2).

There are two types of normal stress difference: N_1 which is along the vorticity vector (along the shaft axis) and N_2 along the radius of the geometry.[Ferry1980] As the second normal N_2 force is challenging to measure, most studies are limited to measuring N_1. For a cone angle <4° coupled with a plate and neglecting internal effects, the total normal force can be directly linked to the first normal force using the Equation 2.11.

Experimentally, negative values of the total normal force F can also be measured when plates are pulled closer together. The reduction in the N_1 value thus measured can be due to inertia effects dependent on the power four of the distance from the centre and Ω^2 when using a cone and plate geometry. The Equation 2.13 including the density of the material ρ (g/mL) can be used to correct experimental values.[Walters1975]

For parallel plate geometry, the first N_1 and second normal N_2 force cannot be determined independently, but their difference can be derived from F by taking into account the shear rate gradient in the Equation 2.12. Consequently, by doing one experiment with a cone and plate and another using parallel plates, it is theoretically possible to resolve N_1 and N_2. Such approach, however, results in large experimental errors.[Ferry1980]

2.2.4 Oscillatory measurements

Viscoelastic fluids are partly viscous and partly elastic, but in what proportion? Oscillatory tests are specifically designed to answer this question by applying periodic strains γ_0 at a frequency ω whilst measuring periodic stress σ^* lagging by a phase angle δ. Since the

measured stress σ^* has two parts, it is practical to use the complex notation $e^{i\theta} = cos\theta - i\ sin\theta$ with i being the unit imaginary number. By measuring the raw stress σ^* and the δ, the modulus associated with the elastic proportion of the material (storage G') which respond in phase ($\delta = 0$) can be deconvolved from the modulus related to the viscous portion (loss G'') which is out of phase ($\delta = \pi/2$).

$$\frac{\sigma^*}{\gamma_0} = \frac{\sigma e^{i(wt+\delta)}}{\gamma_0} = \frac{\sigma}{\gamma_0}(\cos(\omega t + \delta) - i\sin(\omega t + \delta)) = G^* = G' + iG'' \qquad \text{Equation 2.16}$$

Given in Pa^{-1}, the storage J' compliance is a measure of the energy stored and recovered in each cycle whilst the loss J'' informs on the energy dissipation capability of the material. They become particularly useful to compare materials under similar strain amplitudes and frequencies. The complex notation also simplifies the description of the complex compliance J^* given in Pa^{-1} which is the ratio of strain on stress or the inverse of the complex modulus G^*.

$$\frac{1}{G^*} = \frac{1}{G' + iG''} = J^* = \frac{{\gamma_0}^*}{\sigma} = J' - i\,J'' \qquad \text{Equation 2.17}$$

Even though $G^* = 1/J^*$, its components are generally not reciprocal, i.e. $G' \neq 1/J'$ and $G'' \neq 1/J''$. Using Equation 2.17 however, these quantities are connected to one another by the following four equations using the phase angle δ value.

$$G' = \frac{J'}{(J')^2 + (J'')^2} = \frac{1/J'}{1 + \tan(\delta)^2} \qquad \text{Equation 2.18}$$

$$G'' = \frac{J''}{(J')^2 + (J'')^2} = \frac{1/J''}{1 + \tan(\delta)^{-2}} \qquad \text{Equation 2.19}$$

$$J' = \frac{G'}{(G')^2 + (G'')^2} = \frac{1/G'}{1 + \tan(\delta)^2} \qquad \text{Equation 2.20}$$

$$J'' = \frac{G''}{(G')^2 + (G'')^2} = \frac{1/G''}{1 + \tan(\delta)^{-2}}$$ Equation 2.21

From oscillatory measurements, we can also calculate the plateau modulus $G'_N = \mathrm{G}'|_{\omega \to \infty}$, that is the storage modulus at high frequencies. G'_N is an indicator of the material's capacity to store energy which is dependent on the average molecular weight between entanglements M_e of the sample by Equation 2.22.[Ferry1959; Doi1987]

$$M_e = \rho \bar{R} T / G'_N.$$ Equation 2.22

ρ is the density (Kg/m^3) and $\bar{R} = 8.314$ L*kPa*K^{-1}*mol^{-1}, the perfect gas constant. The relaxation time τ_p of the sample obtained from Equation 2.15 can also be derived from G' and G'' by determining the frequency at which they become equal $\left(\tau_p = \omega^{-1}|_{G'=G''}\right)$, designated as the cross over point. The zero shear viscosity η_0 can be determined using G'_N and the relaxation time τ_P using.[Porter1995]

$$\eta_0 = G'_N \tau_P$$ Equation 2.23

However, this equation only holds below the LVE limit of materials. Hence it is essential that the G'_N is measured at strain smaller than the LVE limit. Therefore most oscillatory experiments are performed within the LVE regime. Because longer chain polymers will relax more slowly than shorter ones, the relaxation time was also found to be proportional to the square of the polymer's molecular weight when entanglement is neglected ($\tau_P \propto M_W^2$).[Rouse1953] The complex viscosity η^* can also be determined from oscillatory measurements by dividing the moduli by the angular frequency ω (s^{-1}), having two components like the complex modulus.

$$\eta^* = G^*/\dot{\gamma} \qquad \eta' = G''/\dot{\gamma} \qquad \eta'' = G'/\dot{\gamma}$$ Equation 2.24

The in-phase component η' is often simply called dynamic viscosity. Its measurement is particularly useful since it is often equivalent to η_0 at very low frequencies. However, the dynamic viscosity will decrease monotonously with increasing frequencies and therefore cannot be directly equivalent to η outside the linear viscoelastic regime.

2.2.5 Extensional flow

Fluid flow has two components: shear and extensional flow. In opposition to shear flow, extensional flow occurs when the different layers across the material are not flowing parallel to one another, but purely along the deformation vector. For instance, extensional flow occurs when pulling chewing gum out of a mouth. Pure shear flow is relatively easy to obtain, but extensional often comes with a shear flow component. Sometimes called elongation flow, extensional flow is often important for processes such as polymer melt fibre spinning, which involves mostly extension.[Petrie1979] In some cases, the measurement of the extensional viscosity χ is as important as the shear viscosity to predict flow behaviour. The response to shear can be qualitatively and quantitatively different to extensional flow. Any abrupt change in the geometry or transient can bring the strain rates to values sufficiently high to fracture macromolecule chains.[Knudsen1996] Practically, polymer chain fracture is the phenomenon responsible for engine oil limited lifespan. Spinning involves mostly uniaxial flow where the extension is only along one direction vector and is expected to play an important contribution in the fibre processing toward the end of the spinning duct.[Knight2000] For the uniaxial extension of Newtonian fluids, the extensional viscosity χ is theoretically three times the shear viscosity ($\chi = 3\eta$).[Ferry1980] However for non-Newtonian fluids like silk feedstocks, this is only true at vanishing rates.

$$\lim_{\dot{\epsilon}\to 0} \chi = \frac{\sigma}{\dot{\epsilon}} \approx 3\eta_0$$ Equation 2.25

The χ/η ratio at equivalent rate is described as the Trouton ratio T_r and is often used to estimate the material's viscoelastic response. Similar to synthetic polymer melt spinning, extensional flow is expected to play an important part in the natural silk spinning process as it can provide the high deformation rates required to stretch the long protein molecules and align them along the deformation axis.[Vollrath1999] However, extensional rheology is a difficult technique as the geometry of the sample is not fixed. Hence to calculate the extensional viscosity, the sample's neck has to be measured whilst recording the force. The aqueous nature of silk feedstock makes extensional rheology measurement even more challenging[Kojic2006] as the sample can dry during tests. Since extensional flow occurs later in the spinning process in combination with shear flow and we did not have access to an extensional rheometer, we focused on shear flow for studying silk's rheology.

2.3 Infrared spectroscopy

2.3.1 Infrared spectroscopy instrumentation

Infrared spectroscopy is a well-established analytical technique to inform on the chemical composition of samples based on their molecular vibration transitions, which absorb in the infrared range. Therefore, a range of instruments are commercially available from various manufacturers such as Thermo, Perkin Elmer, Bruker, and Varian. Because of the long wavelength of the infrared radiation, most modern instruments will use a modulated polychromatic light source deconvolved by Fourier transformation to collect spectra giving its name to Fourier Transform Infrared (FTIR) spectrometry technique.

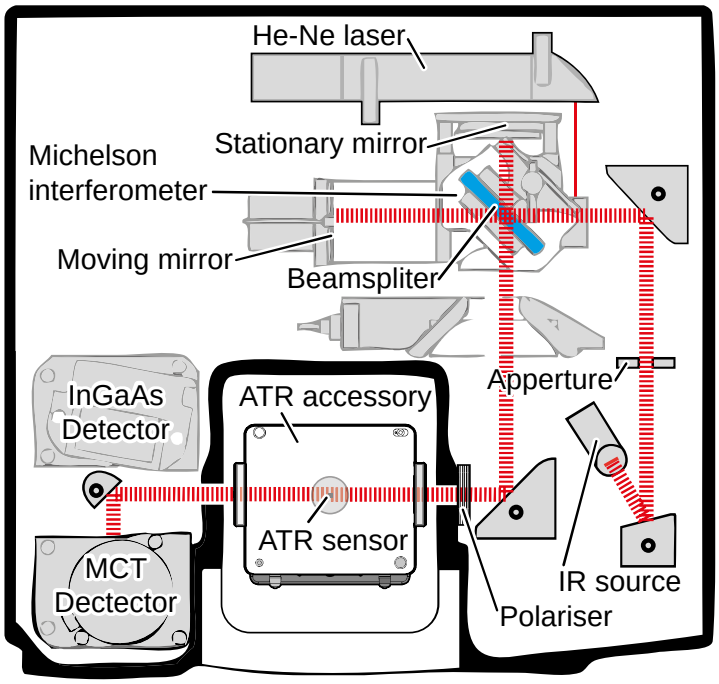


Figure 2.6 Infrared beam path of modern Fourier transform infrared spectrometer (Thermo Nicolet 6700).

Figure 2.6 shows the beam path and the principal parts of a modern FTIR (Nicolet 6700 spectrometer, Thermo, Madison, USA). The polychromatic light is generated by a heated black body emitting mostly between 14000 and 400 cm^{-1} (0.8 and 25 µm). Once emitted from the source, the dimension of the beam is determined by an aperture. A larger aperture improves flux, but also increases the beam spot obtained in the sample compartment. Consequently, there is always a trade-off between light flux and having a well-defined angle of incidence in the attenuated total reflection accessory. After the aperture, the beam is directed into the Michelson interferometer for modulation.[Michelson1887] As shown in blue on Figure 2.6, the potassium bromide beam splitter of the interferometer reflects around half of the light whilst allowing about half through, at a 45° angle. With its two mirrors, the "+" shape assembly makes the infrared beam interfere with itself before being reflected out. By moving one of the two mirrors, the interferometer thus generates an optical retardation modulating the intensity of the infrared light $I(t)$ such that:

$$I(t) = B(\bar{\nu}) \cos 2\pi \bar{\nu}(2\upsilon t) \qquad f_{\bar{\nu}} = 2\bar{\nu}\upsilon$$

Equation 2.26

where B is the radiation intensity, $\bar{\nu} = c/\lambda$ is the light frequency, υ is the velocity of the moving mirrors), t is the time and $f_{\bar{\nu}}$ is the modulated frequency. For instance, infrared light of 30 THz (1000 cm^{-1}) can be modulated at only 1000 Hz using υ = 0.5 cm/s. Hence with a modulated frequency in the kHz regime, light fluctuations become detectable in real time. The beam is then reflected through a holographic grid polariser either transverse-electric (s) or transverse-magnetic (p). The calibration of the polarisation for infrared spectroscopy is given in Figure A.12 of Appendix 2, page Z. An attenuated total reflection (ATR) accessory then collects and focuses the IR beam on the diamond crystal where attenuated total reflection occurs. By placing a sample in contact with the ATR sensor crystal, a part of the evanescent wave can be absorbed without having the beam path going through the sample. Samples can also be measured by directly illuminating through a film sample in the sample compartment. After the sample compartment, the modulated light is directed to either the pyroelectric Deuterated Tri-Glycine Sulfate (DTGS) or a liquid nitrogen cooled photoconductive Mercury Cadmium Telluride (MCT) detector.

2.3.2 Infrared absorption

From each scan of the interferometer's moving mirror, an optical retardation interferogram $I(t)$ is recorded over time and converted into a frequency based single beam spectrum $I(\bar{\nu})$ by a Fourier transform. The transmittance spectrum $T(\bar{\nu}) = I/I_0$ is later obtained by dividing the $I(\bar{\nu})$ measured for the sample by $I_0(\bar{\nu})$ of the background (no sample). The absorbance is calculated by the negative logarithm of $T(\bar{\nu})$, $A = -log(I/I_0)$. All spectra presented in the thesis are given in absorbance unit A.

In addition to the reduced mass of the atoms involved in the vibration, the frequency of the infrared absorption will depend on the electron density around the molecular bonds. Isotopic labelling can be used to change the vibration frequencies and can therefore be a useful investigative tool. Changes in the neighbouring bonds to an atom can also affect the frequency observed as they can contribute to electron delocalisation.

The absorption is proportional to the cosine squared of the angle between the electric vector of the infrared light and the vibration transition dipole vectors.[Benedict2008] Consequently, by polarising the infrared beam linearly along a direction, it is possible to quantify the orientation of the vibration modes. If the direction of the vibration mode vector's relative to the macromolecule chain is known, the molecular orientation can be deduced from linearly polarised infrared spectra.

The absorption is also proportional to the number of molecular bonds in the beam path. Hence if the beam hits the sample at a normal angle, non-saturated absorbance A can be directly related to the concentration c of the sample in accordance with the Beer–Lambert law $A = \varepsilon l c$, where ε is the molar absorptivity and l is the path length.[Zhu1998a; Zhu1998b]

2.3.3 Attenuated Total Reflection (ATR)

As proteins strongly absorb, a film of just a few microns thick can extinguish entirely the infrared light radiation in the mid infrared, burying the signal under the noise. To overcome the transmission saturation issue, attenuated total reflection (ATR) offers a convenient solution. ATR spectroscopy is based on the total internal reflection phenomenon than occurs when light is travelling through a high refractive index medium and hits an interface with a lower refractive index. Fahrenfort was the first to apply this effect to spectroscopy to probe rough or highly absorbing samples.[Fahrenfort1961] If the incident angle θ is larger than the

critical angle θ_c defined by Snell's law, the incident beam is then reflected with the same angle, $sin\ \theta_c = n_2/n_1$.[Harrick1967] n_1 is refractive index of the first medium (diamond = 2.38) and n_2 is the refractive index of the second (air = 1, water = 1.33 or silk = ~1.54).[Perry2008]

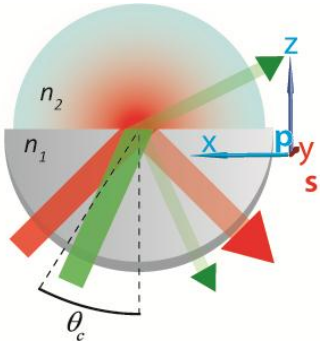


Figure 2.7 Attenuated total reflection schematic. The green arrow represents an incident beam below the critical angle θ_c which is reflected and refracted. The red arrow represents a light beam above θ_c reflected internally and producing an evanescent wave.

As shown by the green arrow on Figure 2.7, if θ is smaller than θ_c, the beam is refracted in the second medium of refractive index n_2. If $\theta > \theta_c$ however (red arrow), the beam is reflected at the interface and stays in the denser medium. Even if the beam is totally reflected, an evanescent wave is generated in the second medium and can be absorbed by the sample. This phenomenon (ATR) allows absorption from a sample without passing the beam through it. From its initial value at the interface, this wave decreases exponentially normal to the interface. The penetration depth d_p is dependent on the wavelength λ and defined by $d_p = \lambda/2\pi n_1\sqrt{sin^2\theta - (n_2/n_1)^2}$ and is around 0.8 µm for air above diamond at 1500 cm^{-1} whilst it is around 1.1 µm for 23 % silk feedstock .[Harrick1967]

Transmission spectra are essentially governed by the sample's extinction coefficient (k) unlike ATR spectra which can be also strongly affected by the refractive index of the sample (n_2) and the internal reflection element (IRE) n_1.[Hansen1965a; Hansen1965b] The effect of the refractive indices can however be mitigated by the use of a high refractive index IRE and low refractive index sample as demonstrated for silk feedstock films.[Boulet-Audet2010]

2.3.4 Coupling a shear cell with an infrared spectrometer

To input shear stress to the liquid silk feedstock, a purpose built shear cell was constructed to couple with infrared spectroscopy for the measurements performed in Chapter 3.

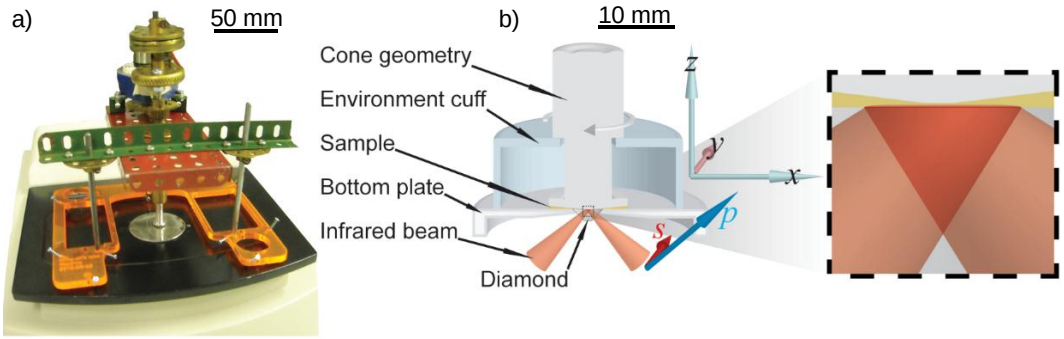


Figure 2.8 a) Coupling of a purpose built shear cell with a Smart Orbit ATR assessor (Thermo, Madison, USA). b) Cone and plate geometry with the laboratory referential coordinate system.

Figure 2.8a shows the Meccano® based purpose built shear cell powered by a 5V electric motor. The motor could only rotate at a single angular velocity resulting in a shear rate of 5 s^{-1}. The shearing cell was leveled using a spirit level by adjusting slightly the heights of the three legs. Any normal stress higher than 20 kPa resulted in lifting the geometry. Gap was set using a 30 µm filler gauge and was maintained by a weight on the shaft. The 10 mm cone measuring system was machined out of aluminium at a 1° angle. Figure 2.8b shows that the cone geometry was centred on the ATR sensor, probing around the stagnation point. Consequently, the velocity direction was averaged around the beam spot. To prevent sample dehydration the geometry was sealed with an environment cuff. Because the exact voltage required to shear the sample could not be measured, the stress response was unknown and the flow properties could not be calculated.

2.3.5 Coupling infrared spectrometer with a rheometer

To measure the sample's flow properties whilst collecting infrared spectra, an infrared spectrometer needed to be coupled with a rheometer.

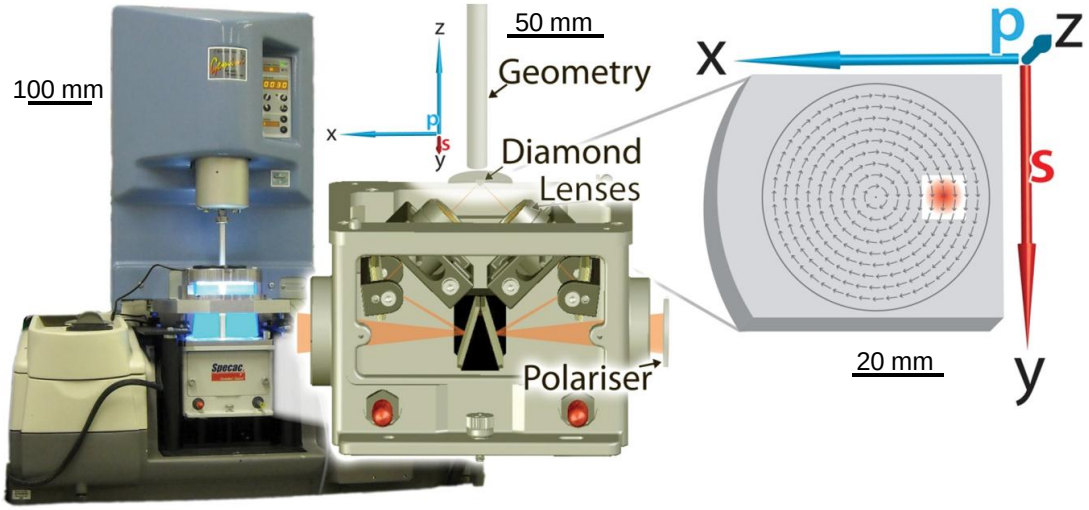


Figure 2.9 Coupling of the rheometer and the infrared spectrometer with laboratory referential.

As presented in Figure 2.9, the purpose built Rheo-IR setup used in Chapter 5 and Chapter 6 consisted of a Bohlin Gemini HR Nano 200 rheometer (Malvern Instruments, UK) mounted on a Golden Gate Attenuated Total Reflection (ATR) accessory (Specac, UK) embedded in a Nicolet 6700 FTIR spectrometer (Thermo Scientific, Madison, WI). The coupling was made possible by building a platform resting on the sample compartment with four aluminium pillars. The bridge of the Golden Gate accessory which normally holds the anvil was removed to give enough clearance to the platform. The bottom plate of the rheometer was removed to allow a 160 mm long geometry to reach the ATR accessory's puck with the embedded diamond sensor (2 by 2 mm). The geometry centre of rotation was offset by 3 mm from the centre of the diamond ATR element. The flow field was essentially oriented along the y axis and the s polarisation. As a result, both s (y) and p (xz) polarised spectra are highly sensitive to the molecular orientation. The s polarisation is nearly blind to the vibration modes oriented perpendicular to the flow field and the p polarisation probed only slightly along the flow. The coupling of infrared and rheology data is presented in Appendix 2.

2.3.6 2D correlation

First introduced by Noda et al.,[Noda1988b] 2D infrared spectroscopy (2D IR) was inspired by 2D NMR spectroscopy. The nuclear spins on which NMR is based relax in microseconds, but molecular vibration modes relax in only picoseconds. Because the use of the vibration harmonics as perturbation is challenging, other types of perturbation were exploited such as mechanical, thermal, pressure, chemical, optical and electrical stresses.[Noda1988a; Marcott1991] Originally, the perturbation needed to be sinusoidal, but this limitation was later lifted by the development of a more generalised formalism.[Noda1993] 2D analysis can also be used for nearly any type of spectroscopy including UV-vis, Raman, CD and fluorescence. 2D correlation spectroscopy allows the simplification of complex spectra with many overlapping bands by enhancement of the spectral resolution. It facilitates the assignment of overlapping components by spreading the spectra over an additional dimension. In addition, this method can link the impact of the perturbation on two different techniques (hetero-correlation).[Kubelka1999]

To calculate a generalised 2D correlation spectrum, a Fourier transform of the dynamic spectra (kinetic) is required to convert the time domain into frequencies.[Noda1990] The forward Fourier transform $\hat{f}(\nu_1, t)$ of the fluctuating spectral intensity $I(\nu_1, t)$ at a given frequency $\nu_1$is given by

$$\hat{f}I(\nu_1, t) = \int_{-\infty}^{+\infty} I(\nu_1, t)\mathrm{e}^{-\mathrm{i}\omega\mathrm{t}}\mathrm{dt} \quad \hat{f}I(\nu_1, t) = \hat{f}^{Re}I(\nu_1, t) + i\hat{f}^{Im}I(\nu_1, t) \qquad \text{Equation 2.27}$$

where $\hat{f}^{Re}(\nu_1, t)$ and $\hat{f}^{Im}(\nu_1, t)$ are the real and imaginary components respectively. Similarly, the Fourier transform's conjugate (equal real part, opposite imaginary part) observed at a wavenumber ν_2 is

$$\hat{f}^{*}I(\nu_2,t) = \int_{-\infty}^{+\infty} I(\nu_2,t)\mathrm{e}^{-\mathrm{i}\omega\mathrm{t}}\mathrm{dt}$$
$$\hat{f}^{*}I(\nu_2,t) = \hat{f}^{Re}I(\nu_2,t) - i\hat{f}^{Im}I(\nu_2,t)$$

Equation 2.28

For the time-domain dynamic spectra measured at ν_2 and ν_1, the complex 2D correlation intensity squared modulus is calculated from the product of the Fourier transform with its conjugate as

$$\phi(\nu_1,\nu_2) + \mathrm{i}\psi(\nu_1,\nu_2) = \frac{1}{\pi\mathrm{T}}\int_0^{+\infty} \hat{f}I(\nu_1,t)\cdot\hat{f}^{*}I(\nu_2,t)\mathrm{dt}$$

Equation 2.29

where T is time period, $\phi(\nu_1,\nu_2)$ is the synchronous spectrum and $\psi(\nu_1,\nu_2)$ is the asynchronous correlation spectrum. Along with the selection rules, ϕ and ψ were calculated for silk's conversion kinetic using 2DShige (Kwansei-Gakuin University).[Morita2007]

2.3.7 Principal Component Analysis (PCA) and Linear Discriminant Analysis (LDA)

Infrared spectra typically contain thousands of data points, which are not however all inter-dependent and informative. Particularly useful for large datasets, multivariate analysis allows the reduction of the number of variables to facilitate visualisation. For this reason, we used Principal Component Analysis (PCA) on the infrared spectra cocoon library. One of the most commonly used multivariate analysis,[Pearson1901] PCA is extensively used for infrared spectra analysis.[Hu2006b; Czarnik-Matusewicz2009; Zhang2009] PCA is an orthogonal linear transformation translating the observations from an initial dimensional space with many variables to a final dimensional space with fewer variables whilst preserving the maximum amount of variance. If the 2 or 3 first principal components represent most of the total variability, a 2 or 3D plot can be used to clearly visualise the variations between observations (spectra). The dataset is simplified to fewer variables using most of the information available in the spectra. Hence,

PCA is often employed to reduce the number of variables in preparation for another multivariate analysis method such as Linear Discriminant Analysis.

The Linear Discriminant Analysis (LDA) method is typically employed for pattern recognition and classification.[Fisher1936a] Like PCA, LDA explains the variability of the data by a linear combination of variables. Instead of finding the factor expressing the most variability, LDA aims to identify the best factors discriminating between the different classes given in the training dataset. LDA has been used extensively to discriminate sample types based on their infrared spectra.[Kansiz1999; Mariey2001; Chaudhury2011]

Hierarchical Clustering Analysis (HCA) allows the rapid visualisation in a dendrogram or tree of the level of similarity or dissimilarity between different classes of observations by regrouping them. Groups can be calculated using two strategies, agglomeration (bottom up) or divisible (top down). The distance between classes can be given using several methods, including the Euclidean and the Manhattan distance. To build the dendrogram, different criteria can be used such as single-linkage clustering, average linkage clustering and Ward's clustering.[Hartigan1975] From a quantitative distance matrix the resulting HCA provide an ultrametric tree with quantifiable branch lengths. All of the multivariate analyses were performed using custom macros in MATLAB (Matworks) and XLSTAT (Addinsoft, France) and TQ analyst professional (Thermo, US).

2.3.8 Self-Modelling Curve Resolution (MCR)

Although a direct measurement, the centre of gravity used in Chapter 3 and Chapter 5 does not allow the deconvolution of the different effects observed. Difference spectra are informative, but only give insights on the changing fraction of the system. Ideally, deconvoluting the pure spectrum of each component and their concentration would

provide more quantitative information from the kinetic measured. Another sub group of multivariate analysis is particularly useful for evolutionary process involving the changes unknown mixtures, self-Modelling Curve Resolution (MCR). This modelling technique can be applied even when little is known about the system.

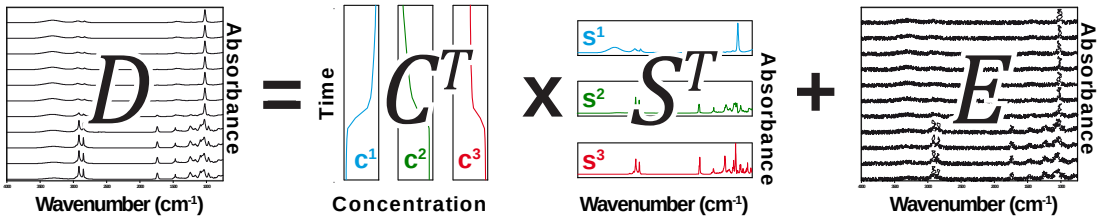


Figure 2.10 Matrices involved in the deconvolution of dynamic spectra

As shown on Figure 2.10, MCR algorithms for spectroscopy are designed to deconvolve the different pure component spectra (S^T) and their relative concentration as a function of time (C^T) from the raw data kinetics (D). Since $D = C^T \times S^T$, many combinations of C^T and S^T can result in the same matrix D. Consequently, the use of this modelling approach can result in a small E residual, but can also be inexact. Such optimisation algorithms are predisposed to falling into false minima because of the rotational ambiguity between C^T and S^T. A solution to this issue is to use a hybrid method including some constraints like the self-Modelling Curve Resolution alternating least squares (MCR-ALS) algorithm developed by Tauler et al.[Tauler1991; Tauler1993a; Tauler1995b] These constraints are derived from applying the physical laws governing the system such as the conservation of mass and absorptivity principles.).

The MCR-ALS optimisation algorithm requires an initial estimate of S^T or C^T along with the number of components T. Firstly, T can be deduced from the knowledge of the number of compound types present in the system or the Eigenvalues calculated from the Single Value Decomposition (SVD)[Golub1996] or Principal Component Analysis (PCA).[Pearson1901; Jackson1991] Once the number component exceeds the pure components, the Eigenvalues will decrease

sharply. Thus the initial estimate of the pure spectra S^T can be estimated from the analysis of the pure constituents. Initial estimates can also be obtained from pure spectra analysis like SIMPLISMA,[Windig1991] which identifies the purest spectra observed during the kinetics. Evolving factor analysis (EFA) can be also employed to obtain an initial C^T estimate.[Maeder1987]

With the initial estimate as a starting point, the MCR-ALS algorithm optimises the fit using some optional constraints. Non-negativity constraints can be applied to the S^T and/or C^T. As concentration or absorbance cannot have negative values, this assumption can easily be made for infrared spectra. Another potential constraint is the unimodality, the presence of only one peak, which can be applied to concentration for a single pathway irreversible process. The unimodality can also be applied to individual components of UV-vis spectra, but cannot be assumed for multi peak infrared spectra. In addition, closure conditions can be applied if the mass is conserved or the system is closed. The closure condition will ensure that the sum of concentration will remain constant during the evolving process, thus the concentration gained by one pure species is lost by another. If the concentration or the pure spectra is known at a given point, the selectivity condition can be applied. For instance, this is applicable to chemical reactions which have zero product concentration initially and zero reagents left at the end.

2.4 Small Angle Scattering (SAS)

To cover the larger lengths scales involved in silk's spinning, small angle scattering was employed.

2.4.1 Small Angle Scattering (SAS) theory

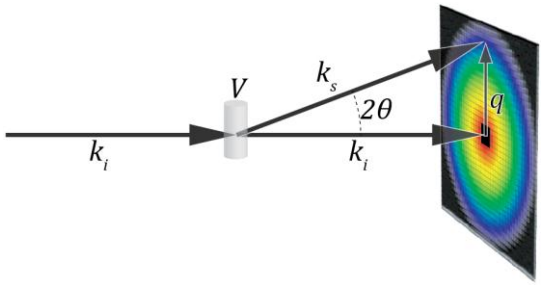


Figure 2.11 Schematic of the scattering vector for a typical small angle scattering experiment.

For both neutron and X-rays, the scattering vector (or momentum transfer) q is simply the vectorial difference of the scattered vector $\vec{k}_s$ and the incident vector $\vec{k}_i$ as illustrated in Figure 2.11. Using trigonometry, q is directly linked to the diffraction angle 2θ and the wavelength λ using Equation 2.30.[Guinier1939]

$$q = |\vec{q}| = \left|\vec{k}_s - \vec{k}_i\right| = \frac{4\pi sin\theta}{\lambda}$$

$$\lim_{\theta \to 0} \frac{4\pi sin\theta}{\lambda} = 2\pi \frac{2\theta}{\lambda}$$

Equation 2.30

Alternatively, the scattering vector is sometimes referred to as $S = 2\theta/\lambda$, corresponding to $S = q/2\pi$.

2.4.1.1 Scattering contrast

If the detector is placed at a distance much greater than the size of the sample, the scattering amplitude $A(q)$ becomes proportional to the sum of all N wave functions of n particles:

$$A(\vec{q}) \propto \sum_{n=1}^{N} e^{-i\vec{q}\vec{r_i}}$$ Equation 2.31

For convenience, the amplitude $A(q)$ can be described as a continuous function for a given sample volume V_R by

$$A(\vec{q}) = \int_{V_R} \rho(\vec{r}) e^{-irq} \mathrm{d}V_R \propto \int_{V_R} \rho(\vec{r}) e^{-i\vec{r}\cdot\vec{q}} \mathrm{d}^3\vec{r}$$ Equation 2.32

where $\rho(\vec{r})$ is proportional to the neutron scattering length density or the electron density for X-rays at a point r. With Euler's formalism, $A(\vec{q})$ can be calculated from the 3D Fourier transform of $\rho(r)$.[Geissler2000] Only the square of the modulus $I(q) = |A(q)|^2$ is detectable experimentally (that is the phase and thus the imaginary part of the modulus is unknown) and can be determined from the product of $A(q)$ with its complex conjugate $A^*(q)$. The complex conjugate is a number with the same real part, but opposite sign imaginary part $(a + ib)^* = a - ib$ or in polar form $(re^{i\Phi})^* = re^{-i\Phi}$.

$$I(q) = |A(q)|^2 = A(q) \cdot A^*(q) = \int_{V_R} \int_{V_{R'}} \rho(r)\rho(r')\, e^{-iq(r-r')} \mathrm{d}V_R\, \mathrm{d}V_{R'}$$ Equation 2.33

The contrast between phases $\rho(r)$ is expressed by the autocorrelation function $\gamma(R)$ as:

$$\gamma(r - r') = \gamma(R) = \frac{1}{V_R} \int_{V_R} \Delta\rho(r)\Delta\rho(r + R) \mathrm{d}V_R$$ Equation 2.34

By inserting the autocorrelation function into the intensity function,[Svergun2003] Equation 2.33 becomes:

$$I(q) = \int_{V_R} V_R \gamma(R) e^{-iRq} \mathrm{d}V_R$$ Equation 2.35

2.4.1.2 Form factor

For non-oriented samples (isotropic) in the diluted regime, only the spherical average of the intensity is measured, $I(q) = \langle I(q) \rangle_{spherical}$. The probability distance function $p(R)$ is given by the Equation 2.36.

$$p(R) = (R)^2 V \langle \gamma(R) \rangle_{spherical} = \frac{1}{\pi} \int_0^{\infty} \frac{(R)q}{2\pi} I(q) \sin((R)q) \, \mathrm{d}q \qquad \text{Equation 2.36}$$

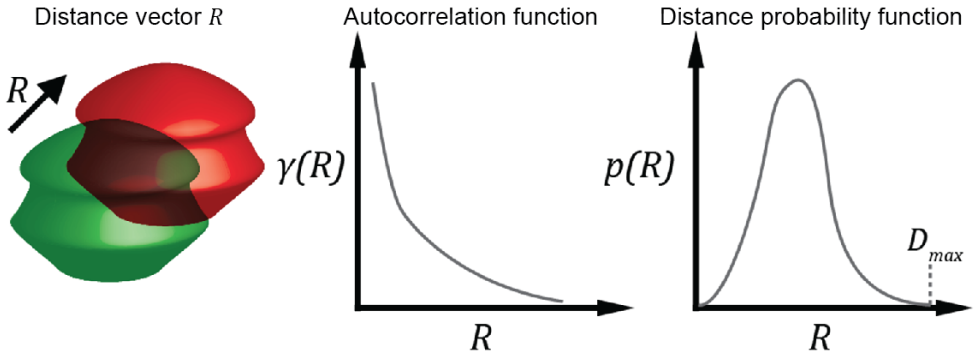


Figure 2.12 Visual representation of the Distance vector R, autocorrelation function $\gamma(R)$ and distance probability function $p(R)$

As plotted on Figure 2.12, the probability distribution $p(R)$ is a unimodal function of R vanishing at the boundary D_{max} for homogenous particles with a constant $\rho(R)$.[Svergun2003]

2.4.1.3 The low q limit for X-ray scattering (Guinier region)

In order to fully characterise the system, the scattering intensity of the full q range from 0 to ∞ would have to be determined. Since this is not possible experimentally, some assumption of the boundary values must be made. The scattered intensity $I(q)$ can be expanded in a series of power of $O(q)$ which can be approximated to the first term close to the origin ($q \to 0$). The intensity $I(q)$ is then represented by

$$I(q) = I(q)\left[1 - \frac{1}{3}R_g^2 q^2 + O(q^4) + \cdots\right] \cong I(q)\, e^{-\frac{1}{3}R_g^2 q^2}\Big|_{q \to 0} \qquad \text{Equation 2.37}$$

$$-\frac{1}{3}R_g^2 = ln(I(q))dq^2|_{q\to 0}$$

where R_g^2 is the radius of gyration.[Guinier1955] The square of the radius of gyration R_g^2 is defined as the average area over all molecules of the sample and over time such that:

$$R_g^2 = \frac{1}{N}\langle \sum_{K=1}^{N} (r_k - r_{mean})^2 \rangle \qquad \text{Equation 2.38}$$

where r_{mean} is the mean position, r_k is the position of particle k and N is the number of particles. Objects with the same volume can therefore have different radius of gyrations based on their shape. In a Guinier plot $ln\big(I(q)\big)$ is plotted as a function of q^2, the slope thus being proportional to $-R_g^2/3$,the intercept giving the intensity at $q = 0$. For full spheres, R_g will be relatively small compared to its radius ($R_g = radius * \sqrt{3/5}$) whilst for rods, the R_g will be comparatively larger due to their rods' lengths ($R_g = length * \sqrt{1/12}$).[Svergun2003] For small angle X-ray scattering (SAXS), the X-ray scattering amplitude at $q = 0$ is proportional to the number of electrons in the sample n_e.

$$A(0) = \int_{V_R} \rho(\vec{r}) e^{-ir0} \mathrm{d}V_R = \int_{V_R} \rho(\vec{r}) \mathrm{d}V_R = n_e \qquad \text{Equation 2.39}$$

Therefore the scattering intensity $I(0)$at q = 0 after solvent subtraction is proportional to the square of the difference between the number of electrons from the solvent and buffer.

$$I(0) = n_e^2 - n_{e0}^2 \qquad \text{Equation 2.40}$$

Because of this relationship, the concentration normalised intensity is proportional to the molecular weight M_w

$$\frac{I(0)}{c} = \frac{N_A M_w (1-\rho_0\psi)^2}{\mu^2} \quad or \quad M_w = \frac{I(0)}{c}\frac{\mu^2}{(1-\rho_0\psi)^2 N_A} \qquad \text{Equation 2.41}$$

where ψ is the electronic partial specific volume (ρ_0 is the density, c is the concentration), N_A is Avogadro number (6.022*10^{23} mol^{-1}) and μ is the ratio of the mass on the number of electron per mole ($M_w/(mass * N_A^{-1})$).[Jacrot1981] μ depends on the composition of the sample, but can be approximated to 1.87 for silk proteins and 1.80 for H_2O. The number of scattering events measured will depend on the scattering length of the electrons $b_i(\vec{q})$ which is given by the product of the scattering length of a single electron multiplied by the integral over all electrons

$$b_i(\vec{q}) = r_e f(\vec{q}) = \frac{1}{4\pi\varepsilon_0}\frac{\acute{e}^2}{m_e c^2}\int_{Atom} \rho(\vec{r}) e^{-i\vec{r}\cdot\vec{q}} \mathrm{d}^3 r \cong \frac{1}{4\pi\varepsilon_0}\frac{\acute{e}^2}{m_e c^2} * n_e \qquad \text{Equation 2.42}$$

where $f(\vec{q})$ is the atom's form factor, n_e is the number of electrons in the volume V_r and r_e is the scattering length of one electron equal to 2.8179*10^{-15}m.[Griffiths2005] $\acute{e}$ is the charge of one electron (−1.60 * 10^{-19} F*V), ε_0 is the vacuum permittivity (8.8541* 10^{-12} F/m), c is the speed of light (2.9979 *10^9 m/s) and m_e is the mass of one electron (9.1093 *10^{-28}g or 0.5109 MeV/c^2). For small angle X-ray scattering, the integral approaches the number of electrons n_e which can be estimated by the molarity and atomic number of the sample probed.[Koch2003]

2.4.1.4 The high q limit for X-ray scattering (Porod region)

At high q, the scattering correlation is much smaller than the sample's length scale, providing short distance local information. In the case of a uniform electron density distribution with a sharp sample/solvent interface and no inter-particular interactions ($S(q) = 1$), the scattering intensity will show an asymptotic behaviour at high q.[Porod1951;

[Porod1952] The scattered intensity at high q is thus related to the area to volume ratio by the following equation.

$$\frac{Area}{Volume} = \frac{1}{2\pi(\Delta\rho)^2 V} q^4 I(q)\Big|_{q\to\infty}$$ Equation 2.43

Experimentally, the slope of the $log(I(q))$ as a function of $log(q)$, a so-called Porod plot, provides the inverse of the excluded volume parameter $1/v_{excluded}$. As the intensity at high q is often very weak, an accurate background subtraction and a good signal to noise ratio are necessary to yield accurate values for the area and volume of the scattering entities in the sample.

Hence, by using the scattering intensity over these limits, $I(q)$ can inform on the general size and shape of the sample in solution. However, the shape of the $I(q)$ curve will depend on the detailed three dimensional structure of the object probed. For monodisperse and diluted samples, *ab initio* fitting can lead to reliable shape and size. Unfortunately, native silk feedstocks are polydisperse and their concentrations are too high to neglect inter-particle interactions $S(q) \neq 1$.

2.4.1.5 Orientation distribution

Unlike spectroscopy techniques such as infrared, Raman and NMR spectroscopy, scattering can provide the entire orientation distribution. This distribution can be described using a single parameter, the Hermans orientation parameter, S.[Hermans1946; Alexander1969; Finnigan2005; Wang2007; Okura2011] However, many orientation distributions can lead to the same S value. Using multiples parameters, the orientation distribution function is best described by a Legendre polynomial series which gives a unique solution[de Gennes1972; Bower1981; Hamley1996; Pople1998]

$$I(\varphi) = \sum_{n=0}^{\infty} (n + 1/2)\langle P_n \rangle P_n cos\varphi \qquad \text{Equation 2.44}$$

where $\langle P_n \rangle$ is the order parameter of even degree n, and $P_n\ cos\varphi$ is the n^{th} Legendre polynomial. By assuming centrosymmetry, the odd terms should equal zero, simplifying the series. As the first parameters are more important, neglecting the higher order parameters simplifies further the fitting calculation without much impact on the goodness of the fit distribution. Once the four first parameters are scaled[Bower1981] and the Taylor series expanded, the scattering intensity is expressed by

$$\begin{aligned}
&(\varphi) \\
&= I_{iso}\left[\langle P_0\rangle + \left(\left(2+\frac{1}{2}\right)\langle P_2\rangle\left(\frac{3cos^2\varphi - 1}{2}\right)\right)\right. \\
&+ \langle P_4\rangle\left(\left(4+\frac{1}{2}\right)\langle P_4\rangle\left(\frac{35cos^4\varphi - 30cos^2\varphi + 3}{8}\right)\right) \\
&+ \left(\left(6+\frac{1}{2}\right)\langle P_6\rangle\left(\frac{231cos^6\varphi - 315cos^4\varphi + 105cos^2\varphi - 5}{16}\right)\right) \\
&+ \left(\left(8\right.\right. \qquad \text{Equation 2.45} \\
&\left.\left.\left.+\frac{1}{2}\right)\langle P_8\rangle\left(\frac{6435cos^8 - 12012cos^6\varphi + 6930cos^4\varphi - 1260cos^2\varphi + 35}{128}\right)\right)\right]
\end{aligned}$$

where $< P_2 >, < P_4 >, < P_6 >$ and $< P_8 >$ are the order parameters of each polynomial, $< P_0 >$ being always equal to one.[Bower1981] The scaling parameter I_{iso} given in Equation 2.45 provides the intensity independent of the orientation. For a perfectly isotropic (non-oriented) orientation distribution, all the order parameters are equal to 0 and the intensity is I_{iso} at every azimuthal angle φ. The upper and lower boundaries allowed for each order parameter will depend on the other values, but cannot be above 1 nor below -0.5.[Bower1981;]

[Lafrance1991] Positive values of $< P_2 >$ indicate a preferential orientation along the symmetry axis whilst negative values represent a perpendicular preferential orientation.

2.4.2 Small Angle X-ray Scattering (SAXS) instrumentation

All Small Angle X-ray Scattering (SAXS) experiments were performed at the European Synchrotron Radiation Facility (ESRF) in France on the Dubble beamline BM26B. A monochromatic beam of 12 KeV (1.033 Å) was produced from a double Si(111) crystal monochromator with equatorial and meridional focusing on the sample. To achieve a beam spot size of ~300 x 500 µm at the sample position. Photons were counted by a Pilatus 1M detector (Dectris, Baden, Switzerland) with 1043 by 981 (height x width) array of 172 µm square pixels. By positioning the detector 4.5 m away from the sample, the instrument covered a q range from 0.003 to 0.18 $Å^{-1}$. The sample transmission was calculated from the ratio of the transmitted beam measured intensity by a photo diode on the beam stop to the intensity measured by a gas ionisation chamber before the sample. As detailed in Figure A.20 of Appendix 4, the absolute intensity was calibrated using an Eltex A1050 plastic film with known thickness and scattering length.[Russell1988] Rat tail tendon collagen was used as a standard to determine the centre of the beam and the q scale (see Figure A.21 of Appendix 4, page KK).

2.4.3 Scattering data analysis

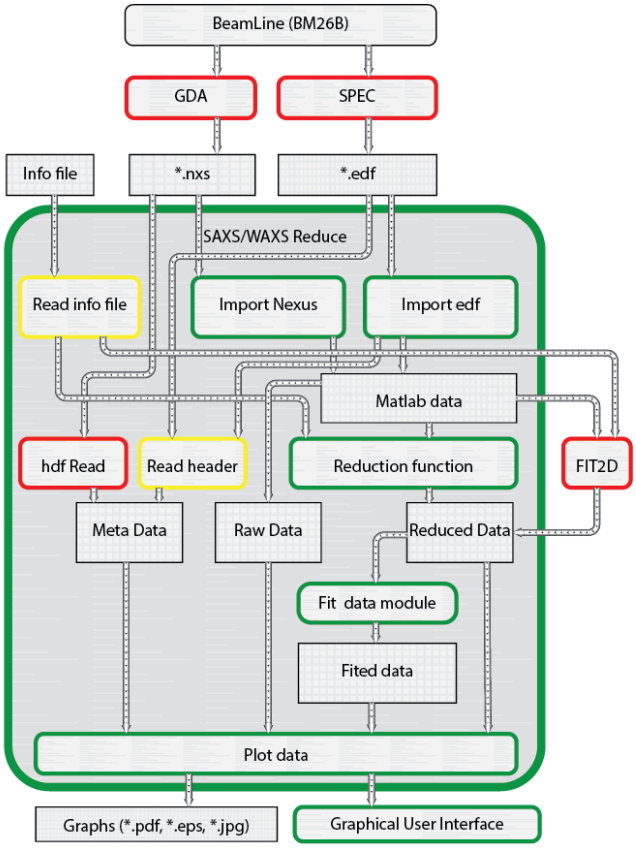


Figure 2.13 Small angle X-ray scattering data analysis MATLAB programming flow chart.

Figure 2.13 shows all the different MATLAB modules required for SAXS data analysis. The green boxes represent the modules I wrote whilst the yellow boxes are the MATLAB sub routines that were modified from code written by Lian Apostol and Giuseppe Portale. The external modules called by our script are illustrated with a red stroke such as FIT 2D written by Andy Hammersley of the ESRF. The MATLAB HDF read module was written by Lian Apostol.

2.4.4 Small Angle Neutron Scattering (SANS) instrumentation

Small Angle Neutron Scattering (SANS) experiments were performed at ISIS (STFC, UK) on SANS2D of target station 2, which provided 10 Hz neutron pulses with a flux of

approximately 100 /cm^2*s^{-1} This time-of-flight (TOF) instrument was designed to produce a high flux of cold (low energy neutrons) from the decoupled hydrogen moderator with wavelengths between 2 to 16.5 Å using counter-rotating disk choppers.[Heenan2011] The neutron beam was guided using highly reflective nickel surfaces. The transmission of each sample was calculated from the incident and transmitted intensity of the neutron beam before and after the sample counted by low sensitivity Li^6 doped glass scintillators coupled to photomultipliers. The small angle scattering was detected using a 96.5 by 96.5 cm Ordela21000N ^{3}He-CF_4 multi-wire proportional detector (Ordela, Oak Ridge, USA) with a pixel resolution of 5 x 5 mm^2. The detector was positioned 4 meters from the sample to cover a 5 to 160 mrad arc, giving access to a large q range from 0.005 to 0.6 Å^{-1}. The incident beam at the sample was defined by a cadmium mask, probing most of the sample cell.

Chapter 3

Shear-induced aggregation studied by time resolved infrared spectroscopy

This chapter was adapted in part from a manuscript titled *"Rheo-attenuated total reflectance infrared spectroscopy: a new tool to study biopolymers"* published in Physical Chemistry Chemical Physics (January 2011).[Boulet-Audet2011] This work presents the investigation of silk's conversion kinetics under a naturally relevant stress, shear flow. The combination of a shear cell with an infrared spectrometer brought new insights into silk's transition from liquid to solid by monitoring both the conformation and the molecular orientation under flow. The information obtained from this study deepened our understanding of the shear-induced aggregation process. Additionally it provided further insights into the development of new silk solubilisation methodologies. To better understand how silk is spun, this chapter investigated the effect of shear stress on reconstituted silk feedstocks. The experimental work, data analysis and manuscript redaction was conducted by Maxime Boulet-Audet whilst Chris Holland and Fritz Vollrath edited the chapter.

3.1 Abstract

Whilst rheology is the reference technique to study the mechanical properties of unspun silk, we know little about the structure and the dynamics that generate them. By coupling infrared spectroscopy and shearing forces to study silk fibroin conversion, we aimed at addressing this gap in our knowledge. Here silk's conversion process has been studied dynamically using polarised attenuated total reflection Fourier transform infrared

spectroscopy whilst applying shear. This method revealed silk's protein conformation and molecular orientation *in situ*. Our results show that the silk conversion process starts with a pre-alignment of the proteins followed by a rapid growth of the β-sheet formation and then a subsequent deceleration of the growth. This tool has the potential to provide further insight into silk but also any biopolymer solution, opening a new window into a biological material's response to shear stress.

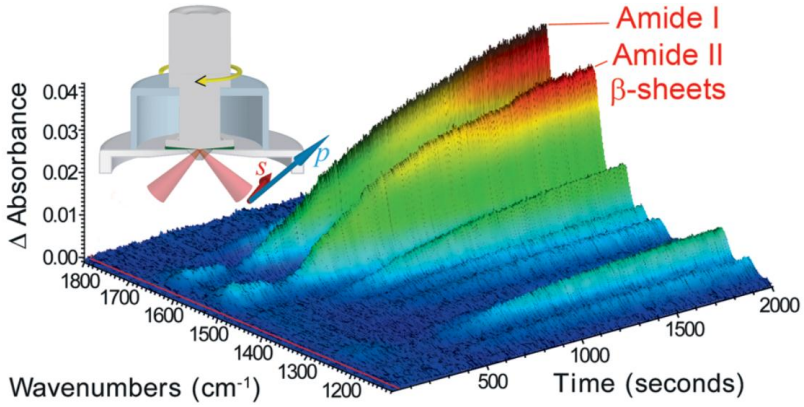


Figure 3.1 Graphical abstract of "Rheo-attenuated total reflection infrared spectroscopy: a new tool to study biopolymers" published in Physical Chemistry Chemical Physics.[Boulet-Audet2011]

3.2 Introduction

The network of hydrogen bonds responsible for its impressive toughness is also making silk regeneration/reconstitution a challenge.[Yamada2001] Indeed, the reconstitution of silk is known to have a major effect on the mechanical properties, making it much stiffer and more brittle than its natural counterpart.[Holland2007] Silks are typically reconstituted using strong chaotropic agents that are known to disrupt the proteins.[Holland2007] Even if it might be impossible to "unspin" silk completely,[Porter2008] we should still be able to optimise this process, provided that we have the appropriate tools to determine the quality of a reconstituted silk fibroin (RSF) solution.

Mechanical stress is known to be able to trigger the conversion of silk.[Liivak1998; Knight2000] Thus, rheology became one of the leading techniques to study RSF[*Chen2001a; Hossain2003a; Holland2007; Nagarkara2008; Zainuddin2008; Mo2009a*] and a very useful tool to evaluate the "spinnability" of RSF solutions.[Holland2007] Nonetheless, with the improvement of the reconstitution process, a finer discrimination of RSF from native silk dopes became necessary, requiring a multidimensional approach for "spinnability indicators".

The shear-induced crystallization of polymers has been the object of many rheo-optical studies including small angle X-ray scattering (SAXS),[*Kumaraswamy2004; Kanaya2007; Scelsi2008*] neutron (SANS),[*Kanaya2007*] light (SALS)[*Pogodina2001*] and wide angle X-ray scattering (WAXS).[*Kumaraswamy2004*] Despite being a model biopolymer,[*Vollrath2006a*] silk has been investigated in only few rheo-optical studies, such as a Couette cell by SAXS[*Rössle2004*] or NMR spectrometry.[*Ohgo2008*] These studies were limited by either having to use dilute solutions, long acquisition times, or both. Since time resolved Fourier Transform Infrared (FTIR) spectroscopy is a well-established technique to determine silk protein secondary structure[*Chen2001a; Chen2003; Boulet-Audet2008; Li2008; Chen2009; Mo2009a*] and has an exceptionally fast acquisition speed (50 ms down to 2 ns in step-scan mode), it is perfectly suited to combine with shearing devices. FTIR has been previously combined with parallel plate[*Kornfield1989*] and extensional flow devices using an attenuated total reflection (ATR) accessory,[*Wise1998*] however these approaches required large sample volumes and/or dilute samples. The use of a cone and plate shearing device presents a suitable alternative, allowing small highly concentrated samples to be studied with minimal shear history caused by the loading.[*Holland2006*]

We evaluated the combination of shear and infrared spectroscopy as a method to provide deep physiochemical insights into the shear sensitivity of silk macromolecules by monitoring *in situ* their molecular structure during controlled shear-induced transitions.

More generally, we also set out to evaluate the coupling of shear and infrared spectroscopy as a technique to assess the quality of RSF by providing a new set of "spinnability" indicators.

3.3 Materials and methods

3.3.1 Reconstituted silk fibroin (RSF)

Bombyx mori cocoons were degummed according to standard preparation methods and solubilised in 9M lithium bromide solution (< 70 °C).[Holland2007] After solubilisation, silk solutions were dialysed at 4 °C in dialysis tubing (VISKING® MWCO 12000-14000; pore diameter of 25 Å) against stirred demineralised water changed four times over 12 hours. A subsequent concentration step was performed by hanging the dialysis bags at 4 °C in a gentle air stream. A wide nozzle was used at the end of the dialysis bag to facilitate loading onto the ATR crystal. Completely converted samples were obtained by placing a fibroin sample onto the ATR crystal surrounded by an environment cuff containing methanol vapour.

3.3.2 Spectral acquisition

A Nicolet 6700 Fourier transform infrared spectrometer equipped with a MCT-A detector was combined with a single bounce diamond attenuated total reflection (ATR) sampling accessory (Thermo Electron Corp., Madison, WI). The diamond's internal reflection element (IRE) had a refractive index of 2.417 with an angle of incidence of 45°. The penetration depth of the evanescent wave for diamond was around 1.2 µm at 1650 cm^{-1} and varies with the wavelength.[Harrick1967] For molecular orientation measurement, the electric field of the infrared beam was polarised perpendicular (s) or parallel (p) to the plane of incidence with

a motorized zinc selenide holographic wire grid polarizer with 2700 grooves/mm (Thermo Scientific, Madison, WI). For fast kinetic experiments, only the *s* polarisation was used. A large aperture was selected to probe a ~2 mm^2 area while keeping a well-defined beam spot. Spectra were acquired at a 4 cm^{-1} resolution from 6000 to 500 cm^{-1} using a Happ-Genzel apodization, a Mertz phase correction and no additional zero filling. Static spectra were obtained from the average of 32 scans whilst the kinetics studies were recorded using 5.05 second time frames of 22 scans at a 5.0632 cm/s mirror speed. All spectral operations were executed using Omnic 7.3 (Thermo Scientific, Madison, WI). The only applied correction was an offset at 4000 cm^{-1}. The absorbance variation profiles were plotted by using the average integrated absorbance over a 10 cm^{-1} region. The centre of gravity of the amide I band was plotted using the 20% upper portion of the 1700-1594 cm^{-1} region for a more sensitive monitoring of the conformation. The point at which the first detectable changes occurred (take-off point) was calculated using the detection limit of the amide I band centre of gravity, three times the standard deviation of the blank average for two consecutive time frames. The growth point was defined as the absolute maximum of the second differentiate determined by a partial least squares linear regression over a 70 second mobile average.

3.3.3 Dry weight quantification

An additional drying step was performed once the RSF was placed onto the ATR crystal. The samples were dried using a gentle dry air stream as spectra were recorded to determine the concentration using a calibration curve built using TQ analyst edition 7.2 (Thermo Electron Corp. Madison, WI). The dry weight of the 94 standards was measured from 0.05 to 0.30 grams of RSF dried under vacuum for at least 12 hours. The method used was the partial least squares (PLS) with three factors (representing 94 % of the variance) on the

3900-2500 cm^{-1} and 1430-500 cm^{-1} regions. The predicted concentration values were calculated using the factor's eigenvalues. The quantification curve correlation coefficient was 0.987 and the average uncertainty of the dry weight was 3%.

3.3.4 Experimental setup

The Shear-IR setup consisted of a purpose built shear flow cell mounted on the single bounce diamond ATR accessory preceded by the polarizer. The geometry used for all shearing experiments was a 10 mm tungsten cone with a 1° angle (CP1/10). The ATR accessory's stainless steel plate served as the bottom plate of the geometry whilst the rotating cone (0.0874 rad/s) provided a constant shear rate of 5 s^{-1}. The strain was calculated by multiplying the time by the shear rate. The 30 µm gap was maintained by the shearing devices whilst the weight of the shaft could compensate for a normal force up to 20 kPa. To ensure the sample did not dry during shear, the system was sealed with an environment cuff.

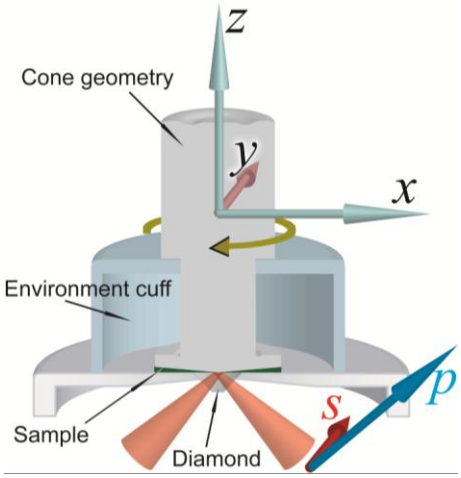


Figure 3.2 Experimental setup used for the Shear-IR measurements with the polarisation vector relative to the laboratory coordinate system.

As illustrated in Figure 3.2, the infrared beam propagates along the x axis. The s-polarised light only probes along the y axis, whilst p-polarised light probes along both x and z axes.

Thus, the theoretical value of p on s polarised spectra (R^{ATR}) is 2 for non-oriented (isotropic) samples with a 45° angle of incidence.[Harrick1967] A R^{ATR} lower than 2 means a preferential orientation in the plane of the ATR crystal and a R^{ATR} higher than 2 is out of the plane. The geometry is concentric to the beam spot evenly distributing the strain around the z axis. The quantification of the orientation along the z axis would be theoretically possible by assuming a cylindrical symmetry and decomposing the spectra into their components.[Fringeli1992] However, R^{ATR} was used directly to qualify the orientation since the interfering H_2O content made the spectral decomposition challenging.

3.4 Results and discussion

3.4.1 Silk shear-induced conversion kinetic

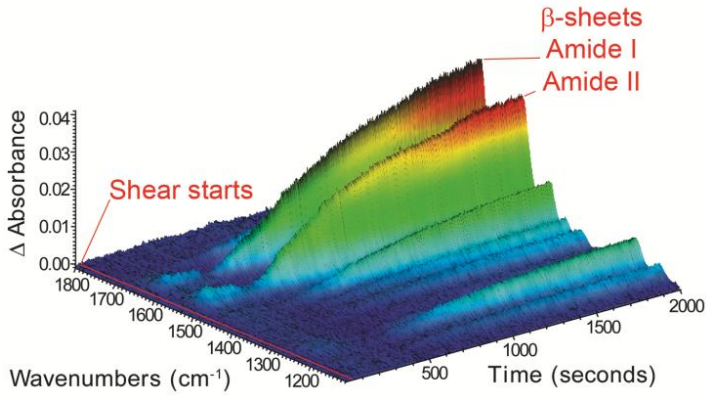


Figure 3.3 Difference spectra of a 68±3 % RSF sample under 5 s^{-1} shear rate as a function of time.

Figure 3.3 shows the typical conversion kinetics of a concentrated RSF sample under shear (5 s^{-1}) after subtraction of the initial unsheared sample spectrum. Shearing the material faster than native silk's relaxation time, typically 2 to 5 s^{-1},[Holland2006] should in theory trigger a change in silk protein conformation from disordered structures to β-sheets.[Li2001] After the start of shearing, the subtle variations in the signal are due to changes in the local concentration whilst the sample is homogenising. By probing only the bottom layer of the

sample (~1.2 µm at 1650 cm^{-1}),[Harrick1967] ATR is sensitive to the local concentration and can detect precipitation or phase separation. The rapid growth of the β-sheets occurs a few hundreds of seconds later. Once a notable proportion of β-sheets were generated, RSF samples started to become solid, increasing the normal force drastically,[Holland2006] lifting the cone geometry. As a result, the sample either stuck to the bottom plate or started rolling out of the geometry. As the sample became detached from the geometry, the β-sheets growth rate slowed rapidly. Importantly, the observed three-phase conversion kinetics induced by the mechanical stresses is in agreement with the results obtained using other types of stress.[Li2001; Nagarkar2010]

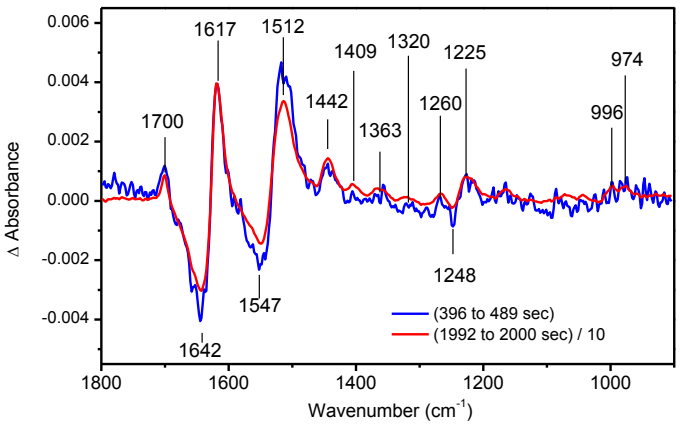


Figure 3.4 Difference spectra at the beginning of the growth (blue curve) and after the gelation divided by a factor of 10 (red curve).

FTIR spectroscopy is very sensitive to protein conformations.[Goormaghtigh2006; Barth2007] As shown in Figure 3.4, the difference spectra at the beginning of the fast growth (blue) and at the end of the kinetic (red) are similar, once put on a relative scale. They both show increasing β-sheet peaks at 1512, 1614 and 1700 cm^{-1} as well as negative peaks due to unordered structures lost at 1547 and 1642 cm^{-1} (for band assignment in Table 3.1 and Table 7.1). The stacked curves indicated that gained and lost structures in the early stage of the conversion process are comparable to those formed at a later stage.

Position (cm^{-1})	Assignment	Preferential Orientation relative to the protein backbone	References
1700	Amide I, β-sheets/ β-turns	∥	*Miyazawa1961; Moore1976; Bandekar1979; Garside2005; Teramoto2005*
1642	Amide I, unordered	⊥	*Venyaminov1990; Goormaghtigh1994a; Sonoyama2000; Jeong2006*
1617	Amide I, β-sheets	⊥	*Moore1976; Muller1993; Garside2005; Taddei2005; Boulet-Audet2008*
1547	Amide II, unordered	∥	*Yoshimizu1990; Sonoyama2000; Lv2005; Jeong2006*
1512	Amide II, β-sheets	∥	*Venyaminov1990; Yoshimizu1990; Muller1993; Sonoyama2000; Lv2005; Jeong2006; Boulet-Audet2008*

Table 3.1 Assignment of the main fibroin bands

The conversion kinetics can be easily visualised by directly plotting the absorbance variation of vibrational modes. However, if the sample starts to roll between the upper and lower plates, the absolute absorbance will decrease proportionally to the contact surface. To overcome this potential issue, the centre of gravity of the amide I band's upper part can be used as a single variable conversion indicator independent of the surface contact. The point at which the first variation in the infrared signal is detected (take off point) and the point at which the β-sheet content starts to increase rapidly (growth point) can be accurately measured with the second differential of the centre of gravity.

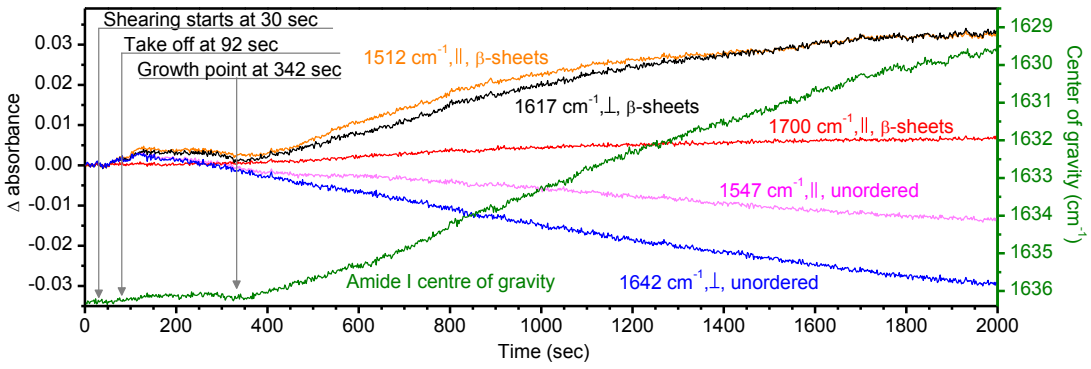


Figure 3.5 Difference absorbance and centre of gravity of the major bands of a 68±3 % RSF sample under 5 s^{-1} shear rate as a function of time

It is possible to distinguish in Figure 3.5 the three steps of the conversion process by plotting the components that varied the most. If put on a relative scale, the 1700 and 1617 cm^{-1} components assigned to the β-sheets, as well as the 1642 and 1547 cm^{-1} assigned to unordered structures, have very similar kinetics confirming that these components are

associated with the same or joined structures. Since spectra were s-polarised, the contrasting kinetics observed for the 1617 and 1512 cm^{-1} components could be explained by their different orientations relative to the protein backbone.[Moore1976; Marsh1997; Boulet-Audet2008]

3.4.2 2D correlation analysis

By using shear stress as a perturbation, we can spread IR spectra on an additional axis to help resolve overlapping peaks.[Noda1990] This analytical approach described in section 2.3.6 correlated components perturbed simultaneously ϕ (in-phase) from those perturbed non-simultaneously ψ (out-of-phase). The selection rules listed in Figure 3.6c allowed the determination of the sequence of spectral changes under perturbation.[Noda1990]

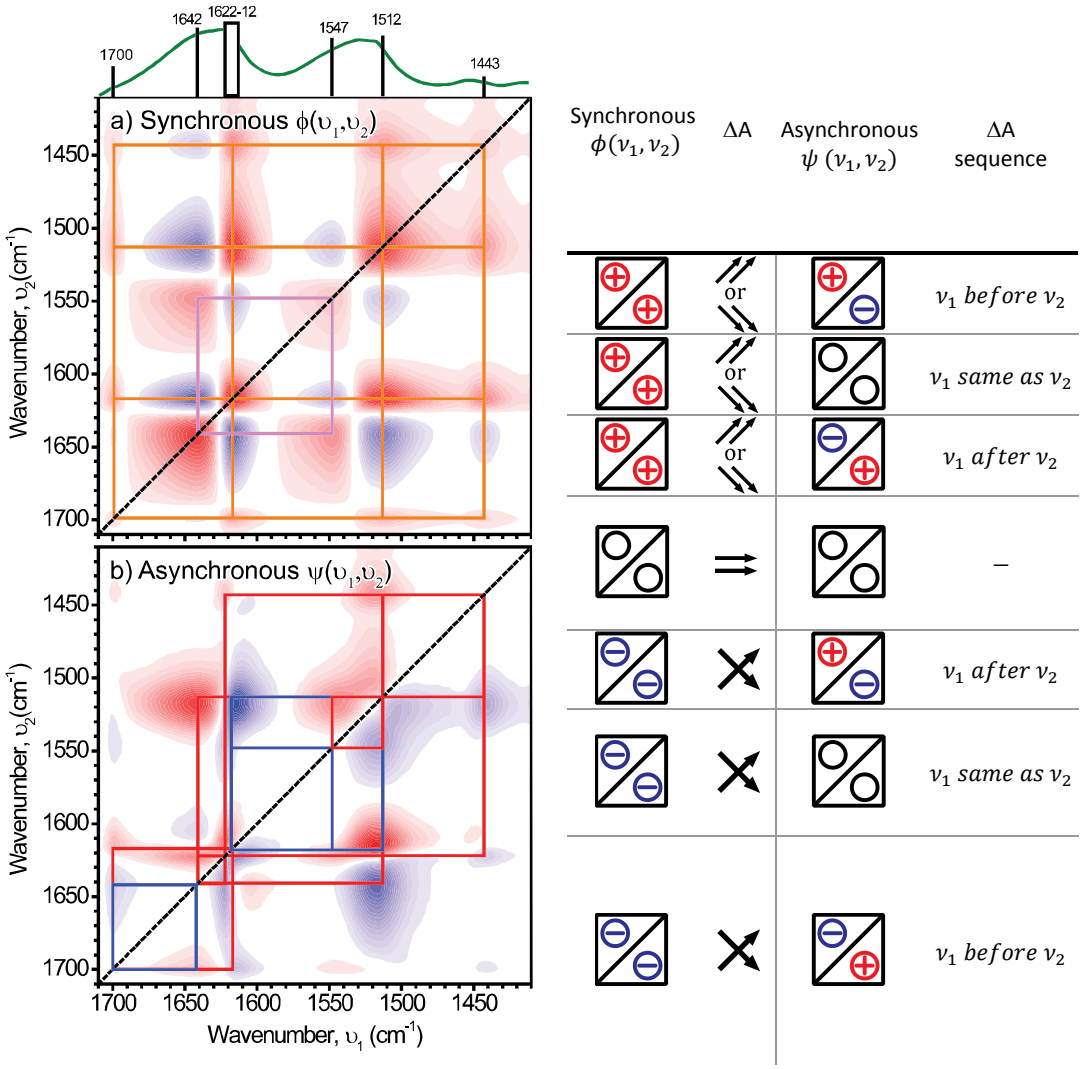


Figure 3.6 a) Synchronous spectrum generated from the RSF shear-induced conversion presented in Figure 3.3. The orange squares represent the band rising synchronously whilst the purple box indicates components decreasing synchronously. The color scale ranges from -1.4E^{-4} (deep blue) to +1.4E^{-4} (bright red). b) Asynchronous spectrum. The red squares represent the pair of components with ν_1 before ν_2 whilst the blue square represent the component pairs where changes in ν_1 occur after ν_2. The color scale ranges from -9.4E^{-6} (deep blue) to +9.5E^{-6} (bright red). c) 2D Correlation selection and temporal rules.

The synchronous correlation intensity $\phi(\nu_1,\nu_2)$ presented Figure 3.6a characterises the degree of coherence between in-phase ($\delta = 0$) signals. It reveals the synchronicity between the bands associated with gained β-sheets at 1700, 1617, 1513 and 1443 cm^{-1} (orange correlation squares) and lost unordered structures 1642 and 1548 cm^{-1} (magenta correlation square). In contrast, the asynchrone intensity $\psi(\nu_1,\nu_2)$ plotted in Figure 3.6b is proportional to the phase difference between the varying components. Orthogonal signals ($\delta = \pm\pi/2$) give little synchronous intensity but have maximum intensity on the

asynchronous $\psi(\nu_1, \nu_2)$ 2D spectra. No peaks are observed on the diagonal line of Figure 3.6b since every frequency component is in phase with itself. On the other hand, off diagonal peaks found on the asynchronous plot reveal gained or lost intensity occurring out-of-phase. The absence of asynchronous peaks between bands at 1700 and 1512 cm^{-1} proves that β-sheets vibration modes are increasing together. Similarly, the absence of peaks between 1642 and 1548 demonstrates that unordered components disappeared simultaneously.

From these spectra it is also possible to extract the temporal relationship between higher wavenumbers ν_1 (horizontal axis) and lower wavenumbers ν_2 (horizontal axis) using the asynchronous intensity sign. The strongest asynchronous peak at ν_1= 1512 / ν_2= 1617 cm^{-1} indicates that the 1512 cm^{-1} is rising before 1617 cm^{-1} as seen on Figure 3.5. As the 1512 cm^{-1} component is associated with the Amide II vibration mode parallel to the back bone, this observation could be explained by the molecular alignment of early β-sheets formed in the crystal's plane H-bonding. The second most important peak at ν_1= 1642 / ν_2= 1512 cm^{-1} shows that unordered structures start to decrease before the earliest β-sheets bands changes, which is also shown by the off-diagonal peaks at ν_1= 1642 / ν_2= 1617 cm^{-1} and ν_1= 1548 / ν_2= 1512 cm^{-1}. In addition, the weak ψ peak at ν_1= 1700 / ν_2= 1617 cm^{-1} suggests that β-sheets (1617 cm^{-1}) are formed slightly before β-turns (1700 cm^{-1}). Consequently, 2D correlation revealed that unordered structures are affected before the β-sheets vibration modes parallel to the β-strand, followed by the perpendicular vibration modes and the β-turns. Since the extinction coefficient is higher for β-sheets than unordered structures, the detection limit of unordered structure is expected to be lower.[deJongh1996] The phase difference between the parallel and perpendicular mode could be explained by the use of *s* polarised light probing only in the plane the ATR crystal and an anisotropic system. Moreover, the elongated peak at ν_1= 1622 / ν_2= 1612 cm^{-1} suggests that the perpendicular

mode of the β-sheets is shifting to lower frequency during the conversion process. This shift could be attributed to change in the β-strand morphology[Kim2001] or be the product of band overlap between the decreasing 1642 cm^{-1} and the rising 1612 cm^{-1} components.

3.4.3 Conformation analysis

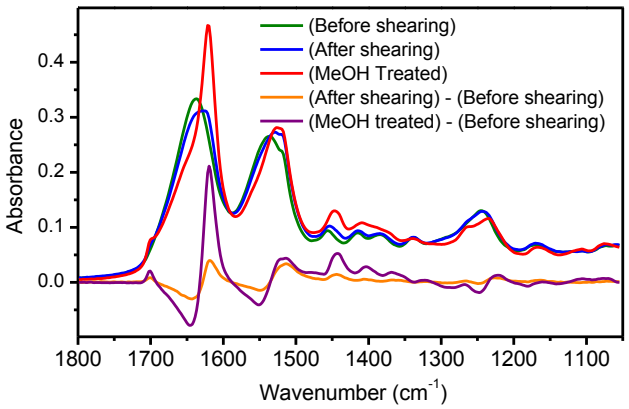


Figure 3.7 ATR FTIR spectra before, after 2000 sec of shearing at 5 s^{-1}, after MeOH vapour treatment and their difference.

To estimate the relative amount of β-sheets formed by controlled shearing, a sample with the same concentration was converted using methanol vapour. As shown in Figure 3.7, the peaks associated with β-sheets are much more prominent in the sample converted by alcohol (purple curve). The difference between the amide I and II ratio could be explained by the lack of molecular orientation in the MeOH converted sample. After subtraction of the static spectrum, the difference obtained with methanol is many times (> 3x) greater in the amide I region. This result suggests that the conversion process is far from being completed when the RSF sample starts to gel under shear stress. According to this observation, shearing forces triggered RSF's conversion, but did not drive it to completion. Since the geometry was lifted at this point, it was difficult to assess if shearing stress was still applied at this point and if more stress could have been applied with a larger normal force. On the other hand, the reconstituted analogue might not behave like native silk. Hence, to remove the doubts of the choice of sample, native silk extracted from the

silkworm was used in the subsequent chapter. In addition, *in vivo* other sources of stress might play an important role such as extensional flow[Knight1999b] and changes to the pH and ionic concentrations.[Magoshi1994; Knight2001] Hence to answer this question univocally, more representative samples and a better instrumentation are needed.

3.4.4 The effect of concentration

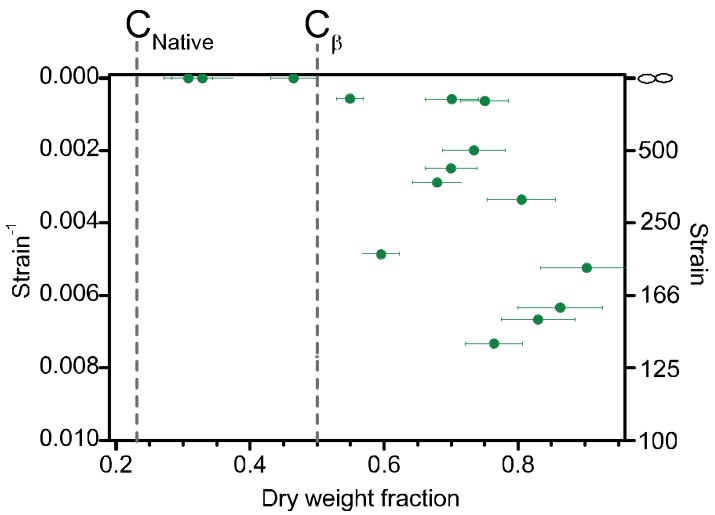


Figure 3.8 Strain (time * shear rate) at the growth point as a function of the dry weight fraction (concentration). The critical RSF concentration is marked as C_β and the native concentration of natural silk is marked as C_{native}.

Sample concentration is one of the critical parameters governing a silk solution's rheological behaviour.[Holland2007] As displayed in Figure 3.8, the strain required to initiate the fast growth of β-sheets (growth point) depended on the concentration like rheology "spinnability indicators".[Holland2007] The variability can be explained by the tolerances of the purpose built rheometer, the sample loading or the RSF reparation method. For a given RSF batch, the growth point indicated that the concentration required for conversion is over a certain threshold C_β of ~50%. This critical concentration is more than twice the concentration of native silk feedstocks which are known to be shear sensitive.[Holland2006; Holland2007] Hence, it could be that that higher concentration is necessary for achieving enough molecular entanglement for the flow stress energy to be converted into molecular

rearrangement. Without the response to stress required for calculating the viscosity this hypothesis cannot be tested. Thus, the experimental platform was improved to address this issue in the following chapters.

Without response to stress, the concentration dependent growth point could still be used as a complementary indicator of the RSF quality since previous experiments investigating the rheological "spinnability" indicators did not exceed the C_β (reaching only 36% DW).[Holland2007] Three out of the fifteen kinetic data sets recorded never converted under a 5 s^{-1} shear ($strain^{-1}$ = 0). Over the concentration range, the growth point varied by more than an order of magnitude, from 133 to 2745 strains.

As shown in Figure 3.5, the 1512 cm^{-1} has a faster conversion kinetic than the 1617 cm^{-1}. This observation could imply that these components do not have the same molecular orientation or they are part of different structures with distinct kinetics.

3.4.5 Polarisation rotation measurements

To determine RSF's molecular orientation, both polarisations must be recorded in order to calculate the dichroic ratio $R^{ATR} = p / s$. Unfortunately, it comes at the price of acquisition speed as our motorised polariser takes more than 30 seconds to move between each polarisation direction. By using a RSF sample of slightly lower concentration (60 ± 3 % instead of 68 ± 3 %), the conversion occurs over a longer time scale. While staying above C_β, it permitted a suitable acquisition time for both polarisations to be recorded in alternation.

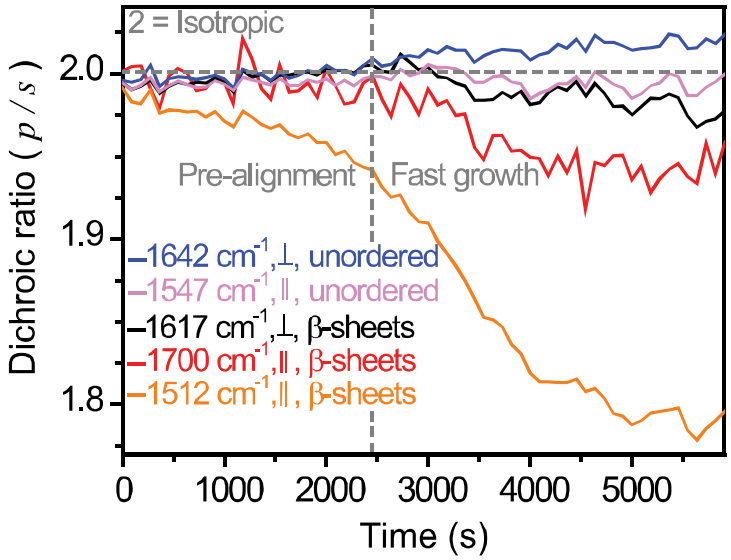


Figure 3.9 Dichroic ratio of the 1512, 1547, 1512, 1617 and 1642 cm^{-1} components dichroic ratio as a function of time for a 60 ± 3 % RSF sample.

As shown in Figure 3.9, the dichroic ratio of the 1512 and 1700 cm^{-1} components decreased during the conversion process, suggesting a certain degree of molecular orientation of these vibration modes. The dichroic ratio measured for these two vibration modes (particularly the weak 1700 cm^{-1} component) would have decreased even faster if the interfering bending mode of water present in the Amide I region was subtracted. The orientation of the 1512 cm^{-1} mode also explains the different kinetic observed compared to the 1617 cm^{-1} component shown in the Figure 3.5.

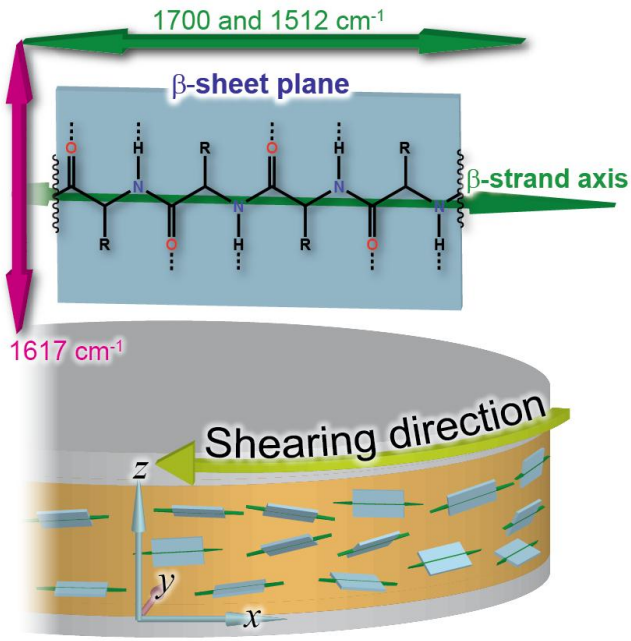


Figure 3.10 Schematics of the sheets' orientation relative to the setup referential.

The full determination of the biaxial orientation of the β-sheets requires two orthogonal components. However, the orientation of the β-strands constituting the β-sheets can be qualified by using only the Amide II mode which is parallel to the backbone.[Marsh1997] The decrease of the dichroic ratio of the 1512 cm^{-1} component measured suggests that β-strands aligned in the plane of the ATR crystal, along the shearing direction (illustrated in Figure 3.10). This observation is in agreement with previous studies claiming that the β-sheets formed under mechanical stress are oriented parallel to the direction of the deformation or the resulting fibre axis.[Marsh1955a; Simmons1996; Vollrath1999; Vollrath2001; Boulet-Audet2008] Furthermore, the dichroic ratio of the 1512 cm^{-1} component shows a decrease before the growth point observed around 2500 seconds. This observation supports the hypothesis that silk passes through a pre-alignment step prior to the formation of the β-sheets and the gelation.[Vollrath1999] The vibration modes perpendicular to the β-strands[Moore1976; Marsh1997] at 1547 and 1617 cm^{-1} displayed a R^{ATR} close to 2. As illustrated in Figure 3.10, this result suggests that β-sheet planes are randomly distributed around the β-strands and the backbone of the protein.

3.5 Conclusions

This work demonstrated for the first time the coupling of shear flow cell and polarised ATR-FTIR spectroscopy to study shear sensitive biological materials. This powerful new tool allowed the study of RSF conversion *in situ* for various concentrations, deepening our understanding of the aggregation kinetics. Our experiments showed that the silk conversion passes through three phases; pre-alignment, fast β-sheet growth and a deceleration of the growth rate. The polarisation measurements allowed the identification of a pre-alignment step occurring before the rapid growth of the β-sheets. This result suggests that the protein chains must already be partially aligned to form the well oriented crystallites found in the fibres.[Simmons1996; Rousseau2006; Boulet-Audet2008] The β-strands were found to be aligned along the shearing direction. However, the β-sheet planes did not show any preferential rotational orientation around the β-strands' axis. This observation supports the hypothesis of the oriented nano-fibrils similar to "String of beads"[Vollrath2006b] rather than a structure of pleated stacks of β-sheets. Most importantly, this technique also provided an additional indicator of RSF 'quality' i.e. spinnability with the critical concentration for shear sensitivity.

We further observed that the amount of β-sheets induced by shearing RSF was only a small fraction of what could ultimately be formed by the material. Thus, shearing forces are unlikely to be held entirely responsible for silk's conversion as the sample becomes solid well before gaining its full crystalline content. Consequently, the extensional forces occurring after the gelation must complete the orientation of the chains and the conversion process. Finally, we observed that conversion kinetics were strongly dependent on the concentration once a threshold is reached. As each technique brings additional insights, combining them all together will eventually be essential to link all parts of the silk processing.

Chapter 4 Native silk conversion kinetics studied by small angle scattering

This chapter consists of the small angle work conducted at the Dubble BM26B Beam line of the ESRF synchrotron radiation source and SANS2D at the ISIS neutron sources. In addition to providing information on the nanoscale structure of native silk during spinning, this study introduces the measurement of silk's response to stress to calculate its flow properties. For this work, we used a conventional shear cell and designed a novel *ex situ* shearing platform to monitor the spontaneous shear-induced conversion kinetics. I performed the entire data analysis and wrote the manuscript. On the other hand, Lian Apostol and Giuseppe Portale wrote some of the Matlab modules included in the code I developed for reducing the scattering patterns. Due to the demanding nature of the beamline experiments Ann Terry, Imke Greving, Tom Gheysens and Chris Holland assisted in the sample preparation and the operation of the instruments. Chris Holland, Ann Terry, Tom Gheysens and Fritz Vollrath contributed to the editing of this chapter.

4.1 Abstract

The remarkable mechanical properties of silk fibres originate from their multi-scale hierarchical structures formed when aqueous solutions of silk proteins undergo solidification. As liquid native silk denatures upon flow stress, rheology can provide shear as a biologically relevant source of stress whilst measuring the response to flow. To relate flow properties to nanoscale structures change during silk's processing, we measured both rheology and the small angle scattering. Small angle scattering revealed that structures larger than 70 Å are affected during spinning whilst 126 Å represents the minimum length

scale of alignment of the nanoscale domains. In addition to providing the critical shear rate for triggering aggregation, our platform allowed us to estimate the potential contribution of shear stress to 7% of the total process. We also quantified the spontaneous conversion kinetic rate for a range of shear history. The insights into natural spinning gained will support our efforts to fully understand the natural spinning process by highlighting the potential importance of other biologically relevant sources of stress such as extensional flow and acidification.

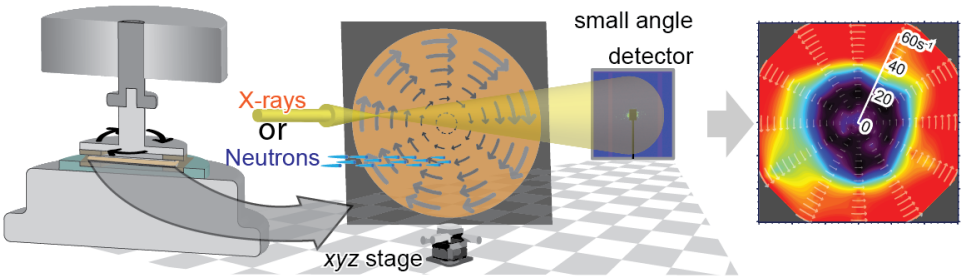


Figure 4.1 Chapter 4 graphical abstract

4.2 INTRODUCTION

Thanks to its distinct interaction with water,[Porter2012; Porter2013] silk denatures, changes conformation and self-assembles under controlled stress to solidify on demand[Humenik2011; Vollrath2013b] and form fibres solid with exceptional toughness.[Gosline1999 Gosline1986; Vollrath2001] Unlike other structural proteins, silk's multi-scale hierarchical structure is rapidly formed in the optimised spinning apparatus.[Vollrath2006b; Moriya2008a; Moriya2008b; Davies2013] *In vivo*, these stresses include pH drop and concentration change in cationic ions and most importantly flow stress as silk is particularly sensitive to shear forces.[Holland2012c; Boulet-Audet2013; Vollrath2013b] Hence by providing biologically relevant shear stress, rheology represents the most suitable technique to test silk's natural behaviour. Through flow under conditions akin to those experienced in the spinning duct, this technique has the ability to carefully control the

energy input whilst measuring the liquid silk's deformation to calculate its flow properties as it is spun.[Kojic2006; Holland2007; Moriya2008a; Holland2012b; Boulet-Audet2013]

The structural cause of the flow property change needs to be investigated further to comprehend silk's spinning process. The structures of unspun and spun silk has been characterised by a wide range of techniques listed in Table 1.1. At the molecular level, silk has a β-sheet secondary structure giving a characteristic spectroscopic signal by infrared,[Chen2002a; Boulet-Audet2008] Raman,[Shao1999; Li2001] nuclear magnetic resonance spectroscopy,[Asakura2004] and circular dichroism.[Li2001; Chen2008] Additionally, wide angle X-ray scattering also reveals the semi-crystalline nature of spun silk fibres,[Warwicker1954] whilst dynamic light scattering (DLS) reveals the large scale aggregation process in solutions[Hossain2003b] and small angle neutron scattering allows the determination of native silk's nanoscale structure in solution.[Greving2010] However, to link silk's structure and function, it needs to be probed whilst it is performing its function in order to address this gap in our knowledge. Such combination of shear stress with probing radiation includes confocal microscopy,[Holland2012b] NMR[Ohgo2008] and infrared spectroscopy.[Boulet-Audet2013] X-ray scattering is commonly employed to study liquid crystals of di-block polymer crystallisation.[Pople1998; Castelletto2002; Lemaire2002; Meins2012] Thanks to bright synchrotron sources, it allows the study of nanoscale structures under flow with a sub-second time resolution for the identification of transient structures.

These advantages led scientists to use X-ray scattering to study silk under flow stress *in situ*.[Rössle2004; Martel2008a; Martel2008b] Unfortunately, these previous studies have only focused on artificial reconstituted silk feedstocks to try to understand how silk is spun despite the variability of RSF preparation methods.[Holland2007; Boulet-Audet2013Greving2010, Wang2013] We address this potential issue by opting for native silk fibroin extracted directly from *Bombyx mori*

silkworm glands instead. This approach provided consistent samples representative of the natural material spun by animals whilst rheology provided biologically relevant stress. Using silk straight from the gland provides samples with a comparable concentration as *in vivo* (220 ± 30 mg/ml). This is of particular importance as intermolecular interactions are concentration dependent. Lower concentrations cannot necessarily predict high concentration protein behaviour.[Chari2009; Mosbaek2012] In addition, diluting liquid reduces the shear sensitivity.[Chen2002b]

For diluted systems, Couette cells allow *in situ* measurement of both X-ray scattering and rheological properties.[Rössle2004] Unfortunately, undiluted native silk feedstocks have viscosity higher than 1000 Pa·s[Holland2006] and stick to the geometry's wall, making it challenging to load without inducing uncontrolled shear history. In addition, Couette cells commonly require larger volumes. In contrast, parallel plates are easier to load and require smaller sample volume. In addition, their first normal force calculation is more straightforward. Hence, we opted for parallel flow. The geometry's main limitation is the in situ coupling of rheology measurements with the beam as rheometers typically have a vertical rotation axis and the beam path is normally horizontal. Although it is possible to build horizontal rheometer,[Sharma2010] they are uncommon and cannot achieve the same level of sensitivity. In addition, native silk must be loaded horizontally as it would otherwise slowly flow due to gravity. Thus the rheological properties of silk could not be measured simultaneously. Instead, we opted for a simple shearing cell to monitor native silk spinning *in situ*, one shear rate at a time.

To measure the flow properties before probing the sample, we developed a novel method to transfer the parallel plate geometry from a rheometer to the beamline. It permitted the evaluation of silk's rheological properties whilst inputting a known amount of shear history.

In addition, the parallel plate geometry generated a linear shear rate gradient allowing the probing of a shear history range by simply mapping a single cell. From these two complementary experiments, we obtained novel insights into the nanoscale structures formed during natural silk spinning.

4.3 Experimental method

4.3.1 Native silk preparation

Native silk samples were prepared from *Bombyx mori* silkworms kept at 22 ± 2°C degrees and fed leaves from white mulberry trees (*Morus alba*) or processed leaf diet. Once cocoon construction started, larvae were stored at 9 ± 1°C to slow their metabolism and prevent spinning. To optimise yields from each silkworm (0.16 ± 0.05 g per worm, n = 119), a complete dissection of both silk glands was performed. Silk glands were extracted within 5 minutes before being transferred to a petri dish filled with demineralised water where the epithelium was removed with tweezers under a microscope. As the liquid silk is highly sensitive to mechanical stress, great care was taken to avoid damaging the dope inside the silk gland during peeling. The peeled glands were then transferred into another petri dish filled with water and stirred gently to remove the soluble sericin protein coating the glands. It took on average 52 ± 4 minutes to complete all these steps for each of the 119 worms dissected for all experiments. To prevent dehydration, samples were then stored for 12 to 24 hours at 4 ± 1°C in sealed containers with wet tissues.

4.3.2 Small Angle X-ray Scattering (SAXS) beamline

Small angle X-ray scattering (SAXS) experiments were performed at Dubble BM26B, ESRF, France. A 12 KeV (1.033 Å) monochromatic beam was produced by a double Si (111) crystal

monochromator with equatorial and meridional focusing. The beam was focused to a beam spot size of 300 x 500 µm (h*w). SAXS patterns were collected by a Pilatus 1M detector (Dectris, Baden, Switzerland) with 1043 by 981 square pixels of 172 µm. By positioning the SAXS detector 4.5 m away from the sample, the instrument covered a q range from 0.003 to 0.18 $Å^{-1}$, the sample detector distance being calibrated by hydrated rat tail tendon collagen. The sample transmission was calculated from a photo diode on the beam stop and a gas ionisation chamber before the sample compartment. The absolute intensity was calibrated using a Eltex® A1050 polyethylene plastic with known absolute scattering intensity.[Russell1988]

4.3.3 Small Angle Neutron Scattering (SANS) beamline

Small Angle Neutron Scattering experiments were performed at ISIS (STFC, UK) on the SANS2D instrument. This time of flight instrument was designed to produce a high flux of cold (low energy neutrons) from a decoupled hydrogen moderator with 2 to 16.5 Å wavelengths using counter-rotating disk choppers.[Heenan2011] The neutron beam was collimated by a series of nickel coated glass guides and B_4C and cadmium apertures. Low sensitivity monitors served to calculate the transmission and normalise the scattering intensity. Neutron scattering events were detected using a 96.5 by 96.5 cm Ordela21000N ^3He-CF_4 multi-wire proportional detector (Ordela, Oak Ridge, USA) with a resolution of 5 mm for 193 pixels. The detector was positioned 4 meters from the sample to cover a 5 to 160 mrad arc, giving access to a wide q range from 0.005 to 0.6 $Å^{-1}$. The incident beam at the sample was defined by a circular 8 mm diameter cadmium mask probing most of the sample cell and integrating the shear rates profile. To obtain scattering patterns with satisfactory statistics, it took at least 1.5 hours to collect 60 µAh with the target station average power of 40 µA.

4.3.4 *In situ* X-ray scattering platform

The brightness/flux and collimation of the latest generation synchrotron X-ray sources allows a far greater time resolution than benchtop sources. Time frames of only 50 ms proved sufficient to obtain scattering patterns with acceptable statistics, enabling the probing of silk's shear-induced conversion.

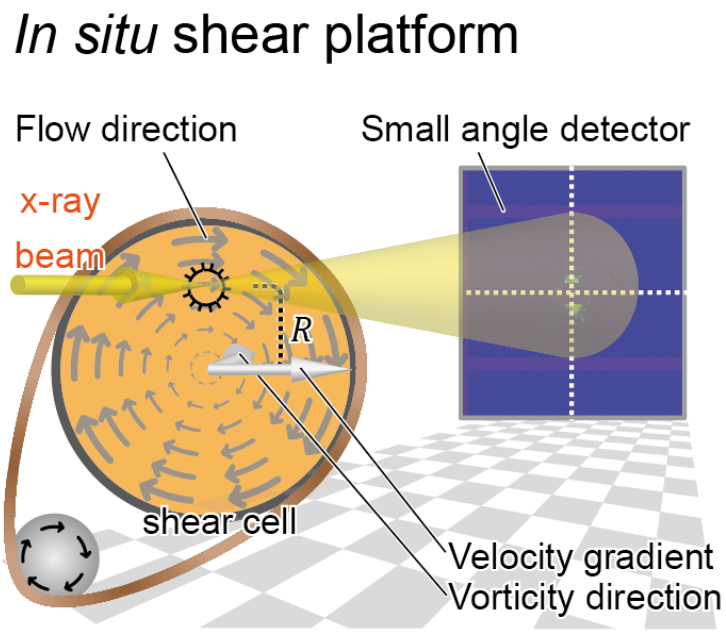


Figure 4.2 Schematic of the shear cell SAXS platform for *in situ* measurements showing the shear cell as well as the velocity gradient and vorticity vector. The scattered beam is detected by the small angle detector several meters back.

As illustrated on Figure 4.2, we opted for a parallel plate system (CSS450, Linkam, Guildford, UK) which offered a shear rate gradient and is easily loaded horizontally before mounting the cell vertically onto the beamline. To allow enough time for sample homogenisation and reduce the time interval between each experiment, samples were preloaded with native silk feedstock on 70 mm interchangeable disks compatible with the shear cell. Those disks were made of 1 mm thick stainless steel covered with a 55 µm thick Kapton™ film with a 3 mm wide window at 7.5 mm from the cell's centre to let the X-ray beam pass through this and the hole in the temperature control unit whilst the fixed plate at the top had a diamond

window. The gap between the two plates of the assembly was set to 700 µm to make a compromise between scattering intensity and sample volume. The parallelism was ensured by carefully adjusting the four pins separating the two halves of the shear cell (±10 µm). Four to six glands were combined to completely fill the interchangeable cells. After loading, samples were first homogenised for 300 seconds at <1 s^{-1}, below liquid silk's linear viscoelastic limit, slower than the relaxation time. Thereafter, samples were sheared at a constant rate from 1 s^{-1} (0.09 rad/s) to 100 s^{-1} (9.33 rad/s). Three repeats were performed at 1 s^{-1}, 5 s^{-1}, 10 s^{-1} and 100 s^{-1}. As shown on Figure 4.2, the parallel plate geometry creates a linear shear rate gradient from 0 s^{-1} at the centre to $\dot{\gamma}_R = R\Omega/h$ at the rim, where $\dot{\gamma}$ is the shear rate, R is the radius Ω is the angular velocity and h the gap thickness. All measurements were made at 25°C.

4.3.5 *Ex situ* shear method

To study the spontaneous conversion process, we designed an *ex situ* shear method where samples were sheared in 20 mm diameter interchangeable cells before they were transferred onto the SANS or SAXS beamline.

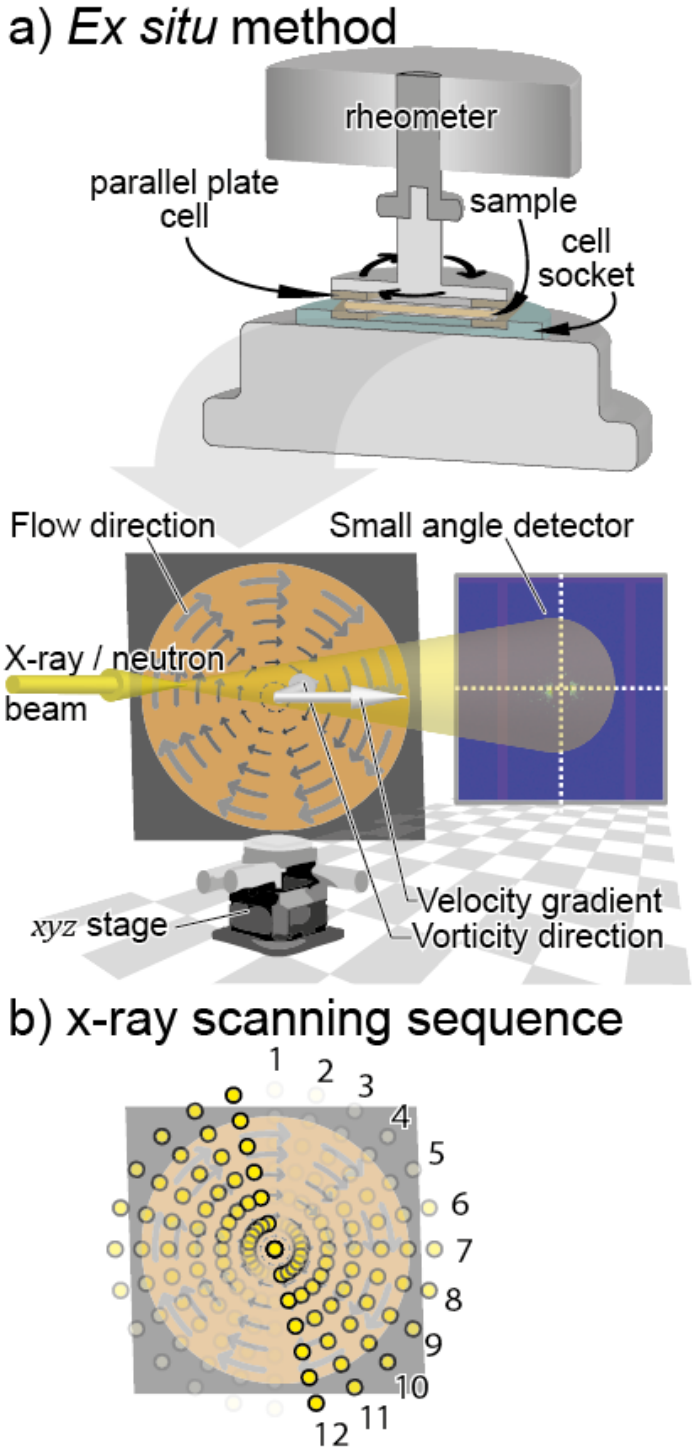


Figure 4.3 a) Schematic of the Rheology followed by SAXS or SANS platform for spontaneous conversion studies. b) Sequence used for scanning the cell used multiple x-ray scattering patterns.

As shown schematically in Figure 4.3a, samples were pre-loaded on the bottom half of the interchangeable cells; the plates of these cells were made from 0.5 mm thick polycarbonate window for SAXS and 1 mm thick sapphire windows for SANS (UQG Ltd., Cambridge, UK).

For both SANS and SAXS, the frame supporting the window masked the outer perimeter, limiting the field of view to a diameter of 17.3 mm.

Before studying the system using either X-rays or neutrons, the flow properties of the native silk samples were measured using a MCR300 for the SAXS and a MCR 501 (Anton Parr, Graz, Austria) for the SANS. Initially zeroed using an empty cell, the gap was set to 700 µm before loading the interchangeable cells. Because the gap could not be zeroed for the pre-loaded cell the gap accuracy depended on the thickness tolerance of the purpose built cells (± 10 µm). In the 220 µl parallel plate geometry, a linear shear rate gradient was generated from the centre (stagnation point) to the cell's rim, as shown by the arrows' length on Figure 4.3. Oscillation tests were first performed with an exponential frequency sweep from 623 to 0.623 rad/s at a 0.002 target strain, within the linear viscoelastic regime of native liquid silk.[Holland2006] Afterwards, samples were homogenised with a low shear rate (<1 s^{-1} at the rim, 0.07 rad/s) for 300 seconds. Thereafter, native silk was sheared for 10 seconds at maximum of 100 s^{-1} at the rim (7 rad/s) (n = 10). The flow properties measured are given in Figure A.17 of Appendix 3, page FF.

Afterwards, the interchangeable cells were immobilised to maintain the gap as well as their relative position using purpose built brackets. The locked cells were later sealed with Parafilm (Pechiney Plastic Packaging Company, Chicago, USA) and wet tissues to prevent dehydration until the end of the experiment <20 hours later.

4.3.6 Visual imaging data collection and analysis

For the visual imaging of the sample after shear in the interchangeable cells, digital photographs were taken using a Canon PowerShot A630 (Canon Inc., Tokyo, Japan) against a matt black background under consistent illumination, aperture, distance and focal length.

The only imaging treatment was a desaturation using Adobe Photoshop (Adobe, San Jose, USA). The conversion from Cartesian to cylindrical coordinates was performed using custom MATLAB (Mathworks, Natick, USA) code. The raw brightness levels of the 100 radial bins (1 s^{-1} / bin) represent the average intensity for all azimuthal angles.

4.3.7 SAXS data collection and analysis

The SAXS cells were mounted vertically for mapping using an xyz stage. Each scattering pattern was the result of 50 ms exposure for *in situ* shear and 1 s for *ex situ* shear to increase the signal to noise ratio. In addition, a constant illumination control experiment confirmed our exposure time choice (see Figure A.23, page NN). For *ex situ* shear, scattering patterns were collected on a straight line from one extremity of the cell's rim to the other, passing by the centre. One pattern was collected every 500 µm, corresponding to 5 s^{-1} increments. To map the entire cell, successive lines of scattering patterns were rotated around the stagnation point as shown in Figure 4.2b and Figure A.24 at page OO.

Scattering patterns were acquired as Nexus files using GDA (Diamond Light Source, Didcot, UK) and edf files using Spec (Certified Scientific Software, Cambridge, USA). For the data reduction, analysis and visualisation, a custom MATLAB (Mathworks, Natick, USA) application written by Maxime Boulet-Audet, Lian Apostol and Giuseppe Portale was used. Raw images have been reduced to 27 logarithmic radial bins and 61 azimuthal bins. The scattering intensity was normalised for the fluctuation of the incident beam using a low efficiency ionisation chamber monitor and the transmission by a photodiode monitor located on the beam stop. Sometimes inhomogeneities such as dust particle or air bubbles could cause the transmission value to vary for certain frames. Therefore, scattering patterns with transmission values outside a two standard deviation interval (95% confidence) were rejected. After normalising for the higher transmission of the reference

(empty) cell, its intensity was subtracted from each sample scattering to remove the scattering associated with the cell alone. The absolute intensity (cm^{-1}) was calibrated from the high density polyethylene Eltex® A1050 plastic scattering peak intensity which is known to be 24.5 cm^{-1}.[Russell1988]

The q range was normalised from the known d spacing of hydrated rat tail collagen. The centre of the cell was located by scanning the cell vertically and horizontally. The local shear rate for each scattering pattern could be thus calculated from the xyz stage position. Using MATLAB, the isotropic scattering intensity I_{iso} and the $< P_2 >, < P_4 >, < P_6 >$ and $< P_8 >$ order parameters for each of the 27 radial bins were calculated by fitting the azimuthal distribution using an expanded Legendre polynomial series.[de Gennes1972; Lafrance1991; Hamley1996; Pople1998] For the 3D visualisation of I_{iso} and $< P_2 >$, the values from q = 0.01 and 0.02 $Å^{-1}$ were averaged and the data plotted using MATLAB.

4.3.8 SANS data collection and analysis

For SANS experiments, the sample's position relative to the neutron beam was kept constant at the cell's centre for the duration of the >5400 seconds per frame collection time. During the course of the SANS, experiment the temperature was kept constant at 25°C using a water circulator system (JULABO, Seelbach, Germany). The collected scattering patterns were reduced using Mantid (http://www.mantidproject.org). All azimuthal bins were averaged to calculate the isotropic intensity. The transmission values were calculated from low efficiency monitors before and after the sample. After normalising for the higher transmission of the reference, its intensity was subtracted from each sample scattering to remove the scattering associated with the empty cell. As shown on Figure A.20 of Appendix 4 (page JJ), the absolute intensity (cm^{-1}) was calculated by the beamline scientist using a known scattering intensity Eltex polymer standard.

4.4 Results and discussions

4.4.1 Comparing neutron and X-ray scattering

To assess the suitability of X-ray scattering to measure NSF of 22 ± 3 % under a 0.7 mm path length without inducing radiation damage, small angle neutron scattering (SANS) was compared to small angle X-ray scattering (SAXS) under similar conditions. A similar comparison was performed on shear-induced conversion on NSF.

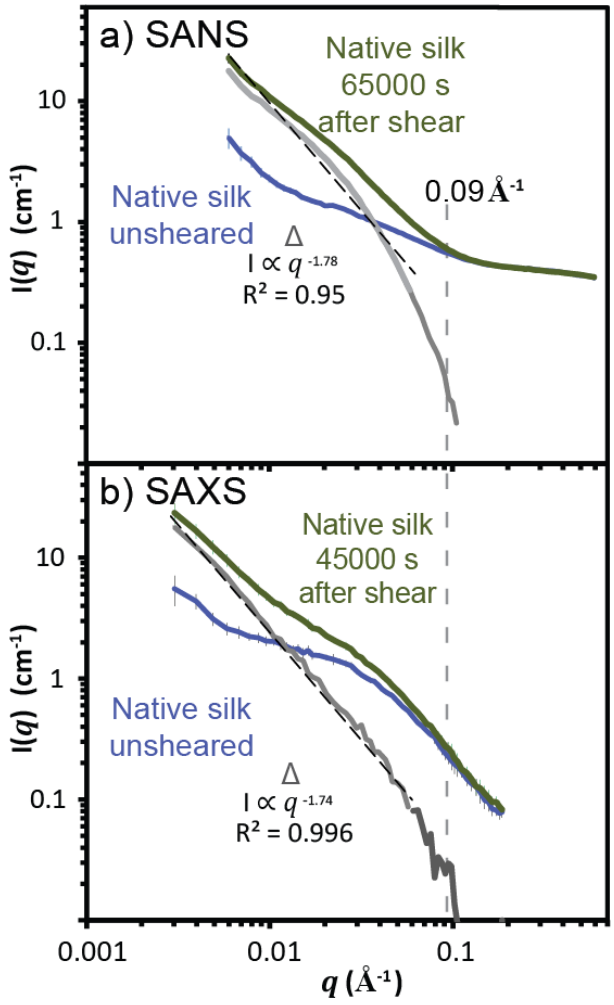


Figure 4.4 a) Small angle neutron scattering curves for unsheared native silk (blue curve) and 65000 seconds after shearing native silk at ~30 s^{-1} (green curve). The difference between sheared and unsheared (grey line) is fitted with a power function from 0.003 to 0.05 A^{-1}. b) Small angle X-ray scattering curves for unsheared native silk (blue curve) and 45000 seconds after shearing native silk at ~30 s^{-1} (green curve). The difference between the two (grey line) is fitted with a power function from 0.007 to 0.05 A^{-1}. The error bars are calculated from the

standard deviation of the azimuthal bins. The higher intensity above 0.09 Å^{-1} for SANS compared to SAXS could be due to the incoherent scattering background

Figure 4.4a and b show the SANS and SAXS isotropic intensity as a function of the scattering vector q before and after shear. From the scattering curves, small angle scattering highlights the effect of shear stress on native silk's nanoscale structure. Differences were observed only below 0.09 Å^{-1} for both SANS and SAXS, suggesting that length scales larger than $d = 2\pi/q = 70$ Å are affected by shearing. At high q, wide angle scattering tells us that crystalline lattices formed in silk are smaller than 8 Å.[He1999] Since no changes in the scattering are observed during silk's processing between these two boundaries, it suggests that the intermediate lengths scales from 8 to 70 Å are persistent. Such length scales correspond to the size of silk protein string of beads model with individual balls of 40 Å.[Vollrath2006b] It has been hypothesized that silk is stored as amyloid stacks in the gland before being aligned during the spinning process along the fibre axis.[Knight1999b; Vollrath2009]

The rise at low q can either be due to an increasing underlying structure factor $S(q)$ or a change in the form factor $P(q)$. Native silk is well above the concentration where inter-particle interactions are normally assumed to negligible, typically <10 mg/mL,[Lindner2002; Putnam2007] invalidating certain assumptions like Guinier's approximation.[Guinier1955] Diluting the sample is commonly used for deconvoluting $S(q)$ from $P(q)$,[Glatter1982] this would have made the sample less shear sensitive.[Chen2002b] In addition, protein-protein interactions can differ drastically depending on the concentration regimes[Chari2009, Mosbaek2012] and the scope of this study was the investigation the natural spinning process under comparable conditions. To help resolve the ambiguity introduced by the structure factor, we subtracted the scattering intensity of unsheared NSF from sheared NSF to enlighten the shear-induced structural changes (grey curves on Figure 4.4). The SANS difference curve varies according to a single power-law function $I \propto q^n$ between 0.003 and 0.05 Å^{-1} with a n coefficient of -1.78 (R^2 =

0.95). Similarly in Figure 4.4b, the SAXS intensity difference followed the same function with a n coefficient of -1.74 (R^2 = 0.996). Amongst the different explanations for such monotonous variation of $I(q)$ could be the increase in the structure factor. Alternatively, it could be the result of a form factor becoming more associated with surfaces, as would for example occur if a flexible molecule were to unfold, increasing the surface scattering at low q.[Svergun2003; Kim2006; Rubatat2007]

To extract additional information on the shape and size of proteins, different shapes models are typically fitted to the SAS curves.[Pedersen1996; Martel2007; Jacques2010] The strong structure factor present at high concentration invalidates assumptions required for the use of models such as the worm-like chain.[Pedersen1996] In addition, the close interactions of water with the protein at such high concentrations[Levy2004; Porter2012] makes solvent subtraction challenging. Most models also assume known polydispersity or monodisperse systems, which is regrettably not the case for native silk dope as it contains at least three types of proteins: heavy chain, light chain and P25.[Shimura1976; Mita1994; Zhou2000; Sehnal2004] Because of the constraints associated with studying the silk feedstocks in their natural state, we were not in a position to model with confidence the scattering intensity to calculate an absolute shape.

Since the shear-induced structural changes observed were similar for both SANS and SAXS, we concluded that changes in the scattering intensities were not the result of the X-ray radiation damage. Consequently, we could take advantage of the better spatial and temporal resolution of synchrotron X-rays. The higher spatial resolution also allows the localised illumination of the shearing cell to determine the orientation of the area probed.

4.4.2 Orientation under shear

The smaller beam spot of SAXS probed only an area of ~300 by 500 µm to record scattering patterns at a given radial position and thus at a specific shear rate. To mimic the spinning process, native silk fibroin was sheared in a parallel plate assembly producing a shear rate gradient. As conversion is rapidly triggered under such flow stress, scattering patterns were collected every 0.2 seconds for 50 ms before, during, and after shearing the sample at different rates to investigate the shear-induced aggregation *in situ*. Scattering were then reduced into azimuthal bins to be in a position to visualise the expected streak when sheared.[Yang1997; Riekel2001]

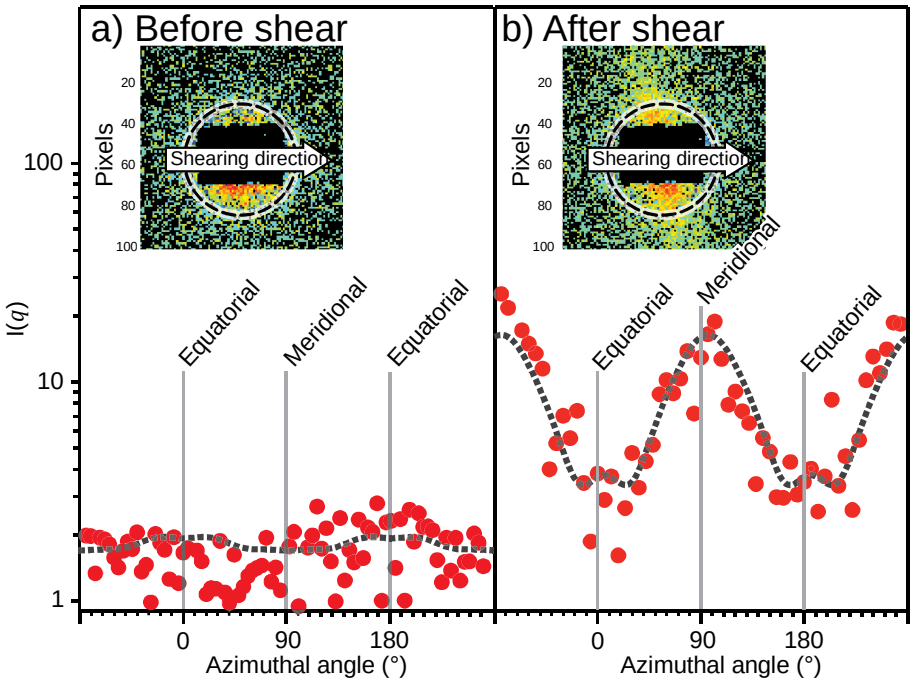


Figure 4.5 a) Scattering intensity at q = 0.01 Å^{-1} (dashed line) as a function of the azimuthal angle for native silk for a 50 ms exposure before shear. b) After 1 second at 100 s^{-1}. The dashed line is the result of the fit Legendre polynomial function fit.

The inset of Figure 4.5a shows the SAXS scattering pattern around the beam stop before shearing. The scattering was non-oriented (isotropic) but the X-ray beam was not perfectly aligned with the centre of the beam stop resulting in slightly more scattering below than

above. By integrating the intensity at q = 0.01 Å^{-1}, Figure 4.5a shows clearly the isotropicity of the scattering pattern with a flat azimuthal distribution. Figure 4.5b shows a typical anisotropic scattering pattern collected in just 50 ms during shear at 100 s^{-1}. When sheared the anisotropy was always observed along the meridional axis, perpendicular to the velocity direction (white arrow). Meridional streaks are the result of the alignment of the long axis of molecules along the shearing direction (equatorial axis) as previously observed for sheared reconstituted silk feedstocks.[He1999; Rössle2004] A similar meridional streak is observed in spun silkworm and spider silk fibres.[Yang1997; Riekel2001] Shear-induced anisotropy observations have also been made by other techniques such as birefringence,[Kataoka1977, Asakura2007] FTIR[Boulet-Audet2013] and SIPLI.[Holland2012c]

To evaluate the degree of anisotropy, the coordinate system was converted from Cartesian to cylindrical with 6° azimuthal bins (61 in total). By selecting only one radial bin at a low q but just outside the beamstop (dashed line in Figure 4.5), $I(q)$ varied as a function of the azimuthal angle, peaking at 90 and 270° (Figure 4.5b). The orientation distribution obtained by SAXS is often described by the Hermans' orientation parameter.[Hermans1946; Alexander1969; Finnigan2005; Wang2007; Okura2011] Although this parameter is suitable for narrow orientation distributions, it inaccurately describes broader distributions such as ours. Instead, sheared native silk's broad orientation distribution was better fitted by the developed Legendre polynomial of Equation 2.44.[de Gennes1972; Lafrance1991; Hamley1996; Pople1998; Burger2010] By assuming centrosymmetry, the odd terms are equal to zero, simplifying the expression. As the contribution of each term is decreasing with n, neglecting the higher order parameters has little impact on the distribution fit. We thus restricted the calculation of the Legendre polynomial series to the first four non null terms, $\langle P_2 \rangle, \langle P_4 \rangle, \langle P_6 \rangle$ and $\langle P_8 \rangle$. Thereafter, the distribution was scaled with the isotropic intensity (I_{iso}) which would be measured if no orientation was observed. As shown on Figure 4.5b, the experimental value of $\langle P_4 \rangle$ and

above seems close to their most probable values in this case, indicating that the $\langle P_2 \rangle$ alone could have been sufficient to accurately describe the orientation distribution.

In situ probing: shear-induced conversion study

To localise the q range at which anisotropy is observed, the first two order parameters $\langle P_2 \rangle$ and $\langle P_4 \rangle$ calculated by fitting the orientation distribution using the developed Legendre polynomial series (Equation 2.45). The resulting order parameter values were plotted as a function of q and time for aligned samples sheared at high rates (100 s^{-1}).

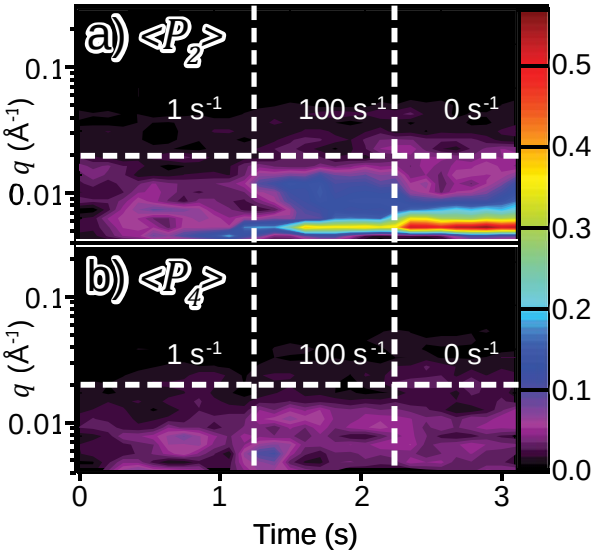


Figure 4.6 a) Second order parameter $\langle P_2 \rangle$ difference and b) fourth order parameter $\langle P_4 \rangle$ difference as a function of time and q for a native silk sample sheared at 100 s^{-1} for 1 second.

As shown in Figure 4.6, the $\langle P_2 \rangle$ values calculated before shear at very low q (0.003 to 0.01 $Å^{-1}$) were non-zero. We therefore only describe the anisotropy at $q > 0.01$ $Å^{-1}$. After only 1 second of shearing at 100 s^{-1}, the $\langle P_2 \rangle$ value increased drastically whilst $\langle P_4 \rangle$ only rose slightly at the low q. No significant changes in the $\langle P_6 \rangle$ and $\langle P_8 \rangle$ were measured. Since the $\langle P_2 \rangle$ increased only at q values below 0.05 $Å^{-1}$, it suggests that only structures larger than 126 Å aligned under shear. This is consistent with our observed persistent length scales < 70 Å. Hence, our results suggest that only strings longer than three beads of 40 Å[Vollrath2009] are aligning along the velocity direction. Hence, to follow the development of the larger scale

structures alignment, we integrated the $\langle P_2 \rangle$ values from 0.01 to 0.02 Å^{-1} (between dashed lined of Figure 4.6). The $\langle P_2 \rangle$ allowed us to quantify the orientation induced by shearing native silk feedstocks at 1, 5, 10 and 100 s^{-1} as a function of time and accumulated strain.

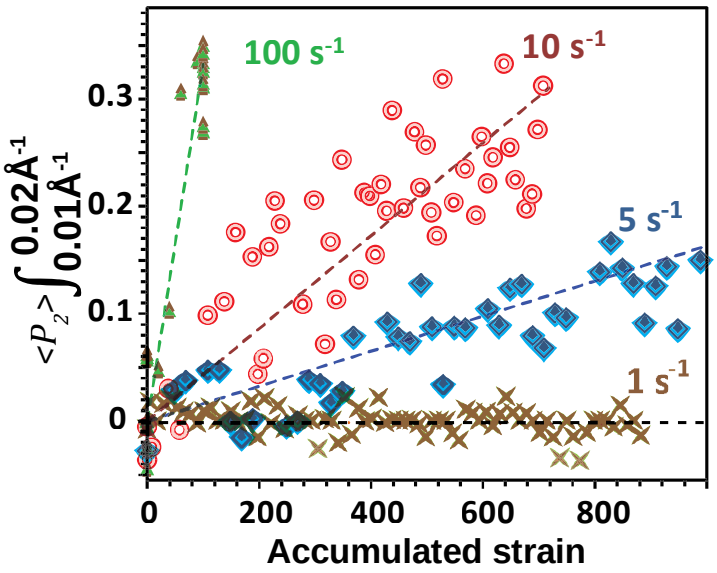


Figure 4.7 Second order parameter $\langle P_2 \rangle$ as a function of time for native silk sheared at 1, 5, 10, and 100 s^{-1} integrated from q = 0.01 to 0.02 Å^{-1}.

Illustrated by brown crosses on Figure 4.7, shearing native silk at only 1 s^{-1} did not induce any orientation, even after an extended period of time. An oscillatory test suggesting no structure development validated this interpretation. This result is in agreement with previous silk rheology studies claiming that native silk's linear viscoelastic limit is between 2 and 5 s^{-1}.[Holland2006; Moriya2009] Therefore, shear stress inputted below this rate would have no effect as native silk could relax quickly enough. In stark contrast, native silk was substantially oriented after shearing at 100 s^{-1} for only a few seconds (green triangles). Plotting the $\langle P_2 \rangle$ as a function of accumulated strain resulted in distinctive slopes for each rate used. Therefore to get equivalent level of orientation, native silk required more strain at lower rates. Consequently, our results suggest that silk's alignment is strain dependent passed a critical shear rate, like the polymer solutions.[Scirocco2004] Consequently, shearing silk at higher rates than its corresponding relaxation time promotes alignment but might not

necessarily trigger a change in protein conformation if the rate is lower than a critical value $\dot{\gamma}_c$.[Boulet-Audet2013] Hence the scattering intensity rise at low q on Figure 4.4b could be the result of conformation conversion and/or domain alignment. Wide angle scattering giving rise to Brag peaks at q > 1 Å^{-1} could help in discriminating these effects.[Rössle2004]

Ex situ probing: Spontaneous conversion study

As confirmed by several studies,[Li2001; Dicko2010; Boulet-Audet2011; Boulet-Audet2013] once triggered, silk's conformation conversion continues spontaneously without any further stress input. At room temperature, this process can be easily followed by continuing SAXS collection once shearing has been stopped. However, studying the spontaneous conversion requires the sample to be static, which could cause localised radiation damage. Instead of making the sample flow, different areas of the sample can be probed for each exposure time in order to measure the entire shear rate gradient generated by the parallel plate geometry.

In addition to providing shear flow, the rheometer measured the sample's response to calculate its flow properties. An oscillatory frequency sweep was first performed to verify that the flow properties measured were comparable to those of previous studies (see Figure A.17 of Appendix 3, page FF).[Holland2006; Holland2007; Moriya2009; Boulet-Audet2013] After the oscillatory measurement, a viscosity test was conducted, creating a linear shear rate from 0 s^{-1} at the centre of the cell to 100 s^{-1} at the rim (10 mm from the centre). At low rates the viscosity is rate independent with no changes in the first normal force. By shearing at higher than the equivalent relaxation time (1 to 5 s^{-1}), silk undergoes shear thinning (viscosity decrease) whilst the recoverable strain starts to generate an upwards normal force. Shearing native silk at higher rates than a critical value threshold $\dot{\gamma}_c$ (20 to 50 s^{-1}), causes the viscosity to increase (shear thickening) as β-sheets are formed, changing the hydrogen bond network between protein chains.[Zhang2002; Boulet-Audet2013] Shortly after, sheared native silk starts

to gel and slips from the walls of the geometry. For this reason, shearing had to be stopped 10 seconds after the beginning of the test to prevent slippage.[Holland2006] After shear, the cell's two plates were immobilised and removed from the rheometer, photographed and mapped 1200 seconds later by SAXS using a xyz stage. Sample gelation prevented the whole sample from flowing under gravity over the lengthy spontaneous conversion process. In addition, the sample was stored horizontally at 25 ± 2 °C between each series of measurements.

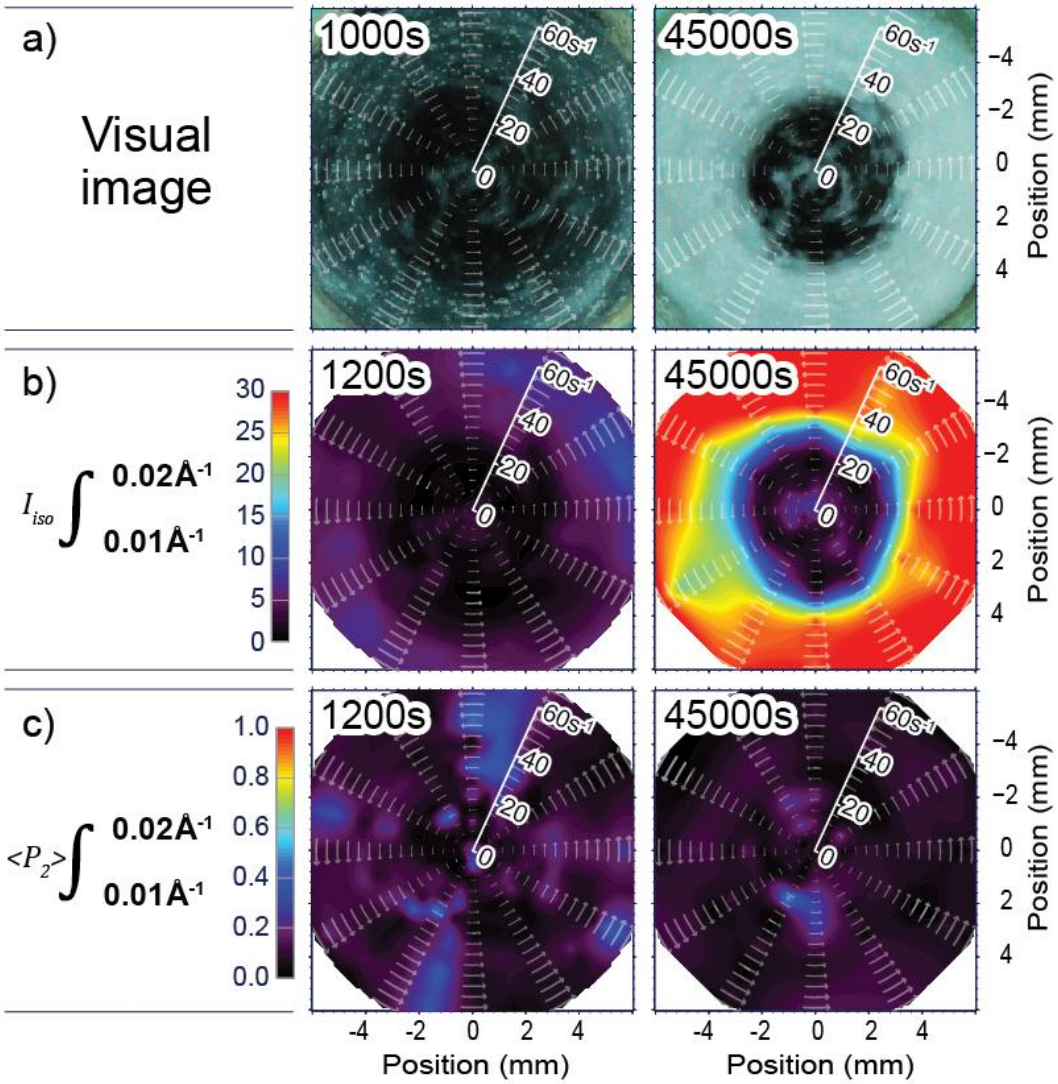


Figure 4.8 a) Representative visual image 1000 seconds after shear and 45000 seconds after shearing native silk. b) Map of the isotropic scattering intensity I_{iso} between 0.01 and 0.02 Å^{-1}. c) Map of the calculated $< P_2 >$ between 0.01 and 0.02 Å^{-1}.

Optical photographs were taken against a black background to follow the evolution of the turbidity. After 1000 seconds Figure 4.8a shows a faint doughnut shaped pattern similar to the one observed by shear-induced polarised light imaging (SIPLI) in parallel plate.[Mykhaylyk2008; Holland2012c] Due to the shear rate gradient, the cell's outer perimeter was sheared above $\dot{\gamma}_c$ whilst the centre was not. The photographs revealed that the outer rim became very turbid after shear whilst the centre remained mostly clear. As shown in Figure 4.8b, the isotropic scattering intensity I_{iso} also showed the faint ring-like pattern shortly after shearing as the intensity rose in the cell's perimeter. After 45000 seconds this motif was even clearer as I_{iso} increased mostly on the outer perimeter over time. Unlike visible light however, X-rays could still mostly pass through the turbid sample: transmission values only decrease from 99 to 97 ± 1%. As for the orientation, Figure 4.8c shows a small increase in the degree of orientation, 1200 seconds after shear on the outer perimeter with $\langle P_2 \rangle$ values reaching 0.3 along the vertical axis, where the cell was first probed. Although those initial $\langle P_2 \rangle$ values were comparable to the values presented in Figure 4.7, scattering patterns collected thereafter showed much less orientation. This could be due to the relaxation of the orientation and/or increasing scattering from isotropic structures later formed. Since the centre of the cell appears to have preserved more anisotropy than the rim, it leads us to believe that the apparent decrease in $\langle P_2 \rangle$ is due to the increasing isotropic scattering intensity presented on Figure 4.8b.

Regardless of the causes, our results imply that fibrils formed spontaneously after stress are not as well aligned as those formed during shear stress. As alignment is key to fibre tensile strength,[Porter2005] it would be preferable for artificially spun fibre to form most fibrils under continuous flow stress. The proportion of β-sheet structures formed under shear stress can be assessed by recording the entire conversion kinetic.

By taking multiple photographs between the images presented in Figure 4.8, we monitored the turbidity using the brightness level of the sample against a black background, which is proportional to the amount of scattered light. Since aggregates scatter light more than clear unspun silk feedstock, the sample's turbidity can be related to silk's conversion process. Knowing the distance from the centre, the brightness level could be plotted as a function of the shear rate sustained.

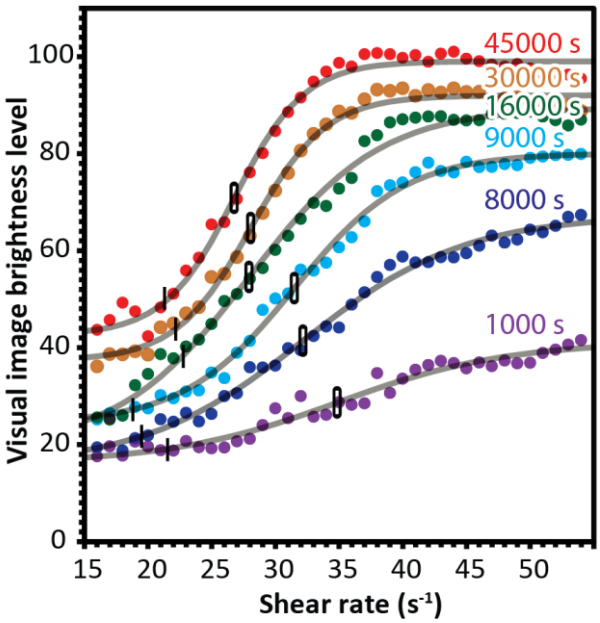


Figure 4.9 Brightness level of the visual images as a function of the local shear rate after shearing native silk for 10 seconds. The grey curves represent the sigmoid fit of the brightness level distribution. The double vertical bars show the inflexion point $\dot{\gamma}_{1/2}$ and the single vertical bars represent the onset of the curve ($\dot{\gamma}_{1/2} - w$).

Figure 4.9 illustrates the dependency of brightness on the shear rate sustained by native silk at different time intervals from 1000 to 45000 seconds. Visually the sample was completely clear and homogenous all across the cell before shearing, which would have resulted in a constant brightness value around 18 before shear. Over time, the brightness level increased across the entire cell, but the difference in brightness between the centre and outer perimeter grew even further over time resulting in the doughnut shaped pattern. The brightness values as a function of the shear rate had "s" shape profile. Such functions characterise the cumulative distribution function or integral of most probability functions

such as Gaussians. Hence these functions are typical for protein folding kinetics based on a probabilistic mechanism.[Khorasanizadeh1993; Porter2008] The brightness distribution could thus described as a sigmoid function

$$I = I^{min} + \frac{I^{max} - I^{min}}{1 + e^{-(\dot{\gamma} - \dot{\gamma_{1/2}})/\frac{w}{2}}} \quad \text{Equation 4.1}$$

where $\dot{\gamma}$ is the shear rate, $\dot{\gamma}_{1/2}$ is the shear rate at the inflection point (half height), w is the width of the transition, I^{min} is the minimum intensity and I^{max} the maximum intensity. Drawn as grey curves on Figure 4.9, Equation 4.1 fitted the brightness levels with only small residuals. $\gamma_{1/2}$ changed from 35 to 26 s^{-1} over the time frames, but the onset of the curves given by $\gamma_{1/2} - w$ remains roughly constant at 21 ± 2 s^{-1}. Visual imaging thus suggests that isotropic fibrillation does not propagate over long distances as the centre of the cell was mostly clear even after 45000 seconds.

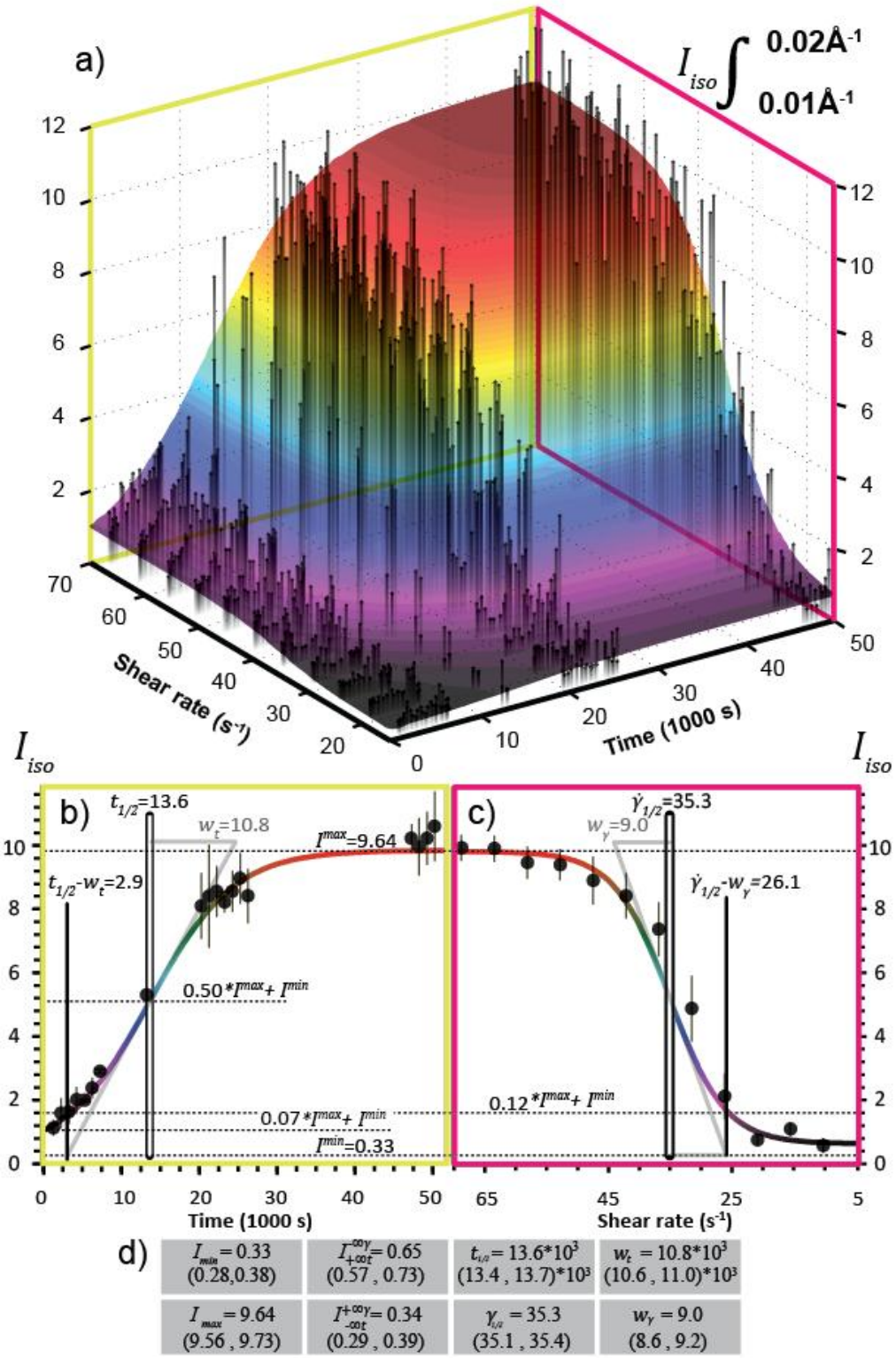
In parallel to the visual imaging of the cells, successive SAXS patterns were collected along lines from one edge to the other, passing by the centre of the cell. Each line was rotated by 15 degrees around the centre to probe a fresh portion of the sample with each line. This method allowed us to study the spontaneous aggregation kinetics under a range of shear histories in a single experiment and in a single cell. It thus reduces the inherent variability associated with native silk sample preparation and loading.[Holland2006; Holland2012c]

To verify that the scattering intensity kinetics follow a typical protein denaturation model at every shear rate $\dot{\gamma}$ probed, the intensity was fitted with the following two dimensions sigmoid function:

$$I_{iso}(\dot{\gamma},t) = I_{min} + \frac{I_{+\infty t}^{-\infty\gamma} - I_{min}}{1 + e^{-(\dot{\gamma}-\dot{\gamma}_{1/2})/\frac{w_\gamma}{2}}} + \frac{I_{-\infty t}^{+\infty\gamma} - I_{min}}{1 + e^{-(t-t_{1/2})/\frac{w_t}{2}}} + \frac{I^{max} - I_{min}}{\left(1 + e^{-(\dot{\gamma}-\dot{\gamma}_{1/2})/\frac{w_\gamma}{2}}\right) * \left(1 + e^{-(t-t_{1/2})/\frac{w_t}{2}}\right)}$$

Equation 4.2

where I_{min} is the minimum intensity, $I_{-\infty t}^{+\infty\gamma}$ is the intensity at negative infinity time and positive infinity shear rate, $t_{1/2}$ is the half process time, w_t is the width of the kinetic, $I_{+\infty t}^{-\infty\gamma}$ is the maximum intensity at positive infinity time and negative infinity shear rate, w_γ is the width of the shear rate profile, and $I_{\gamma t}^{max}$ is the intensity at maximum shear rate as well time. The fitted parameters obtained from Equation 4.2 are given in Figure 4.10d.



I_{min} = 0.33 (0.28,0.38)	$I^{\infty\gamma}_{+\infty t}$ = 0.65 (0.57 , 0.73)	$t_{1/2}$ = 13.6*10^3 (13.4 , 13.7)*10^3	w_t = 10.8*10^3 (10.6 , 11.0)*10^3
I_{max} = 9.64 (9.56 , 9.73)	$I^{+\infty\gamma}_{-\infty t}$ = 0.34 (0.29 , 0.39)	$\dot{\gamma}_{1/2}$ = 35.3 (35.1 , 35.4)	w_γ = 9.0 (8.6 , 9.2)

Figure 4.10 a) Integrated isotropic scattering intensity I_{iso} between 0.01 and 0.02Å as function of time as well as the shear rate for a representative sheared native silk sample. b) I_{iso} as a function of time for a shear of 70 s^{-1}, yellow box. The I_{iso} represents the average of each shear rate radial bin and the error bars their associated standard deviation. c) I_{iso} as a function of the shear rate of after 45000 seconds, pink box. d) 2d sigmoid function parameters with 95% confidence bounds in bracket, R^2 = 0.98.

Figure 4.10a shows the isotropic scattering intensity I_{iso} as a function of the shear history and time. I_{iso} at the rim is double the value at the centre, even after only 1200 seconds. In contrast to the visual imaging brightness at low shear rates < 20 s^{-1}, I_{iso} barely rose above the initial value even after 45000 seconds. It shows a much increased I_{iso} for high shear rates and long conversion times. This observation suggests a nucleation dependent mechanism as low stress did not nucleate enough fibrils to initiate spontaneous aggregation. In this perspective, scattering intensity could be related to the probability of an activation event under a certain work over time.

Figure 4.10b shows the conversion kinetics at higher rates than this threshold (yellow frame). At $\dot{\gamma}$ = 70 s^{-1}, the extrapolation of I_{iso} using the fitted equation revealed that just after shear the conversion process was only 7 ± 1 % of the final value after 10 seconds. Considering that sample slippage typically occurred after <15 s at this rate, it implies that shear stress alone cannot induce much further aggregation. On the other hand, spontaneous conversion can complete the process as I_{iso} plateaued over half a day. From this curve, the half conversion time thus calculated was 13600 seconds (black double line on Figure 4.10b). This result is comparable with the long time scale measured by circular dichroism on diluted silk fibroin solution spontaneous conversion.[Li2001]

To evaluate the effect of stress independent of time, we can look silk's scattering intensity at equilibrium. The magenta pane in Figure 4.10c shows I_{iso} as a function of the shear rate after 45000 seconds, near the completion of the aggregation completion. Subtracting the width of the transition w_γ from $\dot{\gamma}_0$ gives a velocity profile boundary of 26.3 s^{-1}, corresponding to 12% of the total process. Using this boundary with the viscosity value, it possible to determine how much specific work w was required for fibrillation using Janeschitz-Kriegl's equation $w = \int_0^t \eta[\dot{\gamma}(t)]\,\gamma^2(t)dt$.[Janeschitz-Kriegl2003] Assuming a viscosity at

the onset rate of η(26.3 s^{-1}) = 300 Pa·s,[Boulet-Audet2013] the work required for triggering the conversion was estimated at 2 MPa or MJ/m^3. This value is comparable to hydrogenated polybutadienes,[Mykhaylyk2008] or high-density polyethylene, but about an order of magnitude higher than the value reported for native silk using SIPLI.[Holland2012c] This discrepancy could however be explained in part by different boundary criteria of the techniques and a synthetic polymer melt would have been preferable for comparison. The onset shear rate value is however similar to the $\dot{\gamma}_c$ value of 50 ± 20 s^{-1} determined from the onset of shear thickening by Boulet-Audet et al.[Boulet-Audet2013] and the 15 s^{-1} reported by Terry et al.[Terry2004]

On the other end of the curve in Figure 4.10c, shearing native silk at rates higher than $\dot{\gamma}_{1/2} + w_\gamma$ = 44.3 s^{-1} (88% conversion completion) created enough aggregates to ensure conversion completion before plateauing. Although the number of nuclei fibrils initially formed by shear stress might be larger, the spontaneous conversion does not complete faster under a higher shear rates history as they appear to have the same t_0. A possible explanation for this observation could be that the nuclei start competing for the β-sheets precursor to form the fibrils as in a limiting reagent reaction.[Zimmerman1977; Jenkins2010] Since the spontaneous conversion is slow, stress-driven conformational transition would be required to form silk quickly.

Thus, it is expected that partially formed silk would not be able to achieve its full stiffness potential and could present intermediate tensile properties.[Porter2005] As long as the secreted silk is solid, the long time scale involved for the spontaneous completion of the process would not be present a major constraint for silkworms as they build their cocoon over days. It is only once the whole cocoon is completed that the non-woven fibre mat can perform its protective function. In contrast to the dragline of spiders, where partially converted silk threads would be detrimental as the animal relies on them immediately after they are spun.

Even if enough work was inputted to trigger the conversion, more stress would have been required to drive the process to completion within less than one hour. Consequently, other sources of stress, such as extensional flow, might be complementing shear stress when tensile performance is required rapidly.[Knight2000; Asakura2007; Boulet-Audet2013] In the spinning apparatus, the point where shear forces cannot be applied because of wall slippage would have to be at the end of the duct narrowing in order to prevent plugging. This interpretation agrees with the calculation of Moriya et al.[Moriya2009] suggesting a critical shear rate $\dot{\gamma}_c$ reached at the onset of the silkworm's silk press, where the duct's diameter becomes constant. At this point, extensional flow would take over as the main source of stress to drive the conversion and align chains. Supporting this interpretation, the molecular orientation measured by Raman spectromicroscopy is much greater following spiders' drawn down taper,[Lefèvre2008] the structure thought to be equivalent to the worm's silk press.[Knight2000; Asakura2007] Our study's conclusions are in accord with this hypothesis as sample slippage due to gelation occurs well before completion of the conversion process under shear. Hence, it highlights the potential importance of other biologically relevant sources of stress, such as extensional flow and pH drop, for the design of biomimetic spinning devices.[Knight1999b; Vollrath2001]

4.5 CONCLUSIONS

Small angle scattering (SAS) allowed the study of native silk's nanoscale structures both during and after shear-induced aggregation, under a range of shear histories. Both SANS and SAXS revealed that changes are only observed for length scales larger than 70 Å in the shear-induced conversion process, confirming the relevance of small angle scattering techniques. Between 70 Å and 8 Å (the minimum measured in this study) no changes were observed. This length scale could correspond to the diameter of individual beads of 40 Å in

silk's string of beads model.[Vollrath2009] SAXS also revealed a shear-induced alignment of native silk along the shearing direction, supporting birefringence,[Kataoka1977, Asakura2007] FTIR[Boulet-Audet2013] and SIPLI measurements,[Holland2012c] as well as previous SAXS studies.[Rössle2004] From the observed meridional streak also observed in fibres,[Yang1997, Riekel2001] we estimate that only nanoscale structures larger than 126 Å are aligning under flow (i.e. three "beads" of the fibroin).

To follow the spontaneous conversion of native silk, we developed a transferable cell platform permitting the measurement of silk's flow properties before X-ray scattering *ex situ*. Once the conversion was triggered, this method allowed the study of silk's self-driven structure development under a range of shear rates in a single cell. From the scattering intensity varying in a *"s"* shape function, our results support the protein denaturation kinetic probabilistic model.[Birge1985; Porter2008] For the first time, we quantified the spontaneous conversion kinetics half-time ($t_{1/2} = 13900$ seconds) of native silk under biologically relevant conditions. Under such a long time scale, our silk samples would have dried before completing the process if they were not sealed. This also means that if the conversion is triggered inside the silk worm, complete gelation of its gland could occur within a day. We also found that only around 7% of the process is completed at the point where shearing force becomes ineffective due to gelation and wall slippage. Although probing on a different length scale, this result corroborated findings of Chapter 3 suggesting that other types of stress might be involved in silk's conversion. By probing a range of shear rate histories simultaneously, we determined the effective shear rate window to be from 6.3 to 44.3 s^{-1}, within the biologically relevant shear rate range.[Moriya2009] The lower boundary of this window was interpreted as the critical rate for triggering the nucleation of fibrils, whilst the upper bound represents the maximum effective rate where additional stress makes little difference to the conversion rate.

In summary, small angle scattering gave us novel insights into the natural spinning process by probing the structure development on the nanometre scale whilst it undergoes its shear-induced denaturation. This study quantified for the first time the conversion process' extent before shearing forces cannot contribute anymore as well as the time required for complete aggregation under a biologically relevant stress. These findings should contribute to the knowledge base for designing the next generation of bio-inspired apparatus spinning artificial, but natural-like fibres.

Chapter 5

Silk protein aggregation kinetics revealed by Rheo-IR

This chapter consists mainly of the work presented in a manuscript titled *"Silk protein aggregation kinetics revealed by Rheo-IR"* published in Acta Biomaterialia.[Boulet-Audet2013] Using a new ATR accessory and a rheometer instead of shear cell, this work addressed the issues identified in Chapter 3 by improving the spectroscopy instrumentation as well as the source of shear stress. Thus, this body of work represents the technical culmination of our combinatorial approach to study the spinning process. The novel rheo-IR platform developed directly linked silk's molecular structure to its flow properties during similar processing conditions. It also allowed the direct comparison of natural and artificial silk analogues to assess their quality as feedstocks. Maxime Boulet-Audet has performed the entire experimental work, data analysis and manuscript writing whilst Chris Holland, Ann Terry and Fritz Vollrath contributed to the editing of this chapter.

5.1 Abstract

The remarkable mechanical properties of silk fibres stem from a multi-scale hierarchical structure created when an aqueous protein "melt" is converted to an insoluble solid via flow. To directly relate silk proteins' structure and flow response, we developed a novel technology 'platform' (Rheo-IR) that couples rheology and infrared spectroscopy. This technique provided a new window into silk processing by linking shear thinning to an increase in molecular alignment with shear thickening affecting changes in silk protein

secondary structure. Compared to other static characterisation methods applied to study silk, Rheo-IR proved particularly useful at revealing the intrinsic difference between natural (native) and reconstituted silk feedstocks. Hence, Rheo-IR offers important novel insights into natural silk processing. Besides its intrinsic academic merit, it might also be useful when designing reconstituted silk analogues alongside other polymeric systems whether natural or synthetic.

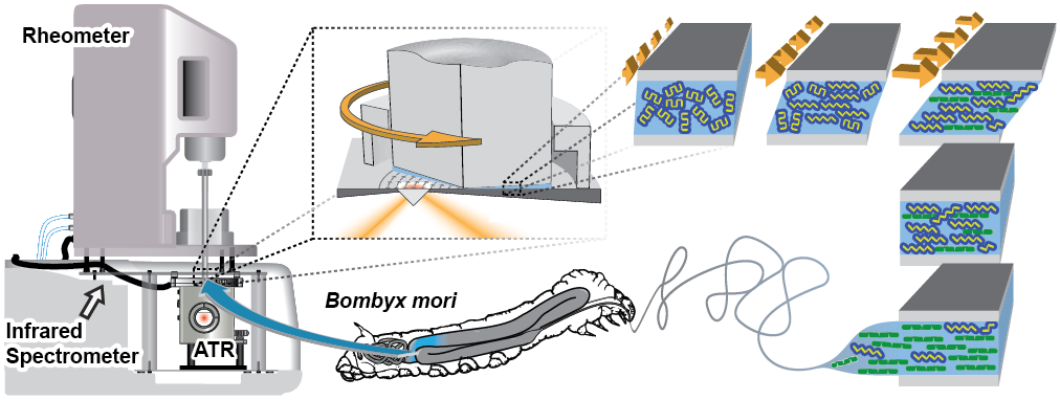


Figure 5.1 Graphical abstract of "Silk protein aggregation kinetics revealed by Rheo-IR" submitted in Acta Biomaterialia.

5.2 Introduction

The conversion of an aqueous silk protein solution into a solid may be achieved through the use of a wide range of external stresses, including heat,[Putthanarat2002] acoustic waves,[Kim2004] electric current,[Leisk2010] solvent interactions,[Chen2003; Jeong2006] pH,[Dicko2004; Rammensee2008] and metallic ion concentration.[Foo2006] However within the animal (spider or silkworm), native silk feedstocks appear to have been selected primarily to respond to flow, resulting in rapid but controlled protein denaturation and aggregation.[Knight1999b; Knight2000; Vollrath2001; Terry2004; Holland2006; Holland2012c] Thus, to gain a better understanding of what is assumed to be a highly optimised pultrusion spinning process,[Davies2013] the flow properties of native silk feedstocks (dope) have attracted substantial attention.[Ochi2002a; Terry2004; Kojic2006; Holland2007; Moriya2009; Holland2012a] Here

the study of flow i.e. rheology has proven very valuable for revealing the close similarities between native silkworm and spider feedstocks.[Holland2006] Combined with direct visualisation, rheology has also showed that native silk feedstocks behave like conventional polymer melts, but at much lower temperatures and requiring substantially less energy to solidify.[Holland2012c] Despite much progress, the kinetics and mechanism of flow-induced structural changes in silk proteins is still poorly understood beyond macroscopic observations.

As indexed in (Table 1.1), several techniques have been employed to investigate the structural features present in silk's hydrated state which proved helpful at determining silk's protein conformation and nanoscale structure. Furthermore silk's solid, denatured and semi-crystalline states are revealed when a feedstock has been converted by stress.[Putthanarat2002; Chen2003; Dicko2004; Kim2004; Foo2006; Jeong2006; Rammensee2008; Leisk2010] However few studies have achieved this conversion through the application of the most biologically relevant stress type, which is flow.[Ohgo2008] A rheo-optical platform will allow us not only to apply such stress/strain but also to monitor it. Whilst rheo-spectrometry has often been used to study conventional polymer melts,[Pogodina2001; Kumaraswamy2004; Kanaya2007; Scelsi2008] only a single study coupled rheological to structural measurements of silk and only for a reconstituted silk feedstock (RSF).[Rössle2004] Reconstituted silks can be an economic source of large quantities of spinning feedstock, yet RSF preparation requires strong chaotropic agents to disrupt the β-sheets secondary structure present in silk fibres[Miyazawa1961] and their quality varies enormously alongside their flow properties.[Holland2007Yamada2001, Greving2010, Wray2011] In addition, once those poor feedstocks are dehydrated and spun, the resulting fibres and films typically exhibit disappointing mechanical properties.[Elices2011Matsumoto1996, Seidel2000, Lazaris2002, Yao2002, Shao2003 Zuo2006Yamada2001; Greving2010; Wray2011]

In order to fill the knowledge gap concerning native and RSF silk feedstocks' structural response to flow, we have coupled spectroscopy to rheology (Rheo-IR). Infrared spectroscopy is sensitive to most molecular vibrations and can probe the molecular orientation of any polymer melt when the infrared beam is polarised. More specifically, IR is sensitive to protein concentration, conformation and alignment.[Chen2003; Boulet-Audet2008; Li2008; Chen2009; Mo2009a; Boulet-Audet2011] In addition, probing samples with Attenuated Total Reflection (ATR) avoids the absorbance saturation of protein and water bands in the mid infrared regime by only measuring the emerging evanescent wave absorption. Unlike DLS or circular dichroism, ATR also allows the analysis of silk samples 'straight from the gland' and at native concentration.[Holland2006; Mo2009a] This study extends our previous work on the shear-induced conversion of RSF presented in Chapter 3 to include native silk feedstocks (NSF) and for the first time relate molecular alignment and conformation to changes in bulk rheology *in situ*.

5.3 Materials and methods

5.3.1 Reconstituted Silk Feedstock (RSF)

Reconstituted silk feedstocks were prepared following the method given in section 2.1.2. After dialysis, bags were hung for 3 days at 4 °C in a gentle air stream to concentrate the silk solution to 22 ± 3 % dry weight fraction and remove air bubbles. No opaqueness was observed by visual inspection in any of the samples thus prepared. Samples were not concentrated further once loaded onto the ATR accessory.

5.3.2 Native Silk Feedstock (NSF)

Native silk feedstock samples were produced using the procedure described in section 2.1.1.2. In total 13 samples were prepared for Rheo-IR testing. Only the posterior part of *Bombyx mori* silkworm gland was used to ensure sample consistency, prevent dilution and ensure freshness.

5.3.3 Rheo-IR experimental platform

The Rheo-IR experimental platform consisted of a Gemini 200 HR Nano Rheometer (Malvern Instruments, UK) coupled to a Nicolet 6700 Fourier transform infrared spectrometer equipped with a MCT-A detector and a Golden Gate single reflection diamond attenuated total reflection (ATR) accessory (Specac, UK). The rheometer was mounted on top of the ATR accessory similar to commercial alternatives (Resultec analytic equipment, Germany)[Feustel2006] and is shown schematically in Figure 5.1a. The rheometer had a torque range sensitivity of $1*10^{-8}$ to $2*10^{-1}$ Nm. Aiming at achieving homogeneous shear rate across the probed area, a cone and plate geometry system was used. The cone was a 210 mm long by 10 mm diameter aluminium rod cut at a 1 ± 0.03° angle and truncated by 30 μm, and had a $41*10^{-9}$ g/m^2 moment of inertia as measured by the instrument. The geometry could hold 2.3 µl of sample, but was slightly overfilled before gently trimming the excess material before each test.

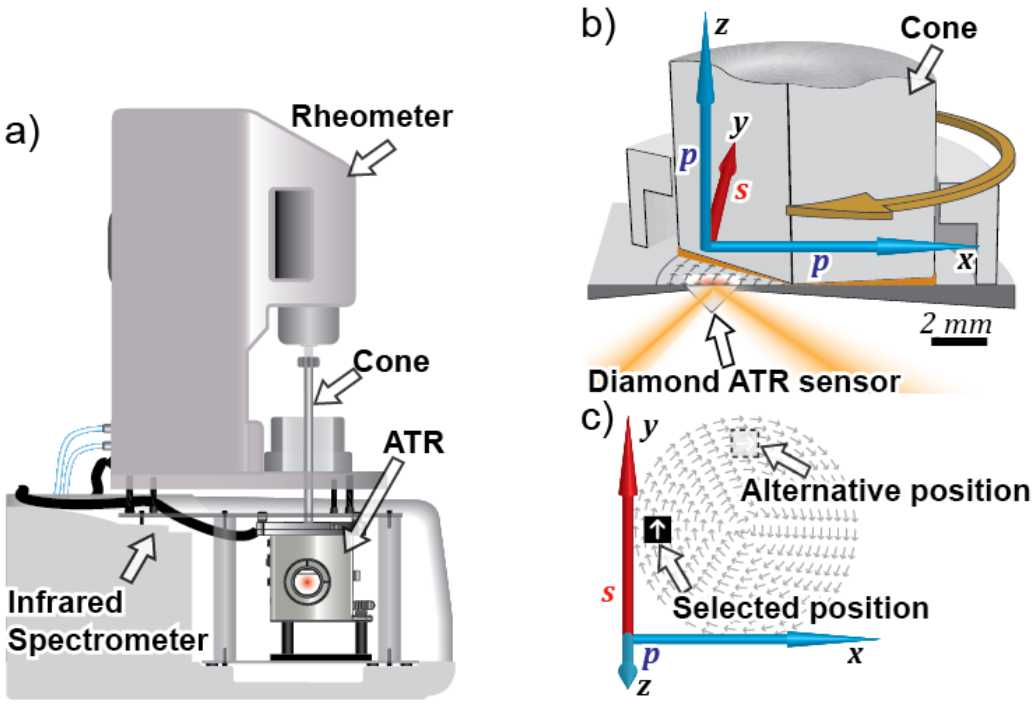


Figure 5.2 a) Schematics of the Rheo-IR setup consisting of a rheometer mounted onto the infrared spectrometer equipped with an attenuated total reflection accessory. The bottom plate of the geometry is the spectrometer's ATR accessory made of a tungsten carbide disk with an embedded diamond prism. b) Cross-sectional view of the Rheo-IR geometry with the laboratory coordinate system and the polarisation vectors. c) Top view of the flow field in relation to the laboratory coordinate system and the polarisation vectors.

Specac's maximum roughness tolerance specification for Golden Gate's bottom plate was 200 nm. The working temperature was maintained at 25 ± 1 °C by the ATR accessory across the whole bottom plate. To prevent any drying of the sample during measurements, an environmental cuff filled with water-soaked wet tissues sealed the geometry (see Figure 5.1b). The geometry's parallelism was verified using a high precision spirit level precise to 0.02°. As illustrated in Figure 5.1b-c, the ATR sensor was positioned 3 mm away from the centre of geometry rotation along the beam propagation direction (x axis) to simplify the interpretation of the orientation; it shows the shear flow field in relation to the polarisation vectors. The infrared beam had an ellipsoidal footprint of ~1060 by ~750 µm (length*width) along the beam path. The beam was reflected internally, at an angle of incidence of 45° giving an evanescent wave penetration depth around 1 µm, depending on the

wavelength.[Harrick1967] Thus, the ATR sensor mostly probed the velocity profile close to the static bottom plate since the geometry is 52 µm thick at a radial distance of 3 mm.

The electric field of the infrared beam was polarised using a motorised zinc selenide holographic wire grid polarizer (Thermo Scientific, Madison, WI); s-polarised light only probed vibration modes along the y axis, the velocity or shearing direction, whilst p-polarised light selectively probed vibration modes along the x and z axes, the vorticity and velocity gradient directions, respectively. One of the advantages of our custom built rheo-IR setup is the ability to change the position of the probed area relative to the flow direction, either along the s polarisation (y axis) or the p polarisation (x axis) by simply moving the rheometer laterally with respect to the infrared sensor (see Figure 5.1c). For an infrared beam at an incidence angle of 45°, the theoretical value of the dichroic ratio ($\mathrm{R_{ATR}} = \mathrm{A_P}/A_S$) of polarised spectra is 2 for a non-oriented (isotropic) sample.[Harrick1967; Fringeli1980] If the refractive index of the sample is known (~1.54 for silk[Tsukada1991]), the second Legendre orientation parameter $< P_2 >$ can quantify the orientation using $\mathrm{R_{ATR}}$.[Fringeli1980] However, for our rapid dynamic experiments, both polarisations would have to be acquired simultaneously during shear which was not possible with our current experimental setup as the polarisation could only be changed every 30 seconds using a motorised polariser. To obtain quantitative information, band decomposition would also need to be performed on the amide I band. Decomposing the amide bands into their components can be subjective as many solutions can give a reasonable fit when many broad and overlapping peaks are present. The initial optimisation parameters choice can also strongly influence the final result.

In order to avoid such confounding issues, we qualitatively measured the protein orientation and conformation using the amide bands centre-of-gravity (COG), which is

commonly used to follow dynamic processes.[Stuart2004; Boulet-Audet2011] Although the COG does not provide direct measurement of the intensity of the underlying components, it has the advantage of being an objective metric. Due to the low noise level and precise frequency measurements of infrared spectra, the COG can be very accurately measured (± 0.1 cm^{-1}).[Griffiths1986] The COG has the additional advantage of being independent of absolute intensity variations.

5.3.4 Experimental procedure

After sample loading onto the ATR assembly, two types of rheological measurements were performed. For NSF, the linear viscoelastic region validation for the Rheo-IR setup is shown on Figure A.14 of Appendix 3, page DD. For NSF and RSF, oscillatory tests from 623 to 0.623 rad/s were performed, with a target strain of 0.002 and n = 13 for NSF and n = 13 for RSF. Thereafter samples were subjected to a viscosity test under either a slow exponential shear ramp 0.0018 to 150.6 s^{-1}, $\gamma(t) = 0.0014e^{0.0445t}$ (0 to 100 s^{-1} in 251 seconds, n = 7) or a fast shear rate ramp, from 0.03 to 1062 s^{-1}, $\gamma(t) = 0.0196e^{1.42t}$ (0 to 100 s^{-1} in 6 seconds, n = 6). The slow exponential shear ramp was chosen to be consistent with published literature[Holland2006; Holland2007; Holland2012b] whereas the faster shear rate profile follows estimated amount of shear within a duct as calculated by Moriya et al.[Moriya2009] In order to prevent overloading the rheometer's normal force transducer, shearing was stopped once the thrust reached 250 kPa of first normal force N_1. The fast exponential shear ramp has the additional advantage of reaching higher shear rates without surpassing the N_1 threshold. The zero shear viscosity η_0 was calculated by averaging the five highest viscosity data points measured at near zero rates and the plateau modulus G_N has been calculated from the average of the three highest data points, free of instrumental error, at high frequencies. As a precaution during the oscillatory tests, infrared spectra were also recorded and no

variation in the infrared signal was detected, confirming that we did not reach the viscoelastic limit of native silk.

Static spectra were collected from the average of 64 scans (17 seconds). Dynamic FTIR spectra were recorded using 19 scans per time frame for slow exponential ramps (5.05 seconds) or 2 scans per time frame for fast exponential ramps (0.53 seconds). The rheology data collection consistently started 11 seconds after the spectroscopy. Spectra were recorded at a 4 cm^{-1} resolution from 6000 to 500 cm^{-1}. The only applied correction was a constant baseline correction, the level of which was equal to the average intensity measured from 4000 to 3950 cm^{-1}. The centre of gravity (COG) of the amide I band was calculated from the 20 % upper portion of the 1700-1594 cm^{-1} region and the amide II's COG from the 10% upper portion of the 1594-1480 cm^{-1} region. The dry weight was quantified with a partial least squares calibration curve using TQ Analyst 7.2 (Thermo Electron Corp. Madison, WI) as described elsewhere.[Boulet-Audet2011] The average uncertainty on the dry weight is 3 % (w/w).

5.4 Results and discussion

5.4.1 Oscillatory test

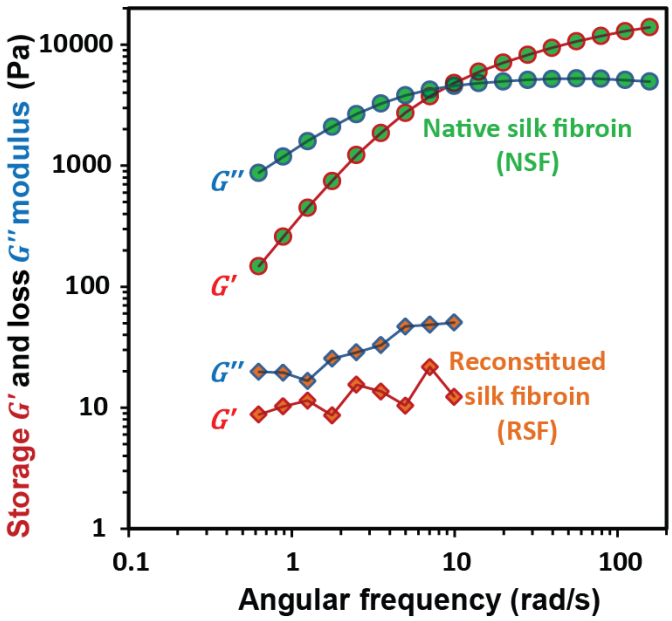


Figure 5.3 Storage modulus G' (red lines) and loss modulus G'' (blue lines) as a function of the angular frequency for a representative native (green circles) and reconstituted (orange diamonds) silkworm feedstock (22 ± 3 % w/w).

To test the ability of native and reconstituted silk feedstock to store and dissipate energy, an oscillatory sweep was first performed for each sample. Figure 5.3 shows data from one representative sample of NSF (green circles) and RSF (orange diamonds) in response to an oscillatory frequency sweep. The protein concentration for every sample was 22 ± 3 % w/w for both NSF and RSF, as calculated from *in situ* measurements of protein/water absorbance between 1500 and 900 cm^{-1}. Although the same angular frequency range is covered for both sets of samples, the phase angle δ for RSF became too large above $\omega = 10\, rad/s$ for accurate calculation and so the data range was truncated. It is clear that the response and values of the moduli of the two sets of samples are distinct. NSF shows a clear crossover point in the storage (elastic) G' and loss (viscous) G″ moduli where they

become equal ($\tan(\delta) = 1$). This crossover appears at 10 ± 2 rad/s, giving a relaxation time $\tau_p = \omega^{-1}$ of 0.6 ± 0.1 seconds with the values of the moduli and relaxation time being consistent with previous measurements.[Kojic2006]

As plotted in Figure 5.3, the response of RSF is very different to that of NSF. Since the elastic modulus is lower than the viscous modulus over the range of frequencies measured, none of the RSF samples showed a crossover point, making the calculation of the relaxation time impossible. The absolute values of the moduli of RSF are also substantially lower than those of NSF. At high frequencies, the plateau modulus ($G_N = G'|_{\omega\to\infty}$) gave us a parameter representative of the sample's elastic energy storage potential.[Ferry1980] The average plateau modulus G_N for NSF samples was 13 ± 3 kPa, in sharp contrast with only 0.008 ± 0.006 kPa for RSF. Upon comparison with the published RSF data from Holland et al.,[Holland2007] the moduli measured for the RSF in our study are higher, which is most likely due to a lower degree of degradation caused by reducing exposure to high temperatures during reconstitution.[Wray2011; Wang2013] The three orders of magnitude gap in G_N revealed the distinct levels at which native silk and artificial feedstocks can store and dissipate mechanical energy. This result supports the hypothesis that RSF and NSF are two different kinds of materials with RSF appearing to behave more like a non-Newtonian fluid with a small frequency dependency of the modulus.[Holland2007]

5.4.2 Static infrared spectroscopy

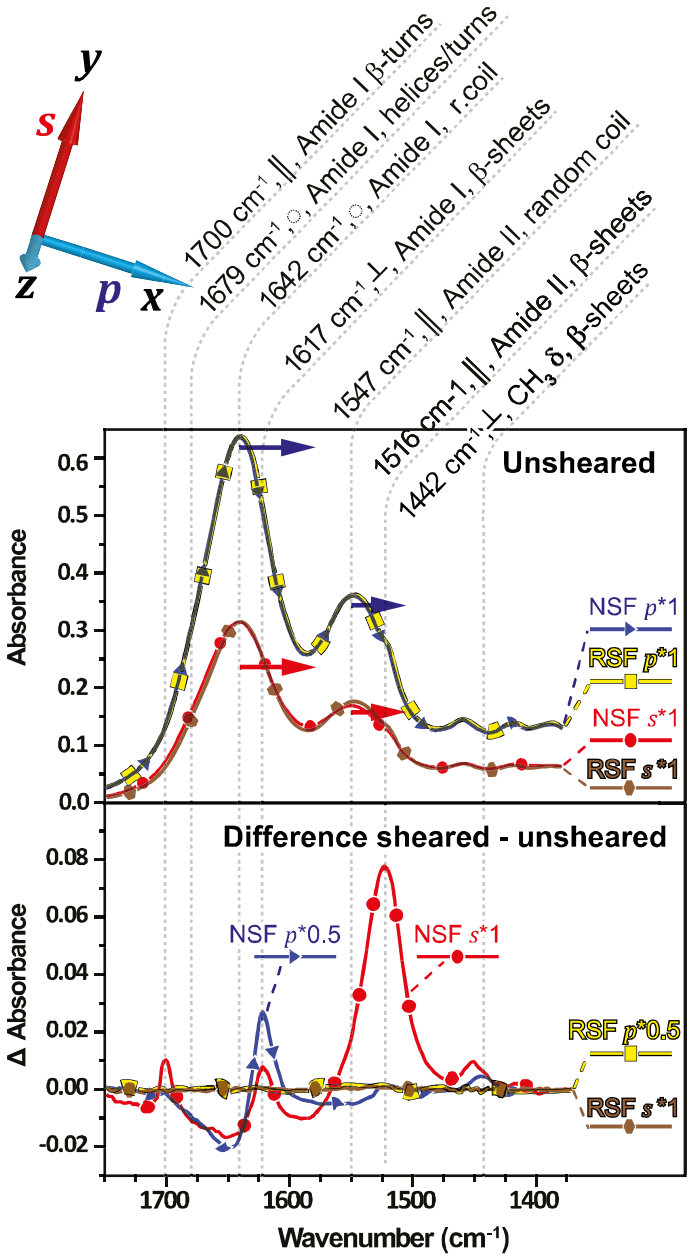


Figure 5.4 a) Native silk feedstock spectrum before shearing (blue line with arrows for p polarisation and red line with circles for s polarisation), reconstituted silk feedstock before shearing (yellow line with squares for p polarisation and brown line with hexagons for s polarisation). b) Difference between after and before the slow exponential shear ramp profile for native silk feedstock and reconstituted silk feedstock with assigned components.[Miyazawa1961; Moore1976; Venyaminov1990; Yoshimizu1990; Muller1993; Goormaghtigh1994a; Sonoyama1997; Sonoyama2000; Garside2005; Lv2005; Taddei2005; Teramoto2005; Jeong2006; Boulet-Audet2008] The p polarisation difference spectra were multiplied by 0.5 for comparison. The flow direction vector relative to the laboratory coordinate system is represented on top left corner.

Infrared spectroscopy is commonly used to assess protein secondary structure (conformation) as vibrational modes frequencies of the amide bands are dependent on hydrogen bonding and the 3 dimensional structures formed.[Goormaghtigh1994b] Both NSF and RSF show typical protein peaks, including the amide I and II peaks at 1642 and 1547 cm^{-1} respectively.[Moore1976; Goormaghtigh1994b] For non-oriented (isotropic) samples, both s and p polarised spectra give the same spectral line shape, with p polarisation having twice the absorbance of s.[Harrick1967] This is the case for unsheared NSF and RSF, as plotted in Figure 5.4a. Such information is useful in order to determine unwanted orientation induced from sample loading. Despite their distinctly different rheologies, the mid infrared spectra of static or sheared samples of both native (blue line with arrows and red line with circles, respectively) and reconstituted silk (yellow line with squares and brown line with hexagons, respectively) are indistinguishable.

In addition to FTIR, other spectroscopic techniques such as Raman,[Rousseau2004] near-infrared,[Mo2009b] NMR[Zhu2008] and circular dichroism[Greving2010] appear to be blind to the difference between reconstituted silk and native silk. The inability of spectroscopy alone to discriminate between static natural and reconstituted silk solution explains why reconstituted silk is often perceived as a suitable native silk analogue and is widely used to investigate silk's processing.[Hossain2003b; Rössle2004; Sukigara2004; Xu2005; Xie2006; Kino2007; Li2008; Ohgo2008; Yuan2010] The marked difference in flow properties measured by rheology thus casts doubt on the sensitivity of those standalone techniques to evaluate the quality of the analogues. A solution to this issue is thus to combine spectroscopy with silk's distinct response to flow stress.

When a biologically relevant stress was applied, the difference between the two materials became very clear. These dissimilarities can be highlighted by plotting the difference

between sheared and unsheared spectra for each polarisation, as shown in Figure 5.4b. Overall, the difference spectra revealed increases in intensity at peaks 1700, 1617, 1516, and 1442 cm^{-1} associated with anti-parallel β-sheets and β-turns,[Moore1976; Li2001; Boulet-Audet2008] and absorbance decreases at 1679, 1642 and 1547 cm^{-1} assigned to random coil, turns and helical secondary structures (α and/or 3_{10} helices).[Miyazawa1961; Moore1976; Venyaminov1990; Yoshimizu1990; Muller1993; Goormaghtigh1994a; Sonoyama1997; Sonoyama2000; Garside2005; Lv2005; Taddei2005; Teramoto2005; Jeong2006; Boulet-Audet2008]

When considering the polarisation of the spectra, we hypothesised that the protein chains and associated vibrational modes will be aligned along the velocity direction (y axis) and will be probed predominantly by the s polarisation (red curves) whilst any structures with modes perpendicular to the protein backbone will be probed mainly by the p polarisation (blue curves). The bands at 1642 and 1679 cm^{-1}, which are associated to the random coil and helical/turns secondary structures respectively, have about the same intensity change in both polarisations, indicating that these structures have little preferential orientation. Since the 1516 and 1700 cm^{-1} components appear only in s polarisation for the sheared NSF, it suggests they are aligned along the velocity direction. The intensity increase at 1617 cm^{-1} is only slightly higher for p polarisation indicating a weaker orientation perpendicular to the velocity vector. Consequently, molecular alignment should have little influence on the amide I band position when using s polarisation. The amide I COG shift is thus mostly due to the change in conformation. In contrast, anisotropy will strongly shift the amide II COG to lower wavenumbers because of the 1516 cm^{-1} component at lower wavenumbers. Therefore in contrast to the amide I band position, the position of the amide II band appears to be a good indicator of both conformational change and orientation.

5.4.3 Coupling rheology and infrared spectroscopy

Clearly, it is possible to obtain key structural changes in conformation and orientation by observing the amide bands COG. This information can then be related to changes in bulk rheological measurements obtained during a viscosity test. For both NSF and RSF, we observe shifts in the COG of the amide I and II bands alongside changes in viscosity η and first normal force difference N_1. Figure 5.5 shows representative steady shear rate responses for two samples of NSF and RSF each. Figure 5.5a-b represent a slow exponential ramp from 0.0018 to 150.6 s^{-1} and c and d a fast shear rate ramp from 0.03 to 1062 s^{-1}. For clarity, the relevant amide I band shifts of the COGs are plotted in the upper panes (a and c) and those of the amide II in the lower ones (b and d). Four response regions with increasing shear rates were identified and labelled from I to IV. At the bottom of Figure 5.5, we illustrated our interpretation of the four regions observed for native silk feedstock with cartoons adapted from the "aquamelt" model presented by Holland et al.[Holland2012b; Holland2012c].

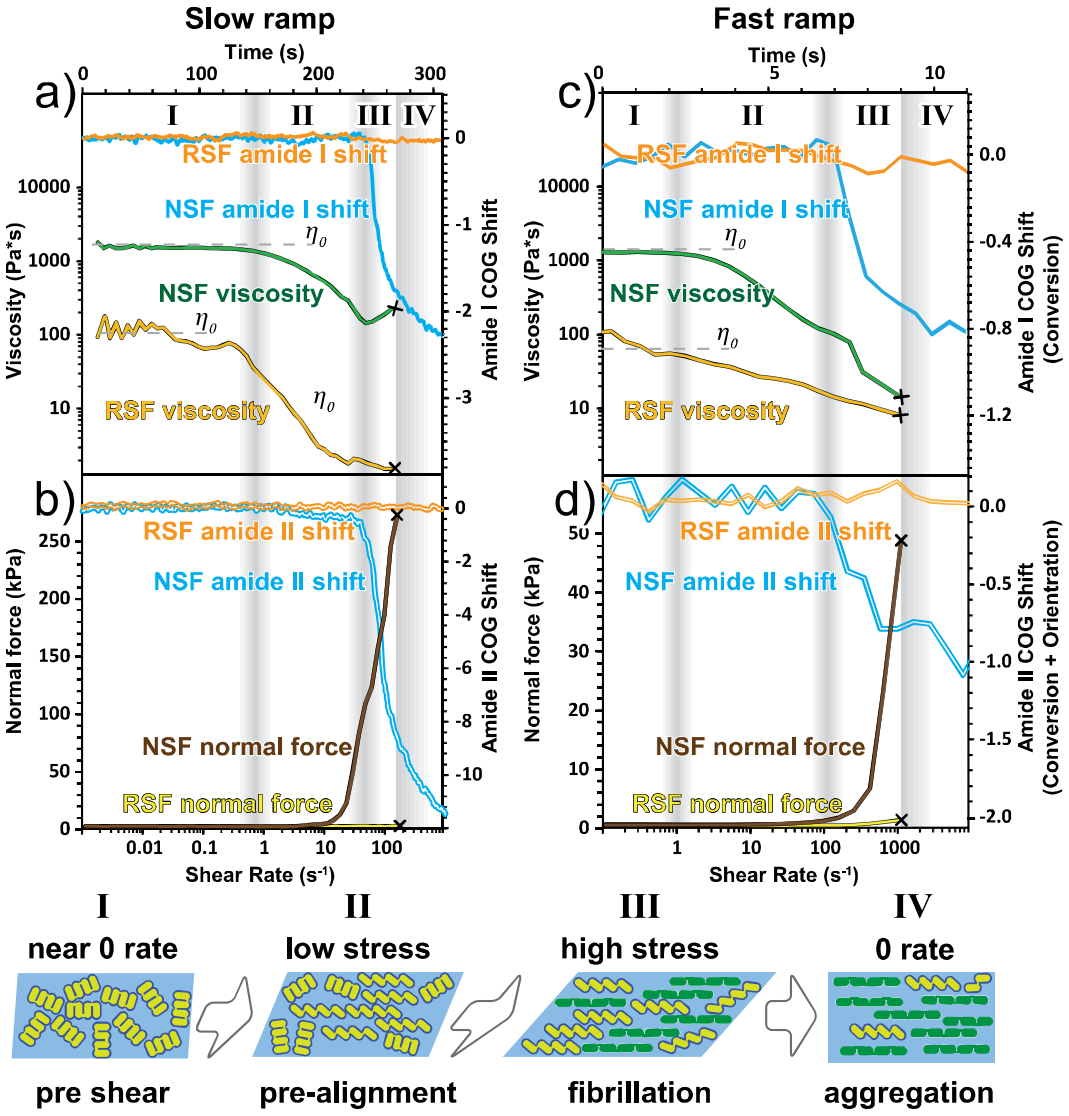


Figure 5.5 Viscosity, first normal force, amide I and II centre of gravity shift as a function of the shear rate and time for NSF and RSF for two exponential shear ramps (slow ramp a and b , fast ramp c and d). The black crosses represent the end of the shearing after the exponential shear ramp or once the 250 kPa threshold was reached. The unspun silk molecules are represented by yellow cartoons with its outer hydration shell represented by a blue outline and the converted fibroin illustrated as dark green string of beads.

Region I

Both NSF (green curves) and RSF (orange curves) exhibited a plateau region at vanishing shear rates giving the zero shear viscosity $\eta_0 = \eta|_{\eta \to 0}$.[Terry2004, Holland2006, Kojic2006, Holland2007] This Newtonian plateau is always observed for both types of feedstocks (Figure 5.5a and c) at rates below 1 s^{-1}. At 1.2 ± 0.4 kPa·s, the zero shear viscosity value calculated for NSF is consistent with observations previously reported by Holland et al.[Holland2006] However in our

case, η_0 for RSF was one order of magnitude lower (0.09 ± 0.05 kPa·s) for the slow shear ramp despite being for the same concentration (within the error). A similar difference was measured with the fast shear ramp, 1.3 ± 0.4 kPa·s for NSF compared to 0.19 ± 0.08 kPa·s for RSF. The difference in zero shear viscosity between the NSF and RSF could therefore be due to a difference in the degree of intermolecular interactions.[Ferry1980] Consistent with a higher G_N, the η_0 measured for RSF is higher than those of Holland et al.[Holland2007] which could be the result of a slightly different sample preparation method. Within this plateau region, the rheological parameters are invariant and there are also no observable shifts in the COG of the amide bands, suggesting no detectable changes in the molecular structure.

Region II

When the sample's viscoelastic limit was reached, the viscosity of both NSF and RSF started to decrease around $\dot{\gamma}_\tau = 3 \pm 2$ s^{-1} for both slow and fast shear rate ramps. This shear thinning behaviour has been previously reported.[Terry2004Holland2006,Holland2012aMoriya2009] Interestingly, FTIR spectra show no fluctuation in amide I COG for NSF and RSF suggesting no detectable changes in the protein secondary structure. On the other hand, the COG of the amide II band for NSF only (Figure 5.5b) started to shift slightly as an indicator of the molecular orientation. During this region of shear thinning behaviour, the first normal force difference N_1 for NSF becomes non-zero as the sample begins to push against the walls of the geometry, typically interpreted as the result of an increase in recoverable elastic strain of the molecules.[Rivlin1948; Porter1995] For RSF, even at higher shear rates, no increases in N_1 was measured. Thus the shear thinning response of NSF is likely to be due to greater molecular alignment and a subsequent reduction in internal friction. Associating these results with birefringence measurements in the silkworm spinning apparatus, an increase in alignment is also seen in the common duct after the feedstock of both glands combine.[Kataoka1977, Asakura2007]

Similarly to highly concentrated polymer melts, the region I and II of NSF can be fitted by the Carreau-Yasuda constitutive model of $\eta = \eta_0\left(1 + \left(\dot{\gamma}\tau_p\right)^a\right)^{(n-1)/a}$, where τ_p is the relaxation time, n is the power-law exponent characteristic of the shear thinning rate and a is the rate of transition.[Yasuda1981] With a fit of R^2 > 0.99 for native silk, this relation gives us a n of 0.16 ± 0.02, a of 1.0 ± 0.2 and τ_p of 0.3 ± 0.2 s, close to other reported values.[Kojic2006; Holland2012b] These values are representative of a high concentration polymer with a strong shear-thinning behaviour resulting from the reduction in internal friction as protein chains are able to disentangle and align under shear rates faster than their relaxation time.[Graessley1967; Ferry1980] In contrast, no molecular alignment is observed for RSF, possibly due to protein degradation during the reconstitution process creating smaller polymer chains and faster relaxation times.

Region III

For the slow shear rate ramp of NSF (Figure 5.5a), shear rates above a critical value ($\dot{\gamma}_i$ = 50 ± 20 s^{-1}) led to shear thickening with the flow of NSF becoming unstable with an abrupt rise in the apparent viscosity. The point at which this instability occurred for our NSF is close to the value of 40 s^{-1} reported for *Samia ricini*, but higher than the 4 s^{-1} given for the middle and posterior division of *Bombyx mori* reported by Moriya et al.[Moriya2009] and the 15 s^{-1} measured by Terry et al.[Terry2004] This difference in $\dot{\gamma}_i$ for native silk fibroin from *Bombyx mori* could be due to (i) the different geometries used, (ii) dissimilar dissection techniques, (iii) other gland sections measured or (iv) an effect of the loading method. Coinciding with the onset of shear thickening, a rapid shift of both the COG of the amide I and II was also observed (Figure 5.5a and b). Simultaneously, N_1 also increased from ~100 kPa to our self-imposed 250 kPa threshold as the sample's elastic recoverable strain continued to grow, as shown in Figure 5.5b and d. As the amide I band shift is closely associated with the

formation of β-sheet structures, the observed thickening and increase in N_1 is most likely the result of subsequent protein aggregation or shear-induced crystallisation.[Vrahopoulou1987] However, for the fast shear rate ramp (Figure 5.5c), no clear shear thickening was observed for NSF. Instead, only the gradient decreased with increasing shear rate before further drop in viscosity. At the same time, we observed a marked growth in N_1, although with lower values than for slow shear rate ramp (~50 kPa compared with ~250 kPa, Figure 5.5b and d). Simultaneously, commensurate shifts to lower wavenumbers for NSF's COG of the amide I (-2 cm^{-1}) and amide II bands (-9 cm^{-1}) were also observed. Similar shifts were also present for the fast shear ramp, Figure 5.5c and d, but to a smaller degree. Moreover, $\dot{\gamma}_i$ was higher for the fast exponential ramp, occurring around 100 s^{-1}. As N_1 appears to be proportional to the accumulated strain once a threshold stress is reached (supplementary Figure A.16), this may explain the higher $\dot{\gamma}_c$ observed under a faster shear rate profile. This conclusion is in agreement with spectroscopic evidence suggesting that fewer β-sheets were formed at comparable rates under a faster ramp with fewer accumulated strains.

The rapid increase in N_1 and shift in the amide bands COG may be considered analogous to the jump in birefringence observed in the silk duct.[Kataoka1977, Asakura2007] If we assume that these events are related, as they appear to be, then shear thickening would occur just at the beginning of the silk press.[Moriya2008b; Moriya2009]

In contrast to the shear rate response of NSF, RSF did not show any shear thickening for either the slow or fast shear rate ramps, Figure 5.5a and c. Instead RSF samples continued to exhibit shear thinning with increasing shear rate without shifts in both COGs. Similarly, N_1 displayed only a slight increase at high rates for both the slow and fast shear rate ramps, suggesting an almost non-existent elastic recoverable strain. In previous work, shear-induced conversion was only observed at very high RSF concentrations, above 50

w/w %.[Boulet-Audet2011] The difference in response of NSF and RSF to high shear rates may be due to a lower molecular weight or to the removal of small compounds during the dialysis step.[Yamada2001] Indeed, Greving et al.[Greving2010] showed that there are differences in both size and shape between diluted NSF and RSF. The distinct shape could be explained by differences in the intra- and inter-molecular interactions of the hydrated proteins, accounting for the lack of shear-induced interactions in RSF. As the transition to a β-sheet structure is essential for the spinning process,[Knight2000] our study implies that reconstituted silk prepared in this manner would not be able to be spun at concentrations and shear rates that are comparable to native silk fibroins.

Region IV

Once shear thickening starts, a white plug surrounded by a lower viscosity fluid is quickly formed.[Holland2006; Holland2007] This normally occurs shortly after the normal force reached 250 kPa of normal force and can be avoided by interrupting the shear stress before the end of the shear ramp. As N_1 in the fast exponential shear ramp is lower at equivalent rates, higher rates can be reached without slip and sample ejection. A shear transient with lower accumulated strains would therefore enable native silk feedstocks to be exposed to higher shear rates. Hence exposing the dope to shearing for only brief period of time in region II would permit a longer exposure to the higher rates of region III prior to plug formation. To prevent detrimental duct plugging in the animal, dope gelation/thickening would have to occur only once the narrowing of the duct is completed (i.e. at the silk press), as suggested by the measurement of Moriya et al.[Moriya2009] For spiders, the structure equivalent to the silk press is the draw down taper,[Davies2013] where β-sheet formation is observed.[Knight2000; Lefèvre2008]

Infrared spectroscopy has quantified the protein concentration during the experiment, which did not show any substantial variation for either RSF or NSF. An interesting feature of

Rheo-IR is its ability to continue monitoring the conversion of the NSF by FTIR even post shearing. Although at this stage no more mechanical energy was inputted, the amide bands continued to shift towards lower frequencies, indicating a spontaneous self-assembly process, corroborating previous observations.[Li2001; Holland2012b] However, this process occurred very slowly and took hours to complete as the amide I could shifted to lower frequencies by up to 5 ± 1 cm^{-1} and the amide II band 18 ± 1 cm^{-1}. The amide bands are far from being completely shifted before slippage or ejection systematically occurred. Hence our methodology was unable to complete the conversion of NSF in the short time scale of the natural spinning process. Extensional flow fields might also contribute to provide additional stress to complete the conversion as it is suspected to play an important role in the natural spinning process.[Knight2000]

5.4.4 Effect of the polarisation

As presented in section 3.4.5, the simplest way to evaluate the molecular alignment is by rotating the polarisation. As native silk conversion occurred on a shorter time scale than RSF our experimental setup would be too slow to rotate the polarisation whilst shear-inducing the conversion. Instead of using the approach described in section 3.4.5, two separate experiments with *s* and *p* polarisation selected where performed under the same shear history (300 s at 1 s^{-1} then 10s at 100 s^{-1}).

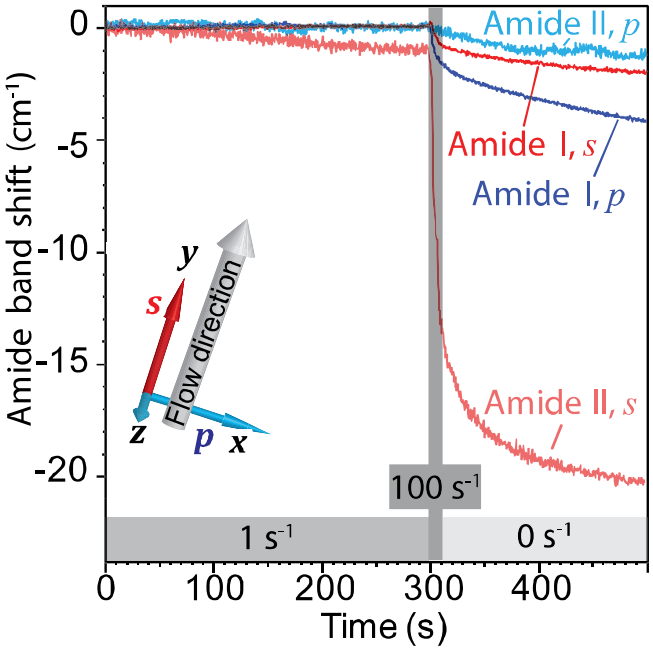


Figure 5.6 Amide I and II band shift as a function of time under low and high shear rates for native silk fibroin samples using *p* and *s* polarisation. The shear rate transient experiment is analogous to the experiment performed in section Chapter 4.

As shown in Figure 5.6, no detectable shifts in the amide I COG were measured whilst shearing native silk at 1 s^{-1} for both polarisations. On the other hand, silk's pre-alignment along the shearing direction is detectable by the amide II band shift using *s* polarisation as shown on Figure 5.5b. As most changes are revealed by *s* polarisation, suggests that changes are occurring mainly along the shearing direction. The difference between polarisations on the amide I band is not as marked as this vibration mode perpendicular to the backbone does not appear to be as oriented perpendicular to the flow vector. These experiment this support the choice of *s* polarisation for monitoring fast kinetic when only a single polarisation can be recorded with high temporal resolution.

5.4.5 Self-Modelling Curve Resolution (MCR)

Although the COGs are simple indicators of the conversion process and the difference spectra show the affected wavenumbers, they provide convoluted information. Ideally, the isolated spectra and the concentration profile of each species would allow a more thorough

interpretation. One way of achieving this is the soft modelling approach, such as the self-Modelling Curve Resolution Alternating Least Squares (MCR-ALS) developed by Tauler et al.[Tauler1991; Tauler1993a; Tauler1995a] The MCR-ALS method designed to deconvolved pure spectra and the concentration profile is described in more details in section 2.3.8. Originally designed to analyse chromatograms, this analytical tool is also well suited to infrared kinetics. Unlike the centre of gravity of the amide bands, the pure components concentration profiles are quantitative metrics.

The number of components must be first chosen. As the spectra are far from changing entirely from one conformation to another, it is reasonable to assign one component to permanent silk protein structures. As some bands grow and others shrink, two more components were attributed to the loss and gained structures. A fourth component was added to fit the effect of the molecular orientation. The initial concentration and spectra were calculated from evolving factor analysis described in section 2.3.8, neglecting ranks with eigenvalue below 1.

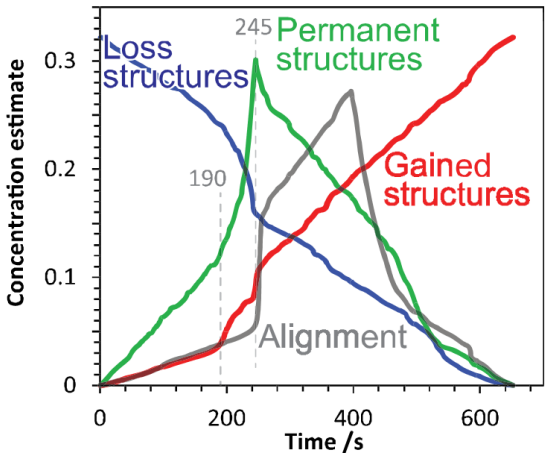


Figure 5.7 Evolving Factor Analysis (EFA) initial estimate of the concentration profile (eigenvalue threshold = 1)

As shown on Figure 5.7, the EFA already identified two transitions at 190 and 245 seconds. However, it gave unrealistic concentration profiles for the permanent structure and alignment components with vanishing values at the end of the kinetic. For the optimisation

of these initial estimates, constraints help lifting the rotational ambiguity between the pure spectra and concentration profile matrices. First, non-negativity conditions for concentration profiles and spectra were imposed as negative values cannot be explained. In addition, the conservation of mass principle allows the closure condition to be applied, forcing the sum of concentration profiles to 1 (except the alignment). Finally, an equality constraint was set for the concentration of permanent structures over the entire kinetic whilst gained structures were forced to zero concentration at time equal zero. Within those constraints, the MCR-ALS optimisation algorithm quickly converged to a solution resulting in the concentration profiles and spectra of the four assigned components.

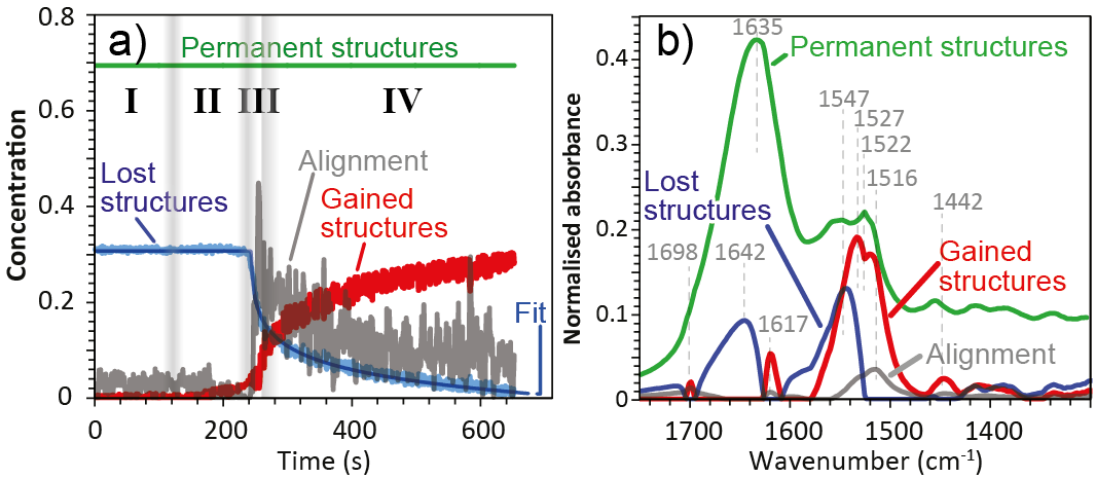


Figure 5.8 a) Four components MCR-ALS deconvolved concentration profile. b) Pure spectra for native silk sheared under an exponential shear ramp.

The concentration profile of the permanent structures (green line in Figure 5.8a) is constant because of the equality constraint imposed. However, the loss structures decreased and the gained increase with the evolving conversion process. Importantly, the algorithm quantified the meta-structures (changeable structure) to be around only 30% of the total structure. This number is likely to be underestimated as the spontaneous conversion process was not entirely completed at the end of the experiment. In addition, the crystallinity content of *Bombyx mori* is normally estimated from 56 to 64%.[Sinsawat2002;]

Martel2007 During the pre-shear regime (region I), no changes occurred for any components. As the sample is shear thinning (region II), the gained structure concentration (red curve) starts to grow slightly as gained structures are formed. Once the critical shear rate $\dot{\gamma}_i$ is reached around 240 seconds, the alignment component rises suddenly. Once shearing stopped, the alignment component concentration decreased over time whilst the meta-structures continued to convert spontaneously, as shown by the amide I band shift in region IV of Figure 5.5a and c. A possible interpretation could be that the alignment relaxed over time, but it is more likely due to the formation of additional isotropic β-sheet structures diluting the orientation initially generated. Fitting the lost structure with an exponential function from the onset of the conversion resulted in an excellent coefficient of determination R^2 of 0.993. It thus suggests that the shear driven conversion kinetic in regions III and IV has an exponential form. Using this function, the optimisation algorithm calculated an onset of 240.3 seconds and a logarithmic first order rate constant of 0.049 s^{-1}.

The associated pure component spectra calculated from the MCR-ALS are given in Figure 5.8b. The spectral line for the permanent structures is dominated by the 1635 cm^{-1} band corresponding to the liquid H_2O maximum absorption of the bending motion. This was expected as native silk feedstock sample contains 100 % – (22 ± 3) % water. On the other hand, silk proteins have higher extinction coefficients k than water,*deJongh1996; Boulet-Audet2010* resulting in greater absorbance at comparable concentration. For gained structures, the bands observed are peaking at similar position as the difference spectra of Figure 5.4 with one band at 1698, 1617, 1527 and 1442 cm^{-1} associated with anti-parallel β-sheets. For the loss structures, the calculated pure spectra primarily shows asymmetric peaks at 1642 and 1547 cm^{-1}, which could be the result of multiple components associated with random coil and β-turns secondary structures.*Miyazawa1961, Moore1976, Venyaminov1990, Yoshimizu1990, Muller1993, Goormaghtigh1994a, Sonoyama1997, Sonoyama2000, Garside2005, Lv2005, Taddei2005, Teramoto2005, Jeong2006, Boulet-Audet2008* As

the gained structures are peaking at lower wavenumbers than the loss structures it results in both amide bands are shifting to lower wavenumbers as a result of the conversion. The small bump at 1522 cm^{-1} on the gained structures spectrum (red curve) and the permanent structures spectrum (green curve) is likely to be associated with the unchanging vibration of the tyrosine side chains.[Barth2000b] The pure spectrum assigned to alignment (grey curve), has similar peaks to the gained structures, but with much lower intensity in the amide I compared to the amide II region. MCR-ALS thus supports our interpretation that the molecular alignment impacts mostly the amide II band COG shift as the preferential orientation of the protein backbone is along the polarisation and the shearing direction.

5.5 Conclusions

By coupling rheology with infrared spectroscopy (Rheo-IR), we have correlated silk protein structure to feedstock flow properties under a range of shear conditions. For native silk feedstocks our results support the hypothesis that shear thinning results from molecular alignment. We propose that this alignment occurs in the common duct of the silkworm's spinning apparatus, a hypothesis supported by birefringence measurements.[Kataoka1977, Asakura2007] Additional support comes from the observation that, after an instability shear rate and strain threshold is surpassed; shear thickening is associated with the onset of a rapid solidification process promoted by β-sheet formation, which would coincide with the start of the silk press.[Knight2000; Asakura2007; Moriya2009] Additionally infrared spectroscopy allowed us to investigate spontaneous protein conversion process post shear. This observation is in perfect agreement with a nucleation mechanism for solidification/fibrillation.[Li2001; Chen2002a; Holland2012b]

We also demonstrated that, whilst static spectra of NSF and RSF are indistinguishable, Rheo-IR highlights their intrinsic differences. Despite RSF undergoing shear thinning, it does not (unlike NSF) shear thicken or solidify under mechanical stress, even at very high rates. Therefore it would be imprudent to assume that traditionally prepared RSFs are representative analogues of native silk, even when they have similar spectra and comparable responses to chemical or thermal stress. Importantly, the fundamental differences in the shear responses of the two materials offers the potential of an explanation to the disappointing properties of the fibres spun from such feedstocks.[*Vollrath2011*]

In summary: Rheo-IR has provided a fresh perspective onto the natural spinning process as well as tool that could also be employed to investigate the processing of practically any polymer melt or solution. Moreover, we envisage that Rheo-IR will be of significant value in helping attempts to refine silk reconstitution processes, which in turn would allow the manufacture of sustainable feedstock analogues akin to native silks and with the potential to be processed in a biomimetic manner into high performance fibres.

Chapter 6

Interrupting silk's processing

This chapter represents the culmination of the thesis' work on spinning by examining a key question formulated in the previous three chapters. Can shear force alone complete silk's processing? To answer this question, I designed a new experimental setup allowing the probing of silk's molecular structure immediately after secretion by silkworms. In addition to providing information at this point, this study addressed the effect of post spinning environmental conditions. This field is of particular interest as Tom Gheysens and Chris Holland from the Oxford Silk Group observed that cocoons spun under low humidity conditions appeared to be soluble under milder conditions than conventional cocoons. They also hypothesised that it could ultimately improve silk fibre reconstitution process. From the tanning behaviour of silk observed by Brunet et al., they hypothesised that controlling silk's spinning conditions could prevent silk's tanning or cross-linking caused by quinone molecules. In addition to writing the manuscript, I designed and performed the entire experimental work and data analysis presented in this chapter. Chris Holland, Tom Gheysens, Ann Terry and Fritz Vollrath contributed with advice, proof-reading and editing.

6.1 Abstract

Post-drawing is widely acknowledged as essential to silk fibres' remarkable mechanical properties by increasing alignment. However, the causes on the molecular level underlying this modulating effect are still speculative. Aiming at elucidating this, we probed silk as quickly as possible after secretion using a novel controlled environment spinning platform coupled with attenuated total reflection infrared spectroscopy sensor. Using our platform,

we found that the protein conformation conversion of silkworm silk continues *ex vivo* after secretion as long as it has enough water to remain a melt above its glass transition temperature. Hence, drying silk fibres quickly after secretion was found to be an effective method to interrupt the spinning process, resulting in fibres with lower β-sheet content. These partially spun fibres could then be degummed without chemicals at room temperature. Moreover, they could be solubilised at room temperature using concentrated lithium bromide, removing the need of prolonged high temperature treatments. The feedstock produced from this method had very similar shear sensitivity and flow properties from liquid native silk extracted directly from the worm. We demonstrated the potential of dry spinning as an energy efficient method for obtaining partially processed silk for consistent analogues with native-like properties.

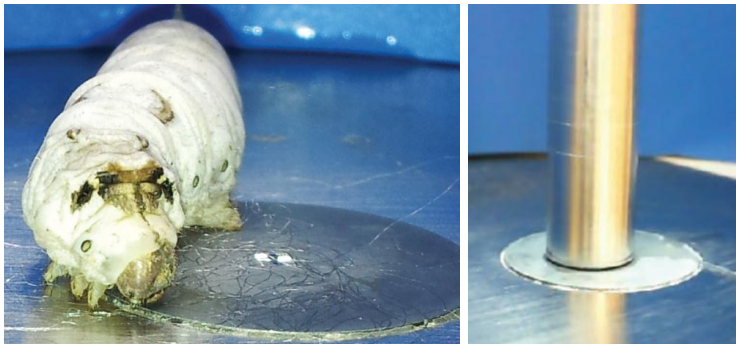


Figure 6.1 Chapter 6 graphical abstract

6.2 Introduction

Mainly made of proteins, silk fibres are a sustainable agricultural product[Vollrath2013a] with excellent mechanical properties[Ashby1995; Gosline1999; Vollrath2001] which are also bio-compatible and biodegradable.[Altman2003; Meinel2005] A common feature of biological materials such as silk is their variability. Many factors can potentially contribute to silk's variability, including the animal's diet, temperature, spinning and storage conditions of the cocoons.[Brunet1974; Magoshi1985; Kerkam1991] Most particularly, silk fibres properties can differ greatly depending on

the spinning conditions,[Shao2002; Mortimer2013] resulting is varying ratio of order and disorder.[Liu2008] Previous studies (Chapter 4 and Chapter 5) provided evidence that only a fraction of the potential ordered β-sheet content of silk is formed under shear-induced denaturation.[Boulet-Audet2013] Moreover, other sources of stress present *in vivo* such as pH drop,[Dicko2004; Rammensee2008] metallic ions concentration change[Foo2006] and extensional flow[Vollrath2001; Kojic2006] could also contribute to inducing the conformation conversion. Furthermore, reeling speed, water vapour, solvent soaking and draw ratio are commonly used to modulate silk fibres' tensile properties.[Liu2008] These insights led us to postulate that the sum of stresses is still not enough to complete the protein conformation conversion *in vivo*, which should continue *ex vivo*.

To deconvolute the effect of *in vivo* spinning, post-processing and ageing, silk's molecular structure would need to be investigated as soon as possible after secretion. Fibre collection, mounting and analysis cannot be done quickly enough to assess the effect post-processing. To overcome this issue, *in situ* measurements are preferable. Using birefringence, Kerkam et al. revealed that silkworm silk is secreted as a lyotropic liquid crystal solidifying when water evaporates *ex vivo.*[Kerkam1991] The degree of β-sheet crystallinity and the water content has not however been quantified yet. In addition, X-ray diffraction of spider forced reeling performed by Riekel et al. revealed that for spider silk, crystallization continues a few millimetres outside the animal,[Riekel2000] emphasising the importance of post-processing for silk fibre's mechanical properties.[Shao2002; Liu2008] However, the effect of the metal pin guide on the thread was unclear. Unfortunately due to likely radiation damage, the same thread portion could not be continuously probed using this approach over time. Of all the techniques typically applied to investigate protein structure (as listed in Table 1.1), attenuated total reflection infrared spectroscopy (ATR-IR) is particularly well suited to probe silk's structure as it can probe a single fibre without heat or radiation damage to

inform on the protein conformation and orientation.[Boulet-Audet2008] By probing fibres spun directly onto the sensor's surface by the silkworm, ATR-IR can quantify the water content, the molecular orientation and the β-sheet crystallinity content (conformation).[Goormaghtigh2006; Boulet-Audet2011] Hence this powerful technique can exploit the instinctive cocoon construction behaviour of silkworms which starts by laying a silk fibre mat. If confined near an ATR accessory, a silkworm will eventually spin a fibre onto the ATR sensor allowing its probing immediately after secretion. Such an approach also had the advantage of probing silk after the animal applies all the naturally occurring types of stress, not only shear flow. In addition, the worm is not immobilised and forced to spin a thread which is known to have an important effect on the fibre properties.[Mortimer2013] This non-intrusive approach also permits the control of the spinning environmental conditions, temperature and humidity. As bounded water is known to play a major role in the silk fibre properties,[Fu2009] this powerful yet simple platform allowed us to study the effect of humidity on the fibres. Using this approach, we thus found that by carefully controlling the post-spinning conditions we can obtain less ordered silks fibres with a lower degree of β-sheet crystallinity, which has important repercussions.

Silk does not necessarily have to be a fibre as it originates from liquid feedstocks which can be reprocessed into any other form factors.[Vepari2007] The simplest way to obtain these useful liquid silk feedstocks is to extract them directly from silkworm glands by means of dissection,[Vollrath2003; Holland2006] but this approach is extremely labour intensive and requires a regular supply of live silkworms. The easiest scalable method to obtain liquid silk consists in dissolving cocoon fibres in chaotropic agent such as LiBr to form reconstituted silk feedstocks (RSF) (see Chapter 3 and Chapter 5). The commercially available *Bombyx mori* is the most commonly used species for making theses RSF as it can be easily sourced, degummed and reeled.[Gheysens2011b] Since spectroscopic techniques such as FTIR ,

Raman,[Rousseau2004] near-infrared,[Mo2009b] NMR[Zhu2008] and circular dichroism[Greving2010] provide equivalent spectra for RSF and native silk feedstock, RSF is commonly used as an analogue for native silk. However, as demonstrated in Figure 5.5, these reconstituted silk feedstocks (RSF) have viscosity typically orders of magnitude lower and are not as shear sensitive compared to native silk feedstocks.[Holland2006; Holland2007; Boulet-Audet2013] Because of their different molecular weight distributions[Yamada2001; Wray2011; Cho2012; Wang2013] and solution neutron scattering,[Greving2010] it is suspected that the difference in flow properties is caused by silk protein fragmentation.[Ferry1959; Mo2009a] Despite doubts being raised on their validity as native silk substitutes, many attempts were made to spin fibres from RSF using various techniques, but with mixed results.[Elices2011Matsumoto1996, Seidel2000, Lazaris2002, Yao2002, Shao2003 Zuo2006] Artificially spun fibre can achieve comparable stiffness or extensibility, but failed to produce strain hardening filaments with comparable toughness.[Vollrath2013b]

On the basis of these observations, we concluded that the process by which RSF is produced greatly needed improving. To solubilise silk fibres requires energy as elevated temperatures. However, heating above silk ’s ~65 °C denaturation temperature[Porter2008] is known to induce some degree of proteolysis, breaking of the protein’s main chain.[Cho2012; Wray2012] Even at high temperatures, tanned silks from wild species which are darker are generally still challenging to dissolve because of the cross-linking of the side chains.[Brunet1974] Hence, minimising the amount of ordered β-sheets and tanning could represent an approach for facilitating solubilisation under lower temperatures and thus limit the degree of proteolysis.

To test this hypothesis, we prepared RSF from fibres spun under controlled conditions using very mild solubilisation conditions. We assessed the “spinnability” of these feedstocks through the coupling of rheology and infrared spectroscopy (Rheo-IR) to determine the

flow properties and the protein's molecular structure under flow. The resulting RSF proved to be remarkably similar to the native silks feedstocks (NSF) directly extracted from *Bombyx mori* silkworms and thus we have called them high fidelity reconstituted silk feedstocks (Hi-Fi RSF). The use of these improved RSF as suitable analogues to NSF will be discussed thereafter.

6.3 Method

6.3.1 Controlled *In situ* spinning experimental setup

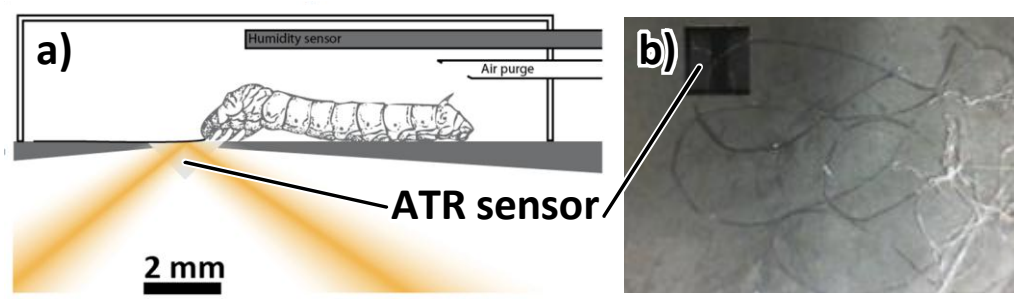


Figure 6.2 a) Schematics of the experimental setup for the *in situ* study of silk's post-spinning by ATR-IR with a *Bombyx mori* silkworm b) Photo of a silk thread spun directly onto the ATR sensor under controlled environmental conditions.

Figure 6.2a shows schematics of the experimental setup used for *in situ* ATR-IR of spinning and post-processing. It is constituted of an environmental chamber containing the silkworm on top of the attenuated total reflection (ATR) accessory (Golden Gate, Specac Ltd., UK) embedded in a Nicolet 6700 Fourier transform infrared spectrometer (Thermo Scientific, Madison, WI). Using a Wetsys (Setaram Instrumentation, Caluire, France), the humidity was controlled between 1% to 96% relative humidity (RH) with an accuracy of 0.1%. The temperature was kept constant at 25 °C for all experiments using the heating element of the ATR whilst controlling the air flow temperature using the Wetsys. Spectra were constantly collected until the silkworm fortuitously spun a thread onto the ATR sensor's

surface. Once absorbance due to protein is detectable, the worm was constrained to prevent any further meddling with the ATR sensor. As a result, the time between secretion and spectra acquisition was limited by the scanning speed of the interferometer (0.25 seconds per scan).

To study the effect of chaotropic agents on silk, a droplet of 9M lithium bromide was deposited directly onto dry spun fibres freshly laid onto the ATR sensor whilst spectra were collected. The diamond ATR sensor offered a penetration depth of around 1 µm depending on the wavelength. The beam spot was approximately of ~1060 by ~750 µm (length*width). Infrared spectra were *s*-polarised using a ZnSe wire-grid. Pictures were taken to record the orientation of the treads relative to the polarisation. The interferometer's mirror speed was set to 3.79 cm/s allowing the recording of one scan every 0.25 seconds covering 6000 to 600 cm^{-1} at a 4 cm^{-1} resolution. Four scans were averaged for each time frame. Spectra were collected and treated using OMNIC 7.3 (Thermo Scientific, Madison, WI). To compensate for the background variation, an offset was applied from the average of the 1730-1750 cm^{-1} region. Spectra were also normalised using the average intensity at 1900-900 cm^{-1} to adjust for the contact dependent absorbance variation.

6.3.2 UV-vis-NIR measurements

All UV-vis-NIR measurements were performed using a Shimadzu UV-2600 spectrometer (Shimadzu, Kyoto, Japan). *Saturnia pavonia* cocoons were obtained from worms reared in-house and spun under controlled conditions (see Appendix 1 for details). Spectra from *Saturnia pavonia* cocoons were recorded in diffuse reflection mode using an integrating sphere from 200 to 1400 nm (50000 to 7142 cm^{-1}).

6.3.3 Native silk preparation

Native silk feedstock from the posterior part of the middle division of the *Bombyx mori* silk gland were prepared and loaded in the rheometer as described in 2.1.1.2. *Attacus atlas* silk glands were extracted from worms reared in-house as described in Appendix 1.

6.3.4 High fidelity reconstituted silk feedstock preparation

The preparation protocol for high fidelity reconstituted silk feedstocks is described and schematised in Appendix 7, page YY.

6.3.5 Rheology and infrared measurements

Oscillatory, viscosity and *in situ* infrared measurements were performed using the Rheo-IR platform described in section 5.3.3 and 5.3.4. 6 RSF and 7 NSF samples were tested.

6.4 Results and discussion

6.4.1 Silk curing infrared spectra

As the first step of building the scaffold for cocoon construction, a confined silkworm spins figure of eight patterns whilst laying a silk mat on the substrate. To measure silk immediately after secretion, we exploited this instinctive animal behaviour. As shown in Figure 6.2, a silkworm will eventually spin a thread onto an attenuated total reflection (ATR) sensor embedded at the bottom of its cell. The silk measured is thus representative of the first secreted making the outermost layer of the cocoon, which has more sericin.[Chen2012a] The sericin gum coating the fibroin filaments bond threads to surfaces, ensuring good contact with the ATR sensor. The emerging evanescent wave (penetration depth >1 μm) probes

both the sericin and the fibroin filament. This experimental setup allowed the recording of spectra during and after secretion with time intervals limited by interferometer speed (0.25 seconds/scan). Hence it was possible to record infrared spectra a fraction of a second after secretion and continue acquisition of the same ~2 mm silk thread segment thereafter under controlled relative humidity (RH) and temperature.

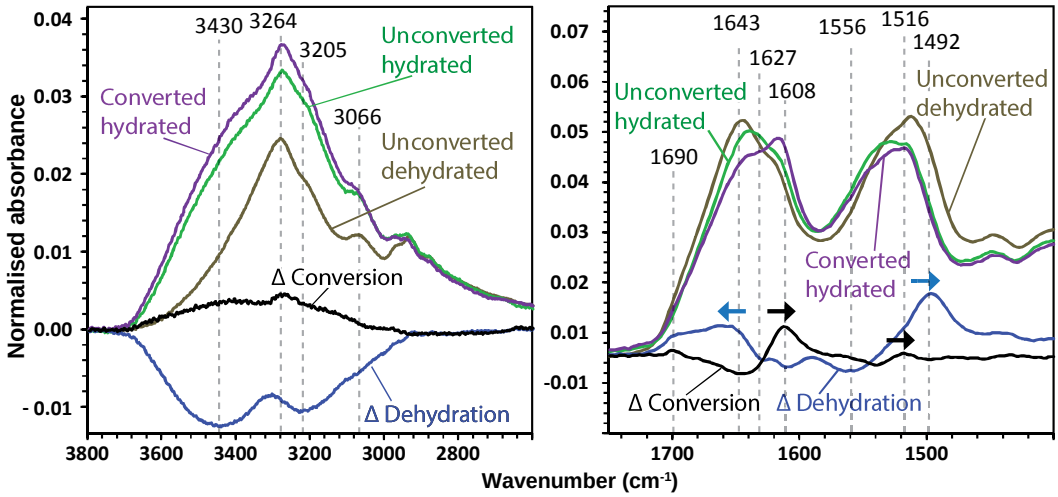


Figure 6.3 Infrared spectra between of *Bombyx mori* native hydrated unconverted (lime), unconverted dried (brown) and hydrated converted (purple) silk as well as the difference between them (blue and black curves). The blue arrows represent the direction of the amide I and II band shift caused by dehydration (reverse for hydration process) whilst black arrows point the direction of the conversion induced shift (irreversible process).

Figure 6.3 shows the infrared spectrum of *Bombyx mori* single silk strands collected shortly after secretion (green curve), similar to the spectrum of unspun native silk extracted straight from the silk gland (see Figure 5.4). By comparing the fresh fibre's infrared spectrum to known concentration standards in a partial least squares method (described in section 3.3.3), the secretion concentration was estimated to be 32 ± 5%. This value is 10% higher than the 22 ± 3% measured for native silk feedstock, but far from being completely dried.[Boulet-Audet2013] This result implies that silkworm silk loses most of its moisture by evaporation outside the body after secretion. However, the higher concentration measured also implies that a small fraction could have been recovered in the spinning duct. If the fibre is rapidly dehydrated with a high flow of dry air, the difference in extinction coefficient k

between protein and water will make the absorbance increase at most wavelengths below 1700 cm^{-1}.[Boulet-Audet2010]

The main impact of dehydration is a broad absorbance decrease at 3300-3400 cm^{-1} due to the vanishing water OH stretching vibration modes.[Max2009] As water is replaced by protein in the probed volume, the absorptivity decrease is less pronounced at 3264 cm^{-1} due to the increasing Amide A vibration mode of silk. At low frequencies, hydration has a strong effect on the water bending mode region around 1640 cm^{-1}, but also the neighbouring amide II region. As shown by the blue curve of Figure 6.3, losing bonded water molecules has difference spectra drastically different from free water. The dehydration decreased the 1556 cm^{-1} amide II component whilst increasing even more the peak at 1492 cm^{-1}, shifting the amide II band to lower wavenumbers and decreasing its intensity. This amide II downshift and the intensity decrease is attributed to stronger hydrogen bond network upon dehydration, weakening the N-H stretching vibration mode.[Myshakina2008] A smaller upshift was observed in the amide I region and could also be explained by the alteration of the hydrogen bonding network.

Before spinning, native silk feedstock has water molecules bounded to the fibroin's backbone, conferring mobility to the protein.[Porter2008; Porter2012; Porter2013] When spun, stressed silk loses its bound water allowing the rearrangement of its conformation into ordered β-sheets with a denser network of hydrogen bonds.[Porter2009] The resulting variability of order and disorder fraction could then represent a mean for the animal to modulate fibre property.

If a freshly spun fibre is exposed to a high humidity environment (>96% RH), it dries very slowly, resulting in distinct difference spectra (black curve of Figure 6.3). The infrared signature observed is typical of conformation conversion from β-turns and helices to β-

sheets observed in Figure 3.4 as well as Figure 5.4 (see Table 7.1 and Table 7.2 for band assignment). The formation of β-sheets gave rise to identifiable peaks at 3264, 1690, 1608 and 1516 cm^{-1}.[Moore1976;Muller1993;Garside2005;Taddei and Monti2005;Boulet-Audet2008] Hence, infrared spectroscopy gave us strong evidence that the conformation conversion process is not completed after secreted in *Bombyx mori* as more β-sheets are formed thereafter. The β-sheets content as secretion is small compared to what can be achieved using alcohol conversion (see Figure 3.7).

6.4.2 Effect of humidity upon silk secretion

Since water provides mobility for the protein to change its conformation,[Zheng1989; Jeong2006] we studied the effect of moisture on freshly spun silk. This was achieved by purging the silkworm's container with known relative humidity air at a given temperature whilst the silkworm was laying its silk mat on the substrate. The relative humidity content and air flow should then be directly proportional to the bonded water content.[Agarwal1997]

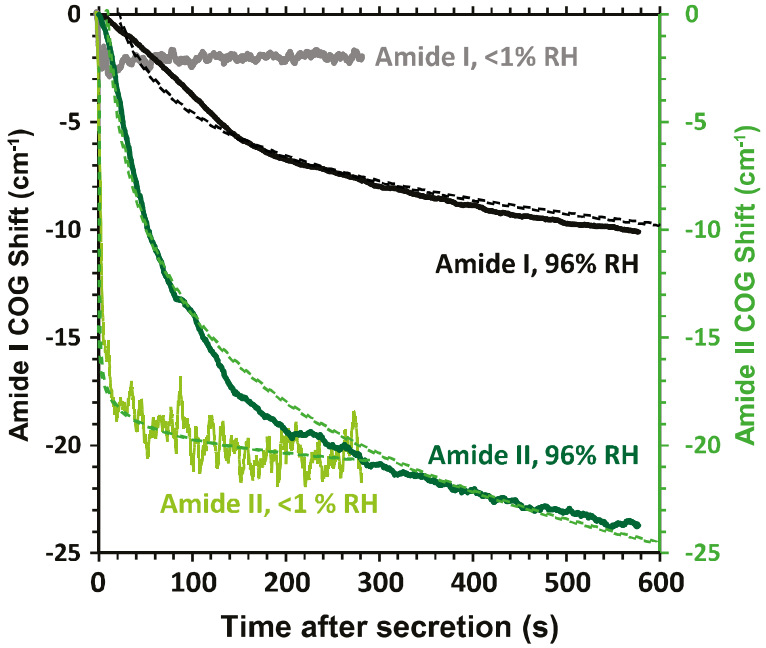


Figure 6.4 Centre of gravity of the amide I and II band as a function of time after secretion for a single *Bombyx mori* fibre spun at 1% relative humidity at ~5 L/min (light curves) and 95% relative humidity at 50 mL/min (dark curves). The dashed lines represent the fitting results of exponential functions.

Figure 6.4 shows the shift of the amide bands due to the effect of water vapour shortly after secretion. At high relative humidity (96% RH), they are both shifting slowly towards lower wavenumbers as the sample is continuing to convert without drying. The exponential fit of the Amide I band resulted in first order rate constant of 2.8 s^{-1} (R^2 = 0.91) whilst the fit of the amide II band gave a rate constant of 6.0 s^{-1} (R^2 = 0.95). The amide I band would take thousands of seconds to stop shifting as the spontaneous conversion process is slow at room temperature (see Chapter 4). In contrast, if we blew dry air (<1% RH) at high flow rate (~5 L/min) into the silkworm's container, a totally different behaviour is observable. Under such conditions, the centre of gravity of the hydration dependent amide II COG shifted towards lower wavenumbers before stabilising after only ~150 seconds as most of the water evaporated quickly. The fitting of the amide II band gave us a first order rate constant of 2.6 s^{-1} with R^2 = 0.64. As the centre of gravity of water's bending mode (1640 cm^{-1}) and amide I band of native silk (1643 cm^{-1}) are very close, this band will be less affected by dehydration than by β-sheet conversion. Since only a very small amide I downshift was

measured, we concluded that reducing silk's water content could thus decrease the protein mobility and prevent further conformation conversion. Consequently, our experiment provided evidence that the incomplete conversion process can be interrupted by drying silk after secretion. These partially spun fibres with lower β-sheet crystallinity content could thus present interesting properties. However, it is equally important to know which conditions are required to preserve their structure as humidity was found to have an effect on fibre mechanical properties, yield stress in particular.[Guan2011]

6.4.3 Effect of humidity of dried fresh silk fibres

These observations led us to hypothesise that the effect of storage humidity on the mechanical properties could be the result of resuming β-sheet crystallisation. To test this hypothesis, moisture was reintroduced into the container after the threads were spun and dried onto the ATR sensor. Fibres were rehydrated slowly under a humidity ramp from 1 to 96% RH at 5% RH/min. By slowly increasing the water vapour content in the environment, the equilibrium water content in the fibre's amorphous region is expected to increase proportionally.[Agarwal1997]

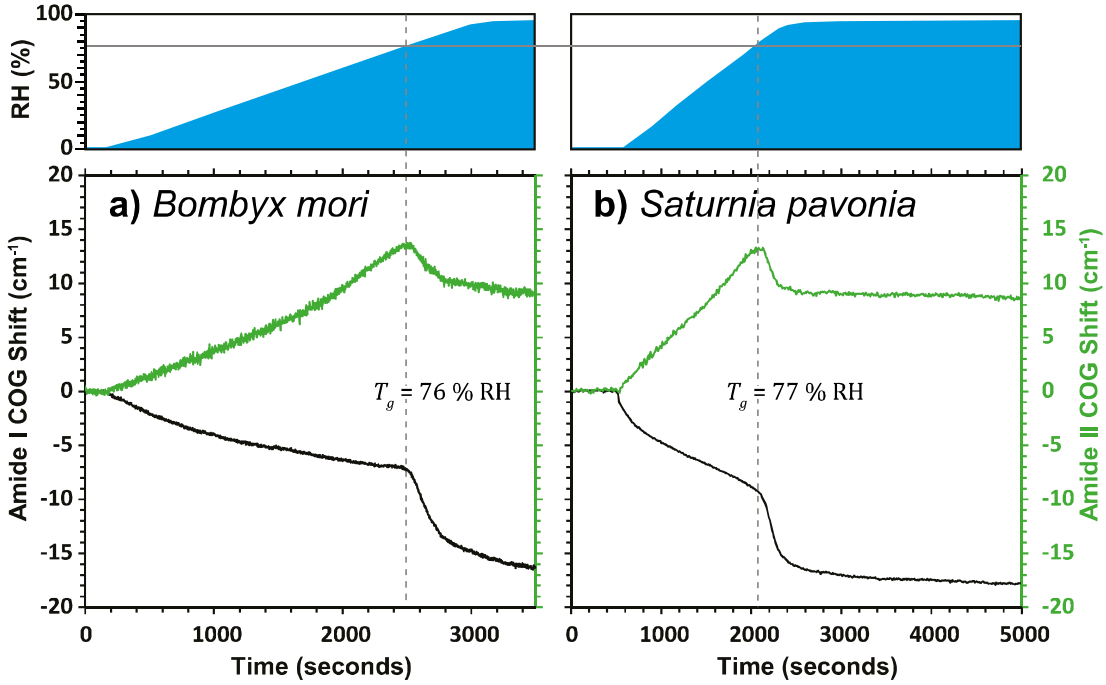


Figure 6.5 a) Rehydration kinetics of few dry spun fibres under a linear humidity increase ramp (1 to 95% RH), infrared spectra and centre of gravity of the amide bands for *Bombyx mori*. b) *Saturnia pavonia.*

Like freshly spun silk, Figure 6.5a shows that dried fibres are also very sensitive to humidity as the amide bands will start to shift shortly after moist air is introduced into the container. As illustrated by the blue arrows on Figure 6.3, hydration has the opposite effect for the direction the amide I and II band shift. The amide I shifted to higher wavenumber whilst the amide II moved to lower frequencies until a critical content of bonded water is reached. Marked by a dashed line, the infrared spectroscopy revealed that β-sheet formation is resumed around 76% RH for *Bombyx mori*. The same behaviour is observed for *Saturnia pavonia* silk as shown on Figure 6.5b, indicating that the phenomenon is not specific to the domesticated silkworm species. At this RH value the water content calculated from the infrared spectra is 9 ± 4 %DW, comparatively lower than the 21 ± 2 % measured by Agarwal et al. at comparable RH.[Agarwal1997] At this point, the amide I band started to drift faster to lower wavenumbers whilst the amide II band shift changed direction from an upshift to a downshift as conversion outweighed the hydration. The equilibrium water content in the fibre must have allowed enough mobility for the self-assembly into β-sheets. At (72 to 80%

RH), the glass transition temperature T_g is also 25 °C when measuring the mechanical properties of silk fibres.[Fu2009] In addition to decreasing the tensile modulus, our results imply that reaching the T_g (by increasing the relative humidity) also allowed the conformation transition to resume in partially converted silkworm silk fibres.

Hydration reversibility

To investigate the reversibility of the process, we rehydrated partially dry spun fibres by increasing the humidity to 40% RH (below its T_g at 25 °C) before drying the fibre again with dry air. As plotted in Figure A.10 of Appendix 2 (page W), the amide I and II centre of gravity both went back to their initial value after increasing the humidity to 40% RH and back to <1% RH. Consequently, this result confirms the reversibility of the water intake. It also implies that no additional β-sheets were formed by remaining under T_g for silk. However, increasing the humidity to lower the T_g below room temperature and then back to <1 %RH resulted in lower amide I and II band position than before as the β-sheet conversion is irreversible.[Boulet-Audet2011; Boulet-Audet2013] To assess if drying silk filaments for an extended period of time can prevent the resuming of the β-sheets conversion, we kept the sample at <1% RH for two days. These fibres also had their protein conformation conversion resumed by reintroducing water vapour into the system (see Figure A.10b, page W). As we proved that rehydration can resume the conversion of silk fibres, it explains the importance of controlling storage conditions for preserving dry spun silk's desirable properties.[Reed2011]

6.4.4 Wild silk curing

Darkening resulting from wild silk tanning

In addition to affecting mechanical properties, humidity is also known to cause coloration change for certain wild silk species. Previous studies revealed that Saturnid silks, like the one produced by *Saturnia Pavonia*, are normally secreted white, but darken when exposed

to humidity.[Levrat1899; Brunet1974] The untanned white silk was found to be less stable than the darker tanned sort under chaotropic conditions. Small quinone molecules were suspected to be at the origin of the darker coloration resulting from the crosslinking of the protein chain through tyrosine residues.[Brunet1974] The absence of such molecules in some strains of *Bombyx mori* silk could explains why their cocoons remain pale under high humidity. To ensure that the effect observed was not due to other secretions from the silkworm whilst spinning its cocoon, a dry spun white piece of cocoon was wetted with only demineralised water. We then recorded the UV-vis spectra of a *Saturnia Pavonia* silkworm cocoon disc over 8000 seconds.

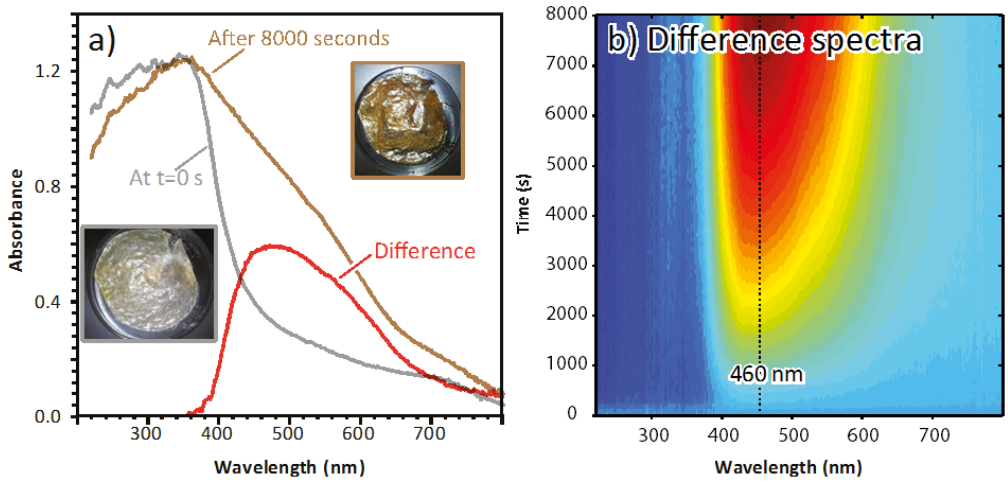


Figure 6.6 a) *Saturnia pavonia* cocoons UV-vis spectra of a dry spun silk cocoon disk before (grey) and 8000 seconds (brown) after expose to humidity. The difference is shown in red b) Difference spectrum as a function of time.

Figure 6.6a shows the stunning difference between the dry spun *Saturnia pavonia* silk before and 8000 seconds after being wetted. The difference spectrum (red curve) gave us a maximum absorbance change around 460 nm (blue). However, the absorbance increased across a broad range of wavelengths (400 to 650 nm) reflecting only a small fraction of the longer wavelengths towards red, giving a dark orange or brown coloration. The tanning

kinetic presented in Figure 6.6b suggests that the process was still progressing when the experiment was stopped.

β-sheet crystallinity in tanned silk

The comparable timescale involved for tanning and conformation conversion led us to hypothesise that these two phenomena are associated. We investigated the potential link between tanning of wild silk and β-sheet content by collecting infrared spectra of white untanned cocoons spun dry and dark brown cocoons spun in a wet environment over several days.

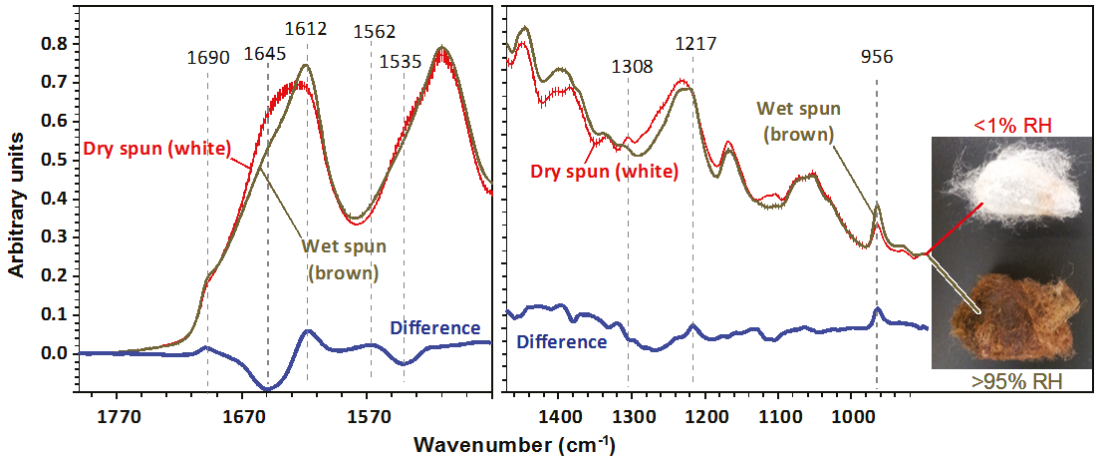


Figure 6.7 a) Arbitrary unit Infrared spectrum of dry and wet spun *Saturnia Pavonia* cocoons (n =30). The absorbance was normalised to the integrated area between 1800 and 900 cm^{-1}.

Figure 6.7 shows the average spectra collected for the lightly tanned and heavily tanned silks. Our results demonstrated that dark cocoons had higher $(A)_n$ β-sheet content with stronger peaks at 1690, 1612 and 956 cm^{-1}. Coincidentally, peaks at 1645 and 1308 cm^{-1} associated with lost precursor structures were weaker. This observation strongly suggests a relationship between both processes. Tanning requires both humidity and oxygen to take place[Brunet1974] whilst β-sheet conversion also requires water but can easily happen in closed cell without air and thus oxygen as shown in Chapter 4. A method to deconvolute both

processes is to induce the conformation conversion in an inert environment before tanning the wild silk with wet oxygen.

Therefore, these insights led to the hypothesis that tanning requires the protein to adopt a β-sheet conformation in order to be tanned by small molecules in the presence of oxygen. It would then make sense from a biological perspective if the tanning process is only allowed by the conformer present in spun silk as it would prevent premature *in vivo* tanning which could disable spinning.

To investigate the reason underlying a final instar *Attacus atlas* silkworm's inability to spin, we dissected the animal and extracted its silk glands.

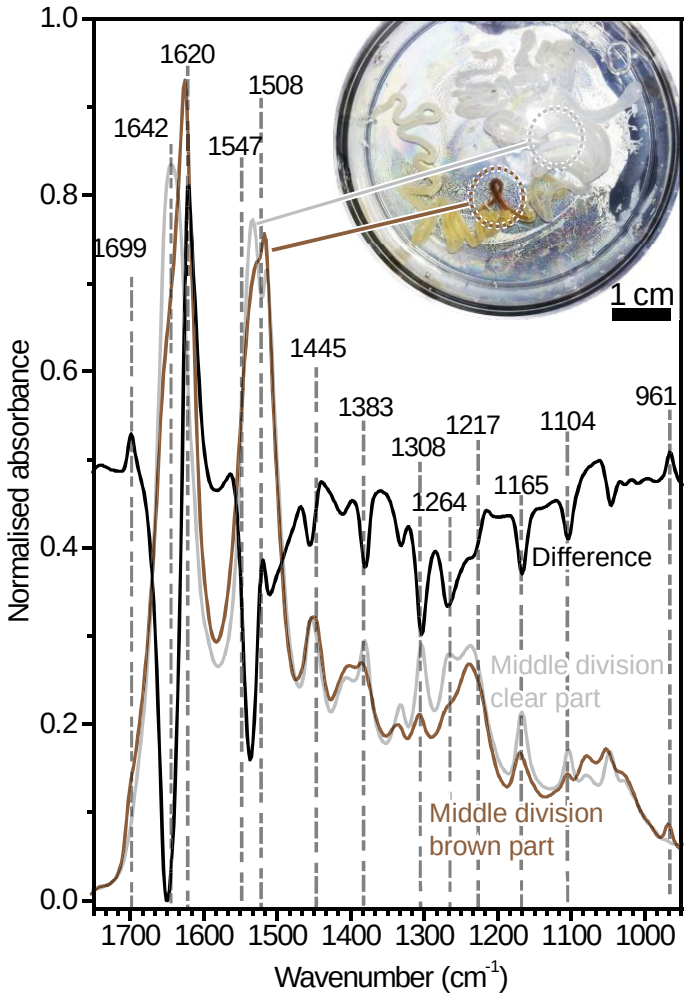


Figure 6.8 Arbitrary unit infrared spectra of dried dope from *Attacus atlas* from the middle division of the silk gland. The absorbance was normalised to the integrated area between 1800 and 900 cm^{-1}.

The infrared spectra of the dried dark silk portion were collected along with the normal clear silk feedstock extracted in the vicinity. As shown on Figure 6.8, their infrared spectra were radically different, the dark silk appearing to have high β-sheet content with strong peaks at 1699, 1620 and 961 cm^{-1} whilst the clear silk feedstock appeared totally unconverted. Since these feedstock portions were never spun out of the animal, environmental effects can be ruled out especially as the entire gland had the same expose to oxygen. This unusual case provided additional circumstantial evidence strengthening our hypothesis that tanning requires the protein conformation conversion and not just the presence of oxygen.

6.4.5 Silk *in situ* solubilisation

As the dry spun silk appears to have lower β-sheet content, it should require less energy to disrupt the hydrogen bonding network. We tested the propensity of dry spun *Bombyx mori* fibres to be solubilised by 9M LiBr at 25 °C and monitored the process *in situ* using ATR-IR.

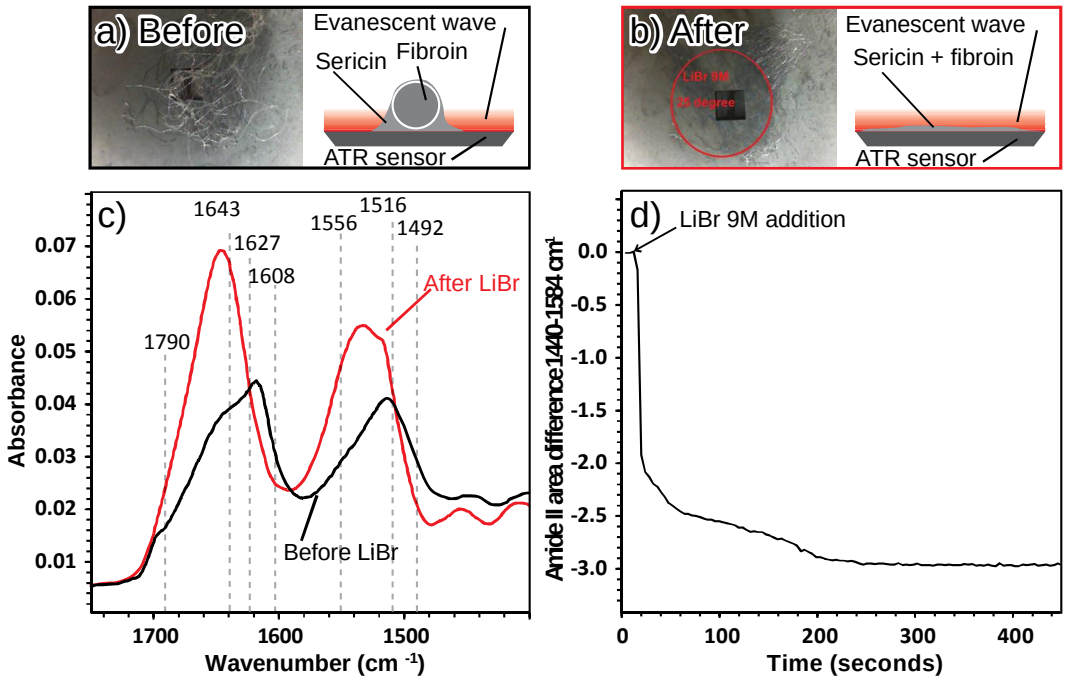


Figure 6.9 a) Dry spun silk before solubilisation b) After solubilisation c) ATR-IR spectra before (black) and after (red) adding LiBr. d) Amide II band area of dry spun silk fibres under LiBr 9M at 25°C.

Figure 6.9a and b clearly show that fibres submerged in concentrated LiBr were solubilised at room temperature leaving only traces on the bottom plate. On the other hand, the fibres that were outside the area covered by the LiBr droplet (red circle) remained intact. As shown on Figure 6.9d, immediately after applying a droplet of LiBr 9M on the fibres, the area of the amide II band started to decrease as silk protein was solubilising. It took around 300 seconds for the reaction to equilibrate at room temperature. Once the chaotropic agent was removed and the ATR sensor dried, Figure 6.9c (red curve) shows that the LiBr was able to disrupt silk's conformation at room temperature removing β-sheet structures. However, the absolute absorbance intensity increased in the process. We attribute this rise

to the increase surface covered by the molten fibre and dried on the ATR crystal. In addition the lower amide II to I ratio indicates weaker anomalous dispersion that is representative of a thinner silk film.[Boulet-Audet2010]

6.4.6 Controlled spinning reconstituted silk flow properties comparison

Since the less converted dry spun fibres appeared to be easier to solubilise, we investigated the effect of using these fibres on the standard reconstitution process. As a first observation, demineralised water at room temperature can dissolve the sericin gum directly from dry spun fibres immersed in it. The removal of most of the sericin gum (< 1 %) was confirmed by infrared spectroscopy based on the sericin peaks listed in Table 7.1. Once degummed and dried again, the resulting fibres could be solubilised under much milder conditions, 5 minutes at 70 °C in 9M lithium bromide at 250 mg/mL. Successive dialysis ensured that most of the lithium bromide was removed which was verified by measuring the resistivity of the solution (< 0.5 μScm^{-1}) using a resistivity meter. Once concentrated to >20 % dry weight, the resulting solution was totally clear and much more viscous than reconstituted silk solutions made from aged cocoons with unknown spinning history (Lo-Fi used in Chapter 3 and Chapter 5). To confirm this observation, the flow properties of our new reconstituted silk feedstocks were measured after the completion of the dialysis to remove the chaotropic agent.

Firstly, an oscillatory sweep was performed as a non-damaging test to determine the response of the fibroin to input energy at different rates as performed in section 5.4.1 and described in section 2.2.4. Using this test, we then compared native silk feedstock (NSF) to

our new dry spun High Fidelity Reconstituted Silk Feedstock (Hi-Fi RSF) of comparable concentration (22 ± 3 %).

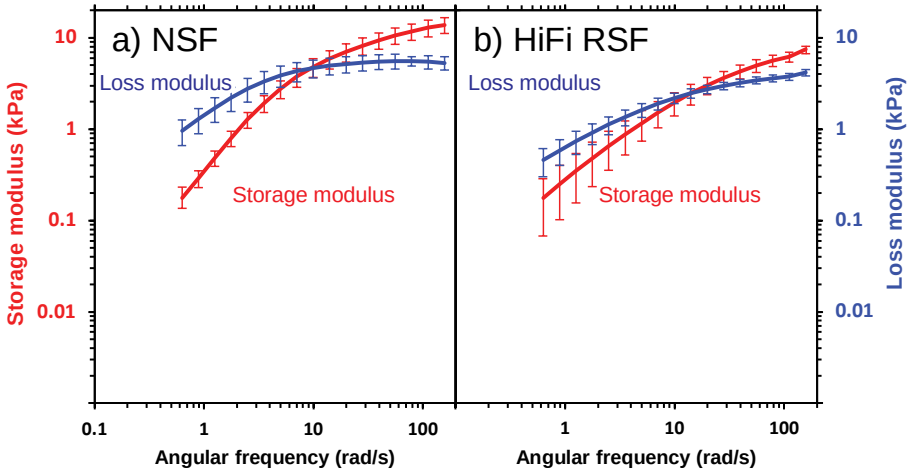


Figure 6.10 a) Native silk feedstock average storage and loss modulus b) High fidelity reconstituted silk feedstock at 22 ± 3 %. The red lines represent the storage modulus G'' whilst the blue line is the loss modulus G''. The error bars represent the standard deviation of the sample probed.

Figure 6.10a shows that NSF behaves like a non-Newtonian polymer melt with a moduli non-linearly dependent on the frequency,[Ferry1980] always showing a crossover point where G' = G'' .[Holland2006; Holland2007; Moriya2009] This crossover occurred at 10 ± 3 rad/s (1.6 ± 0.4 Hz), giving a relaxation time $\tau_p = \omega^{-1}$ of 0.6 ± 0.1 seconds, consistent with previous studies.[Holland2006; Moriya2009; Boulet-Audet2013] Unlike the standard reconstituted silk presented in Figure 5.3 however, our Hi-Fi RSF also showed the same feature at similar frequency (15 ± 6 rad/s or 2.5 ± 0.9 Hz). This crossover point has never been reported for any reconstituted silk analogues and only once for recombinant spider silk solution.[Rammensee2006] Hence, it represents strong evidence of their ability to store mechanical energy. At high frequencies, the plateau modulus ($G_N = G'|_{\omega \to 0}$) is a parameter representative of the sample's potential for storing elastic energy.[Ferry1980] For native silk, the average plateau modulus G_N is 13 ± 3 kPa, very close to the 7 ± 1 kPa value measured for our Hi-Fi RSF, and orders of magnitude higher than the 0.008 ± 0.006 kPa measured for standard Lo-Fi RSF presented in

Figure 5.3. Hence, considering the experimental error, NSF's and Hi-Fi RSF's dynamic flow properties are remarkably similar.

To test the flow properties of silk, a viscosity test using an exponential step shear ramp was performed on NSF and Hi-Fi RSF to evaluate the response to a linear shear stress and the zero shear viscosity η_0. Simultaneously, the feedstock's conformation and orientation were monitored by an ATR-IR sensor as described in section 5.3.3.

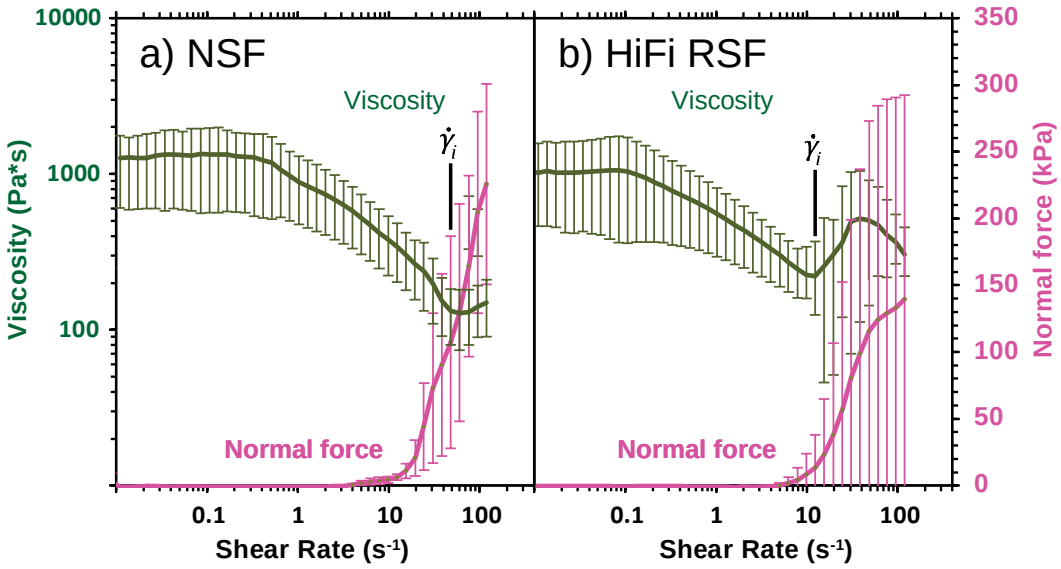


Figure 6.11 a) Native silk average viscosity (green curves) and normal force (magenta curves) for native under an exponential shear ramp. b) High Fidelity Reconstituted Silk Feedstock. The error bars represent the standard variation of the different tests.

At low shear rates, Figure 6.11 shows an initial viscosity plateau for NSF giving a zero shear viscosity (η_0) of 1.3 ± 0.6 kPa·s whilst Hi-Fi RSF had an average of 1.0 ± 0.5 kPa·s, i.e. they were within the experimental error. On the other hand standard RSF prepared according to section 5.3.1 gave only $\eta_0 = 0.09 \pm 0.05$ kPa·s (see Figure 5.4). At low shear rates, the energy input can make the system flow on a macroscopic scale, but is insufficient to perturb the protein conformation as no changes in the infrared spectra occurred. In this plateau region, no changes in the first normal force difference N_1 is detectable. Thereafter once the shear rate become higher than the inverse of the relaxation time $1/\tau_p$ = ~2 s^{-1}, the

viscosity of both NSF and Hi-Fi RSF started to decrease as the chains started to align (see Figure 5.5). As for most non-Newtonian polymer melts, this shear thinning is commonly associated with the reduction in internal friction when sheared faster than its relaxation time.[Suzuki1969; Moriya2009] During the shear thinning region, the first normal force N_1 started to rise with the increasing elastic recoverable strain in both native and Hi-Fi RSF silks.[Porter1995] Because of the non-zero N_1 value, linear viscoelastic theory cannot predict the zero shear viscosity from the plateau modulus ($\eta_0 \neq G_N \bullet \tau_p$). The recoverable strain is a reliable indicator of the feedstock's "spinnability", which is lacking for standard RSF presented in Figure 5.5. Another important indicator of the feedstock's quality is its ability to initiate conformational changes under shear stress.

6.4.7 Compared silk shear sensitivity

As demonstrated in Figure 5.4, stress perturbation is essential to discriminate between silk feedstocks with distinct flow properties since their static spectra are very similar. Hence to monitor the feedstock's protein conformation during shear, infrared spectra were collected during a viscosity test and the centre of gravity of both amide I and II bands were calculated.

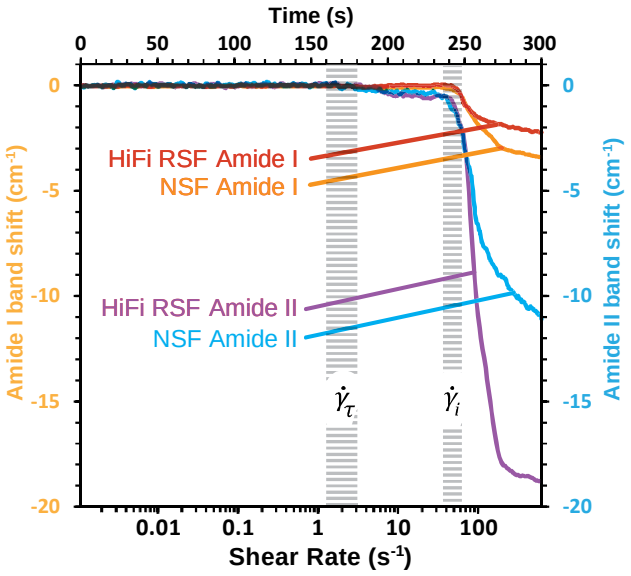


Figure 6.12 Native Silk Feedstock (NSF) and High Fidelity Reconstituted Silk Feedstock (Hi-Fi RSF) amide bands centre of gravity of under an exponential shear ramp from 0 to 150 s^{-1}.

By monitoring the centre of gravity of the amide bands, infrared spectroscopy reveals that both NSF and RSF Hi-Fi have similar sensitivity to shear stress with shifts of the amide bands once the shear rate reaches a critical value $\dot{\gamma}_i$. As shown in Figure 6.12, the viscosity abruptly increases at the same time as the bands associated with the β-sheet conformation are rising, linking the shear thickening to the conformation change.[*Moriya2009; Boulet-Audet2013*] Such a shear-induced conversion occurred for both our Hi-Fi reconstituted and native silk at comparable concentration (22 ± 3 %) whilst no shifts were detected for standard RSF under the same stress profile (see Figure 5.5). As shown in Figure 3.8, lower quality reconstituted silk fibroin at a much higher concentration is required to obtain such shear sensitive material. Consequently, the viscosity, normal force and the mid infrared vibration modes all suggest that our silk Hi-Fi analogues have comparable ability to undergo shear-induced β-sheet formation. It implies that both materials would have comparatively high cohesive energy density of hydrogen bonding.[*Porter2005*]

6.5 Conclusions

The approach adopted in this chapter of controlled environment during spinning allowed *Bombyx mori* and *Saturnia pavonia* silk fibres to be immediately measured by ATR-IR after secretion, revealing that silk is far from being completely dry and far from being completely converted once outside the worm. At this point, we found that secreted silk still contains around 68 % water. It thus suggests that a small fraction of the feedstock's water content has been recovered in the spinning duct. It also showed that the conversion process is still on-going. Therefore, it offers a time window during which *ex vivo* processing is possible as the fibre water content would be above its T_g, explaining why post-drawing can be used to modulate silk fibres' mechanical properties. Since water is essential to the protein's mobility, we found that β-sheet formation can be interrupted by rapidly drying the freshly secreted silk fibres. Subsequently, silk's conversion can also be resumed once enough water is reintroduced to bring silk above its T_g. Thus getting *Bombyx mori* silkworms to spin under dry conditions can result in cocoons with a lower degree of β-sheet crystallinity if they are kept dry afterwards. Our results thus corroborated previous studies highlighting the importance of storage humidity for silk's properties but more importantly raised the possibility of modulating a fibre's properties post-spinning.[Reed2011]

This process is not unique to *Bombyx mori* silkworm silk as it was also observed for dry spun silk from a wild silk species, *Saturnia pavonia*. Previous studies found that some wild silks can change colouration in a wet environment in the presence of oxygen.[Brunet1974] For wild silks in presence of oxygen, we found that tanning only occurred for converted silk feedstock with β-sheets conformation. However, the opposite is not true as conversion can occur without oxygen. Hence, our results led us to believe that wild silk's tanning process requires both stress-induced β-sheet structures and oxygen to take place. The lower

crystallinity of untanned dry spun silk also appears to make these silks easier to solubilise with chaotropic agent ionic liquids, as previously reported.[Brunet1974] Under milder solubilisation conditions, the reconstituted silk feedstock made from those feedstocks had flow properties remarkably similar to native silk feedstocks presumably because of the higher protein molecular weight of the lower fraction of protein denaturation occurring during reconstitution. Our High Fidelity Reconstituted Silk Feedstocks (Hi-Fi RSF) had comparable plateau modulus G_N, zero shear viscosity η_0, recoverable strain-induced normal force N_1 and was capable of shear triggered conformation conversion under similar flow stress. Based on these criteria we propose that our Hi-Fi RSF is the best produced to date.

The ability to control the degree of β-sheet conversion through post-spinning environmental conditions control, has important repercussions as it could cut the energy needed for degumming fibres by more than 50% as the boiling of cocoons is no longer required.[Vollrath2013a] Moreover, our mechanical degumming would no longer require chemicals such as Marseille soap or sodium carbonate. From its liquid form, just like synthetic polymer solutions, reconstituted silk solutions can be processed in many ways to form liquid, fibres, films, hydrogels, foams, sponges, films, micelles, tubes or powders.[Vepari2007; Hardy2008] Consequently, we expect our Hi-Fi RSF, which is akin to native silk, to outperform conventional RSF liquid properties, but also to outperform the resulting solid materials. Subsequently these feedstocks could be used in a wide variety of applications, with potential for bone matrices,[Collins2009] cartilage scaffolds,[Gellynck2008] neural conduits,[Yang2007] sutures,[Halsted1913; Bunning1994] optical wires,[Bunning1994] food sensors,[Omenetto2010] and drug delivery systems.[Dandu2007; Omenetto2010]

Chapter 7

The chemical diversity of silk revealed by infrared spectroscopy

The spinning process studied in the previous chapters focused on *Bombyx mori* silkworm silk as it provides large quantities of native liquid silk feedstock. This domesticated species is only one amongst thousands of silk producing arthropods. Thus, it raises an important question: is *Bombyx mori* a representative model for silk spinning? To answer this question and explore the chemical diversity of silks, the infrared spectra of several unspun feedstocks as well as cocoons from tens of species were compared. This chapter is the result of the data mining of the infrared spectra from all these material sources cataloguing more than a thousand spectra collected by several users of the Oxford Silk Group's IR spectrometer, including Maxime Boulet-Audet, Fujia Chen, Julia Van Campen, Alexander Greenhalgh and Addis Akebede. In addition, Chris Holland, Fritz Vollrath and Ann Terry edited this chapter. In addition to single variable analysis of component markers, multivariate analysis was performed on the dataset helping to identify outlier species and grouping silks in different classes which were later compared to phylogenetic data. This approach revealed that infrared spectroscopy with multivariate analysis could be phylogenetically informative and provide a new tool for taxonomists to systematically classify species.

7.1 Abstract

Using new demineralisation techniques developed by Gheysens et al.,[Gheysens2005; Gheysens2011b] it is now possible to reel silk from the cocoons of wild silkworm species. Amongst the thousands of wild silks available, the challenge is to identify which one would best serve a specific application allowing the sericulture industry to tap into the remarkable biodiversity of silkmoths. This study presents a high throughput multivariate analysis screening method based on the infrared spectra of native silk feedstock and cocoons. Using silk's chemical fingerprint, 37 species were classified and outliers identified based on their dissimilarity. Based on characteristic vibration frequencies, the origin of the chemical difference between these species was linked to their morphology and their phylogeny. This approach proved a convenient and robust alternative to gene sequencing, providing a new route to both biological and material classification of silks.

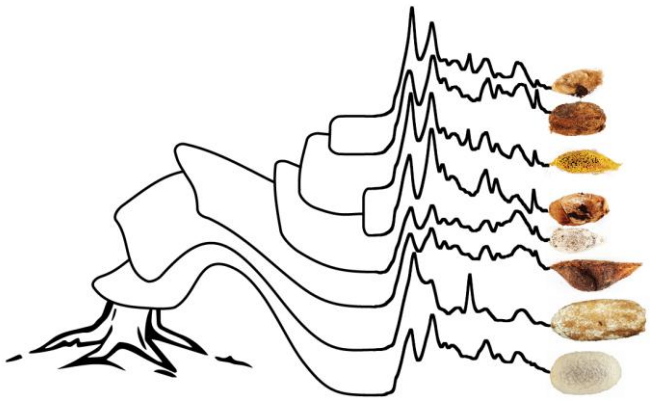


Figure 7.1 Graphical abstract for the "The chemical diversity of silk revealed by infrared spectroscopy" authors: Boulet-Audet, M. Vollrath, F. and Holland, C. manuscript in preparation for submission in Biomacromolecules.

7.2 Introduction

Product of an intensive human selection for thousands of years, *Bombyx mori* and *Bombyx mandarina* have a close common ancestor.[Good2009] The mulberry silkworm, *Bombyx mori* is

one of only few domesticated insect species. Individuals for breeding were chosen based on cocoon characteristics sought by weavers: ease to remove the sericin gum, dyeability, long fibres, feel on skin and whiteness. However, silkworms evolve to spin cocoons for protecting themselves during pupation. Their main biological function is to house the larvae during pupation. This non-woven composite structure[Chen2010a] regulates gases and humidity,[Tuskes1996; Danks2004; Roy2012; Horrocks2013] but also protects the pupae from predation,[Ishii1984] micro-organisms,[Franceschi2005] as well as from the environment.[Waldbaue.Gp1967; Chen2012b]

From rheology measurements, Holland et al. showed that the liquid silk feedstocks flow properties represents a good example of evolutionary convergence.[Holland2006] However, hundreds of thousands of years of differing constraints have resulted in a rich biodiversity of silk cocoons.[Chen2012b] The morphological features of cocoons vary greatly across species,[Chen2012c] but so does the environment in which they are used.[Van der Kloot1953b; Van der Kloot1953a; Brunet1974] Since cocoons are made of a single silk fibroin strand, the principal cause of the macroscopic structure differentiation is the animal's behaviour during construction. Cocoons have a wide range of porosity, from loose mesh to full shells, with or without an exit opening.[Chen2012c] Additionally, some species attach their cocoon to the substrate with a stalk whilst others do not.[Yagi1926] Cocoons are not made only of filaments. Fibroin threads are coated with sericin proteins performing the role of a resin, as found in fibrous composite materials.[Chen2010b] Thanks to their remarkable mechanical properties,[Gosline1986; Shao1999; Shao2002; Boulet-Audet2008] silk fibroin filaments have higher commercial value and have attracted more interest than the cocoon's binding resin. In addition to the proteins produced by the silk glands, some silkworms spread a liquid excretion rich in calcium oxalate onto their cocoon during the construction, hardening and making it toxic to prevent predation.[Takahash.Sy1969; Teigler1972b; Arnott2000; Franceschi2005; P.2007; Gheysens2011b; Chen2012c] This feature can provide an evolutionary advantage to the pupae but makes some wild silk cocoons

challenging to unravel for textile applications. As long fibres cannot be easily obtained from those wild species cocoons, their commercial value is limited. Fortunately, a new technology developed by Gheysens et al. enabling the removal of those crystals permits the unravelling of cocoons previously thought unreelable.[Gheysens2011b; Knight2012]

Compared to the domesticated *Bombyx mori*, relatively little is known about the thousands of other wild silkworm species available.[Scoble1999] The challenge is to find an efficient way of closing the knowledge gap between domesticated and wild silks. Although a useful technique, fibre tensile tests produce variable results and is very time consuming as cocoons need to be reeled first.[Gheysens2011b; Chen2012b] On the other hand when molecular structure properties are paramount, biochemical methods such as silk protein sequencing offer valuable information such as protein size,[Mita1994; Inoue2000; Hwang2001; Sezutsu2007] residue patterns promoting cell adhesion[Navarro2008] and propensity to fold.[Dobson2009] Fibroin protein sequencing also reveals the primary structural diversity of silk. Across species, silk protein sequences have numerous possible permutations leading to varying amino acid content.[Hwang2001] However only a handful of fibroins have been sequenced and indexed, leaving many potentially useful silk primary sequences unknown. In addition, this method often results in partial sequencing of a single fibroin protein leaving the other compounds present in silk cocoons unaccounted for.

To complement biochemical methods, several spectroscopic and scattering techniques are commonly used to study silk proteins. Amongst them, the combination of infrared spectroscopy with attenuated total reflection (ATR) is particularly well suited for studying this material as it can measure rough solids as well as turbid concentrated protein solutions.[Boulet-Audet2011] In addition, ATR-IR can selectively probe the surface of the inside and outside layer of a silk cocoon, providing localised composition information.[Chen2007; Chen2012a]

With minimal sample preparation, this technique can provide information on the level of crystallinity,[Boulet-Audet2008] the fibroin secondary structure,[Goormaghtigh2006] the water content,[Boulet-Audet2011] the amount of sericin,[Teramoto2003] calcium oxalate[Gheysens2011b; Chen2012b] and carbohydrate content[Schulz and Baranska2007;Lu2011] as well as the presence of certain amino acid side chains.[Barth2000b] When combined with multivariate analysis, infrared spectrometry can be used to discriminate complex chemical mixtures based on their chemical fingerprints. For instance bacterial species,[Kansiz1999; Preisner2007; Bosch2008] human hairs types,[Panayiotou1999] and even coffee bean varieties[Briandet1996] can be discriminated using this approach.

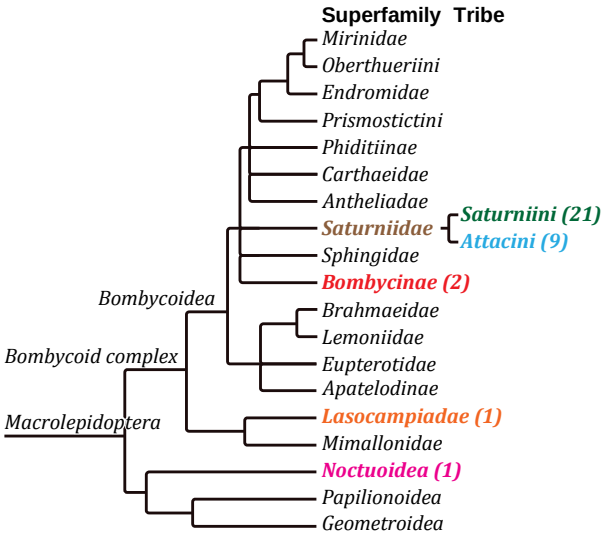


Figure 7.2 Summary of higher-level relationships of the superfamily related to species studies adapted from Regier et al.[Regier2008a] The number in bracket represents the number of species measured in the superfamily.

For these reasons, we evaluated the potential of ATR-IR with multivariate analysis as a high-throughput screening method to classify silk's diversity and identify species of interests. To separate contributions to the spinning process from the post-treatment of silk, 6 species' unspun feedstocks across the Saturniini and Attacini tribes were analysed. As cocoons are easier to source, it was possible to compare spun silk from 37 different species belonging to the superfamily Saturniidae, bombycinae, Lasocampiadae and Noctuoidea on Figure 7.2. Although the samples did not cover all the Lepidoptera superfamilies, this study represents the largest chemical interspecies comparison of silks to date. Thereafter, the spectroscopy

based classification was compared to phylogenetic data from protein coding nuclear genes.[Regier2002;Regier2005;Regier2008;Regier2008;Chen2012] Although the genes compared did not code silk proteins, the analysis revealed a close relationship between the relative dissimilarity between these genes and the chemical composition of Lepidoptera silk. Hence this method could represent a powerful but straightforward hierarchical classification tool for taxonomists to help resolving some of ambiguity in the relationships of Lepidoptera. For instance, it could help lifting the contention surrounding the tribe classification of *Antherina suraka* in the Saturnidae family.[Oberprieler1997]

Simultaneously, the screening analysis also highlighted outlier species producing silk with unusual chemical composition and provided insights into their causes. It was possible to identify which wild silks amongst those measured are the closest to spider dragline silk and could thus present desirable properties. This study demonstrated the potential of infrared spectroscopy as a screening technique to reveal silk's diversity and pinpoint interesting species for further characterisation and consideration for exploitation for high performance fibres.

7.3 Experimental method

7.3.1 Native silk feedstock preparation

Native silk feedstock was extracted from the silk glands of mature silkworms. 6 key species were chosen for study to overlap the species probed by cocoons disks. All wild silkworm eggs were purchased from Worldwide Butterflies (WWB, Dorset, UK). *Actias luna, Antheraea yamamai, Attacus atlas, Saturnia pavionia* were fed with Walnut (*Juglans regia*), Hawthorn (*Crataegus monogyna*), Privet (*Ligustrum vulgare*) and Hawthorn (*Crataegus monogyna*), respectively until the larvae started spinning their cocoon (see Appendix 1 for

more details). Final instar *Bombyx mori* worms fed with white mulberry leaves (*Morus alba*) were purchased (Padova, Italy) for native feedstock extraction. *Nephila edulis* major ampulate glands and dragline were obtained from mature female spiders fed with *Drosophila* and reared in-house under controlled conditions.

7.3.2 Silk cocoon preparation

Bombyx mori and *Gonometta postica* silkworm cocoons were bought from Icipe (African Insect Science for Food and Health) in Kenya. 34 other cocoon species were purchased from WWB, the species chosen represented the four families across the Lepidoptera. At least four 3.5 mm round cocoon disks were cut from each cocoon using a metal punch for analysis by IR. The innermost and outermost layers of those disks were measured by collecting at least 18 spectra from each species for a total of 1185 spectra for the 37 species studied.

7.3.3 Spectral acquisition and treatment

A Nicolet 6700 FTIR spectrometer equipped with a MCT-A liquid nitrogen cooled detector (Thermo Scientific, Madison, WI) was used using a Golden Gate single bounce diamond ATR accessory (Specac Ltd., London, UK). It allowed us toacquire spectra at a 4 cm^{-1} resolution for wavenumbers from 500 to 6000 cm^{-1}. 32 to 64 scans were averaged at a 5.06 cm/s mirror speed. Although the fibres in a cocoon sample are randomly oriented, spectra were collected with the IR beam polarised perpendicularly to the plane of incidence (*s*) with a zinc selenide holographic wire grid polarizer (Thermo Scientific, Madison, WI). The ATR diamond's internal reflection element (IRE) had a refractive index of 2.417 and an angle of incidence of 45°. For this configuration, the evanescent wave emerging out of the IRE could probe around 1 µm deep into the sample, the penetration varying with the

wavelength.[Harrick1967] The evanescent wave only probes the surface with a penetration depth of 1 um and thus only the inner and outer surface could be measured. The liquid state of native feedstock spectra ensured a good contact with the IRE for date collection. As the cocoons have an inherent roughness superior to tens of microns, an anvil was used to press on the cocoon disks to ensure a good contact with the IRE. For acquisition consistency, the pressure applied on cocoon disks was kept to the minimum necessary to obtain an absorbance of 0.1 units for the amide II band. By aiming at keeping the absolute absorbance consistent the anomalous dispersion of the refractive index would be comparable for each spectrum collected.[Boulet-Audet2010] Before each measurement, the crystal was cleaned with wet tissues and demineralised water before a new background was acquired. This method helped compensating for the detector's signal fluctuations as well as preventing cross contamination between measurements.

In order to process the vast quantity of spectra collected, the operations carried out on each spectra were automated using OMNIC 7.3 controlled by a VBA code using OMtalk dialogue protocol (Thermo Scientific, Madison, WI). An offset was first subtracted to all spectra as calculated from the average of the 1950 to 1900 cm^{-1} region. Spectra were then normalised using the integrated absorbance from 1900 to 800 cm^{-1} to compensate for absolute signal variations incurred by differing cocoon contact with the IRE sensor. An ATR correction was applied to simply correct for the evanescent wave penetration depth dependency on the wavelength.[Harrick1967] No liquid water spectrum was subtracted from the native feedstock's solution spectra. For the single component analysis, the relative area of each peak integrated was calculated by subtracting a linear baseline between the interval limits from the integrated absorbance (see example plot in Figure A.9 of Appendix 2, page V).

7.3.4 Multivariate analysis

Multivariate analysis was performed on the spectra's first differential to better highlight the position of the peaks regardless of the absolute absorbance.[Kansiz1999] The multivariate analysis was performed using XLSTAT (Addinsoft, Paris, France). To reduce the number of variables without sacrificing most of the variability, a principal component analysis was performed with the dataset using Pearson's method,[Pearson1901] representing 86% of the variability. The 40 most important principal components scores were selected for cocoon spectra whilst only 10 components were enough to preserve 90% of native silk feedstock spectral variability. The 2% outlier spectra with the largest distance from the species centroid were discarded (23 spectra for cocoons, 1 spectrum for native silk feedstock). For cocoon disks, the 1162 remaining spectra were randomly divided between the training group used to build the model (962 spectra) and the validation group used to test its performance (200 spectra) for the linear discriminant analysis (LDA).[Fisher1936b; Yang2005] From the LDA model, the probed layer of the cocoons was used as a qualitative variable as spectra were greatly dependent on the area probed for some species. Using the LDA model, 70% of cocoon spectra used for validation spectra could be assigned to the right species whilst 75% were assigned to the correct genus. From the remaining 52 spectra of native silk feedstock, 27 were used for training the method whilst 25 were randomly selected to validate the model (100% correct assignment). The hierarchical clustering analysis was performed based on the canonical function's scores from the LDA weighted by their Eigenvalue. The clustering algorithm used was Ward's top-down method using dissimilarity Euclidian distance as metric.[Ward1963; Mariey2001]

7.4 Results and discussion

7.4.1 Native feedstock spectral features

To evaluate the chemical difference of silk feedstocks from key species, 6 feedstocks were selected across the phylogeny tree: *Actias, Attacus, Bombyx, Saturnia* and *Nephila*. These feedstocks covered two known classes of silk protein mixtures. First, the heavy, light chain and P25 fibroin mixture linked with disulphide bonds can be found in the feedstocks of Bombycidae such as *Bombyx mori*.[Shimura1976; Chevillard1986; Mita1994] These three proteins are present in a 6:6:1 ratio.[Inoue2000] Second, the homodimer (double heavy chain, H-H) protein mixture constituted the feedstocks of Saturniidea such as *Antheraea yamamai*, *Actias luna, Attacus atlas* and *Saturnia pavonia*.[Tanaka2001a; Tanaka2001b]

Although spiders are only related to silkworms through their common phylum, the similar flow properties of their feedstocks present a good example of independent evolution converging to a common solution.[Craig1997; Holland2006] Despite these similarities, spider dragline silk has remarkable tensile properties when compared to *Bombyx mori* silkworm silk and it would be of great interest to identify the silkworms whose silk possess similar properties, to spider silk but producing more than arachnids. Hence, we wanted to compare these native protein to spidroins from spider silk by analysing *Nephila edulis*, which we assume has a similar dimer structure to *Nephila clavipes*'s with the abundant MaSp1 and the proline rich MaSp2.[Xu1990; Beckwitt1994; Colgin1998; Brooks2005] Infrared spectra were collected from feedstocks extracted directly from the animal and kept at native concentration.

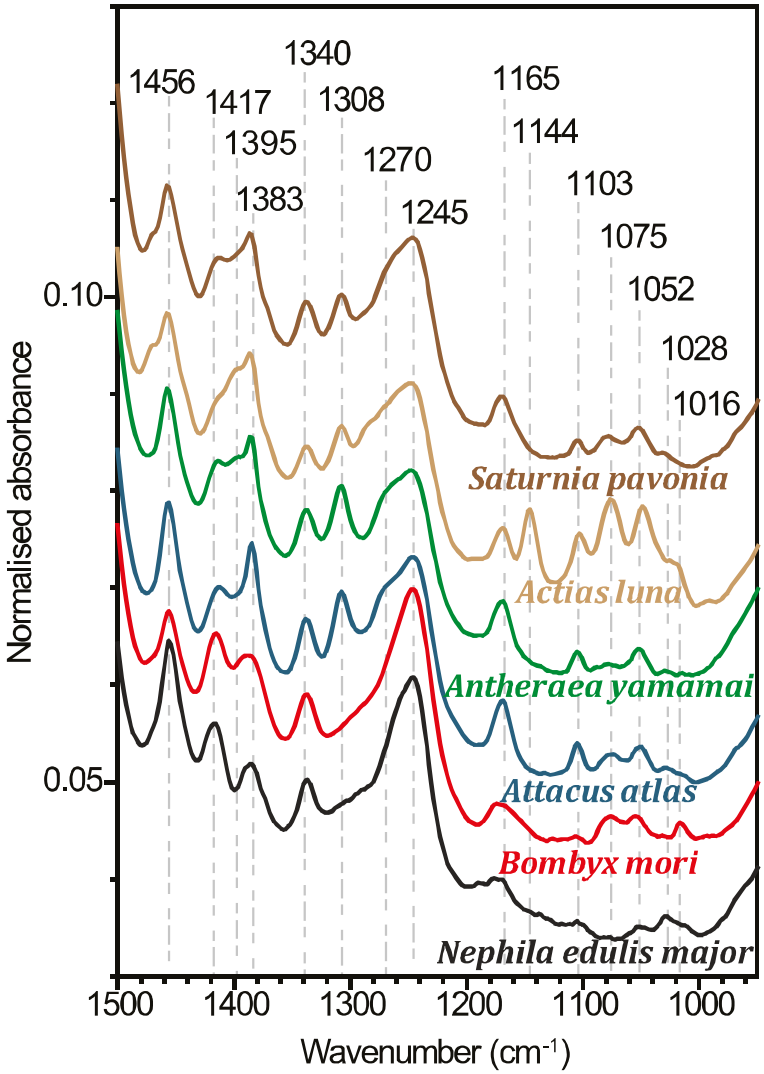


Figure 7.3 Infrared spectra of unspun native silk feedstock from domesticated silkworm silk (*Bombyx mori*), wild silkworm silk (*Attacus atlas, Antheraea yamamai, Actias luna, Saturnia pavonia*) and spider (*Nephila edulis* major ampulate). The 1700 to 1500 cm^{-1} region is not shown since no important difference between species were observed.

Position (cm^{-1})	Assignment	Observation	Reference
1733	υ(C=O)O	Tanned cocoon silks *O. eucalypti* *A. edwardsii*	*Silverstein1981*
1699	Amide I, β-sheets/ β-turns	All spun silks *E. bauhiniae*	*Miyazawa1961; Moore1976; Bandekar1979; Garside2005; Teramoto2005*
1642	Amide I, unordered	All silks	*Venyaminov and Kalnin1990;Goormaghtigh1994;Sonoyama and Nakano2000;Jeong2006*
1620	Amide I, β-sheets	All spun silks *E. bauhiniae*	*Moore1976;Muller1993;Garside2005;Taddei and Monti2005;Boulet-Audet2008*
1547	Amide II, unordered	All silks	*Yoshimizu and Asakura1990;Sonoyama2000;Lv2005;Jeong2006*
1516	Tyr–OH	All silks *A. yamamai*	*Chirgadze1975*
1508	Amide II, β-sheets	All spun silks *E.bauhiniae* *A. panda*	*Venyaminov1990;Yoshimizu1990;Muller1993;Sonoyama2000;Lv2005;Jeong2006;Boulet-Audet2008*
1456	$\delta_{as}(CH_3)$ Ala, Val	All unspun silks *N. clavipes* major	*Colthup1964; Barth2000b; Boulet-Audet2008*
1443	$\delta_{as}(CH_3)$, β-sheets, $(AG)_n$, $(A)_n$	All spun silks *N. clavipes* *A. Panda*	*Moore1976; Barth2000a*
1417	$\delta_s(CH_3)$ Alanine, Valine	All unspun silks *N. clavipes* major	*Moore1976; Barth2000a*
1403	$\delta_s(CH_3)$ Ala, Val	All spun silks *E. bauhiniae*	*Moore1976; Barth2000a*
1395	$\delta(CH_2$, OH) Serine	Silkworm silk *Outermost layer	*Barth2000b; Teramoto2003; Anghileri2007*
1383	$\delta(CH_2)$ $(AG)_n$	All unspun silks *A. attacus* *S. pavonia	*Moore1976; Barth2000a*
1370	$\delta(CH_2)$ $(AG)_n$	All spun silks *E. bauhiniae*	*Moore1976; Barth2000a*
1340	δ(CH) or $w(CH_2)$	All unspun silks	*Colthup1964; Barth2000b*
1315	$\upsilon_s(OCO^-)$ Calcium oxalate	*G. postica* outer cocoon *Antheraea* outer cocoon	*Silverstein1981; Sargut2010; Gheysens2011b; Chen2012c*

Table 7.1 Assignment of the main bands present in silk between 1700 and 1315 cm^{-1}. (δ is bending, υ is stretching, w is wagging, r is for rocking, * is for "strongest for")

Position (cm^{-1})	Assignment	Observation	Reference
1308	Amide III, β-turns	Some unspun silks except *B. mori* and *N. clavipes*	*Bandekar1980; Krimm1986; Rousseau2006*
1270	Amide III, α-helices	All silks	*Krimm1986; Cai2004*
1237-45	Amide III, random coil	All silks	*Yoshimizu1990; Cai2004; Shao2005; Taddei2005*
1217	Amide III, β-sheets	All spun silks **E. bauhiniae*	*Moore1976; Asakura1985; Yoshimizu1990; Cai2004; Shao2005; Taddei2005*
1165	υ_sNCα	All silks **E. bauhiniae*	Moore1976;Barth2000
1130	CH2OH Polyphenols	Tanned cocoon silks **O. eucalypti* **A. edwardsii*	*Schulz2007; Lu2011*
1103	υ(C-O), υ(C-C), Polyphenols or tyrosine	Tanned cocoon silks Most wild silkworm silks **A. atlas*	*Andrus2006* *Barth2000b*
1068-75	υ(C-O),υ(N-C_α) Serine	Silkworm cocoon *Outermost	*Gupta1997; Barth2000b; Anghileri2007*
1052-58	υ(C_β-O) υ(C-OH) Serine	Most silkworm silks **A. luna*	*Gupta1997; Teramoto2003; Taddei2005*
1028	r(CH_2), $(A)_n$, random coil	Unspun *N. edulis* and wild silks	*Moore1976; Taddei2006*
1016	r(CH_2), $(AG)_n$, random coil	Unspun *B. mori* only	*Moore1976; Taddei2005*
998	r(CH_2), $(AG)_n$ β-sheets	**A. panda* **Bombyx*	*Moore1976; Taddei2005*
961	r(CH_2), $(A)_n$ β-sheets	Spun silks exept *A.panda* and *Bombyx* **E.bauhiniae*	*Moore1976; Taddei2005*
779	δ(OCO^-) Calcium oxalate	**G. postica* Antheraea outer	*Silverstein1981; Sargut2010; Gheysens2011b; Chen2012c*

Table 7.2 Assignment of the main bands present in silk between 1308 and 779 cm^{-1}. δ represents bending, υ is for stretching and r for rocking).

Figure 7.3 illustrates the infrared spectra region between 900 and 1500 cm^{-1} showing the most distinctive spectral features indexed in Table 7.1. The bands between 1340 and 1456 cm^{-1} are commonly assigned to the vibration mode of the side chain residue.[Barth2000b] The main spectral feature of this region is the stronger 1383 cm^{-1} band associated with CH_2 bending for wild silks (top four curves), suggesting a higher proportion of longer chain residues for those silks compared to *Bombyx mori* and *Nephila edulis*. Another important distinction is the presence of the well resolved 1308 cm^{-1} component in the amide III region for wild silk feedstocks. Since it vanishes under shear-induced denaturation (see Figure A.7

of Appendix 2, page S) and is not present in cocoon spectra, this component may be a marker of β-turns.[Bandekar1980; Cai2004; Rousseau2006] Since the arginine-glycine-aspartic acid (RGD) residue pattern also adopt β-turn structures[Sukopp2002] it might be related to this peptide sequence. This pattern known for promoting cell adhesion[Navarro2008] is believed to be responsible for *Antheraea mylitta*'s greater fibroblast proliferation rate compared to *Bombyx mori* silk based scaffoldings.[Acharya2009;Silva2013]

The shoulder at 1270 cm^{-1} could be attributed to α-helices,[Krimm1986; Cai2004] which appears stronger in wild silkworm silk feedstock as well. The neighbouring peak at 1245 cm^{-1}, on the other hand, is commonly assigned to random coil secondary structures,[Yoshimizu1990; Cai2004; Shao2005; Taddei2005] which are strongest in *Bombyx mori* and *Nephila edulis*. The 1165 cm^{-1} assigned to the stretching of the N-C_α present for all silk feedstocks is clearly broader for those two species suggesting a wider distribution of conformations.

The well resolved band at 1144 cm^{-1} is only seen on the spectrum of *Actias luna*, which is also the only species of the Attacini tribe measured. Another distinct feature of this species is low cocoon porosity and high density.[Chen2012c] Therefore, this distinct band could be speculatively assigned to the C-O stretching of another type of sericin-like component used as a cocoon hole filler. Degumming the cocoon could represent a method to narrow down the band assignment to the sericin coating.

The 1103 cm^{-1} band appeared on all spectra recorded, although it is much stronger on wild silkworm feedstocks. In the skeletal vibration region, this band is likely to be associated with the C-C stretching of tyrosine aromatic rings, tryptophan or phenolic compounds.[Barth2000b; Taddei2005; Andrus2006], the adjacent component at 1075 cm^{-1} is strongest in *Actias luna* but is also observed in pure sericin spectra[Gupta1997; Barth2000b; Anghileri2007] and is present for all silks, except spider silk which is naturally sericin free. The band at 1052 cm^{-1}

is also assigned to sericin (C-O stretching) and appears clearly in most silkworm silks.[Gupta1997; Teramoto2003; Taddei2005]

Spider silk dope shows a weak peak at 1028 cm^{-1} which is also shared by wild silkworm silks. This peak is due to unordered poly-alanine segments known to be present in most silk sequences.[Moore1976; Hinman1992; Scheibel2004; Taddei2006] As for the 1016 cm^{-1}, the absorption is the greatest in *Bombyx mori* because of repeating alanine-glycine segments[Moore1976; Taddei2005] present in the domesticated species and few others.[Nakajima1981; Tamura1987; Zhou2000]

7.4.2 Silk cocoons spectral features

Since silk feedstocks already have important spectral differences between species, it would be expected that cocoons spun from them would also show substantial variability. In addition, other silkworm secretions, environmental material and leaves can be added to the cocoon's chemical composition. To examine these sources of chemical diversity the infrared spectra of the cocoon's inner and outermost layers from 36 species of silkworms were compared to that of *Nephila edulis* dragline silk. As spider silk was obtained by forced reeling, the fibres' orientation were randomised by making a random coil bundle to remove the anisotropy variability and allow a comparison with the layers of fibres in cocoons which show no preferred orientation.[Chen2012b]

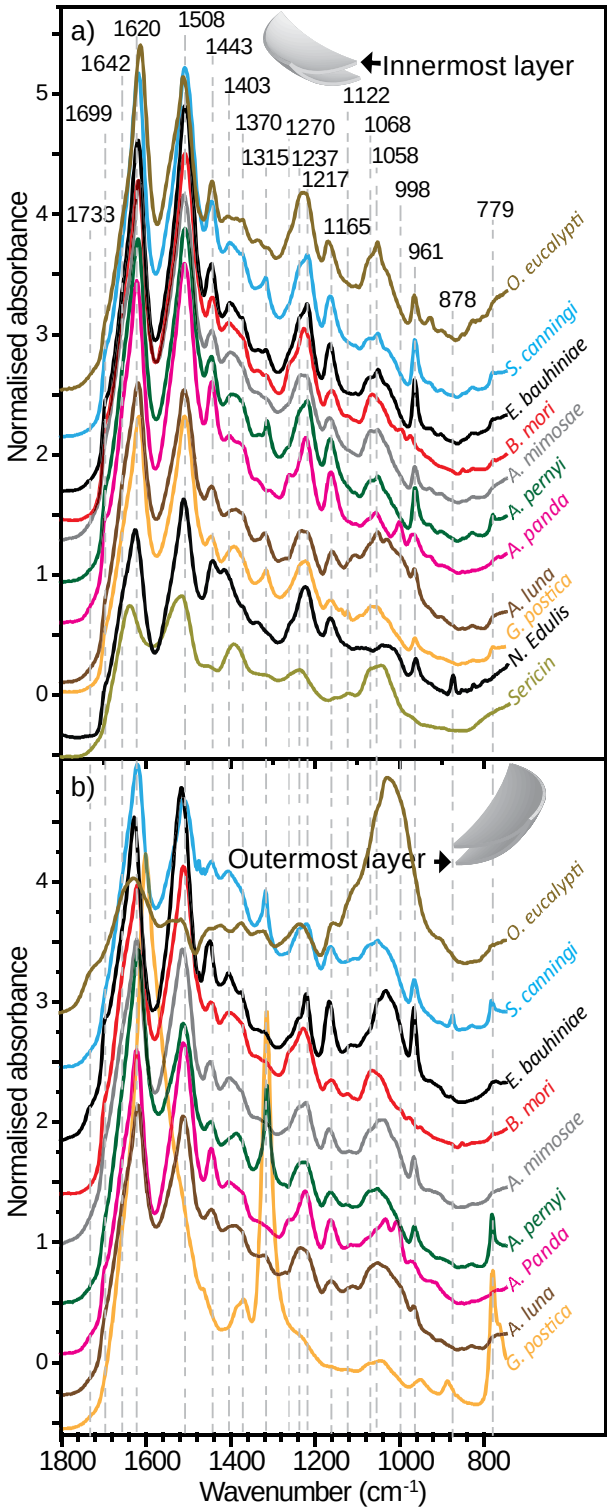


Figure 7.4 a) Infrared spectra of key species innermost layer and sericin spectrum. b) Outermost layer spectra.

Figure 7.4a shows the spectra acquired from the innermost part of the cocoons from representative species. Although they are mainly made of the silk proteins, the cocoons' infrared signature is substantially different from their respective feedstock for several

reasons. As we have demonstrated in Chapter 6, the water content is lower in cocoons than in silk feedstocks. Thus, the O-H bending mode of H_2O at 1640 cm^{-1} vanishes, reducing the ratio of amide I to amide II height (1642/1580 cm^{-1}). As silk is spun, the precursor random coil and helices structures are converted to β-sheet, resulting in decreasing absorbance at 1642, 1547, 1308 and 1247 cm^{-1} and simultaneously, a rise in the β-sheet components at 1699, 1620, 1508, 998 and 961 cm^{-1} indexed in Table 7.1.[Boulet-Audet2011; Boulet-Audet2013] The relative absorbance of these β-sheet peaks can serve as indicators of the degree of crystallinity and the type of repetitive segments which constitute the crystalline regions. The peaks at 1699 and 1620 cm^{-1} in the amide I region are commonly used to determine the anti-parallel β-sheet content but strongly interfere with adjacent components from fibroin and other compounds present in cocoons. In contrast, the low frequency component at 961 cm^{-1} assigned to poly-alanine $(A)_n$ motifs is much better resolved.[Moore1976; Taddei2005] This band is clearly visible in *Nephila edulis* dragline and most spectra of wild silks cocoons, in particular for *Epiphora bauhiniae* (black curve). In contrast, some species like *Bombyx mori* (red curve) and *Anaphe panda* (magenta curve) have two weaker peaks at 998 and 961 cm^{-1} as their β-sheets are constituted of poly(alanine-glycine) repetitive segments instead.[Moore1976; Taddei2005]

Cocoons are multi-layered composite structures with varying properties between the innermost and outmost layers. Consequently, spectra must be collected from each side to accurately evaluate the chemical diversity of the entire structure. As seen on Figure 7.4b, the distinctive features are more prominent in the cocoon's outermost layer than in the innermost layer for the same species. As the amount of sericin is greater on the outermost layer for species like *Bombyx mori*,[Chen2012a] it results in higher relative absorbance of sericin bands at 1395 and 1058 cm^{-1}. The pure sericin spectrum is given in Figure 7.4a for comparison.

Another major difference between the two layers is the amount of calcium oxalate monohydrate ($Ca(COO)_2$) crystals found on the outermost layer of certain species.[Takahash.Sy1969; Teigler1972b; Freddi1993; Freddi1994; Gheysens2011b] For instance, *Gonometa postica*'s infrared spectra of the outermost layer is dominated by vibration modes associated with these crystals at 1315 and 779 cm^{-1} whilst the innermost layer has much weaker bands.[Silverstein1981;Sargut2010;Gheysens2011;Chen2012] Particularly important for *Opodipthera eucalypti*, another distinction between inner and outermost layers comes from the shoulder at 1733 cm^{-1} assigned to the C=O stretching of the carboxylic acid and the C-O stretching of polyphenol hydroxyls around 1000 cm^{-1}.[Silverstein1981; Andrus2006]

In summary, it is possible to use the structural and chemical bands to provide information on the crystallinity, amount of sericin, presence of calcium oxalate and the polyphenol content of the cocoon surface. In order to obtain qualitative data, the peak areas were measured for the corresponding peaks as the absorbance associated with the compounds can be directly linked to their relative concentration.

7.4.3 Comparison of species chemical composition

In order to obtain representative data, the spectra must be normalised to remove any absolute absorbance variation due to different cocoon porosity across cocoons, the normalisation being based on the average absorbance of the entire mid infrared region for all spectra collected. For each spectrum collected, the peaks of interest were integrated to determine the relative content of the 4 principal components: calcium oxalate, β-sheet crystallinity, tannin/phenolic compounds and sericin gum.

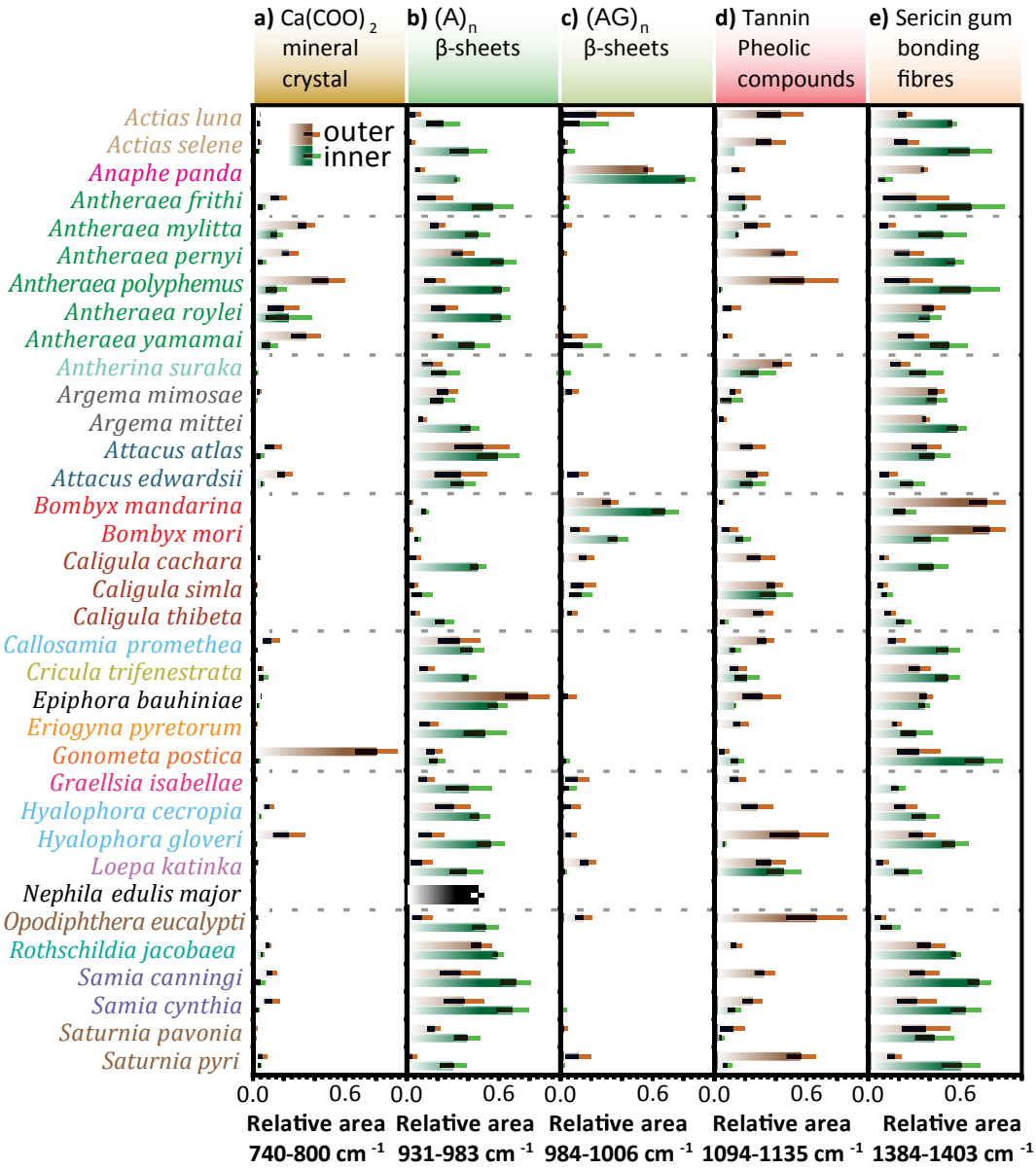


Figure 7.5 a) Relative area of a band assigned to calcium oxalate (740-800 cm^{-1}). b) Relative area of peak associated with $(A)_n$ β-sheets (931-983 cm^{-1}). c) Relative area of a $(AG)_n$ β-sheets assigned band (984-1006 cm^{-1}). d) Relative area of a band associated with tannins band (1094-1135 cm^{-1}) d) Relative area of a sericin marker band (1384-1403 cm^{-1}). The outermost layer is presented by brown bars and innermost layer is represented by green bars. The error bars represent the standard deviation of the different observation. A value of 1 represent the higher area measured amongst all the observations.

Calcium oxalate mineral crystals

Figure 7.5a shows the relative intensity of the band at 779 cm^{-1} by integrating the absorbance between 740 and 800 cm^{-1}. This well-resolved band is a relative indicator of the amount of microscopic calcium oxalate ($Ca(COO)_2$) mineral crystals present on the cocoons. *Gonometa postica* was identified as the species with the most calcium oxalate on its cocoon

followed by silks from the *Antheraea* genus, in agreement with previous reports.[Gheysens2011b] Scanning Electron Micrographs (SEM) can also confirm the presence of the microscopic crystals of the mineral on the surface of the cocoons.[Gheysens2011b; Chen2012b] Silks from the *Samia, Hylophora* and *Attacus* have it as well, but in lower proportions, whilst other species measured have negligible amounts on their cocoon. Like many other species of plants across 200 families, the *Acacia* host plant of *Gonometa postica* is rich in calcium oxalate as it uses it to detoxify calcium ions.[Teigler1972a; Franceschi2005; Martin2012] Also called Raphide, calcium oxalate forms needle like crystals that are very toxic and appear to be a defence mechanism for plants as they could tear the soft tissues of potential predators.[Arnott2000] Since no metabolic pathways to convert the calcium oxalate have been reported, it could be assumed that silkworm species which eat leaves containing calcium oxalate will excrete it thereafter. Therefore, its presence on the cocoon would depend more on the worm's cocoon construction behaviour than its diet. Some species like *Bombyx mori* release their excretions containing calcium oxalate outside the cocoon instead of inside. As plotted in Figure 7.5a, for the majority of silkworm, excluding *B. mori,* these crystals are mostly present on the outermost layer (brown bars), suggesting that they are added at the beginning of the cocoon construction but perhaps runs out during spinning as the innermost layer, the last stratum produced, contains almost no mineral crystals. This behaviour could be advantageous if calcium oxalate is toxic the predators.[Arnott2000] Calcium oxalate is notoriously toxic to humans as it is responsible for kidney stone formation. The edetic acid (EDTA) treatment for dissolving these kidney stones was found equally effective at demineralizing wild silk cocoons containing calcium oxalate crystals.[Gheysens2011b] However, it would be even easier to select the species with the desired amount of calcium oxalate which acts to modulate the mechanical properties of cocoon-based composite materials.[Chen2012b]

β-sheet crystallinity

X-ray scattering proved the presence of β-sheet nanocrystals inside the fibroin filaments.[Warwicker1954] Using the integrated absorbance of the 931 to 983 cm^{-1} region, [Moore1976;Taddei2005] Figure 7.5b shows the relative content of poly-alanine antiparallel β-sheets of all 38 silk cocoons measured. Our results revealed that *Epiphora bauhiniae* has the highest degree of crystallinity amongst the 35 $(A)_n$ containing silks measured, followed by species from the *Samia*, *Antheraea* and *Attacus* genera. For most species, the β-sheet content appears to be greater on the innermost layer. This observation is most likely due to the presence of non-fibroin compounds contributing to the infrared signal more on the outermost layer. In comparison, spider silk dragline from *Nephila edulis* appears to have an average degree of crystallinity compared to the silkworm silk measured. As the crystals are known to be responsible for the material's stiffness,[Porter2005] it would be expected for silk with extreme degree of crystallinity to have a significant variability in tensile properties.[Chen2012b] On the lower end, *Gonometa*, *Argema* and *Caligula* genera seemed to have the lowest β-sheet content amongst all the species studied. Amongst the 37 species tested, only 3 seem to have the $(AG)_n$ repetitive segments, *Bombyx mori*, *Bombyx mandarina* and *Anaphe panda*. On the other hand, none of the Saturnidae show a peak between 984 and 1006 cm^{-1} associated with the $(AG)_n$ structure.[Moore1976; Taddei2005] It is therefore unsurprising that Saturniidae silks differ from the other wild species measured such as the Bombycidae and Noctuidae families (see Figure 7.2).

Tannins and phenolic compounds

Although silk secretions are mostly made of fibroin and sericin, they also contain enzymes and phenolic compounds.[Brunet1974] Glycosides are excreted with silk proteins, but more hydroxyl-containing compounds such as polyphenols can come from an exterior source. In nature, silkworms require a substrate to anchor their cocoon often using a leaf as a support.

As a result, plant polyphenol could diffuse into the cocoon layer through contact with leaves. These water soluble compounds have distinctive infrared spectra from fibroin and sericin as shown in Figure 7.4b for *Opodipthera eucalypti* (brown curve), which uses tree twigs . By integrating the absorbance between 1035 and 1094 cm^{-1}, the relative amount of these molecules can be estimated. Figure 7.5c shows that a few species have phenolic compounds including *Opodipthera eucalypti, Saturnia pyri, Hyalophora gloveri*, *Attacus edwardsii, Antheraea polyphemus* and *Actias luna*. The phenolic compound parameter of Figure 7.5d suggests that they are mostly on the outermost layer. This result is consistent with the fact that only the outermost layer is in contact with the bark or leaf substrate. In contrast, species using stalks as tethers like *Antheraea mylitta* and *Attacus atlas*[Yagi1926] showed low phenolic compound parameter scores.

Sericin protein gum

Sericin proteins are essential to the cocoon construction as they are used to bond fibres together into a 3 dimensional structure. The silkworm could even build a cocoon with only sericin proteins.[Zhang2012c] Sericine gives a distinctive infrared spectrum from fibroin[Teramoto2003](see Figure 7.4), with bands between 1384 and 1403 cm^{-1}. The latter could therefore be used as an indicator of the amount of sericin present. Figure 7.4e suggests that *Bombyx* genus silks have the most sericin along with *Actias*, *Antheraea, Saturnia* and *Samia* genera silks. The results suggest that sericin is more prominent for less porous cocoons whilst very porous cocoons such as *Caligula trifenestrata, Graela isabella* and *Loepa katinka* absorbed much less in this region and so showed less sericin.[Chen2012b] Spiders do not produce sericin and so the *Nephila edulis* fibres did not show any bands assigned to sericin. Infrared spectroscopy showed that *Bombyx mori* cocoons have more sericin on the outermost layer than the inner layer.[Chen2012a] Artificial selection has led to the reduction in sericin as this facilitates extracting the silk from the cocoon. The fact that sericin content

varies across the layers could again be the exhaustion of sericin during spinning in the same manner to calcium oxalate. The domesticated species could thus deplete its sericin feedstock before it uses all the fibroin feedstock. However for wild silk, sericin vibration modes appear less important on the outermost layer when calcium oxalate or phenolic compounds are present. The non-protein content of the outermost layer could explain the difference observed as species with little calcium oxalate or phenolic compound content such as *Epiphora bauhiniae* appeared the have a similar amount of sericin across layers. Since ATR-IR probed only the surface, increasing the proportion of one component at the surface will decrease the measured concentration of others.

7.4.4 Silk species classification

Integrating bands assigned to certain compounds provided direct insights into the silk's chemical composition, however it exploits only a fraction of the information contained within the spectra. The multivariable approach is an efficient way of extracting this information. Hence, we performed a Principal Component Analysis[Pearson1901] to reduce the number of variables from 2853 to 40 of principal components whilst retaining most of the variability. A linear discrimination analysis was performed on the principal components using the known species name and layer probed to train the method. First, the main canonical functions were used to hierarchically cluster the feedstock using their spectral dissimilarity Euclidean distance.

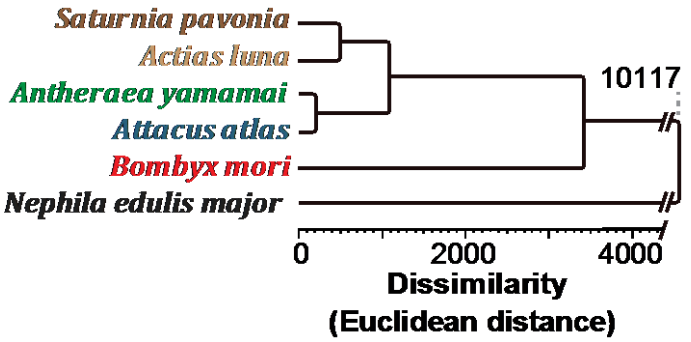


Figure 7.6 Ultrametric tree generated from the infrared of native feedstock main canonical functions.

Figure 7.6 shows that feedstocks from *Actias luna*, *Saturnia pavonia* and *Antheraea pavonia* and *Attacus atlas* share common spectra features such as the 961, 1103 and 1308 cm^{-1} components presented in Figure 7.3. This result corroborates the fact that these four species are more closely related as they belong to the same Saturnidae arthropods superfamily. Although much more distant, the closest to these four species is the silkworm silk *Bombyx mori* feedstock as it is also a silkworm silk feedstock containing sericin proteins.

Relative to silkworm feedstock's dissimilarity, the spider silk feedstock tested has a much greater Euclidean distance. With fewer types of fibroins and free of sericin, spider silk feedstock infrared spectra are very distinct. Once spun, even more variables are involved as environmental conditions and silkworm behaviour are in action.

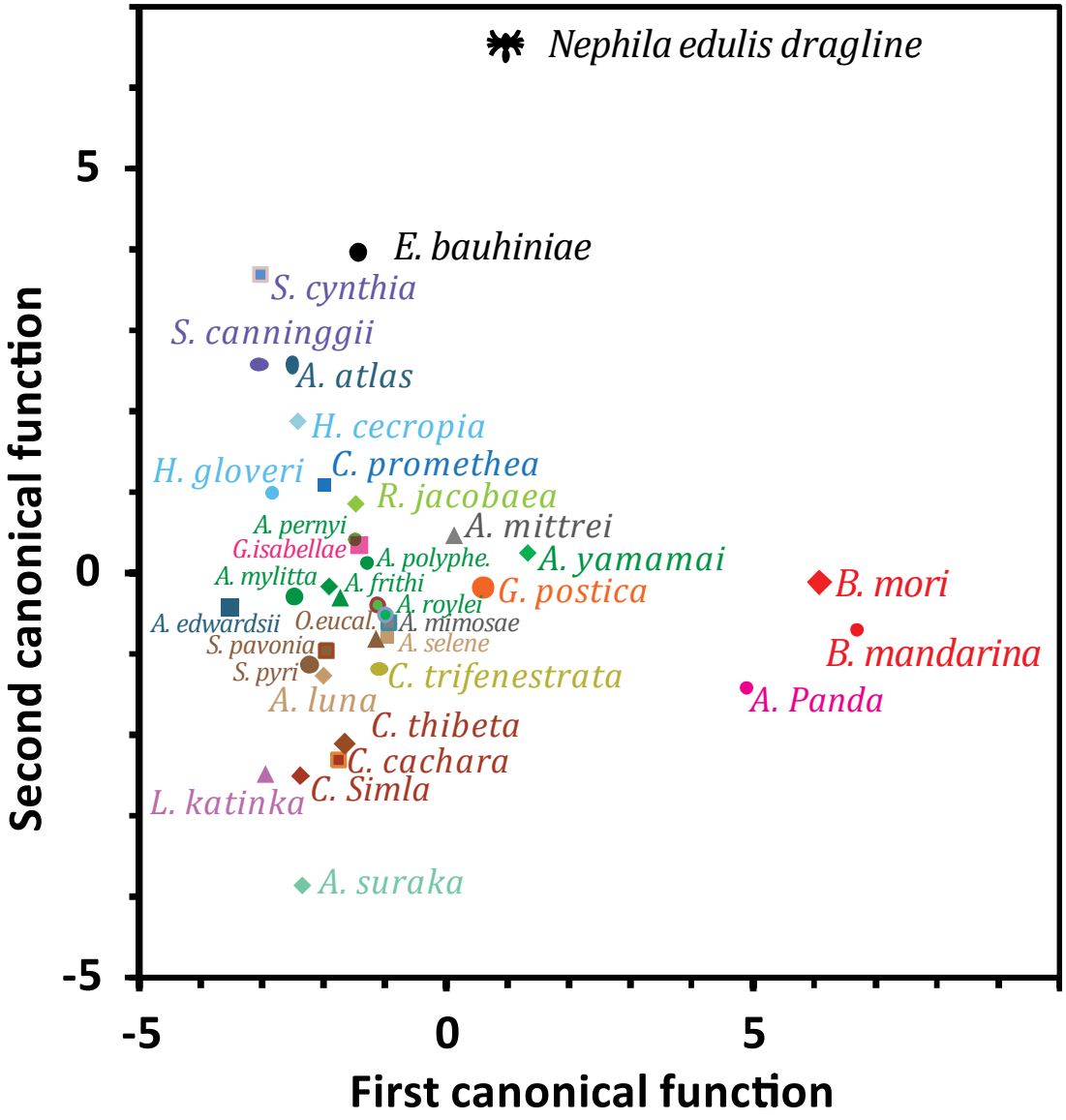


Figure 7.7 First and second canonical function of the cocoon spectra contributing to 62% of species discrimination.

Figure 7.7 shows the values of the two most important canonical functions calculated from of the cocoon spectra obtained from 38 species. This figure clearly shows a main cluster encompassing most wild silkworm species with *Antheraea* silks near its centroid (green markers). *Antherina suraka*, *Leopa katinka*, *Epiphora bauhiniae* and *Samia cynthia* silks are found at the cluster's fringe suggesting a greater dissimilarity with the average of the measured silks. Easily discriminated species outside this cluster such as *Anaphe panda*,

Bombyx mori and *Bombyx mandarina* seemed to be outliers with larger first canonical function scores. *Nephila edulis* dragline silk is also outside the main cluster, easily discriminated from silkworms' silk. Although only the two main canonical functions are represented, this graph implies that *Epiphora bauhiniae* would be the silkworm species of those measured producing the closest silk to *Nephila edulis* dragline. However, more species from other families would need to be probed in order to be categorical in which silkworm species spins 'spider silk'. *Nephila edulis* cannot be described as outlier species since only one spider silk species have been measured in this study. Our chemical composition comparison could thus complement the distinct inter-species morphology of silk cocoons measured by Chen et al.[Chen2012c] To regroup these species into groups and quantify their dissimilarity, a hierarchical clustering analysis (HCA) was performed on the scores of the 10 most important canonical functions weighted by their Eigenvalues before performing the HCA on the cocoons spectra dataset.

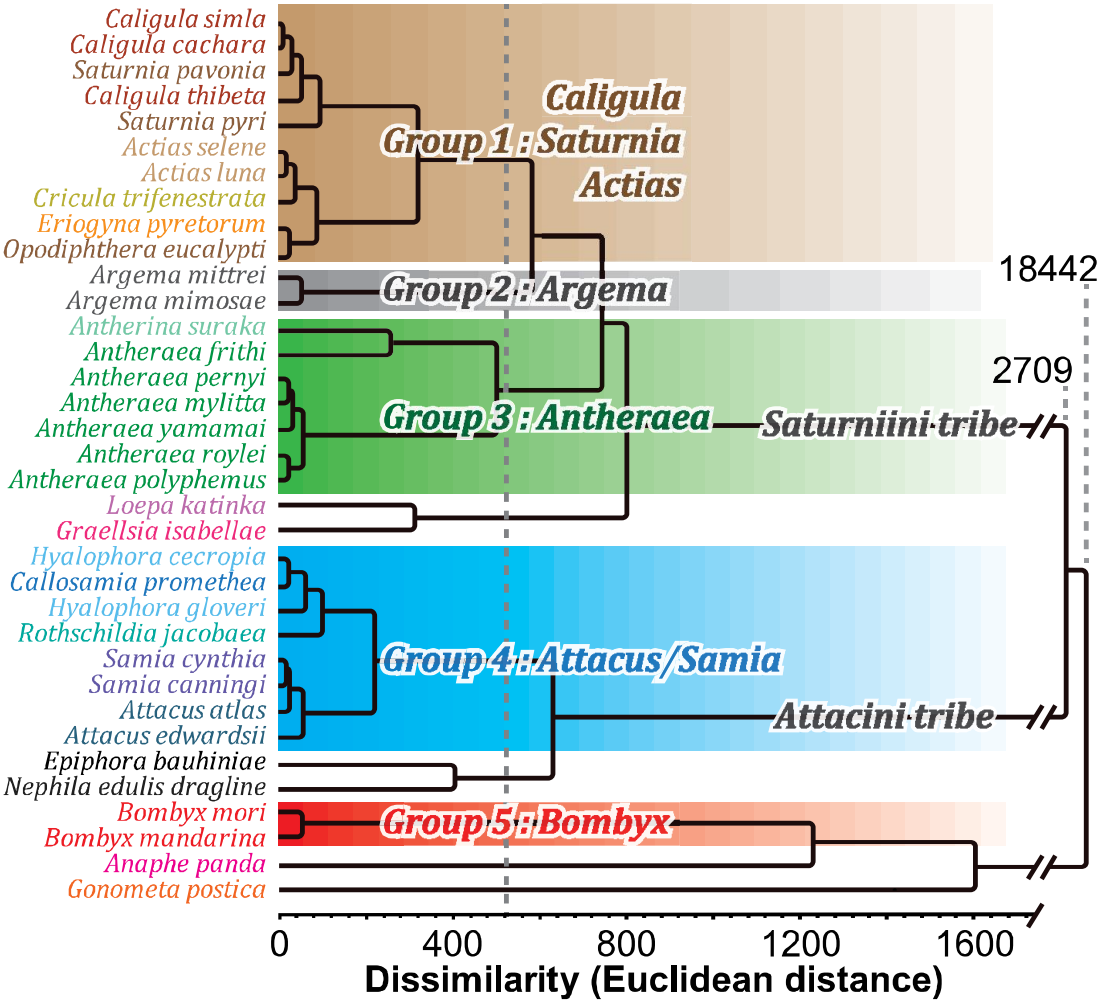


Figure 7.8 Ultrametric tree generated from the hierarchical clustering analysis of cocoon infrared spectra main canonical functions. Species with with Euclidean distance smaller than 525 were regrouped together.

Group 1: Caligula, Saturnia and Actias

Illustrated in brown on Figure 7.8, Group 1 encompassed *Caligula, Saturnia* and *Actias* genus together along with *Opodipthera eucalypti* and *Cricula trifenestrata*. As most species from this group have high absorbance between 1094 and 1135 cm^{-1} in Figure 7.5d, it suggests these species were regrouped partly based on their phenolic content. Except *Cricula trifenestrata*, these species cocoons appeared substantially tanned with a dark brown coloration.[Chen2012c] In addition, these species do not feature calcium oxalate crystals on their surface,[Chen2012c] as confirmed in Figure 7.5a. Group 1 also appears to have lower β-sheet content than the other groups.

Group 2: Argema

The *Argema* genus silks are classed together in Group 2. Unlike other silks from group 1 they do not appear to have high phenolic content and not having calcium oxalate like most *Antheraea* silks. Even if this genus' silk is comparable to neighbouring groups, these factors could explain why it sits in-between.

Group 3: Antheraea

Since *Antheraea* silks have small Euclidean distances, they are all regrouped together in Group 3 with *Antherina suraka*. However, the greater Euclidean distance of *Antherina suraka* from the other species of the group strengthen the hypothesis that this species could be more closely related to the African Bunaeini tribe than other species of the Saturniini tribe as previous studies argued.[Oberprieler1997] Since *Antheraea* is the genus with the most calcium oxalate (Figure 7.5a), the linear discriminant analysis method could have regrouped these silks mainly on crystal content. However, *Antherina suraka* and *Antheraea frithi* show less absorption between 740 and 800 cm^{-1} (calcium oxalate) and are more distant from the other species of this group. In addition, Group 3 of Figure 7.8 seems to have less phenolic compounds than Group 1 and yet has an average amount of sericin. The next closest species to these groups are *Loepa katinka* and *Graellsia isabellae* which appear to have low sericin content and high porosity as common features.[Chen2012b; Chen2012c]

Group 4: Attacus and Samia

Much more distant are the species classified in Group 4, including *Samia, Hyalophora* and *Attacus* genera along with *Callosamia promethea*. The morphology of the cocoons classified together in Group 4 (blue) is characteristic as the innermost layers are much more compact than their outer layers.[Chen2012c] This morphological difference could explain the higher amount of sericin measured on the innermost layer (Figure 7.5e). Adding to the

composition variation between the inner and outmost layers these silks have intermediate content of β-sheets, sericin and tannin when compared to those from Groups 1 and 3.

Branching from Group 4, *Epiphora bauhiniae* is distinctive having the largest amount of $(A)_n$ β-sheets, little phenolic compounds, no calcium oxalate and little sericin. The higher crystallinity content could potentially explain its shiny innermost layer and could result in stiffer fibres.[Porter2008] Although relatively different, this type of silkworm silk has the closest spectra to *Nephila edulis* dragline silk. As Arachnids and Lepidoptera diverged a long time ago from a common ancestor, this result provides additional evidence of silk's evolutionary convergence. Of all the silk cocoons measured, those from the Attacini tribe appear to have a silk the closest to *Nephila edulis* dragline. More specifically, the LDA methods thus points to *Epiphora bauhiniae* being a potential candidate for exhibiting properties similar to spider silk.

Group 5: Bombyx

Bombyx mori and *Bombyx mandarina* silks are in another group. Even though *mandarina* appears to have more $(AG)_n$ β-sheets than *mori* (Figure 7.5c), the difference between their spectra is very small in comparison with the other species presented. This result suggests that the artificial selection of *Bombyx mori* should have played a lesser role than natural selection in differentiating this species from other Lepidoptera families.

Silk from other superfamilies

Although very distant, the closest silk cocoon measured to *Bombyx* is from the *Anaphe panda* moth belonging to the Noctuidae family. Our results suggest that it also has $(AG)_n$ β-sheets, sericin and no calcium oxalate. Testing more silks from these two families would confirm if these silks do share the same spectral features. Social spinning behaviour is another interesting characteristic of *Anaphe panda*, which partners with many other worms

to build a communal cocoon. As the cocoon's structure does not depend on the silk quality of a single individual, different natural selection constraints are at work. Consequently, this behaviour could change the rate of *Anaphe panda's* silk evolution and result in different properties. Also from another superfamily (Lasocampiadae), *Gonometa postica* silk is very distinct from all other species measured with a large Euclidean distance. The innermost layer being similar to Saturnidae silks (Figure 7.4), the major difference is likely to come from the large amount of calcium oxalate found on the outermost layer. These mineral crystals reinforce the structure and thus this species' cocoon is stiffer than other species.[Chen2012c] Using such minerals crystals could thus represent a method for modulating the composite's mechanical properties.

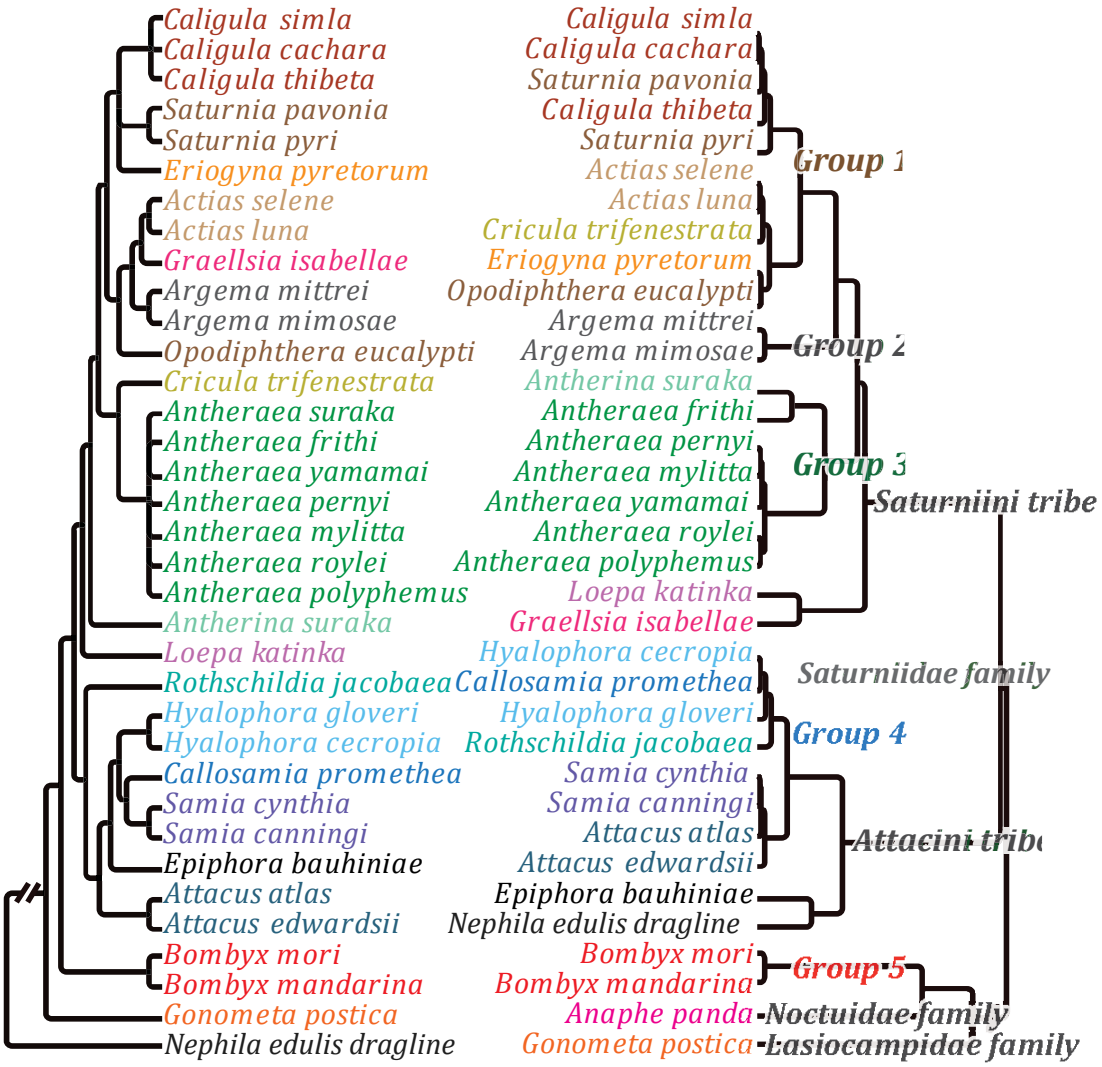


Figure 7.9 a) Cladogram generated from the phylogenetic analysis of Regier et al.[Regier2002; Regier2005; Regier2008a; Regier2008b; Chen2012c] b) Ultrametric tree generated from infrared spectra cocoons main canonical functions.

Presented on Figure 7.9, the ultrametric tree generated from the infrared spectra was compared to the phylogenetic tree built from the sequencing of a few protein-coding nuclear genes performed by Regier et al. [Regier2002; Regier2008a; Regier2008b; Chen2012c]. The genes selected to construct the phylogeny produce proteins with various enzymatic functions such as carbamoylphosphate synthetase (CPS), aspartate transcarbamylase (ATC), dihydroorotase(DHO),[Moulton2004] dopa decarboxylase (DDC),[Fang1997] enolase,[Farrell2001] period[Regier1998] and wingless (wg)[Brower1998]. Although a quantitative comparison is not directly possible, there is a striking similarity between the two trees, suggesting a relationship

between non-silk coding nuclear genes selected by Regier *et al.* and the silkworm cocoon's overall chemical composition, with the exception of a few species. This observation implies that cocoons likely vary due to many genes influencing not just the protein mixture but also the behaviour of the animal.

Despite this similarity, a few silk species appear to the misclassified in Figure 7.9b. For instance, *Cricula trifenestrata* was expected to be closer to the Antheraea silks rather than with species of Group 1. Hence, why would *Cricula trifenestrata* build cocoons with similar composition to Actias despite their distinct porosity?[Chen2012b] A further investigation of *Cricula trifenestrata*'s feedstock would be necessary but perhaps their sericin content is significant. Interestingly, *Graellsia isabellae* silk should have been very similar to Actias silks according to phylogenetic classificaiton, but is classified outside Group 1 along with *Leopa katinka* by our analysis. Their separate classification could be linked to the high concentration of tannins measured on these species' cocoon. Oberprieler et al. suggested that these species could be misclassified,[Oberprieler1994] and our study strengthens the idea that Graellsia and Actias are two distinct genera. As expected, *Epiphora bauhiniae* was classified in the Attacini tribe, but is rather distant from the other species of Group 4, most likely because of its higher crystallinity content.

7.5 Conclusions

Arthropods have evolved thousands of different type of silks with various chemical compositions.[Regier2008b] Using infrared spectroscopy, this study compared native silk feedstock from 6 species and spun silk cocoons from 37 species using a multivariable analysis approach. For native liquid silk, we identified spectral markers unique to wild silkworm silks which we assigned to β-turn secondary structures. If this feature is the

infrared signature of RGD patterns, it could potentially represent an indicator of the feedstock's cell adhesion properties. To test this hypothesis, the native feedstocks of wild silk species without this pattern would have to be measured. The comparison of the dope also enlightened the dissimilarity of Saturnidae silks to Bombycidae silk and spider silk feedstocks. Collecting spectra from silkworm cocoons provided information not only on the spun fibroin but also on the non-protein chemical content. Using specific infrared bands, the relative content of sericin, calcium oxalate, phenolic compounds, poly-alanine and poly(alanine-glycine) β-sheets was evaluated. Thanks to the superficial probing of ATR, the single component analysis revealed which species have more β-sheet structures on either their inner or outermost layers.

To exploit all the information contained in the infrared spectra, a multivariate analysis was performed on the entire data set. This analysis permitted the hierarchical classification of 38 species (including one spider silk) into groups based on their chemical composition. Hence, it revealed the presence of outlier species with very dissimilar spectra which could exhibit distinctive mechanical or chemical properties. Amongst these outliers is *Gonometa postica* which has the most calcium oxalate of all species measured. The species with the most β-sheets, *Epiphora bauhiniae,* also appears to have the closest chemical composition to *Nephila edulis* spider silk dragline. The *Bombyx* genus included species with large dissimilarity with all other species measured and could thus be described as outlier. Consequently, using *Bombyx mori* as model species for silk studies could lead to conclusions not representative of the full range of all types of silks. Although our sampling had a bias towards Saturnidae silk, *Antheraea* silks were found to have median principal component scores. This leads us to speculate that their silks are more representative of the silk biodiversity. Not only did the multivariate analysis classify species of the same genus together, but the ultrametric tree created from the infrared spectra is remarkably close to

the phylogenetic tree generated from genetic data. Since the non-protein content is also probed by this technique, our technique provides information on the silk glands' content, the cocoon construction behaviour of the animal, as well as the external environment. Since it appears to be also phylogenetically informative, this technique could represent an alternative to the costlier genetic sequencing.

With little sample preparation, we demonstrated that infrared spectroscopy of silk is phylogenetically informative, representing an as yet untapped alternative to protein sequencing. As silk cocoons are commonly part of entomology collections, they can be readily sourced and rapidly tested in a non-destructive manner. Hence this novel approach could assist taxonomists to classify ambiguous moth species based on a key aspect of their life cycle. This method would also have the potential of identifying candidate species which are more likely to have desirable silk properties, such as cell adhesion, mechanical properties, ease to reel or solubilise. Amongst the thousands of wild silk types available, there should be species that fortuitously evolved silks surpassing those commonly used for textile and biomedical applications.

Chapter 8

Summary, impact and future directions

To summarise this thesis, the key findings of each chapter are presented below along with their contribution to the overarching conclusions. Thereafter, the impact of these conclusions is discussed and put into a wider scientific context as well as their potential practical applications. Finally, the future directions of the work will be given explaining where the work in this thesis might potentially and hopefully lead.

8.1 Thesis summary

	Chapter 3 Shear-IR	Chapter 4 Shear-SAS	Chapter 5 Rheo-IR	Chapter 6 Silk curing	Chapter 7 Silk diversity
Questions	·How does silk respond to shear stress?	·What is the critical stress? ·Which length scales are involved in the process?	·What is the link between flow properties and structure? ·RSF = NSF?	·Is silk fully formed at excretion?	·Is *Bombyx mori* a suitable silk model? ·Can IR be phylogenetically informative?
Stress applied	·**Shear stress** ·**Chemical stress**	·**Shear stress** ·**Spontaneous**	·**Shear stress** ·**Spontaneous**	·***In vivo* stresses** ·**Spontaneous**	
Probe	·**IR**	·**SANS** ·**SAXS** ·**Offline rheology**	·**IR** ·***In situ* rheology**	·**IR**	·**IR**
System	·***Bombyx mori***	·***Bombyx mori***	·***Bombyx mori***	·***Bombyx mori*** ·***Saturnia pavonia***	·***Bombyx mori*** ·**Wild silks**
Sample type	·**Reconstituted SF**	·**Native SF**	·**Native SF** ·**Reconstituted SF**	·**Spun native silk**	·**Spun native silk**
Improvement requirements	·Biologically representative samples➔ ·Response to flow ➔ ·Different length scales➔	·*In situ* rheology for coupling properties➔	·*In vivo* for including all sources of stress ➔	·More species➔	
Contributions to main conclusions	·RSF's conversion is triggered by shear stress.	·Native silk gels in seconds under shear	·RSF and NSF are indistinguishable by static spectroscopy		
	Response to flow stress is required to evaluate the quality of feedstocks.				
	·RSF converted less with shear stress than with alcohol.	·Shear only partially converted NSF. ·Slow spontaneous conversion completes conversion. ·The orientation generated is also of the nanoscale.	·Shear stresses only partially converted NSF before it becomes ineffective.	·Silk fibres are far from dry at secretion. ·The sum of *In vivo* stresses only partial conversion. ·Most of the conversion environment dependents controlled by the environment.	·The chemical composition varies largely across species. ·Bombyx mori might not be the most representative species. ·IR can be used to classify silk.
	Silk's formation is not fully controlled by the animal.				
	·Standard RSF requires higher concentration than native to convert under the same stress.		·RSF at native concentration does not have recoverable strain	·Fresh silk kept dry is easier to solubilise. ·The milder solubilisation conditions produces better RSF.	**·Many representative species should be studies.** **·IR spectra are phylogenetically informative.**
	Partially formed silk makes better artificial silk feedstocks.				

Table 8.1 Summary of the chapter's contribution to the final conclusions. See Appendix 5 for a complete list.

8.2 How is silk spun?

To understand enough of silk's function to answer "*why is silk spun?*", we must first get a coherent understanding of *"how it is spun?"*. We first attempted in Chapter 3 to replicate the stress involved in the spinning process. Under a naturally occurring source of stress, shear flow, artificial Reconstituted Silk Feedstocks (RSF) were probed by attenuated total reflection infrared spectroscopy (ATR-IR). RSF are often used as analogues as they can also change conformation and generate β-sheets under stress whilst being easy to prepare in large amount. The reconstituted silk analogues prepared did indeed align and form β-sheets under shear, but only at much higher concentrations than at which its natural equivalent is spun. Because RSFs were less shear sensitive, it casted doubts on their validity as silk feedstock analogues. Interestingly, the amount of conversion induced by shear was substantially lower than that induced with the use of chemical stress (alcohol). This initial study led us to hypothesise that more stress was required to form fully silk's β-sheet structure. Because of the doubts on the validity of RSF as analogues and the lack of normal thrust control, it led us to improve our methodology.

Instead of a purpose-built shear cell which was cheap and convenient to build (see Figure 2.8), in Chapter 4 we used a rheometer to apply shear, measure the normal force and maintain a constant gap. In addition, we moved to using native silk feedstock extracted directly from *Bombyx mori* silkworm glands. To link silk's flow properties to the nanoscale structures involved in the spinning process, we also employed small angle X-ray and neutron scattering (SAS). This technique revealed the length and the time scales involved in the shear-induced denaturation of natural silk feedstocks. We found that shear stress can initiate silk's solidification but quickly became ineffective after only a few seconds when the sample started to gel and slip from the cell walls. Slippage was inevitable as the elasticity

became too important to have shear flow, in other words, the sample started to behave like a solid in lower viscosity fluid (biphasic). From the standalone rheological perspective, the processing appeared complete as the sample solidified, but SAS revealed that silk's processing was far from being completed as it took many more hours for a complete spontaneous conversion to occur through the sample. This insightful study reaffirmed our hypothesis, but also stressed the need for *in situ* rheology and optical measurements to directly relate the response to flow stress to the material's structure.

In Chapter 5, we addressed this issue by directly linking the silk's flow properties to its molecular structure by coupling ATR-IR with a rheometer, resulting in a novel tool (Rheo-IR). By carefully comparing standard reconstituted silk analogues to native silk feedstocks at the same protein concentration, we realised that their static infrared spectra were undistinguishable, even though they had drastically different flow properties. This explains why reconstituted silk feedstocks are still commonly used instead of native silk analogues for physicochemical studies[Zhang2012a; Zhang2012c] despite doubts on their "spinnability".[Holland2007] Consequently, the response to flow stress was essential to compare the artificial feedstock quality compared to the "gold standard" native silk which we know is capable of resulting in tough fibres if naturally spun. Lifting long standing ambiguities on the causality link between silk's flow properties and the structural changes, Rheo-IR revealed that silk's conformation conversion is only triggered at the onset of the shear thickening. At this point, the recoverable strain induced a sharp normal force increase,[Porter1995] eventually leading to sample slippage, which can easily be detected by our platform. However when this occurs, the secondary structure conversion is far from being completed, continuing spontaneously thereafter once stress is stopped. Corroborating SAS measurements but on a smaller length scale, this study confirmed that shearing forces alone are unlikely to be entirely responsible for silk's processing. This led us to believe that other sources of stress occurring *in vivo*

could contribute to complete the spinning process, such as chemical perturbations or extensional flow. However, the sum of stresses could still be not enough to complete the silk-spinning process.

To answer this key question, it would have been challenging to input the right amount of chemical and extensional flow stress. Instead in Chapter 6, we use the silkworm's natural spinning behaviour and probed silk immediately after it was secreted by the silkworm and all applied stresses had stopped. Not only did we find that *Bombyx mori* silk is far from being dry once secreted (~35% dry weight), but also that it is a long way from being totally converted and actually the conversion proceeds despite removal of the applied stress. This led us to think that drying these wet silk filaments quickly after secretion could reduce the protein's mobility sufficiently to interrupt the spontaneous conversion process before its completion. In effect, decreasing the water content in the fibre increases silk's glass transition temperature T_g until they solidify.[Fu2009] These dry-spun fibres were found to have a lesser degree of crystallinity than those having aged in uncontrolled conditions. To validate the universality of this effect, I also studied the silk post processing of *Saturnia pavonia*. In addition to their paler coloration, we found that wild Saturnidae had a lower degree of crystallinity when spun dry as well. We thus linked our new insights onto post-processing conditions to silk's tanning (coloration darkening) of wild silks which was known to occur only in humid and oxygenated conditions.[Brunet1974; Gheysens2011a] Hence, our experiments provided evidence that silk's tanning could be permitted by silk's β-sheets conformation.

We also found that the sericin coating of partially spun silk fibres was soluble in demineralised water at room temperature. Thereafter, these degummed fibres could be easily dissolved in concentrated lithium bromide at room temperature (25 °C). Solubilised

under milder conditions, the resulting high-fidelity reconstituted silk feedstocks (Hi-Fi RSF) had flow properties very close from those of native silk whilst being capable of triggering conformation conversion under equivalent biologically relevant flow stresses. Our results implied that our novel Hi-Fi RSF had comparable propensity to use mechanical stress to transform its hierarchical structure. Based on these criteria, we believe we made the best artificial liquid silk feedstock ever reported and the first to deserve the adjective "analogue". In summary, the secret of achieving better reconstituted silk was not to reverse engineer the stress-induced denaturation, but to prevent most of the denaturation from occurring in the first place.

Although we gained several new insights into the spinning process of *Bombyx mori*, it represents only one of many thousands of types of silk present in nature.[Scoble1999; Regier2008b] In Chapter 7, we investigated silks from 36 other species to assess the chemical composition and structural diversity of this variable material. Infrared spectroscopy revealed that wild Saturnid silk feedstocks had distinct precursor secondary structures or molecules which are absent of *Bombyx mori* and spider dragline silks. Hence, compared to the wild silks measured, *Bombyx mori* appears as an outlier and cannot be assumed to accurately represent all type of silks. Using a chemometric approach, we found that silks from closely related species also produced similar silks, hinting that their infrared signature is phylogenetically informative.

8.3 Why is silk spun?

Using the main overarching insights of this thesis linking structure and properties, we now know better how is silk spun, but why is it processed this way? To answer this fundamental question, we must put the spinning mechanism into the wider context of fibrous protein

secretions. Most fibrous proteins are secreted by cells but remain inside the organism to provide structure.[Rudall1971; Mousa1998] Since these proteins are typically insoluble after assembly, they cannot be easily transported. Instead when used externally they normally form deposit structures growing out of the organism. For instance, keratin proteins are secreted from animals epidermis in nails, horns and hairs[Tombolato2010] whilst sclerotin forms the cuticle of arthropods.[Brunet1967] Another example of solid protein secretion is conchiolin which, once mineralised, forms the protective shell of gastropods such as snails.[Grégoire1980] Although these shells provide valuable protection, they cannot be grown readily and snails have to rely on another protein secretion mechanism for on-demand external uses. Serving lubrication, adhesion and protection, snails can quickly eject slime from their large exocrine mucous glands below their mouth.[Chan2007]

The exocrine glands of the velvet worm (*Onychophora*) are a stunning example of the speed at which fibrous proteins can be secreted. This worm uses a pair of disproportionally large tubular glands to eject sticky slime onto remote prey in order to ensnare them.[Baer2012] Once the fibrous proteins are secreted, the animal's behaviour cannot control the material's properties anymore. Although ejected fibrous protein can be secreted quickly, environmental conditions will dictate the material's properties after secretion. On the other hand, *in vivo* grown or deposited fibrous proteins, like keratin, offer full structural control, but are secreted extremely slowly as they are built-up progressively. The velvet worm has not evolved much in hundreds of millions of year whilst sharing the same ancestor of silkworms and spiders.[Craig1997]

Like ejection, spinning is another type of secretion mechanism. After the silk press, silkworms have no means of controlling spinning exempt for post-spinning draw.[Asakura2007] As evidence of the importance of controlling the stress, paralysing silkworms to prevent them

from using their silk press has an important effect on the resulting fibre mechanical properties.[Mortimer2013] The ducts of spiders are innervated providing the animal with a feedback mechanism allowing them to control the stream's diameter, flow rate and thus the flow stress applied[Craig1997; Knight2000; Davies2013] resulting is variable thread tensile properties.[Madsen1999] The gland's morphology and the composition of the feedstock appear to be also indicative of the degree of control permitted by the animal's behaviour. Some glands are round shaped with a rudimentary spinning duct. [Vollrath2001; Dicko2008] Glands such as a spider's aggregate produce silks that can easily flow through the duct.[Nentwig2013] In contrast, some other glands such as the spider's major ampulate produce high-viscosity feedstocks and have progressive tapering with an elaborated spinning duct.[Vollrath2001; Dicko2008] Dicko et al. suggested that more complex glands are required to process silk feedstocks with a greater elastic component caused by higher glycine and lower proline content.[Dicko2008] The Scytodidae spider venom gland could appear to represent an exception to the pulled out spinning mechanism as it ejects silk filaments whilst spitting saliva-like secretions.[Nentwig2013] However, we believe that the ejected low viscosity spit would pull the silk fibres out of the mandible glands similarly to using the wind gusts during ballooning. As shown in Chapter 5, the rheological properties of silks are viscoelastic, which can be interpreted as a middle ground between a controlled deposition solid (grown) and an ejected liquid (pushed out).[Terry2004; Holland2006; Moriya2009]

Using this thesis's advancements in our knowledge, we now understand that these specialised glands of Lepidoptera secrete silk which is only partially formed upon secretion, with curing afterwards dependent on the environmental conditions and post-processing by the animal. By partially assembling the material *in vivo*, spinning provides arthropods with some degree of control over the fibrous protein properties whilst still allowing flow, but only just. Because of silk's high viscosity and its elastic component, it is more readily pulled

out instead of being ejected. Therefore, I propose silk is spun because it is the best mechanism which allows the secretion of a viscoelastic material, by offering the ability to tune the properties with the secretion speed.

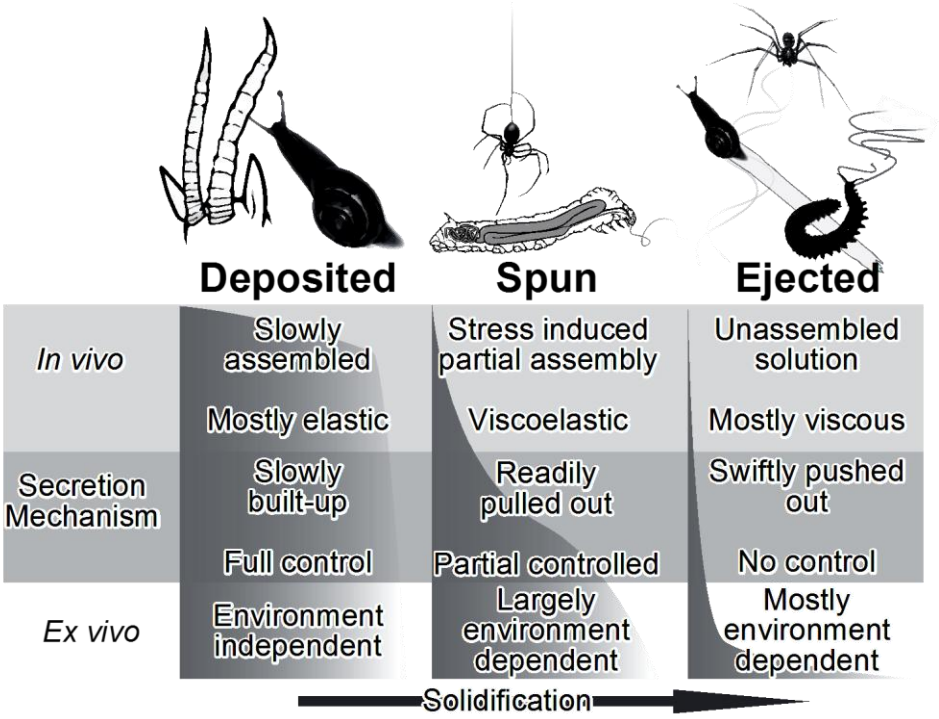


Figure 8.1 A graphical summary representing the techniques used and the types of silk measured for the thesis work. The lower part lists the attributes of deposition and ejection as well as the compromise achieved by spinning. The deposited example is a *Gazella* grown keratin horn and a gastropod shell whilst the ejected example is an *Onychophora* (red velvet worm) and a *Scytodes fusca* (spitting spider).

Figure 8.1 shows the halfway position between deposition and ejection secretion mechanism, which I believe spinning occupies. The degree of stress control should vary depending on the instability of the silk feedstock and the complexity of the spinning apparatus.[Dicko2008] Hence, I would expect spider to have greater degree of control than Lepidoptera silk, for instance. Since silks have evolved many times to the same solution for pulling a thread out,[Craig1997; Holland2006] this compromise is likely to represent the optimised solution for secreting partially solidified proteins.

8.4 Thesis Impact

The main conclusions of this thesis on how silk is spun will certainly make an important contribution to the scientific field. In addition, their practical nature could have an important commercial impact by changing the textile industry practices as well as improving the starting material of silk based biomaterials.

Cocoon infrared spectra could be phylogenetically informative

Silkworms produce cocoons with a wide variety of morphologies, structures and chemical compositions.[Gheysens2011b; Chen2012c] A high signal to noise ratio ATR-IR spectrum can be collected from the surface of a cocoon in less than one minute and is non-damaging. Moreover, entomological collections around the world comprising specimen cocoons from thousands of silkmoth species are available for borrowing.[Suarez2004] Infrared spectra appear to contain information relevant to the phylogeny of silkmoths, which was not entirely surprising considering that silk proteins are expressed by several genes. This approach thus represents a great opportunity to study the diversity of silkmoths. An easier alternative to nuclear gene sequencing, ATR-IR could thus become a valuable tool to help taxonomists tackling systematic classification ambiguities. Because cocoon construction is an important part of the silkmoth's life cycle and depends on the animal's behaviour, it is expected to depend on multiple genes. We would also expect geographical constraints to play an important part in the chemical composition of cocoons as they needed to adapt to their environment. Although they are harder to source, the same approach could be applied to separate animal behaviour and environmental effects.

Response to flow stress is required to evaluate the quality of feedstocks

Infrared spectroscopy and small angle X-ray scattering measurements did not reveal any structural differences between static NSF and RSF and yet their rheologies are very different. This finding has two important implications. Because spectroscopy techniques appear to be blind to the difference when no stress is applied, this emphasized the need of a biologically relevant perturbation to determine the liquid silk feedstock's quality, ideally using rheo-optic platforms. Along this line, we developed novel platforms coupling infrared spectroscopy and small angle scattering to rheology which proved valuable for evaluating samples' stress sensitivity. The main impact of these platforms was to remove ambiguities concerning the structural causes of silk's complex flow properties by directly linking structure, function and macroscopic properties.

Silk's formation is not fully controlled by the animal

Using the insights into spinning derived from our rheo-optic platforms and other *in situ* measurements, we found that silk would be only partially formed at secretion. Its formation is thus dependent on the external environment thereafter. This finding has profound repercussions as it directly supports why post-processing is an effective way to modulate silk's properties. Since secreted silk is still above its humidity dependent glass transition temperature T_g, it can stretch further to increase molecular alignment[Zhou2009] and/or be stressed to induce more β-sheet crystallinity.[Perez-Rigueiro2009] Freshly spun silk fibres can also be simply left above their T_g for several hours at room temperature to let the spontaneous conversion modulate the degree of protein conversion. Although this glass transition appears to be changing the tensile modulus,[Fu2009] the softening allows the irreversible protein conversion. Therefore, it becomes essential to keep silk fibres at temperatures below their glass transition temperature to preserve the remaining "unspun" native conformation. Storage conditions would thus need to be carefully controlled to prevent

undesired crystallisation. This phenomenon was also observed for wild silks implying that it is likely to be applicable to all β silks. For wild silk, however, our work in Chapter 6 provided evidence that the tanning process (darkening) of these silks is dependent on the conformation change from helices and turns to β-sheets. Our novel insight could provide a straightforward explanation as to why the tanning normally occurs *ex vivo*, unlike the exceptional case presented in Figure 6.8. This observation also corroborates the fact that wild silk tanning can be inhibited by desiccation. Hence, this insight could potentially improve the consistency of raw silk production.

Partially formed silk makes better artificial silk feedstocks

The availability of consistent and less crystalline raw silk obtained by dry spinning will certainly have game-changing repercussions for artificial silk feedstock productions. The harsh processing conditions required for solubilising highly crystalline and tanned silks is not without consequences as it is known to cause collateral damage to the protein.[Yamada2001; Wray2011; Cho2012; Wang2013] Instead of trying to reverse silk's denaturation process, which has not been proven to be possible for silk, we prevented it from occurring in the first place. The resulting dry spun fibres required much milder solubilisation conditions, resulting in high-fidelity feedstocks with flow properties and shear sensitivity that were very close from those of native silk feedstocks. Obtaining silk fibres that are only partially denatured then solubilised thus represents a much more convenient approach for obtaining scalable quantities of native-like feedstocks than dissecting individual silkworms. If processed appropriately, we expect our improved artificial feedstocks to also have better solid mechanical properties once spun back into filaments or cast into different shapes. As Figure 6.7 suggests, partially processed silk fibres are also untanned, meaning that dry spinning could also make wild silkworm cocoons easier to degum and solubilise. This could be of

particular interest since wild silk species have varied chemical composition (Chapter 7) and could express distinct interesting properties. For instance, previous reports suggest that the high proportion of RGD pattern could be responsible for *Antheraea myllita*'s better cell adhesion properties.[Acharya2009;Silva2013] Since wild silks such as those from the Antheraea genus are more challenging to reprocess, this method could prove particularly useful for making biomedical materials.

Not only are dry-spun fibres easier to solubilise, but they are also more consistent as the control of the spinning environment removes an important source of variability. In addition, it is also easier to remove the sericin gum from these fibres. Probably because of the lower degree of cross-linking between fibroin filaments and the sericin coating, the gum flakes out and dissolves with ease when immersed in pure water at room temperature. This finding has far-reaching implications as the boiling of cocoons for degumming can represent up to 50% of the processing energy consumption for the silk textile industry.[Vollrath2013b] Ensuring that silkworms spin in a dry environment would be comparatively much cheaper. In addition, this method would remove the need to purchase degumming chemicals such as sodium carbonate or Marseille soap. If implemented in the silk industry, this dry-spinning method should increase quality consistency whilst decreasing production cost, boosting its overall profitability.

8.5 Future directions

This thesis brings many novel insights to silk spinning and *ex vivo* processing, but also raises many additional questions which would be interesting to address. We determined the shear flow properties of silk and studied their structural causes. However, extensional flow is also expected to play an important role silk's processing, perhaps even a more significant

role than shear. As a new direction, it would therefore be interesting to couple extensional rheology with spectroscopy and scattering to determine what are the consequences of extensional flow stress on silk's molecular structure and orientation once shear forces become ineffective due to wall slippage. The geometry of the extensional flow would also need to be of comparable size to the natural spinning controlled duct to ensure that water can diffuse sufficiently slowly for the phase separation to occur.

In Chapter 6, we demonstrated that silk's conversion is continued above a relative humidity of 78% at room temperature, which agreed with the changes in the glass transition temperature observed for silkworm silk.[Fu2009] However in order to obtain the entire glass transition master curve, different temperatures from 0 °C to denaturation temperature (~65 °C) should have been used in addition to room temperature. In addition, such an experiment would have given us access to the temperature dependency of the spontaneous conversion process across the water content range.

This thesis provides evidence implying that the wild silk's tanning process required the protein conformation present in spun silk. A possible explanation for this phenomenon could be that the cross-linking molecules would preferably interact with the specific secondary structure. However, inducing the conformation conversion under an inert atmosphere before introducing oxygen would have allowed the definitive resolving of the tanning from the β-sheet formation phenomenon.

The work presented implies that the amount of crystalline β-sheets formed after secretion is relatively small, but has not been quantified. This could have been done by probing a bundle of dry spun fibres by wide angle scattering. Wide angle X-ray scattering is a well-established technique for fibre diffraction and can provide scattering patterns rapidly.[Riekel2000] However, wide angle neutron diffraction would present an interesting

opportunity to isotopicaly label the β-sheets subsequently formed under spontaneous conversion using deuterated water vapour above the fibre's glass transition. It would thus quantify both their proportion and relative orientation to those formed *in vivo*.

Although not attempted for wild silks, I envisage that dry spun fibre would be also easier to degum as they should not require a demineralisation step to remove the calcium oxalate crystals. In addition, it would be interesting and important to validate that the high fidelity reconstitution process is applicable to all Lepidoptera silks as our experiments imply.

Finally, the flow properties of *Bombyx mori* high fidelity reconstituted silk feedstock (Hi-Fi RSF) lead me to believe that they would be suitable analogues for spinning. Once bio-inspired devices and spinning methods prove effective at producing native-like fibres from native feedstocks, the ultimate test would be to spin these from Hi-Fi RSF. Although the prospects are brighter with improved feedstocks, until we match the fibre's mechanical properties it would be premature to claim that we have managed to copy Nature's remarkable solution for producing high performance fibres.

References

Agarwal, N., D. A. Hoagland, et al. (1997). Journal of Applied Polymer Science **63**(3): 401-410.

Akai, H. (1983). Experientia **39**(5): 443-449.

Alexander, L. E. (1969). X-ray diffraction methods in polymer science. New York, John Wiley & Sons.

Altman, G. H., F. Diaz, et al. (2003). Biomaterials **24**(3): 401-416.

Andrus, P. G. (2006). Technology in Cancer Research & Treatment **5**(2): 157-167.

Anghileri, A., R. Lantto, et al. (2007). Journal of Biotechnology **127**: 508-519.

Arnott, H. J. and M. A. Webb (2000). International Journal of Plant Sciences **161**(1): 133-142.

Asakura, T., A. Kuzuhara, et al. (1985). Macromolecules **18**(10): 1841-1845.

Asakura, T. and Y. Nakazawa (2004). Macromolecular Bioscience **4**: 175-185.

Asakura, T., R. Sugino, et al. (2002a). Protein Sci **11**(8): 1873-7.

Asakura, T., K. Umemura, et al. (2007). Biomacromolecules **8**(1): 175-181.

Asakura, T., J. M. Yao, et al. (2002b). Journal of the American Chemical Society **124**(30): 8794-8795.

Ashby, M. F., L. J. Gibson, et al. (1995). Proceedings of the Royal Society of London Series A-Mathematical and Physical Sciences **450**(1938): 123-140.

Baer, A. and G. Mayer (2012). Journal of Morphology **273**(10): 1079-1088.

Baltimore, D. (1977). Nobel lectures in molecular biology, 1933-1975. New York, Elsevier North-Holland.

Bandekar, J. and S. Krimm (1979). Proceedings of the National Academy of Sciences of the United States of America **76**(2): 774-777.

Bandekar, J. and S. Krimm (1980). Biopolymers **19**(1): 31-36.

Barnes, H. A., J. F. Hutton, et al. (1989). An introduction to rheology, Elsevier.

Barth, A. (2000a). Spectrochimica Acta Part A: Molecular and Biomolecular Spectroscopy **56**(6): 1223-32.

Barth, A. (2000b). Progress in Biophysics & Molecular Biology **74**: 141-173.

Barth, A. (2007). Biochimica Et Biophysica Acta-Bioenergetics **1767**(9): 1073-1101.

Beckwitt, R. and S. Arcidiacono (1994). Journal of Biological Chemistry **269**(9): 6661-3.

Benedict, J. B., J. H. Freudenthal, et al. (2008). Journal of the American Chemical Society **130**(32): 10714-10719.

Birge, N. O. and S. R. Nagel (1985). Physical Review Letters **54**(25): 2674-2677.

Borsboom, M., W. Bras, et al. (1998). Journal of Synchrotron Radiation **5**: 518-520.

Bosch, A., A. Minan, et al. (2008). Journal of Clinical Microbiology **46**(8): 2535-2546.

Boulet-Audet, M., T. Buffeteau, et al. (2010). Journal of Physical Chemistry B **114**(24): 8255-8261.

Boulet-Audet, M., T. Lefèvre, et al. (2008). Applied Spectroscopy **62**(9): 956-962.

Boulet-Audet, M., A. E. Terry, et al. (2013). Acta Biomaterialia **10**(2): 776-784.

Boulet-Audet, M., F. Vollrath, et al. (2011). Physical Chemistry Chemical Physics **13**(9): 3979-3984.

Bower, D. I. (1981). Journal of Polymer Science Part B-Polymer Physics **19**(1): 93-107.

Briandet, R., E. K. Kemsley, et al. (1996). Journal of Agricultural and Food Chemistry **44**(1): 170-174.

Broglie, L. d., W. C. Price, et al. (1973). Wave mechanics; the first fifty years. A tribute to professor louis de broglie, nobel laureate, on the 50th anniversary of the discovery of the wave nature of the electron. New York, Wiley.
Brooks, A. E., H. B. Steinkraus, et al. (2005). Biomacromolecules **6**(6): 3095-3099.
Brower, A. V. Z. and R. DeSalle (1998). Insect Molecular Biology **7**(1): 73-82.
Brunet, P. C. J. (1967). Endeavour **26**(98): 68-74.
Brunet, P. C. J. and B. C. Coles (1974). Proceedings of the Royal Society of London Series B-Biological Sciences **187**(1087): 133 - 170.
Buchner, J. (2004). Protein folding handbook. Weinheim, Wiley-VCH.
Bunning, T. J., H. Jiang, et al. (1994). Silk Polymers **544**: 353-358.
Burger, C., B. S. Hsiao, et al. (2010). Polymer Reviews **50**(1): 91-111.
Cai, S. W. and B. R. Singh (2004). Biochemistry **43**(9): 2541-2549.
Cao, Y. and B. C. Wang (2009). International Journal of Molecular Sciences **10**(4): 1514-1524.
Castelletto, V., J. Fisher, et al. (2002). Colloids and Surfaces a-Physicochemical and Engineering Aspects **211**(1): 9-18.
Chan, B., S. Ji, et al. (2007). Journal of Intelligent Material Systems and Structures **18**(2): 111-116.
Chari, R., K. Jerath, et al. (2009). Pharmaceutical Research **26**(12): 2607-2618.
Chaudhury, S., C. Dicko, et al. (2011). Journal of Bone and Joint Surgery-British Volume **93B**(3): 370-377.
Chen, F., D. Porter, et al. (2010a). Physical Review E **82**(4).
Chen, F., D. Porter, et al. (2012a). Acta Biomater **8**(7): 2620-7.
Chen, F., D. Porter, et al. (2012b). Journal of the Royal Society Interface **9**(74): 2299-2308.
Chen, F. J., D. Porter, et al. (2012c). Materials Science & Engineering C-Materials for Biological Applications **32**(4): 772-778.
Chen, P., H. S. Kim, et al. (2008). Macromolecular Research **16**(6): 539-543.
Chen, X., D. P. Knight, et al. (2009). Soft Matter **5**(14): 2777-2781.
Chen, X., D. P. Knight, et al. (2001a). Polymer **42**(25): 9969-9974.
Chen, X., D. P. Knight, et al. (2002a). Biochemistry **41**(50): 14944-14950.
Chen, X., D. P. Knight, et al. (2002b). Biomacromolecules **3**(4): 644-648.
Chen, X., Z. Shao, et al. (2007). Proteins-Structure Function and Bioinformatics **68**(1): 223-31.
Chen, X., Z. Shao, et al. (2001b). Biophysical Chemistry **89**(1): 25-34.
Chen, X., Z. Z. Shao, et al. (2006). Soft Matter **2**(6): 448-451.
Chen, X., L. Zhou, et al. (2003). Acta Chimica Sinica **61**(4): 625-629.
Chen, Z., X. Hao, et al. (2010b). Sheng Wu Yi Xue Gong Cheng Xue Za Zhi **27**(6): 1292-7.
Chevillard, M., P. Couble, et al. (1986). Nucleic Acids Res **14**(15): 6341-2.
Chirgadze, Y. N., O. V. Fedorov, et al. (1975). Biopolymers **14**(4): 679-694.
Cho, H. J., C. S. Ki, et al. (2012). International journal of biological macromolecules **51**(3): 336-41.
Colgin, M. A. and R. V. Lewis (1998). Protein Science **7**: 667-672.
Collins, A. M., N. J. V. Skaer, et al. (2009). Advanced Materials **21**(1): 75-78.
Colthup, N. B. (1964). Introduction to infrared and raman spectroscopy. New York, Academic Press.
Coulombe, P. A. and M. B. Omary (2002). Current Opinion in Cell Biology **14**(1): 110-122.
Craig, C. (1997). Annual review of entomology **42**: 231-267.
Cunha, C., S. Panseri, et al. (2011). Nanomedicine-Nanotechnology Biology and Medicine **7**(1): 50-59.
Czarnik-Matusewicz, B., M. Matusiak-Kucharska, et al. (2009). Polish Journal of Chemistry **83**(5): 999-1011.

Dandu, R. and H. Ghandehari (2007). Progress in Polymer Science **32**(8-9): 1008-1030.
Danks, H. V. (2004). European Journal of Entomology **101**(3): 433-437.
Davies, G. J., D. P. Knight, et al. (2013). Tissue & Cell **45**(5): 306-311.
de Gennes, P. G. (1972). Comptes Rendus Hebdomadaires des Seances de l'Academie des Sciences, Serie B (Sciences Physiques) **274**(2): 142-144144.
deJongh, H. H. J., E. Goormaghtigh, et al. (1996). Analytical Biochemistry **242**(1): 95-103.
Dicko, C., J. M. Kenney, et al. (2006). Fibrous Proteins: Amyloids, Prions and Beta Proteins **73**: 17-+.
Dicko, C., D. Porter, et al. (2008). Biomacromolecules **9**(1): 216-221.
Dicko, C., D. Porter, et al. (2010). The relevance of silks to amyloids. Functional amyloid aggregation. S. R. a. M. Bucciantini, Research Signpost.
Dicko, C., F. Vollrath, et al. (2004). Biomacromolecules **5**(3): 704-710.
Dobson, C., S. Pechmann, et al. (2009). Protein aggregation prediction systems. T. O. S. T. L. C. C. C. B. T. N. Cambridge Enterprise Limited. WO. **GB2008/051055**.
Doe, N. H. and P. L. Foster (2006). Rotary rheometer magnetic bearing. US, US 4524611 A (Jun, 1986) Richon et al. 73/543.5; US 4630468 A (Dec, 1986) Sweet 73/544.3; US 4878377 A (Nov, 1989) Abel 73/543.2; US 5142175 A (Aug, 1992) Watanabe 310/90.5; US 5777212 A (Jul, 1998) Sekiguchi et al. 73/543.3; US 6218751 B1 (Apr, 2001) Bohlin 310/90.5; US 6359357 B1 (Mar, 2002) Blumenstock 310/90.5; US 6572610 B1 (Jun, 2003) Kovalcheck et al. 606/21. **11364342**.
Doi, M. and S. F. Edwards (1978). Journal of the Chemical Society-Faraday Transactions Ii **74**: 918-932.
Doi, M. E. S. F. (1987). The theory of polymer dynamics. Oxford [Oxfordshire]; New York, Clarendon Press ; Oxford University Press.
Dong, Z. Y., R. V. Lewis, et al. (1991). Archives of Biochemistry and Biophysics **284**(1): 53-57.
Economy, J., F. Frechette, et al. (1977). Flame resistant cloth. US. **05378760**.
Eker, F., X. Cao, et al. (2003). Journal of Physical Chemistry B **107**(1): 358-365.
Elices, M., G. V. Guinea, et al. (2011). Macromolecules **44**(5): 1166-1176.
Fahnestock, S. R. and L. A. Bedzyk (1997). Applied Microbiology and Biotechnology **47**(1): 33-39.
Fahrenfort, J. (1961). Spectrochimica Acta **17**(7): 698-709.
Fan, H. B., H. F. Liu, et al. (2009). Biomaterials **30**(28): 4967-4977.
Fan, L., M. Degen, et al. (2010). The absolute calibration of a small-angle scattering instrument with a laboratory x-ray source. Xiv international conference on small-angle scattering. G. Ungar. **247**.
Fang, Q. Q., S. Cho, et al. (1997). Systematic Biology **46**(2): 269-283.
Farrell, B. D., A. S. Sequeira, et al. (2001). Evolution **55**(10): 2011-2027.
Ferry, J. D. (1959). Reviews of modern physics **31**(1): 130-134.
Ferry, J. D. (1980). Viscoelastic properties of polymers. New York, Wiley VCH.
Feustel, M. (2006). Apparatus for determining rheological properties. United State.
Finnigan, B., K. Jack, et al. (2005). Macromolecules **38**(17): 7386-7396.
Fisher, R. (1936a). Annals of Eugenics **7**: 179-188.
Fisher, R. A. (1936b). Annals of eugenics. **7**: 1936-37.
Foo, C. W. P., E. Bini, et al. (2006). Applied Physics A: Materials Science & Processing **82**(2): 223-233.
Franceschi, V. R. and P. A. Nakata (2005). Calcium oxalate in plants: Formation and function. Annual review of plant biology. **56:** 41-71.
Freddi, G., Y. Gotoh, et al. (1994). Journal of Applied Polymer Science **52**(6): 775-781.
Freddi, G., A. Svilokos, et al. (1993). Journal of Applied Polymer Science **48**(1): 99-106.
Fringeli, U. P. (1992). Chimia **46**(5): 200-214.

Fringeli, U. P. and H. H. Günthard (1980). Infrared membrane spectroscopy. Molecular biology, biochemistry and biophysics. E. Grell. Berlin, Springer Verlag. **31:** 270-332.
Fu, C. J., D. Porter, et al. (2009). Macromolecules **42**(20): 7877-7880.
Garside, P., S. Lahlil, et al. (2005). Applied Spectroscopy **59**(10): 1242-1247.
GB (1986). Animals (scientific procedures) act 1986. 1986 chapter 14. 1986 chapter 14. London, H.M.S.O.
Geddes, A. J., K. D. Parker, et al. (1968). Journal of Molecular Biology **32**(2): 343-358.
Geissler, E. (2000). Structure and dynamics of biomolecules : Neutron and synchrotron radiation for condensed matter studies. New York, Oxford University Press.
Gellynck, K., P. C. M. Verdonk, et al. (2008). Journal of Materials Science-Materials in Medicine **19**(11): 3399-3409.
Gheysens, T. (2011a). Small molecules in silks. Zoology Department. Oxford University press, University of Oxford. **DPhil**.
Gheysens, T., L. Beladjal, et al. (2005). Journal of Arachnology **33**(2): 549-557.
Gheysens, T., A. Collins, et al. (2011b). Biomacromolecules **12**(6): 2257-2266.
Glatter, O. K. O. (1982). Small angle x-ray scattering. London; New York, Academic Press.
Golub, G. H. and C. F. Van Loan (1996). Matrix computations. Baltimore, Johns Hopkins University Press.
Good, I. L., J. M. Kenoyer, et al. (2009). Archaeometry **51**: 457-466.
Goormaghtigh, E., V. Cabiaux, et al. (1994a). Determination of soluble and membranes protein structure by fourier transform infrared spectroscopy ii. Experimental aspects, side chain structure, and h/d exchange. Physicochemical methods in the study of biomembranes. H. J. Hilderson and G. R. Ralston. New York, Plenum Press. **23:** 363-403.
Goormaghtigh, E., V. Cabiaux, et al. (1994b). Determination of soluble and membranes protein structure by fourier transform infrared spectroscopy iii. Secondary structures. Physicochemical methods in the study of biomembranes. H. J. Hilderson and G. R. Ralston. New-York, Plenum Press. **23:** 404-450.
Goormaghtigh, E., J.-M. Ruysschaert, et al. (2006). Biophysical Journal **90**(8): 2946-2957.
Gordon, J. S. (2004). An empire of wealth : The epic history of american economic power. New York, HarperCollins.
Gosline, J. M., M. E. DeMont, et al. (1986). Endeavour **10**(1): 37-43.
Gosline, J. M., M. W. Denny, et al. (1984). Nature **309**(5968): 551-552.
Gosline, J. M., P. A. Guerette, et al. (1999). Journal of Experimental Biology **202**(23): 3295-3303.
Graessley, W. (1967). Journal of Chemical Physics **47**(6): 1942-&.
Greenwoo, J. and P. G. Rose (1974). Journal of Materials Science **9**(11): 1809-1814.
Grégoire, C. (1980). The conchiolin matrices in nacreous layers of ammonoids and fossil nautiloids 1. 1. Mainz, Akademie der Wiss. u.d. Literatur [u.a.].
Gregoriou, V. G., S. Tzavalas, et al. (2004). Applied Spectroscopy **58**(6): 655-661.
Greving, I., C. Dicko, et al. (2010). Soft Matter **6**(18): 4389-4395.
Griffiths, D. J. (2005). Introduction to quantum mechanics. Upper Saddle River, NJ, Pearson Prentice Hall.
Griffiths, P. R. and J. A. De Haseth (1986). Fourier transform infrared spectrometry. New York, Wiley.
Grubb, D. T. and L. W. Jelinski (1997). Macromolecules **30**(10): 2860-2867.
Guan, J., F. Vollrath, et al. (2011). Biomacromolecules.
Guinier, A. (1939). La diffraction des rayons x aux très pétits angles: Application à l'etude de phénomènes ultramicroscopiques. Paris, Masson.
Guinier, A. and G. Fournet (1955). Small-angle scattering of x-rays. New York, Wiley.

Gupta, A., P. Tandon, et al. (1997). Polymer **38**(10): 2389-2397.
Gupta, S., M. Hunter, et al. (2009). Applied Optics **48**(10): D45-D51.
Halsted, W. S. (1913). Journal of the American Medical Association **60**: 1119-1126.
Hamley, I. W., S. Garnett, et al. (1996). Journal of Chemical Physics **104**(24): 10046-10054.
Hansen, W. N. (1965a). Spectrochimica Acta **21**(1): 209-210.
Hansen, W. N. (1965b). Spectrochimica Acta **21**(4): 815-833.
Hardy, J. G., L. M. Römer, et al. (2008). Polymer **49**(20): 4309-4327.
Harrick, N. J. (1965). Journal of the optical society of America **55**(7): 851-856.
Harrick, N. J. (1967). Internal reflection spectroscopy. New York, John Wiley & Sons.
Hartigan, J. A. (1975). Clustering algorithms. New York, Wiley.
He, S. J., R. Valluzzi, et al. (1999). International Journal of Biological Macromolecules **24**(2-3): 187-195.
Heenan, R. K., S. E. Rogers, et al. (2011). Neutron News **22**(2): 19-21.
Henderson, R. (1990). Proceedings of the Royal Society B-Biological Sciences **241**(1300): 6-8.
Hepburn, H. R., H. D. Chandler, et al. (1979). Insect Biochemistry **9**(1): 69-77.
Hermans, P. H. (1946). Contributions to the physics of cellulose fibres. New York-Amsterdam, Interscience Publishers, Inc.
Hinman, M. B. and R. V. Lewis (1992). Journal of Biological Chemistry **267**(27): 19320-19324.
Holland, C., D. Porter, et al. (2012a). Biopolymers **97**(6): 362-367.
Holland, C., A. E. Terry, et al. (2006). Nature Materials **5**(11): 870-874.
Holland, C., A. E. Terry, et al. (2007). Polymer **48**: 3388-3392.
Holland, C., J. S. Urbach, et al. (2012b). Soft Matter **8**(9): 2590-2594.
Holland, C., F. Vollrath, et al. (2012c). Advanced Materials **24**(1): 105-109.
Horrocks, N. P. C., F. Vollrath, et al. (2013). Comparative Biochemistry and Physiology A-Molecular & Integrative Physiology **164**(4): 645-652.
Hossain, K., E. Ohyama, et al. (2003a). Journal of Physical Chemistry B **107**: 8066-80733.
Hossain, K. S., N. Nemoto, et al. (2000). Rheological study on aqueous solutions of silk fibroin. XIIIth International Congress on Rheology, Cambridge.
Hossain, K. S., A. Ochi, et al. (2003b). Biomacromolecules **4**(2): 350-359.
Hossain, K. S., E. Ohyama, et al. (2003c). Journal of Physical Chemistry B **107**(32): 8066-8073.
Hu, X., D. Kaplan, et al. (2006a). Macromolecules **39**(18): 6161-6170.
Hu, Y., B. Y. Li, et al. (2006b). Journal of Physical Chemistry A **110**(39): 11279-11290.
Huemmerich, D., T. Scheibel, et al. (2004). Current Biology **14**(22): 2070-2074.
Huggins, M. L. (1943). Chemical Review **32**(2): 195-218.
Humenik, M., T. Scheibel, et al. (2011). Prog Mol Biol Transl Sci **103**: 131-85.
Hwang, J. S., J. S. Lee, et al. (2001). Biotechnology Letters **23**(16): 1321-1326.
Iizuka, E. (1968). Biochimica et Biophysica Acta **160**(3): 454-&.
Inoue, S., K. Tanaka, et al. (2000). Journal of Biological Chemistry **275**(51): 40517-40528.
Ishida, M., T. Asakura, et al. (1990). Macromolecules **23**(1): 88-94.
Ishii, S., T. Inokuchi, et al. (1984). Japanese Journal of Applied Entomology and Zoology **28**(4): 269-273.
Jabbarzadeh, A., J. D. Atkinson, et al. (2000). Physical Review E **61**(1): 690-699.
Jackson, C. and J. P. O'Brien (1995). Macromolecules **28**(17): 5975-5977.
Jackson, J. E. (1991). A user's guide to principal components. New York, Wiley.
Jacques, D. A. and J. Trewhella (2010). Protein Science **19**(4): 642-657.
Jacrot, B. and G. Zaccai (1981). Biopolymers **20**(11): 2413-2426.
Janeschitz-Kriegl, H., E. Ratajski, et al. (2003). Rheologica acta **42**(4): 355-364.
Jenkins, J. E., M. S. Creager, et al. (2010). Chem Commun (Camb) **46**(36): 6714-6.
Jensen, J. S., M. Egebo, et al. (2008). Journal of Agricultural and Food Chemistry **56**(10): 3493-3499.

Jeong, L., K. Y. Lee, et al. (2006). International Journal of Biological Macromolecules **38**(2): 140-144.
Kanaya, T., G. Matsuba, et al. (2007). Macromolecules **40**(10): 3650-3654.
Kansiz, M., P. Heraud, et al. (1999). Phytochemistry **52**(3): 407-417.
Kaplan, D. L., L. W. Tien, et al. (2012). Dynamic silk coatings for implantable devices. B. H. M. M. Trustees Of Tufts College. WO. **US2012/034490**.
Kataoka, K. and I. Uematsu (1977). Kobunshi Ronbunshu **34**(6): 457-464.
Kerkam, K., C. Viney, et al. (1991). Nature **349**(6310): 596-598.
Kim, H. and S. J. Jeon (2001). Bulletin of the Korean Chemical Society **22**(8): 807-815.
Kim, M. H., C. J. Glinka, et al. (2006). Macromolecules **39**(14): 4775-4787.
Kim, U. J., J. Park, et al. (2004). Biomacromolecules **5**(3): 786-92.
Kim, Y., D. S. Himmelsbach, et al. (2007). Journal of Agricultural and Food Chemistry **55**(11): 4327-4333.
Kino, R., T. Ikorna, et al. (2007). Journal of Bioscience and Bioengineering **103**(6): 514-520.
Knight, D. and F. Vollrath (1999a). Tissue & Cell **31**(6): 617-620.
Knight, D., F. Vollrath, et al. (2012). A method for demineralizing wild silk cocoons to facilitate reeling. M. C. O. S. P. R. R. A. O. Oxford Biomaterials Limited, M. The Chancellor and W. S. O. Scholars Of The University Of Oxford. WO. **GB2011/052113**.
Knight, D. P., M. M. Knight, et al. (2000). International Journal of Biological Macromolecules **27**(3): 205-210.
Knight, D. P. and F. Vollrath (1999b). Proceedings of the Royal Society of London Series B-Biological Sciences **266**(1418): 519-523.
Knight, D. P. and F. Vollrath (2001). Naturwissenschaften **88**(4): 179-182.
Knudsen, K. D., J. G. H. Cifre, et al. (1996). Macromolecules **29**(10): 3603-3610.
Kobayashi, M., T. Tanaka, et al. (2001). Abstracts of Papers of the American Chemical Society **222**: U258-U258.
Koch, M. H. J., P. Vachette, et al. (2003). Quarterly Reviews of Biophysics **36**(2): 147-227.
Kojic, N., J. Bico, et al. (2006). Journal of Experiemental Biology **209**(21): 4355-4362.
Kornfield, J. A., G. G. Fuller, et al. (1989). Macromolecules **22**(3): 1334-1345.
Kratky, O. and G. Porod (1949). Recueil Des Travaux Chimiques Des Pays-Bas-Journal of the Royal Netherlands Chemical Society **68**(12): 1106-1122.
Kratky, O., E. Schauenstein, et al. (1950). Nature **165**(4191): 319-320.
Krimm, S. and J. Bandekar (1986). Advances in Protein Chemistry **38**: 181-364.
Kronenberger, K., C. Dicko, et al. (2011). Naturwissenschaften.
Kubelka, J., P. Pancoska, et al. (1999). Applied Spectroscopy **53**(6): 666-671.
Kumaraswamy, G., R. K. Verma, et al. (2004). Macromolecules **37**(24): 9005-9017.
Kweon, H., S. O. Woo, et al. (2001). Journal of Applied Polymer Science **81**(9): 2271-2276.
Lafrance, C.-P., M. Pézolet, et al. (1991). Macromolecules **24**: 4948-4956.
Lazaris, A., S. Arcidiacono, et al. (2002). Science **295**(5554): 472-476.
Le Couteur, P. and J. Burreson (2003). Napoleon's buttons : How 17 molecules changed history. New York, Jeremy P. Tarcher/Putnam.
Lefèvre, T., S. Boudreault, et al. (2008). Biomacromolecules **9**(9): 2399-2407.
Lefevre, T., F. Paquet-Mercier, et al. (2009). Vibrational Spectroscopy **51**(1): 136-141.
Lefèvre, T., F. Paquet-Mercier, et al. (2011). Biopolymers **97**(6): 322-36.
Leisk, G. G., T. J. Lo, et al. (2010). Advanced Materials **22**(6): 711-+.
Lemaire, B. J., P. Panine, et al. (2002). Europhysics Letters **59**(1): 55-61.
Levrat, D. (1899). Notes sur l'elevage des vers a soie sauvages. Chambre de Commerce de Lyon, Laboratoire d'Étude de la soie. **10**.
Levy, Y. and J. N. Onuchic (2004). Proceedings of the National Academy of Sciences of the United States of America **101**(10): 3325-3326.

Li, G. Y., M. Thomson, et al. (2005). Applied Spectroscopy **59**(12): 1527-1533.
Li, G. Y., P. Zhou, et al. (2001). European Journal of Biochemistry **268**(24): 6600-6606.
Li, X.-G., L.-Y. Wu, et al. (2008). Biopolymers **89**(6): 497-505.
Liivak, O., A. Blye, et al. (1998). Macromolecules **31**(9): 2947-2951.
Lim, S. H., Food, et al. (1990). Sericulture training manual, Food and Agriculture Organization of the United Nations.
Lindner, P. Z. T. (2002). Neutrons, x-rays, and light : Scattering methods applied to soft condensed matter. Amsterdam; Boston, Elsevier.
Ling, S., Z. Qi, et al. (2011). Biomacromolecules **12**(9): 3344-9.
Liu, Y., Z. Z. Shao, et al. (2005). Chemical Communications **19**: 2489 - 2491.
Liu, Y., A. Sponner, et al. (2008). Biomacromolecules **9**(1): 116-121.
Lombardi, S. J. and D. L. Kaplan (1990). Journal of Arachnology **18**(3): 297-306.
Lu, X., J. Wang, et al. (2011). Food Chemistry **129**(2): 637-644.
Lucas, F., J. T. B. Shaw, et al. (1956). Nature **178**(4538): 861-861.
Lv, Q., C. B. Cao, et al. (2005). Journal of Applied Polymer Science **96**(6): 2168-2173.
Machida, J. (1926). Proceedings of the Imperial Academy **2**(8): 421-422.
Madsen, B., Z. Z. Shao, et al. (1999). International Journal of Biological Macromolecules **24**(2-3): 301-306.
Maeder, M. (1987). Analytical Chemistry **59**(3): 527-530.
Magoshi, J., Y. Magoshi, et al. (1994). Mechanism of fiber formation of silkworm. Silk polymers: Materials science and biotechnology. **544:** 292-310.
Magoshi, J. and S. Nakamura (1985). Journal of Polymer Science **23**: 227-229.
Malíšek, V. r. and M. Miler (1971). Vibration spectroscopy. London, Iliffe.
Marcott, C., I. Noda, et al. (1991). Analytica Chimica Acta **250**(1): 131-143.
Mariey, L., J. P. Signolle, et al. (2001). Vibrational Spectroscopy **26**(2): 151-159.
Marsh, D. (1997). Biophysical Journal **72**(6): 2710-2718.
Marsh, R. E., R. B. Corey, et al. (1955a). Biochimica et Biophysica Acta **16**(1): 1-34.
Marsh, R. E., R. B. Corey, et al. (1955b). Acta Crystallographica **8**(11): 710-715.
Martel, A., M. Burghammer, et al. (2008a). Biomicrofluidics **2**(2): 24104.
Martel, A., M. Burghammer, et al. (2008b). Journal of the American Chemical Society **130**(50): 17070-17074.
Martel, A., M. Burghammer, et al. (2007). Biomacromolecules **8**(11): 3548-3556.
Martin, G., M. Guggiari, et al. (2012). Environmental Microbiology **14**(11): 2960-2970.
Martis, V., S. Nikitenko, et al. (2011). Crystal Growth & Design **11**(7): 2858-2865.
Max, J. J. and C. Chapados (2009). Journal of Chemical Physics **131**(18).
Meechaisue, C., P. Wutticharoenmongkol, et al. (2007). Biomedical Materials **2**(3): 181-188.
Meinel, L., S. Hofmann, et al. (2005). Biomaterials **26**(2): 147-155.
Meins, T., K. Hyun, et al. (2012). Macromolecules **45**(1): 455-472.
Michelson, A. A. M. E. W. B. L. (1887). On the relative motion of the earth and the luminiferous aether. London, Taylor & Francis.
Minoura, N., S. I. Aiba, et al. (1995). Biochemical and Biophysical Research Communications **208**(2): 511-516.
Mita, K., S. Ichimura, et al. (1994). Journal of Molecular Evolution **38**(6): 583-592.
Miyazawa, T. and E. R. Blout (1961). Journal of the American Chemical Society **83**(3): 712-719.
Mo, C., P. Wu, et al. (2006). Applied Spectroscopy **60**: 1438-1441.
Mo, C. L., C. Holland, et al. (2009a). Biomacromolecules **10**(10): 2724-2728.
Mo, C. L., P. Y. Wu, et al. (2009b). Vibrational Spectroscopy **51**(1): 105-109.
Moore, W. H. and S. Krimm (1976). Biopolymers **15**(12): 2465-2483.
Morita, S., M. Tanaka, et al. (2007). Applied Spectroscopy **61**: 867-872.

Moriya, M., K. Ohgo, et al. (2008a). Polymer **49**(4): 952-956.
Moriya, M., K. Ohgo, et al. (2008b). Polymer **49**(26): 5665-5669.
Moriya, M., F. Roschzttardtz, et al. (2009). Biomacromolecules **10**(4): 929-935.
Mortimer, B., C. Holland, et al. (2013). Biomacromolecules **14**(10): 3653-3659.
Mosbaek, C. R., P. V. Konarev, et al. (2012). Pharmaceutical Research **29**(8): 2225-2235.
Moulton, J. K. and B. M. Wiegmann (2004). Molecular Phylogenetics and Evolution **31**(1): 363-378.
Mousa, S. A. (1998). Cell adhesion molecules and matrix proteins : Role in health and diseases. Berlin; New York, Springer-Verlag.
Muller, W. S., L. A. Samuelson, et al. (1993). Langmuir **9**(7): 1857-1861.
Mykhaylyk, O. O., P. Chambon, et al. (2008). Macromolecules **41**(6): 1901-1904.
Myshakina, N. S., Z. Ahmed, et al. (2008). Journal of Physical Chemistry B **112**(38): 11873-11877.
Nagarkar, S., T. Nicolai, et al. (2010). Physical Chemistry Chemical Physics **12**(15): 3834-3844.
Nagarkara, S., A. Lele, et al. (2008). Xvth International Congress on Rheology - the Society of Rheology 80th Annual Meeting, **1027**: 573-575.
Nagasaki, Y., T. Yoshihara, et al. (2000). Journal of Physical Chemistry B **104**(13): 2846-2852.
Nakajima, B., K. Hirata, et al. (1981). International Journal of Biological Macromolecules **3**(1): 46-52.
Navarro, M., E. M. Benetti, et al. (2008). Langmuir **24**(19): 10996-11002.
Nentwig, W. (2013). Spider ecophysiology. Berlin; New York, Springer.
Nielsen, S. S., M. Moller, et al. (2012). Journal of Applied Crystallography **45**: 213-223.
Noda, I. (1990). Applied Spectroscopy **44**(4): 550-561.
Noda, I. (1993). Applied Spectroscopy **47**(9): 1329-1336.
Noda, I., A. E. Dowrey, et al. (1988a). Applied Spectroscopy **42**(2): 203-216.
Noda, I., A. E. Dowrey, et al. (1988b). Mikrochimica Acta **1**(1-6): 101-103.
O'Brien, J. P., S. R. Fahnestock, et al. (1998). Advanced Materials **10**(15): 1185-1195.
Oberprieler, R. G. (1997). Metamorphosis Occasional Supplement **3**: 142-155.
Oberprieler, R. G. and W. A. Nassig (1994). Nachrichten des Entomologischen Vereins Apollo **15**(3): 267-303.
Ochi, A., K. S. Hossain, et al. (2002a). Biomacromolecules **3**(6): 1187-1196.
Ochi, A., N. Nemoto, et al. (2002b). Journal of the Society of Rheology Japan **30**(5): 289-294.
Ohgo, K., F. Bagusat, et al. (2008). Journal of the American Chemical Society **130**(12): 4182-4186.
Okura, M., P. Chambon, et al. (2011). Journal of Polymer Science Part B-Polymer Physics **49**(9): 621-628.
Omenetto, F. G. and D. L. Kaplan (2010). Science **329**(5991): 528-31.
Orthaber, D., A. Bergmann, et al. (2000). Journal of Applied Crystallography **33**: 218-225.
P., E. A., L. J. E., et al. (2007). Annual international urolithiasis research symposium renal stone disease, New York, American institute of physics.
Panayiotou, H. and S. Kokot (1999). Analytica Chimica Acta **392**(2-3): 223-235.
Pauli, G. A. (2010). The blue economy : 10 years, 100 innovations, 100 million jobs. Taos, NM, Paradigm Publications.
Pauling, L., R. B. Corey, et al. (1951). Proceedings of the National Academy of Sciences of the United States of America **37**(4): 205-211.
Pearson, K. (1901). Philosophical Magazine **2**(6): 559-572.
Pedersen, J. S. and P. Schurtenberger (1996). Macromolecules **29**(23): 7602-7612.
Pellerin, C., M.-E. Rousseau, et al. (2005). Macromolecular Symposia **220**: 85-98.

Perez-Rigueiro, J., L. Biancotto, et al. (2009). International Journal of Biological Macromolecules **44**(2): 195-202.
Perry, H., A. Gopinath, et al. (2008). Advanced Materials **20**(16): 3070-3072.
Petrie, C. J. S. (1979). Elongational flows : Aspects of the behaviour of model elasticoviscous fluids. London; San Francisco, Pitman.
Petrie, C. J. S. (2006). Journal of Non-Newtonian Fluid Mechanics **137**(1-3): 1-14.
Planck, M. (1901). Annalen der Physik **309**(3): 553-563.
Pogodina, N. V., V. P. Lavrenko, et al. (2001). Polymer **42**(21): 9031-9043.
Pople, J. A., I. W. Hamley, et al. (1998). Macromolecules **31**(9): 2952-2956.
Porod, G. (1951). Kolloid-Zeitschrift and Zeitschrift Fur Polymere **124**(2): 83-114.
Porod, G. (1952). Kolloid-Zeitschrift and Zeitschrift Fur Polymere **125**(1): 51-57.
Porter, D. (1993). Polymer Engineering and Science **33**(7): 437-444.
Porter, D. (1995). Group interaction modelling of polymer properties. New York, Marcel Dekker.
Porter, D. and F. Vollrath (2008). Soft Matter **4**(2): 328-336.
Porter, D. and F. Vollrath (2009). Advanced Materials **21**(4): 487-492.
Porter, D. and F. Vollrath (2012). Biochimica et Biophysica Acta **1824**(6): 785-91.
Porter, D. and F. Vollrath (2013). Soft Matter(3): 643-646.
Porter, D., F. Vollrath, et al. (2005). The European Physical Journal E **16**(2): 199-206.
Preisner, O., J. A. Lopes, et al. (2007). Analytical and Bioanalytical Chemistry **387**(5): 1739-1748.
Putnam, C. D., M. Hammel, et al. (2007). Quarterly Reviews of Biophysics **40**(3): 191-285.
Putthanarat, S., S. Zarkoob, et al. (2002). Polymer **43**(12): 3405-3413.
Ramachandran, G. N., C. Ramakrishnan, et al. (1963). Journal of Molecular Biology **7**(1): 95-99.
Rammensee, S., D. Huemmerich, et al. (2006). Applied Physics A: Materials Science & Processing **82**(2): 261-264.
Rammensee, S., U. Slotta, et al. (2008). Proceedings of the National Academy of Sciences of the United States of America **105**(18): 6590-6595.
Reed, E. J., L. L. Bianchini, et al. (2011). Biopolymers.
Regier, J. C. (2005). Systematic Biology: 254.
Regier, J. C., C. P. Cook, et al. (2008a). Systematic Entomology **33**(1): 175-189.
Regier, J. C., Q. Q. Fang, et al. (1998). Molecular Biology and Evolution **15**(9): 1172-1182.
Regier, J. C., M. C. Grant, et al. (2008b). Systematic Entomology **33**(2): 219-228.
Regier, J. C., C. Mitter, et al. (2002). Insect Systematics & Evolution **33**(1): 9-21.
Reiser, K., R. J. McCormick, et al. (1992). FASEB Journal **6**(7): 2439-2449.
Riekel, C., C. Branden, et al. (1999). International Journal of Biological Macromolecules **24**(2-3): 179-186.
Riekel, C., B. Madsen, et al. (2000). Biomacromolecules **1**(4): 622-626.
Riekel, C. and F. Vollrath (2001). International Journal of Biological Macromolecules **29**(3): 203-210.
Rivlin, R. S. (1948). Philosophical Transactions of the Royal Society of London Series a-Mathematical and Physical Sciences **241**(835): 379-397.
Rockwood, D. N., R. C. Preda, et al. (2011). Nature Protocols **6**(10): 1612-1631.
Rössle, M., P. Panine, et al. (2004). Biopolymers **74**(4): 316-327.
Rouse, P. E. (1953). Journal of Chemical Physics **21**(7): 1272-1280.
Rousseau, M.-È., L. Beaulieu, et al. (2006). Biomacromolecules **7**(9): 2512-2521.
Rousseau, M. E., T. Lefèvre, et al. (2004). Biomacromolecules **5**(6): 2247-2257.
Roy, M., S. K. Meena, et al. (2012). Biointerphases **7**(1-4).
Rubatat, L. and O. Diat (2007). Macromolecules **40**(26): 9455-9462.

Rudall, K. M. and W. Kenchington (1971). A Rev Ent **16**: 73-96,2 pls.
Russell, T. P., J. S. Lin, et al. (1988). Journal of Applied Crystallography **21**: 629-638.
Sargut, S. T., P. Sayan, et al. (2010). Crystal Research and Technology **45**(1): 31-38.
Scelsi, L. and M. R. Mackley (2008). Rheologica acta **47**(8): 895-908.
Scheibel, T. (2004). Microbial Cell Factories **3**(14): 1-10.
Scheller, J., K. H. Guhrs, et al. (2001). Nature Biotechnology **19**(6): 573-577.
Schulz, H. and M. Baranska (2007). Vibrational Spectroscopy **43**(1): 13-25.
Scirocco, R., J. Vermant, et al. (2004). Journal of Non-Newtonian Fluid Mechanics **117**(2-3): 183-192.
Scoble, M. J. (1999). Geometrid moths of the world, CSIRO Publishing.
Sehnal, F. and M. Zurovec (2004). Biomacromolecules **5**(3): 666-674.
Sezutsu, H., H. Kajiwara, et al. (2007). Bioscience Biotechnology and Biochemistry **71**(11): 2725-2734.
Shao, J. Z., J. H. Zheng, et al. (2005). Journal of Applied Polymer Science **96**(6): 1999-2004.
Shao, Z., F. Vollrath, et al. (1999). Polymer **40**(10): 2493-2500.
Shao, Z. Z. and F. Vollrath (2002). Nature **418**(6899): 741-741.
Sharma, J., S. M. King, et al. (2010). Nuclear Instruments & Methods in Physics Research Section a-Accelerators Spectrometers Detectors and Associated Equipment **620**(2-3): 437-444.
Shen, Y., M. A. Johnson, et al. (1998). Macromolecules **31**(25): 8857-8864.
Shimura, K., A. Kikuchi, et al. (1976). Journal of Biochemistry **80**(4): 693-702.
Sigurdsson, E. M. C. M. G. M. (2012). Amyloid proteins : Methods and protocols. New York, Humana Press.
Silverstein, R. M. B. G. C. M. T. C. (1981). Spectrometric identification of organic compounds. New York, Wiley.
Simmons, A. H., C. A. Michal, et al. (1996). Science **271**(5245): 84-87.
Sinsawat, A., S. Putthanarat, et al. (2002). Polymer **43**(4): 1323-1330.
Sirichaisit, J., V. L. Brookes, et al. (2003). Biomacromolecules **4**(2): 387-394.
Sköld, K. P. D. L. (1986). Neutron scattering. Orlando, Academic Press.
Sonoyama, M., M. Miyazawa, et al. (1997). Applied Spectroscopy **51**(4): 545-547.
Sonoyama, M. and T. Nakano (2000). Applied Spectroscopy **54**(7): 968-973.
Stuart, B. (2004). Infrared spectroscopy fundamentals and applications. Chichester, Eng.; Hoboken, N.J., J. Wiley.
Suarez, A. V. and N. D. Tsutsui (2004). Bioscience **54**(1): 66-74.
Sukigara, S., M. Gandhi, et al. (2004). Polymer **45**(11): 3701-3708.
Sukopp, M., L. Marinelli, et al. (2002). Helvetica Chimica Acta **85**(12): 4442-4452.
Sun, Z., G. Qin, et al. (2013). Journal of the American Chemical Society **135**(9): 3675-3679.
Sutherland, T. D., J. S. Church, et al. (2011). Plos One **6**(2): e16489.
Suzuki, H., T. Kotaka, et al. (1969). Journal of Chemical Physics **51**(4): 1279-&.
Svergun, D. and M. Koch (2003). Reports on Progress in Physics.
Taddei, P., T. Arai, et al. (2006). Biomacromolecules **7**(1): 259-267.
Taddei, P. and P. Monti (2005). Biopolymers **78**(5): 249-258.
Takahash.Sy, G. Suzuki, et al. (1969). Journal of Insect Physiology **15**(3): 403-&.
Takahashi, Y., M. Gehoh, et al. (1999). International Journal of Biological Macromolecules **24**(2-3): 127-138.
Tamura, T., H. Inoue, et al. (1987). Molecular & General Genetics **207**(2-3): 189-195.
Tanaka, K. and S. Mizuno (2001a). Insect Biochemistry and Molecular Biology **31**(6-7): 665-677.
Tanaka, T., J. Magoshi, et al. (2001b). Journal of Thermal Analysis and Calorimetry **64**(2): 645-650.

Tashiro, Y., T. Morimoto, et al. (1968). J Cell Biol **38**(3): 574-88.
Tauler, R. (1995a). Chemometrics and Intelligent Laboratory Systems **30**(1): 133-146.
Tauler, R. and D. Barcelo (1993a). Trac-Trends in Analytical Chemistry **12**(8): 319-327.
Tauler, R., E. Casassas, et al. (1991). Analytica Chimica Acta **248**(2): 447-458.
Tauler, R., A. Izquierdoridorsa, et al. (1993b). Chemometrics and Intelligent Laboratory Systems **18**(3): 293-300.
Tauler, R., A. Izquierdoridorsa, et al. (1995b). Chemometrics and Intelligent Laboratory Systems **27**(2): 163-174.
Teigler, D. J. and H. J. Arnott (1972a). Tissue & Cell **4**(1): 173-185.
Teigler, D. J. and H. J. Arnott (1972b). Nature **235**(5334): 166-167.
Teixeira, S. C. M., G. Zaccai, et al. (2008). Chemical Physics **345**(2-3): 133-151.
Teramoto, H. and M. Miyazawa (2003). Journal of Insect Biotechnology and Sericology **72**(3): 157-162.
Teramoto, H. and M. Miyazawa (2005). Biomacromolecules **6**(4): 2049-2057.
Terry, A. E., D. P. Knight, et al. (2004). Biomacromolecules **5**(3): 768-772.
Tombolato, L., E. E. Novitskaya, et al. (2010). Acta Biomaterialia **6**(2): 319-330.
Tomita, M. (2011). Biotechnology Letters **33**(4): 645-654.
Tomlin, S. G. and C. R. Worthington (1956). Proceedings of the Royal Society of London Series a-Mathematical and Physical Sciences **235**(1201): 189-&.
Tsukada, M., M. Nagura, et al. (1991). Journal of Applied Polymer Science **43**(4): 643-649.
Tuskes, P. M. T. J. P. C. M. M. (1996). The wild silk moths of north america : A natural history of the saturniidae of the united states and canada. Ithaca, N.Y., Comstock Pub. Associates.
Um, I. C., H. Y. Kweon, et al. (2001). International Journal of Biological Macromolecules **29**(2): 91-97.
Utracki, L. A. and M. R. Kamal (1982). Polymer Engineering and Science **22**(2): 96-114.
van Beek, J. D., L. Beaulieu, et al. (2000). Nature **405**(6790): 1077-1079.
Van der Kloot, W. G. and C. M. Williams (1953a). Behaviour **5**: 141-156.
Van der Kloot, W. G. and C. M. Williams (1953b). Behaviour **5**: 157-174.
Venyaminov, S. Y. and N. N. Kalnin (1990). Biopolymers **30**(13-14): 1259-1271.
Vepari, C. and D. L. k. Kaplan (2007). Progress in Polymer Science **32**(8-9): 991-1007.
Vollrath, F. (2003). Precursor silk feedstock for forming filaments. WO. **EP0212033**.
Vollrath, F., R. Carter, et al. (2013a). Life cycle analysis of cumulative energy demand on sericulture in karnataka, india BACSA Biserica 2013.
Vollrath, F. and D. P. Knight (1999). International Journal of Biological Macromolecules **24**(2-3): 243-249.
Vollrath, F. and D. P. Knight (2001). Nature **410**(6828): 541-548.
Vollrath, F. and D. Porter (2006a). Applied Physics A: Materials Science & Processing **82**(2): 205-212.
Vollrath, F. and D. Porter (2006b). Soft Matter **2**: 377-385.
Vollrath, F. and D. Porter (2009). Polymer **50**(24): 5623-5632.
Vollrath, F., D. Porter, et al. (2011). Soft Matter **7**(20): 9595-9600.
Vollrath, F., D. Porter, et al. (2013b). Mrs Bulletin **38**(01): 73-80.
Vrahopoulou, E. P. and A. J. McHugh (1987). Journal of Non-Newtonian Fluid Mechanics **25**(2): 157-175.
Waldbaue.Gp and Sternbur.Jg (1967). Ecology **48**(2): 312-&.
Walters, K. (1975). Rheometry. London; New York, Chapman and Hall ; Wiley.
Wang, B. N., R. D. Bennett, et al. (2007). Journal of Physical Chemistry C **111**(16): 5859-5865.
Wang, Q., Q. Chen, et al. (2013). Biomacromolecules **14**(1): 285-COVER4.
Ward, J. H. (1963). Journal of the American Statistical Association **58**(301): 236-&.

Warwicker, J. O. (1954). Acta Crystallographica **7**(8-9): 565-&.
Warwicker, J. O. (1956). Transactions of the Faraday Society **52**: 554 - 557.
Warwicker, J. O. (1960a). Journal of Molecular Biology **2**(6): 350-362.
Warwicker, J. O. (1960b). Journal of the Textile Institute **51**: T289 - T293.
Wenk, E., A. J. Wandrey, et al. (2008). Journal of Controlled Release **132**(1): 26-34.
Windig, W. and J. Guilment (1991). Analytical Chemistry **63**(14): 1425-1432.
Wise, G. M., M. M. Denn, et al. (1998). Aiche Journal **44**(3): 701-710.
Wold, S., M. Sjostrom, et al. (2001). Chemometrics and Intelligent Laboratory Systems **58**(2): 109-130.
Wray, L. S., X. Hu, et al. (2011). Journal of Biomedical Materials Research Part B-Applied Biomaterials **99B**(1): 89-101.
Wray, L. S., J. Rnjak-Kovacina, et al. (2012). Biomaterials **33**(36): 9214-9224.
Wynne, A. (1997). Textiles. Oxford, UK, Macmillan Education.
Xia, X. X., Z. G. Qian, et al. (2010). Proceedings of the National Academy of Sciences of the United States of America **107**(32): 14059-14063.
Xie, F., H. Zhang, et al. (2006). International Journal of Biological Macromolecules **38**(3-5): 284-288.
Xu, M. and R. V. Lewis (1990). Proceedings of the National Academy of Sciences of the United States of America **87**(18): 7120-7124.
Xu, Y., Y. Zhang, et al. (2005). International Journal of Biological Macromolecules **35**(3-4): 155-161.
Yagi, N. (1926). Journal of Experimental Zoology **46**(2).
Yamada, H., H. Nakao, et al. (2001). Materials Science & Engineering C-Biomimetic and Supramolecular Systems **14**(1-2): 41-46.
Yang, H., J. Irudayaraj, et al. (2005). Food Chemistry **93**(1): 25-32.
Yang, Y., F. Ding, et al. (2007). Biomaterials **28**(36): 5526-5535.
Yang, Z., D. T. Grubb, et al. (1997). Macromolecules **30**(26): 8254-8261.
Yasuda, K., R. C. Armstrong, et al. (1981). Rheologica acta **20**: 163-178.
Yoshimizu, H. and T. Asakura (1990). Journal of Applied Polymer Science **40**(9-10): 1745-1756.
Yuan, Q. Q., J. R. Yao, et al. (2010). Polymer **51**(26): 6278-6283.
Zainuddin, T. T. Le, et al. (2008). Biomaterials **29**(32): 4268-4274.
Zhang, C., D. Song, et al. (2012a). Biomacromolecules **13**(7): 2148-2153.
Zhang, J. E., E. Pritchard, et al. (2012b). Proceedings of the National Academy of Sciences of the United States of America **109**(30): 11981-11986.
Zhang, L. P., I. Noda, et al. (2009). Applied Spectroscopy **63**(6): 694-699.
Zhang, S. G., D. M. Marini, et al. (2002). Current Opinion in Chemical Biology **6**(6): 865-871.
Zhang, X. H., M. M. R. Khan, et al. (2012c). International Journal of Biological Macromolecules **50**(2): 337-347.
Zheng, S. D., G. X. Li, et al. (1989). Applied Spectroscopy **43**(7): 1269-1272.
Zhou, C.-Z., F. Confalonieri, et al. (2000). Nucleic Acids Research **28**(12): 2413-2419.
Zhou, G. Q., Z. Z. Shao, et al. (2009). Advanced Materials **21**(3): 366-370.
Zhou, L., X. Chen, et al. (2005). Journal of Physical Chemistry B **109**(35): 16937-16945.
Zhu, C. J. and P. R. Griffiths (1998a). Applied Spectroscopy **52**(11): 1403-1408.
Zhu, C. J. and P. R. Griffiths (1998b). Applied Spectroscopy **52**(11): 1409-1413.
Zhu, Z. H., K. Ohgo, et al. (2008). Express Polymer Letters **2**(12): 885-889.
Zimm, B. H. (1945). Journal of Chemical Physics **13**(4): 141-145.
Zimmerman, S. S. and H. A. Scheraga (1977). Proceedings of the National Academy of Sciences of the United States of America **74**(10): 4126-4129.

Appendices

Appendix 1 Silkworm rearing

Bombyx mori\Bombycidae\Lepidoptera\Insecta\Arthropoda

Bombyx mori were obtained from CRA-API Apiculture and Sericulture research unit, Padova, Italy and were fed white mulberry tree (*Morus alba*) leaves. Once they started spinning the scaffold of their cocoon, showing their ability to spin, silkworms were stored at 9 ± 1°C to slow their metabolism and prevent them from spinning. For no more than 9 days, they were stored at this temperature before being used in experiments. Several strains of *Bombyx mori* exist but only two were studied, the standard white variety and the darker zebra (yellow variety)



Figure A.1 a) *Bombyx mori* (white) silk gland. b) *Bombyx mori* yellow strain worm. c) *Bombyx mori* yellow strain moth emerging from its cocoon. The coin showed on the picture had a diameter of 18 mm.

Figure A.1a shows a silk gland extracted from a *Bombyx mori* worm before its feedstock was extracted. Figure A.1b shows the zebra variety which has a darker skin and produces yellow coloured silk as pictured on Figure A.1c. This species is particularly sensitive to diseases and cleanliness is essential to their survival. Upon delivery, worms were divided into smaller groups containing fewer than 10 individuals to prevent the spread of diseases. Everything getting in contact with their environment was thoroughly cleaned with a fresh Virkon® solution. Silkworms were always handled with gloved hands.

Actias luna\Saturniini\Saturniidae\ Lepidoptera\Insecta\Arthropoda

Actias luna eggs hatched several weeks after they were left at room temperature to stop their hibernation.



Figure A.2 Aerial photography of the parks surrounding the University of Oxford. The locations of the trees from which leaves were collected are marked by arrows.

Once emerged, *Actias luna* were fed Walnut from a single tree identified by an arrow on Figure A.2. By putting foliage branches in water inside a large container this species required minimum oversight and care. Changing the branches every 2 or 3 days was enough to feed them and maintain a reasonable degree of hygiene.



Figure A.3 a) *Actias luna* last instar worm. b) *Actias luna last* silk glands. c) *Actias luna* cocoon. The coin showed on the pictures had a diameter of 18 mm.

Figure A.3a shows a *Actias luna* final instar worm which grew to around 5 centimeters long with small orange spots along its green body. Once dissected, Figure A.3b shows the long coiled silk glands than can be extracted from the animal. Because of their smaller size and narrower diameter compare to *Bombyx* mori silk glands, peeling the epithelium was challenging. Instead, its feedstock could only be obtained by puncturing the gland's epithelium and collecting the silk ejected by osmotic gradient. An undisturbed *Actias luna* will normally construct a dark cocoon similar to the one shown on Figure A.3c.

Antheraea yamamai\Saturniini\Saturniidae\Lepidoptera\Insecta\Arthropoda

Antheraea yamamai eggs were the first amongst wild species to hatch. Fed on hawthorn leaves, which can be sources all over the Zoology Department of the University of Oxford (see Figure A.2). Since hawthorn leaves are relatively small and thin, cut leaves had to be changed every day. To reduce the worm's maintenance requirements, tree branches tip were soaked in water to keep them hydrated. Although it helped preserving the leaves, 6 worms unfortunately drowned. Hence to use this method, it is preferable that worms are bigger than 3 mm in diameter and all access to water should be restricted. In addition, two worms stabbed themselves on the thorns of the branches and died subsequently. To address this issue, thorns were removed manually from the branches. Three more were killed by inadvertence during transfer and cleaning operations. In addition, an unknown disease started to spread during their last instar killing all the remaining worms but three.

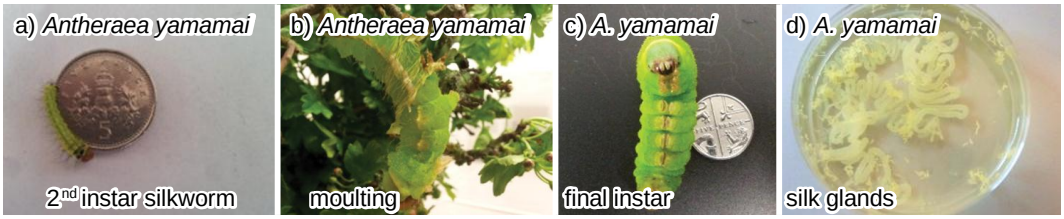


Figure A.4 a) *Antheraea yamamai* second instar worm. b) *Antheraea yamamai* moulting. c) *Antheraea yamamai* final instar worm. d) *Antheraea yamamai* silk gland. The coin showed on the pictures had a diameter of 18 mm.

Figure A.4a shows the second instar *Antheraea yamamai* worms were around 16 mm long with a mass of 4.8 ± 0.8 g. Despite their small size they could move very quickly and had very strong grip. If pulled off their substrate, their grip was in fact stronger than their legs can sustain since they would tear before losing grip. Figure A.4b pictures a worm undergoing its last moult. For the larvae to moult properly it is essential that it is left alone as removal could prove dangerous. The safest way to move the specimen proved to be the transfer of the twig they are attached on to another fresh branch. The full size final instar is pictured on Figure A.4c whilst its glands are shown on Figure A.4d. Unlike the other silk gland extracted, *Antheraea yamamai* glands had a light green/yellow hue which must be responsible for the cocoon's distinctive coloration.[Chen2012c]

Attacus atlas\Attacini\Saturniidae\Lepidoptera\Insecta\Arthropoda

Attacus atlas were fed with evergreen privet (*Ligustrum vulgare*) which can be sourced easily as it constitutes many house hedges around Oxford (see Figure A.2 for location). Since privet preserves very well, its branches could be changed only once every 3 or 4 days. However, the final instar larva could devour many leaves per day.



Figure A.5 a) *Attacus atlas* second instar worm. b) *Attacus atlas* final instar worm next to the ATR accessory of the infrared spectrometer. c) *Attacus atlas* silk glands. The coin showed on the picture had a diameter of 18 mm.

Figure A.5a shows a second instar *Attacus atlas* worm with its white flaky skin. Belonging to the Attacini tribe, its morphology is distinct from the Saturniini tribe caterpillar reared. It had long fleshy spikes whilst its body is covered with a white hydrocarbon wax (determined by infrared spectroscopy, data not shown). This wax could easily detach from its skin when handled, leaving white dandruff-like flakes on substrates. However as it grows, the proportion of white flakes decreases to be replaced by green skin. As shown on Figure A.5b, *Attacus atlas* can become even larger than an average human thumb, much larger than the other species reared in-house with a mass of 14 ± 5 g. They reached up to 14 cm in length and around 2 cm in diameter. Righteously named Atlas, these large larvae pupate into one of the world's largest moth. Figure A.5c shows its silk glands, which are relatively small compared to the larvae size. Feedstocks required for experiment were extracted using the same method as described for the other wild silk species.

Saturnia pavonia\Saturniini\Saturniidae\Lepidoptera\Insecta\Arthropoda

Saturnia pavonia also eat hawthorn leaves which were source locally in the University Park (see Figure A.2). *Saturnia pavonia* proved to be the easiest species to rear in-house and suffered no mortality as all larvae reached the spinning stage.

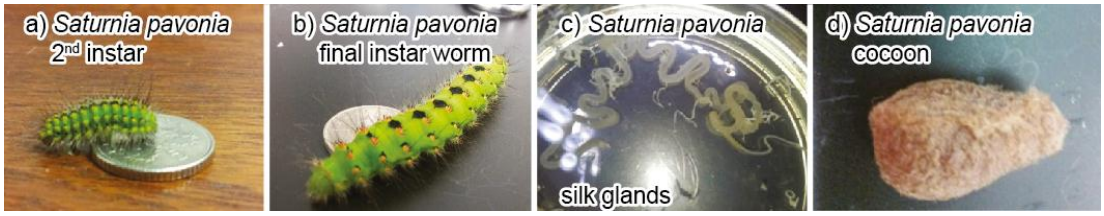


Figure A.6 a) *Saturnia pavonia* second instar worm. b) *Saturnia pavonia* final instar worm. c) *Saturnia pavonia* silk glands. d) *Saturnia pavonia* tanned cocoon. The coin showed on the pictures had a diameter of 18 mm.

Once hatched, *Saturnia pavonia* were very hairy and completely black, but with each moult the proportion of green skin increased. Figure A.6a shows a second instar *Saturnia pavonia* compared to a 5p coin whilst the pane b pictures the full size final instar. Figure A.6c shows that its glands were as narrow and long as the other wild silkmoth species. On the other hand, *Saturnia pavonia* cocoons have a distinctive bell shape leaving a one way opening for the moth to emerge after pupation (see Figure A.6d).

Appendix 2 Spectroscopy supplementary material

Wild silk shear induced denaturation

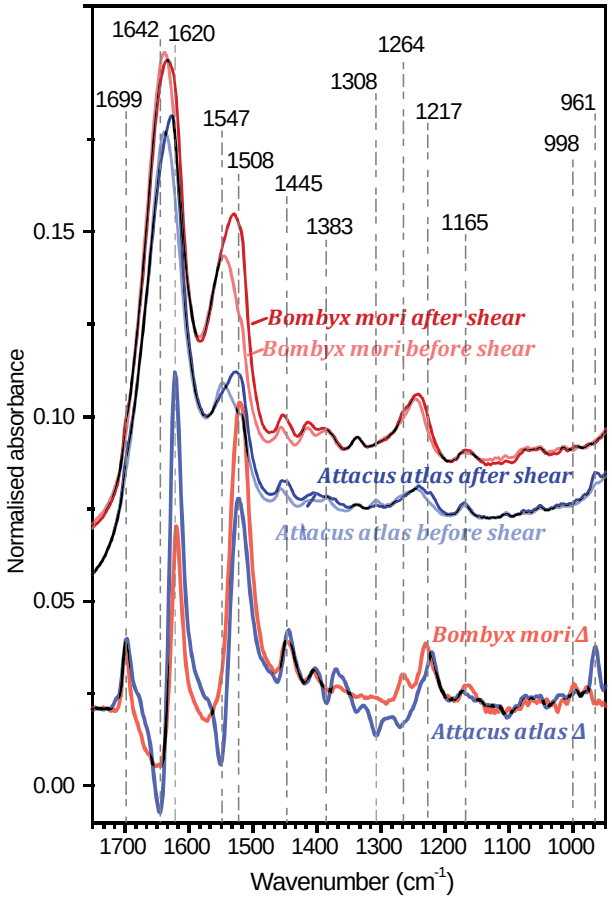


Figure A.7 Infrared spectra before and after shear-induced denaturation of *Bombyx mori* (red curves)and *Attacus atlas* (blue) along with their corresponding difference spectrum.

Figure A.7 shows the spectra of *Bombyx mori* (red) and *Attacus atlas* feedstock before and after shear induced conformation conversion. In both cases, the shear induced denaturation led to the rise of peaks assigned to β-sheets at 1699, 1610 and 1508 cm^{-1}. However, major distinctions are observed on the difference spectra including a missing peak at 998 cm^{-1} assigned to poly(alanine-glycine) for *Attacus atlas*. Instead the wild species has only one sharp peak at 961 cm^{-1} assigned to poly(alanine). In addition, the amide III region of the difference spectra is also indicative a different conformation conversion

process for the wild silk. The peak at 1264 cm^{-1} associated with helical structures decreases for *Attacus atlas* instead of increasing as for *Bombyx mori*. Most surprisingly the only peak observed in Saturnidae at 1308 cm^{-1} (see Figure 7.3) vanishes as the wild silk is processed. Hence, this peak which we assigned to β-turns should be part of the structures precursor to the poly(alanine) β-sheets formation.

Dry weight fraction quantification by partial least squares

Thanks to their distinctive infrared signature, it is possible to use FTIR to determine the concentration of a sample in solution. For the quantification of the protein-water concentration in Chapter 3, Chapter 5 and Chapter 6, a calibration curve built with known concentration standards is necessary. In its simplest form a linear relation exists between the concentration and the area (or height) of one peak. This simple linear model is good enough for many applications, but does not use all the information contained in the spectrum. Instead the wealth of information from the whole spectrum could be exploited by performing a Partial Least Squares (PLS) method. PLS is the most commonly used multivariate linear regression method and is implemented in most infrared spectroscopy quantitative methods.[Li2005; Kim2007; Jensen2008] PLS algorithms aim at finding the multidimensional direction in the original space that explains the maximum variance into a new coordinate system.[Wold2001] This method is particularly useful when the number of variables (spectra data point) is larger than the number of observations (number of standards) and when some variables are collinear (dependent to one another).

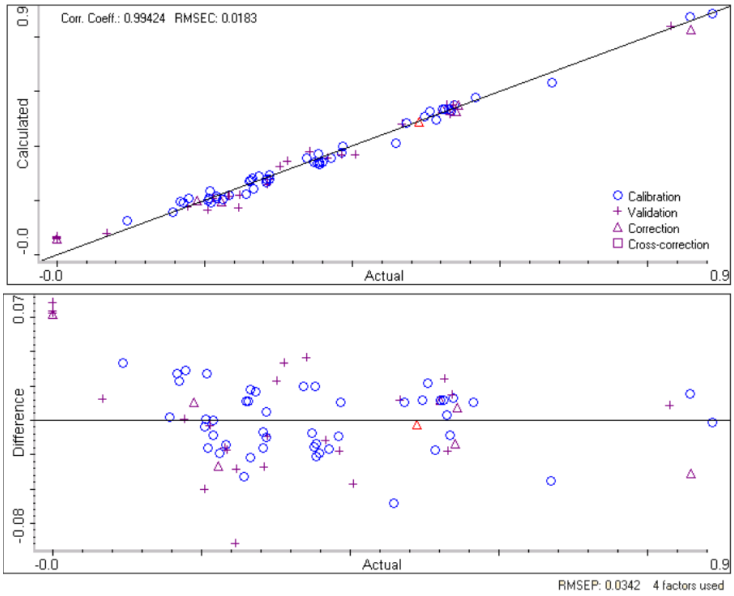


Figure A.8 Partial Least squares (PLS) calibration curve for the dry weight quantification based on 4 factors.

The model can then be used to evaluate the concentration value, the dry weight, of samples and yields an average uncertainty of 3% as shown on Figure A.8. Although less accurate than dry weight measurement, this method does not take one day of sample drying to get the result. The concentration for each collected spectra required much less sample (> 1 µL) than a dry weight measurement.

Infrared peak integration

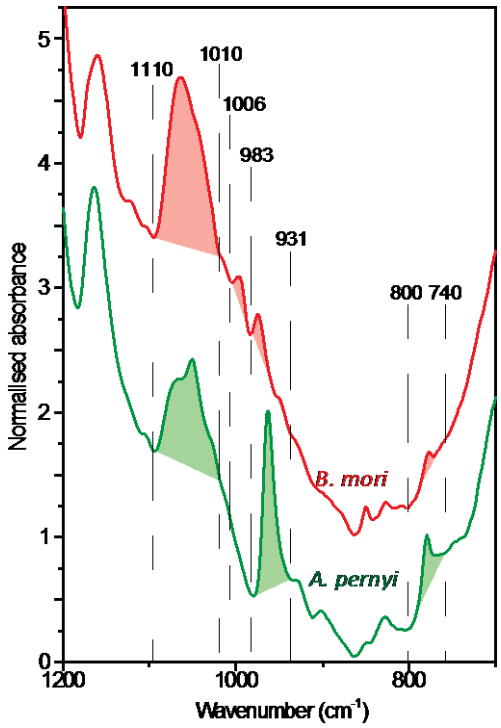


Figure A.9 Low frequency infrared band of *Bombyx mori* and *Antheraea Pernyi* with integrated bands. A linear baseline between the regions boundaries was subtracted from the integrated area.

For peak integration, a linear base line was subtracted between the integration boundaries. As shown on Figure A.9 by the colourer area, only the absorbance above the baseline was integrated. This simple integration method ensured that underlying contributions from other components would have a lesser impact on the integrated value.

Water intake reversibility

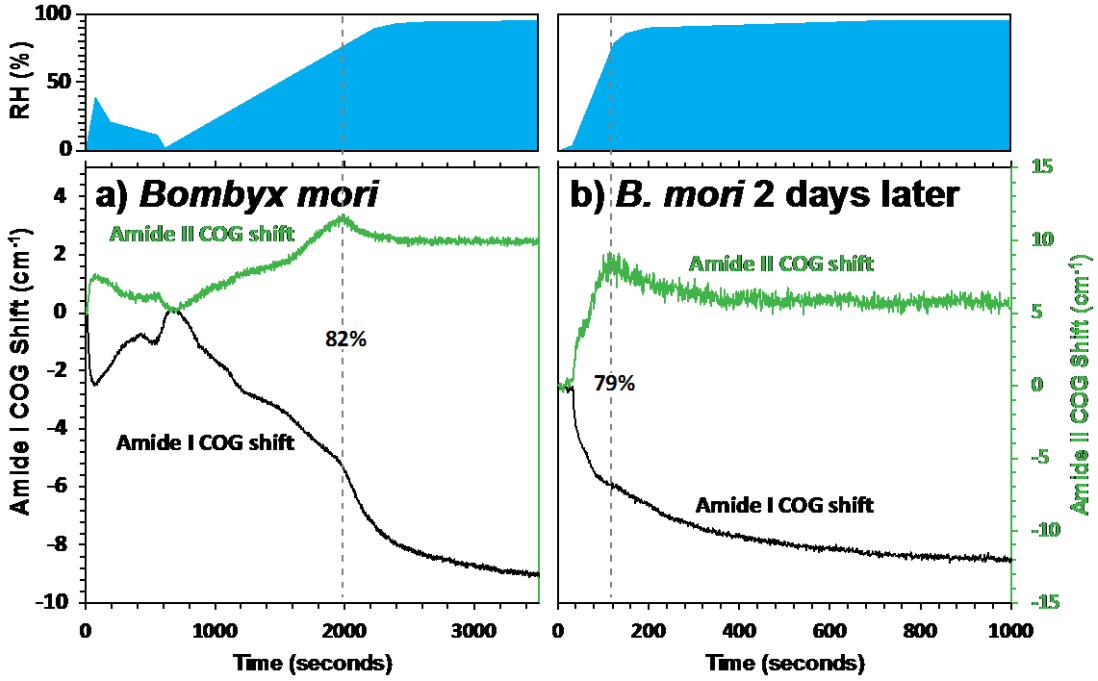


Figure A.10 a) Rehydration kinetics of few *Bombyx mori* dry-spun fibres under a humidity cyclic ramp, centre of gravity of the amide bands b) Rehydration kinetics of few 2 days old dry-spun fibres under a linear humidity increase ramp, centre of gravity of the amide bands.

Figure A.10a clearly shows that the amide I and II centre of gravity (COG) measured for freshly spun fibres are highly sensitive to the humidity level as the bonded water content could be detected by infrared spectroscopy. Increasing humidity shifted the amide I band towards higher wavenumber whilst the amide II band shifted to lower wavenumber. Increasing the humidity to 40% RH and back to <1% RH was however entirely reversible as the COG reverted back to their original values. However, increasing the RH to lower the T_g below the room temperature resumed the conversion process leading to amide I and amide II shifts to lower frequencies. As shown on Figure A.10b, using a fibre that was kept dry for 2 days did not prevent the resuming conversion once humidity was reintroduced.

Sericin content in silkworm glands

Silk fibroin proteins are produced by cells in the posterior part of the worm's glands before being coated with several layers of sericin protein.[Machida1926;Akai1983] The sericin's main function is to bond the two secreted filaments together as well as the fibre layers for the cocoon construction.[Chen2012a] Sericins are very brittle offering a poor interface bonding whilst fibroins filaments confer the tenacity to the biological composite material.[Chen2010a] In order to study only the rheological properties of fibroin the sericin coating can be washed out from the entire gland (section 2.1.1.2). Alternatively, using only the posterior part of the gland can provide samples with little sericin. The main problem with this approach is the low yields resulting from partial dissections. To increase yield, a bigger fraction of the gland can be used, but the position of the sericin coating's beginning needs to be known. To localise where sericin is present, infrared spectroscopy can be used since both proteins result in distinctive infrared spectra (see Figure A.11 and Figure 7.4). The difference is primarily due to their distinct amino acid content, sericin being richer in serine residues. A silk gland from a *Bombyx mori* silkworm was thus peeled and cut into 23 sections which where solubilised separately in demineralised water. Each solution was then dried onto the ATR accessory of the spectrometer to form a thin film for infrared spectra collection.

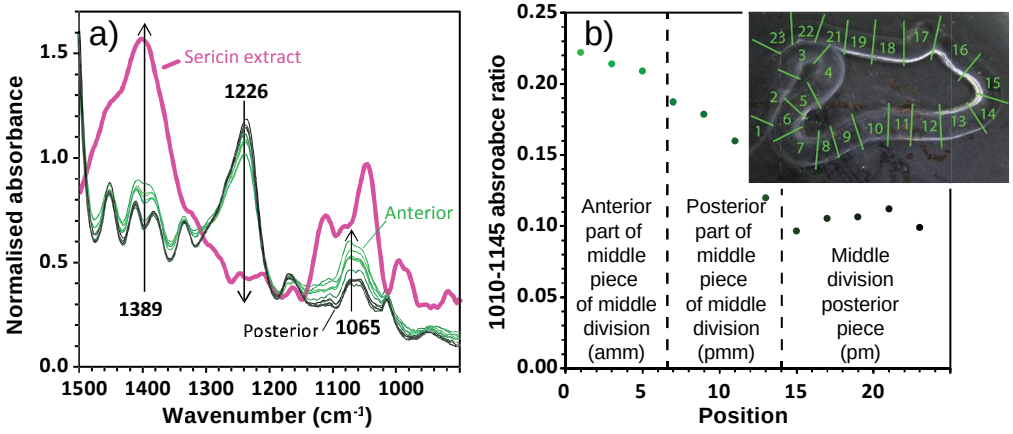


Figure A.11 a) infrared spectra of silk solution casted films on the ATR accessory as a function of the position (dark green posterior, light green anterior part). b) Absorbance ratio of the 1010-1145 region between the silk dope and a sericin extract.

Figure A.11a shows the dried film infrared spectra of film cast from silk dope collected at different positions as well as the spectrum of pure sericin extracted from the gland's outermost layer. The spectra's most affected region is from 900 to 1500 cm^{-1}, commonly associated with C-O stretching vibration modes. Additional components rose at 1389 and 1065 cm^{-1}. Spectra from the posterior part of the gland (dark green) also show more intense amide III band at 1226 as the sericin spectrum (pink curve) does not appear to have strong bands in the region. The most important change in the spectra when multiple portions of the gland are probed is the absorption of the 1010 to 1145 cm^{-1} region which can be used as a sericin indicator.

As plotted on Figure A.11b the absorption of this spectral region is highly dependent on the probed position until no more sericin is present between positions 13 and 15. This position corresponds to the first fold in the silk gland, delimiting the posterior part of middle piece of the middle division (*pmm*) and the middle division posterior piece (*pm*).[*Machida1926;Akai1983*] Consequently, using position 15 and above optimises yields whilst ensuring samples with little sericin are prepared. Using the 1010-1145 cm^{-1} region only we estimated the sericin's

detection limit at ~1 % w/w. Silk glands were thus cut at the first fold for the washing-free dissection technique described in section 2.1.1.2.

Polarisation calibration

In ATR mode, the effective penetration depth gives the sample thickness which would be required to get an equivalent absorbance. At 45° angle of incidence, p polarisation probes along the x and z axis making its effective penetration depth twice the value of s polarisation, which samples only along y. The absorption ratio between both polarisations will be equal to 2 ($R_{iso}^{ATR} = A_P/A_S$ = 2) for isotropic thick films.[Harrick1965; Fringeli1992] For intermediate angles between polarisation p and s, the reflection will vary according to a cosine squared function of the angle θ_{pol} between the electric field and the vibration mode.[Gregoriou2004; Benedict2008] For small absorbance values A will also follow the same relation once the phase angle δ is corrected.[Nagasaki2000; Boulet-Audet2008]

$$A(\theta_{pol}) = A_P \sin^2(\theta_{pol} - \delta) + A_S \cos^2(\theta_{pol} - \delta)$$

Equation A.1

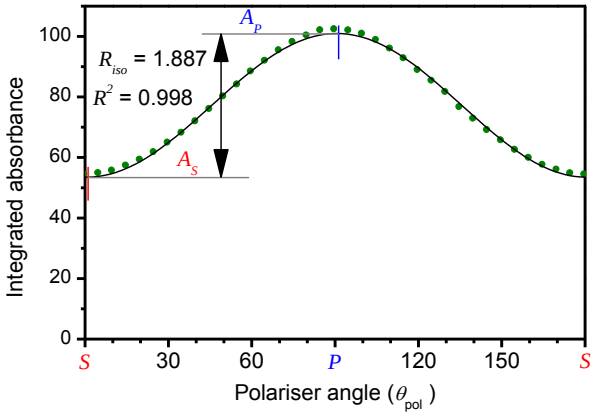


Figure A.12 Integrated absorbance between 4000 and 2600 cm^{-1} of the water O-H stretching modes as a function of the angle of the polariser.

Figure A.12 shows the calibration of the polariser and ATR accessory system. The absorbance measured for liquid water was fitted with Equation A.1 to calculate the phase angle δ and the absorbance using p-polarised light A_P and s-polarised light A_S. It followed

the cosine squared relation rigorously and a phase angle δ of only 0.5° was found, proving that the polariser was well aligned with the incidence angle plane. However, the dichroic ratio R_{ATR}^{ISO} of 1.887 measured was slightly lower than the theoretical expected value of 2. The deviation from the ideal value could have been the result of the incidence angle distribution given by a finite size aperture or an angle of incidence slightly larger than 45°. Hence the ratio R_{ATR} was normalised to equal the theoretical value in order to compensate for the deviation of the Golden-Gate ATR accessory.

The predictable absorbance variation given by polarisation rotation could constitute a perturbation method for deconvoluting overlapping peaks originating from anisotropic structure using Multivariate Curve Resolution Alternating Least Squares (MCR-ALS)[Tauler1993b] or 2D correlation analysis.[Nagasaki2000] The cosine square dependency on the anisotropic bands could also have the benefit of improving the models by incorporating an additional constraint based physical effects.

Infrared and rheology data coupling with rheology data

To exploit the full potential of the Infrared spectrometer's software capability (Omnic, Thermo, Wisconsin, USA), the OmTalk dynamic library was used to automate the spectrometer's operations. Since OmTalk was only guaranteed to work seamlessly with Microsoft's .NET platform, custom programs were written in Visual Basic. OmTalk commands allowed the control of each component of the spectrometer making it possible to perform new tasks such as rotating the polariser between two positions between each spectra collection.

For the Rheo-IR platform, the challenge for coupling spectroscopy and rheology data resided in the fact that both instruments could not be operated by a single script. Instead, the data acquisition timing was carefully synchronised. Thereafter, time stamps were used

to couple the data using a custom VBA macro. Since the time interval was not the same between each data set, data points were interpolated based on the time registered by the infrared spectrometer. The script was written to automate parts of the data collection and analysis processes, such as baseline offset, ATR correction and spectra normalisation. The amide I and II bands' centre of gravity of spectra was also calculated using such script. By enabling the data collection, this macro ensured that even casual users could collect infrared spectra and metadata in a consistent manner. Metadata consistency is particularly important to ensure a correct interpretation of the spectra. This macro proved useful also for controlling the ATR accessory's temperature controller in order to perform FTIR experiments under a temperature ramp. The custom macros written are summarised in Table A.1.

Macro name	Language and library	Application	Reference
Alternating polarisation rotation	VB.net OmTalk	Alternates between s and p polarisation for dichroism kinetics or acquiring spectra at intermediate angles	Chapter 3
Data acquisition GUI	VB.net OmTalk, Spectra Library, Excel 2007	Guides the user in the acquisition of the spectra of sample batch, prompt for fresh background, test the cleanliness of the ATR element, back-up to the spectra database and export to excel.	Chapter 7
Golden-Gate Temperature controller	VB.net	Control the temperature of the Golden-Gate ATR accessory and controls the data acquisition.	Chapter 6
Omnic Data import	VBA OmTalk, Excel 2007	Imports batches of *.spa files into an excel spreadsheet; performs various spectral treatments such as background normalisation.	Chapter 3 Chapter 7
FTIR centre of gravity profile import	VBA Excel 2007	Imports batches infrared spectra and calculated the centre of gravity of certain bands.	Chapter 3 Chapter 5
Oscillation import	VBA Excel 2007	Imports batches of *.dow files containing the oscillatory data into an excel spreadsheet and plot them, calculates rheological parameters such as the crossover points.	Chapter 5 Chapter 6
Viscosity import	VBA Excel 2007	Imports batches of *.dvw files containing the viscosity data into an excel spreadsheet and plots them.	
Rheo-IR data coupling	VBA Excel 2007	Couples the data from the rheometer and FTIR of the same experiment together.	

Table A.1 List of macros written for task automation, data acquisition, data analysis and data visualisation.

Appendix 3 Rheology supplementary material

Viscosity calibration for the Rheo-IR platform

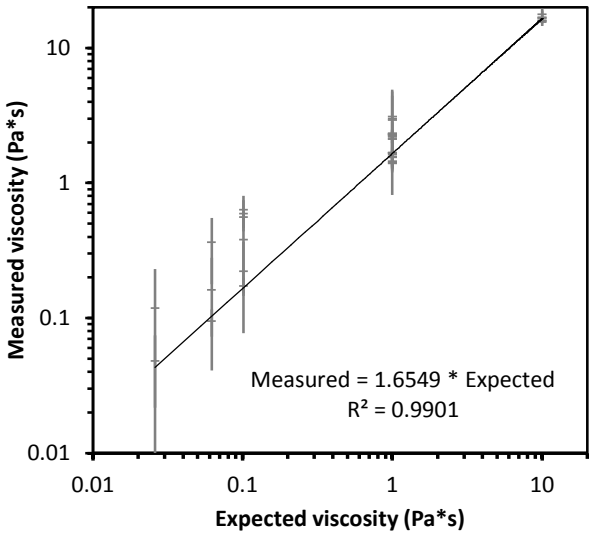


Figure A.13 Rheo-IR calibration curve comprising 39 independent measurements of calibration oils of 0.026, 0.101, 1 and 10 Pa·s provided by Malvern Instruments.

As seen on Figure A.13, the viscosity measured for our calibration oils were systematically 65% higher than their expected value. We use this 1.65 factor to normalise our raw viscosity readings to ensure the accuracy of the measurements. This plot also gives an appreciation of the relative uncertainty related to independent measurements with different loadings. The relative error becomes important (one order of magnitude) only for samples with viscosity of 0.1 Pa·s or below. In addition to the calibration curve, the normalised zero shear viscosity measured for native silk (1300 Pa·s) is similar to previously published values using similar geometry (2000 Pa·s using 8 mm parallel plates)[Terry2004] and (1000 to 5000 Pa·s using cone and plate 1-10 and parallel plate 20mm).[Holland2006; Holland2007] Although a larger geometry would increase the precision of low viscosity sample measurements below 0.1 Pa·s, our calibration curve proved that our Rheo-IR setup can

accurately and precisely measure RSF samples with intermediate viscosity values (10 to 1000 Pa·s).

Linear viscoelastic limit validation

The linear viscoelastic region (LVR) corresponds to the rate regime where the material responds to shear stress linearly. Within this region, G' and G'' should be independent of the applied strain. It is important to know the LVR to perform non-damaging oscillatory measurements. Since a strain γ of 0.002 was proven to be within the LVR of native silk feedstock,[Holland2006] we chose this value for consistency but its linearity regime had to be validated for our new experimental platform.

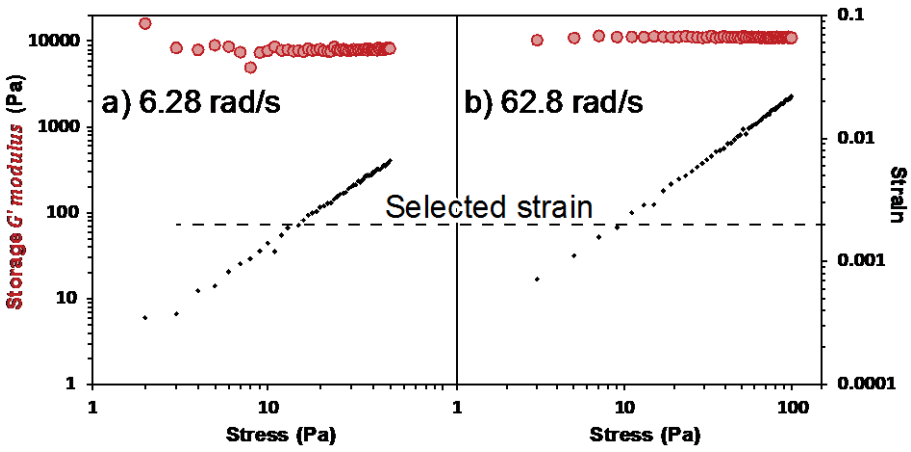


Figure A.14 a) Amplitude sweep from 1 to 50 Pa at 6.28 Rad/s for native silk feedstock b) Amplitude sweep Amplitude sweep from 1 to 100 Pa at 62.8 Rad/s for native silk feedstock.

As sown on Figure A.14 the value of storage modulus G' remained constant over the range of shear stresses at 6.28 Rad/s (1 Hz) and 62.8 Rad/s (10 Hz). This control experiment thus confirms that using a strain γ of 0.002 is comfortably within the linear viscoelastic regime for the range of frequencies used.

Instrumental limit of oscillatory tests

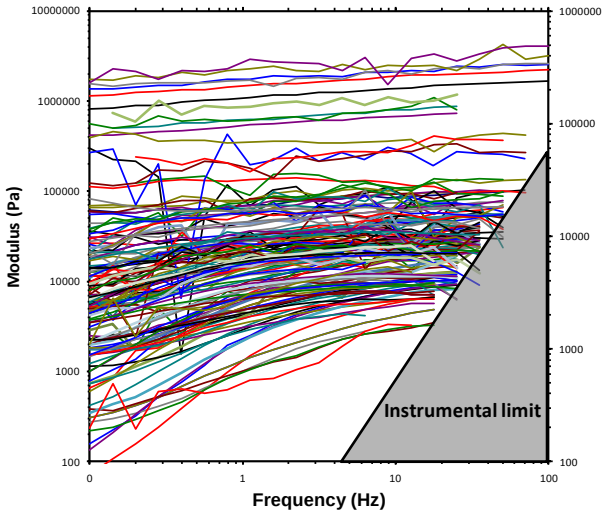


Figure A.15 Storage modulus G' for a range of silk feedstock collected using the Bolhin Gemini Nano Rheometer in the Rheo-IR platform with a strain γ of 0.002.

By plotting the storage modulus of samples with a range of concentration and plateau modulus G_N, Figure A.15 shows clearly the domain beyond which the rheometer cannot determine the phase angle δ and returns an error (grey area). This occurs at a combination of high frequency and low modulus value when δ becomes too large for the instrument which outputs an error.

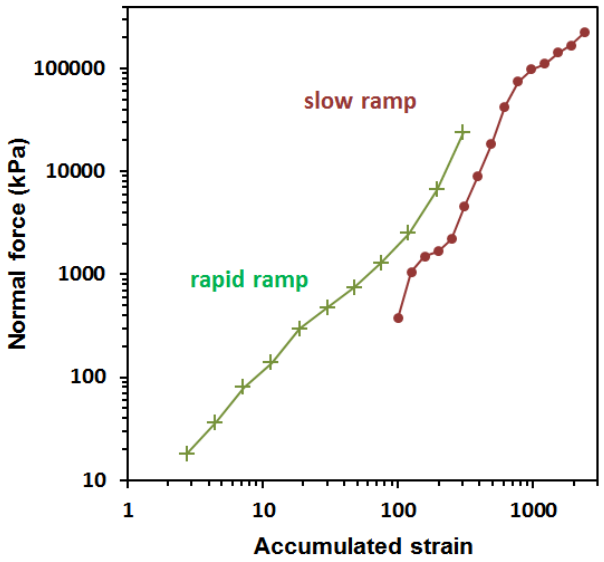


Figure A.16 First normal force as a function of the accumulated strain.

By measuring native silk under two different exponential step ramps, Figure A.16 shows that the first normal force appears to depend on the accumulated strain instead of the shear rate.

Rheology for ex situ SAXS

To validate the quality of the sample, the loading and the experimental setup, a non-damaging oscillatory sweep was first performed using the methodology described in section 4.3.5.

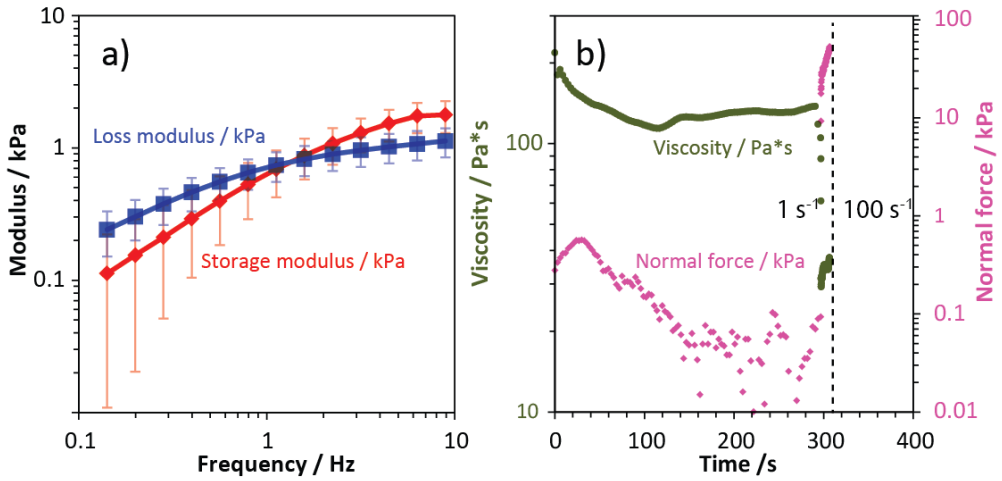


Figure A.17 a) average storage modulus G' (red lines) and loss modulus G'' (blue lines) as a function of the angular frequency for silkworm feedstock. b) Viscosity and first normal force as a function of time for a representative sample sheared at 1 s^{-1} for 300 s and 10 s at 100 s^{-1}

A shown in Figure 5.3a, every native silk sample showed the typical crossover point where $G' = G''$ at 7 ± 2 rad/s, giving a relaxation time $\tau_p = \omega^{-1}$ of 0.9 ± 0.2 seconds (n = 17), consistent with previous measurements.[Moriya2009; Boulet-Audet2011] The calculated plateau modulus ($G_N = G'|_{\omega\to\infty}$) was only 1.7 ± 0.5 kPa, one order of magnitude less than previously reported values (see page 129).[Terry2004a, Holland2006, Moriya2009] Following the oscillatory experiment a constant shear test was performed at low rates (1 s^{-1} at the rim) to measure the zero shear viscosity (η_0) whilst homogenising the sample (see Figure 5.3b). We measured η_0 = 0.20 ± 0.02 kPa·s, once again one order of magnitude lower than

expected.[Terry2004a, Holland2006, Moriya2009 Boulet-Audet2013] Since the shape of the frequency sweep and τ_p are consistent with previous measurements, the differences between absolute values measured for G_N and η_0 are most likely due to an underfilled geometry. As it was difficult to load the exact amount of feedstock and impossible to trim the excess, samples were slightly underfilled (visual observation). As the measured viscosity in a parallel plate geometry is proportional to the power of 4 of the radius,[Ferry1980] a factor of 10 could be explained by a sample with a diameter of 11.2 mm instead of 20 mm. Nevertheless, the cells' field of view was restricted to 17.3 mm in diameter and the SAXS patterns collected close to the outer edge were validated using their transmission value. For neutron scattering experiments a visual inspection of the cells ensured that sample covered the entire unmasked area for neutron scattering experiments.

Once homogenised at low shear rates, the samples were sheared for few seconds at high rate (100 s^{-1} on the edge of the window). As shown in Figure 5.3b, native silk shear thinned when suddenly sheared at high rates, its viscosity dropping from 0.15 ± 0.03 to 0.04 ± 0.01 kPa·s. Simultaneously, the difference between the resulting stress tensor becoming non null resulted in a positive increase of the first normal force difference (N_1 *or* ψ_1)[Doi1978] from 0.1 to 70 ± 20 kPa. The force pushing the two plates apart can be interpreted as the consequence of the recoverable elastic strain of the polymer chains resisting disentanglement in the flow field.[Rivlin1948; Porter1995]

Appendix 4 SAXS supplementary material

SAXS Comparing reconstituted to native silk fibroin

Rheological measurements revealed the intrinsic difference between reconstituted and native silk.[Holland2007] Small angle neutron scattering also showed different shapes between

the natural and artificial counter-part in its diluted state.[Greving2010] Thus, we were interested in corroborating these results by comparing static native and reconstituted silk with similar concentrations (20 ± 3 %) with SAXS.

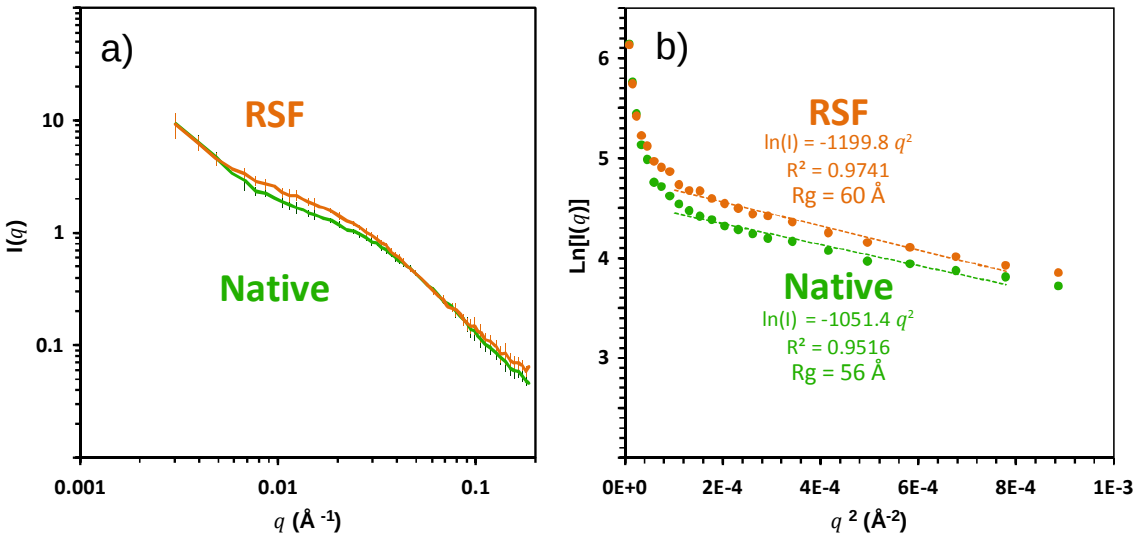


Figure A.18 a) Scattering curves for native silk and reconstituted silk, b) Guinier plot for native and reconstituted silk.

As plotted in Figure A.18a, the small angle scattering curves for native and reconstituted silk are very similar at high concentration as the curves nearly overlap over the whole q range. This result suggests that either they have comparable form factor (sizes and shapes) or the underlying structure factor is dominating the scattering intensity. The Guinier plot on Figure A.18b shows nearly the same initial slope at low q, directly relating to the radius of gyration: $Ln[I(q)] = -(1/3)R_g^2 q^2$. Although the concentration was too high to assume isolated particles with no inter-particle interactions, the calculated R_g values for native were 56 Å and 60 Å for reconstituted silk. These two values are closer than those reported by Greving et al. for native and reconstituted silk, 90 Å and 45 Å respectively.[Greving2010]

SAXS Pixel validation

The scattering intensity at high q for our sample was very weak and the subtraction of the empty cell background can result in negative intensity value for certain pixels. As negative

scattering values do not have any physical meaning, the pixels giving negative counts were masked and ignored during the data analysis.

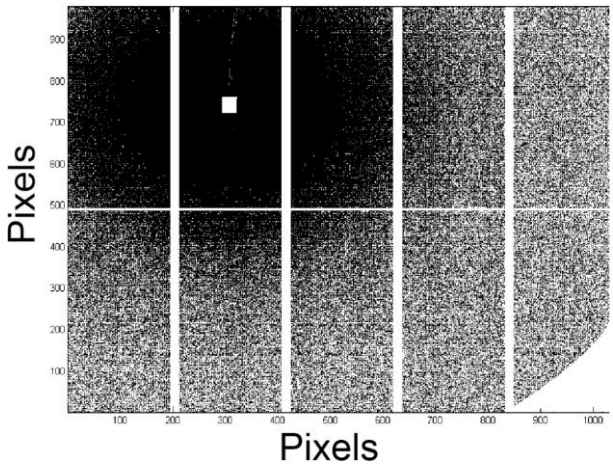


Figure A.19 Detector mask from a typical scattering pattern obtained using a 1M Pilatus detector for native silk fibroin.

Figure A.19 shows a typical scattering pattern mask. The white pixels with null or negative values after background subtraction were rejected. Because of manufacturing limitations, a frame around 10 detector arrays did not contain detector element. To prevent gaps between arrays, virtual pixels were place in between each, outputting -1 values. The pixels behind the beam stop and in the shade of the SAXS vacuum tube (bottom right corner) were masked for the data reduction. Masking these pixels reduced the number of the data points from over a million to few hundreds of thousands, speeding the surface fitting algorithm by several orders of magnitude. If fewer than 10 % of the pixels remained unmasked because of low scattering intensity, the whole scattering pattern was rejected.

SAXS Absolute Intensity calibration

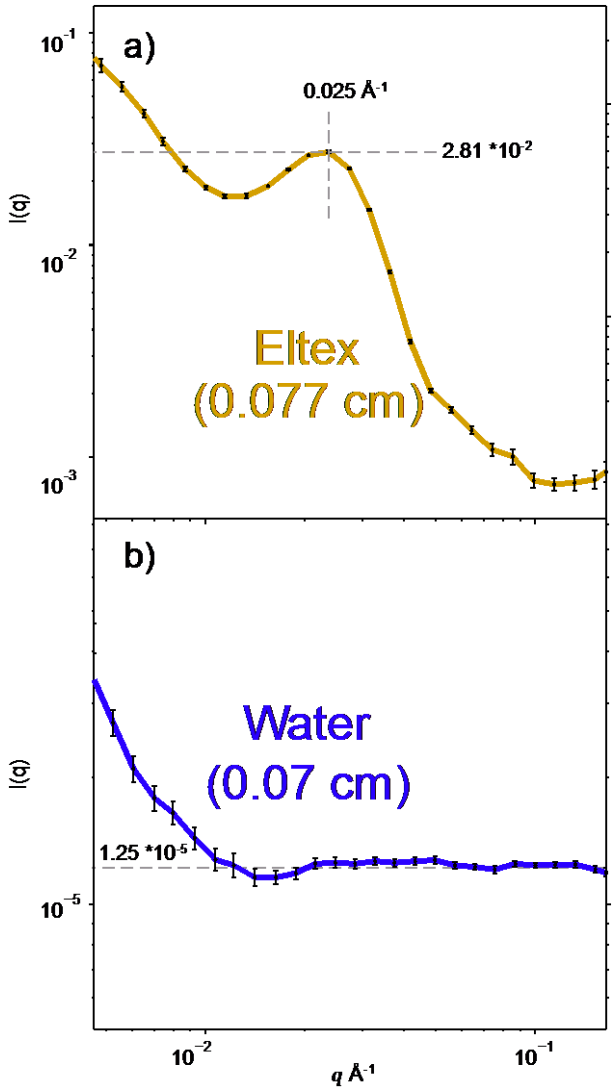


Figure A.20 Uncorrected Eltex intensity left pane (top pane), uncorrected water intensity (bottom pane)

The absolute intensity was calibrated using the well resolved peak at 0.025 $Å^{-1}$of Eltex A1050 plastic shown on Figure A.20a. The scattering intensity of the peak is known to be 24.5 cm^{-1}.[Russell1988] The uncorrected intensity measured was 2.81 $*10^{-4}$ or 7.05 $*10^{-3}$ cm^{-1}, since the thickness was 0.077 cm^{-1}. A calibration factor of 3474 can thus be calculated to correct the absolute intensity. Alternatively, H_2O can be used as a calibrant knowing the scattering length at vanishing q to be 0.01632 cm^{-1}.[Orthaber2000; Fan2010] Water's uncorrected intensity was 3.44 $*10^{-7}$ or 4.9 $*10^{-6}$ cm^{-1}, giving a calibration factor of 3314. As water

scatters less than Eltex, the latter was used for calibration. Although water's scattering was expected to be independent of q, the scattering intensity measured increased slightly below 0.01 $Å^{-1}$ (see Figure A.20b). Unexplained, this rise cannot be due to the cell as its scattering was subtracted leaving air scatter as potential cause.

SAXS Small Q range calibration

The distance between the sample and the detector requires calibration against a known reference sample. For SAXS, the hydrated collagen from a rat tail is a common calibrant since the scattering from the triple helices offers many sharp peaks from which the lattice spacing can be calculated.

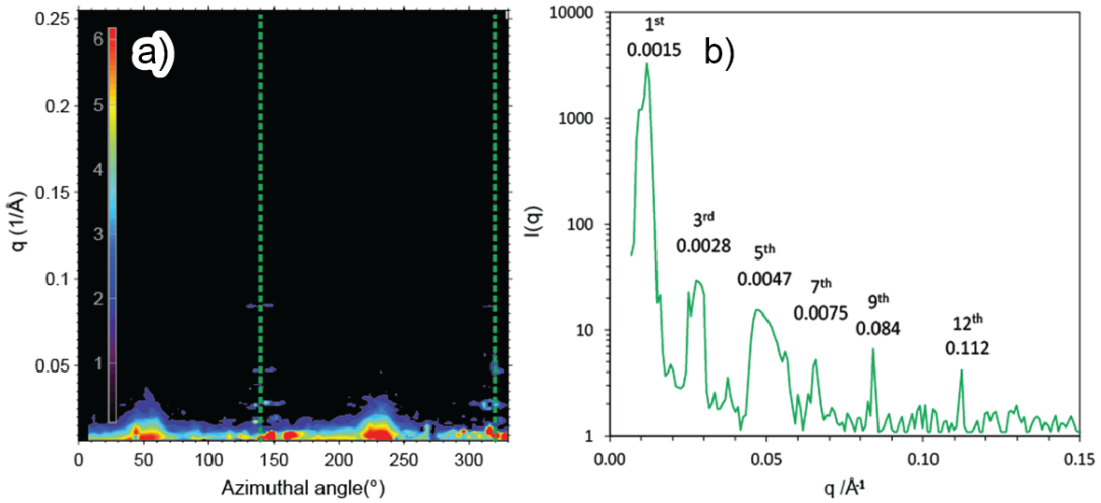


Figure A.21 a) I(q) as a function of the azimuthal angle and q for rat tail hydrated collagen, b) I(q) at 140 degrees for hydrated collagen with helix lattice order labels.

Figure A.21a shows the reduced scattering intensity with strong anisotropic peaks around 140° and 320° azimuthal angle. By averaging the intensity along this line we can clearly see the peaks resulting from the repetitive collagen helices. The wave vector q position of each diffraction order peaks is indexed for different d spacing (typically 671 Å)[Tomlin1956] and can thus calibrate the diffraction angle 2θ. With a series of peaks at known 2θ, the detector

position fitting best (4948.282 mm) the calibration values was calculated using the dimension of the detector's pixels (172 μm) and a tilt angle of the detector (0°).

SAXS Frame validation

For the *in situ* shear experiment, the interchangeable mobile plate of the Linkam cell was made of 1 mm thick steel. A ring shape window was cut at 7.5 mm from the centre to let the X-ray beam through. However, three 0.5 mm wide spokes crossed the window to ensure the cell's structural integrity. Although these spokes only represent 3% of the cell's circumference, they inevitably cause some transmission anomalies. These spokes also presented sharp interfaces for the radiation to reflect from, generating flares on the detector periodically as the mobile plate was rotated. Consequently, the intensity measured at the photo diode will be strongly affected by these scattering anomalies. Much lower transmission values were thus measured then the X-ray beam hit one of the spokes or reflected from their edges. To evaluate the impact of the spokes on the scattering patterns, a native dope sample was slowly sheared at 1 s^{-1} (0.093 rad/s) for 300 seconds whilst recording the scattering patterns for 50 ms every 4 seconds. Every 1/3 of rotation or 22.5 s, a spoke cut the beam path which occasionally coincided with the SAXS acquisition.

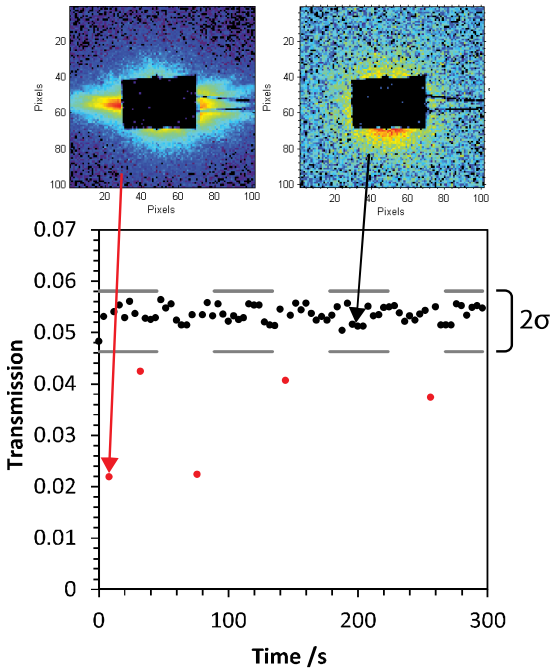


Figure A.22 Transmission for a native silk sheared at $1s^{-1}$ for 300 seconds and corresponding scattering pattern near the beam. The scattering was measured for 1 second every 4 seconds. Rejected time frames outside the 2 σ interval are presented in red.

As shown in Figure A.22, the transmission drops coincide with the presence of flares on the scattering patterns. Thus, by rejecting frames with a corresponding transmission value outside a confidence interval equivalent to twice standard deviation around the average, we can effectively exclude these scattering artefacts.

SAXS Radiation damage

Radiation damage is a well-known issue associated with using bright X-ray sources.[Henderson1990] As X-rays are a form of ionising radiation with enough power to break molecular bonds, special care must be taken to minimise this effect.[Martis2011] For this reason, ESRF's BM26B beamline was specifically designed to minimised radiation damage by using a combination of attenuators, fast shutters and the soft branch of a bending magnet.[Borsboom1998] To minimise radiation damage, we combined two strategies. First, we made silk sample to flow through the probed area to constantly bring fresh sample into the beam. This technique is commonly used for biological samples.[Nielsen2012] Before setting the

flow velocity, the maximum exposure time on the static sample was determined by irradiating a static native silk sample continuously for 30 seconds at 1 second intervals.

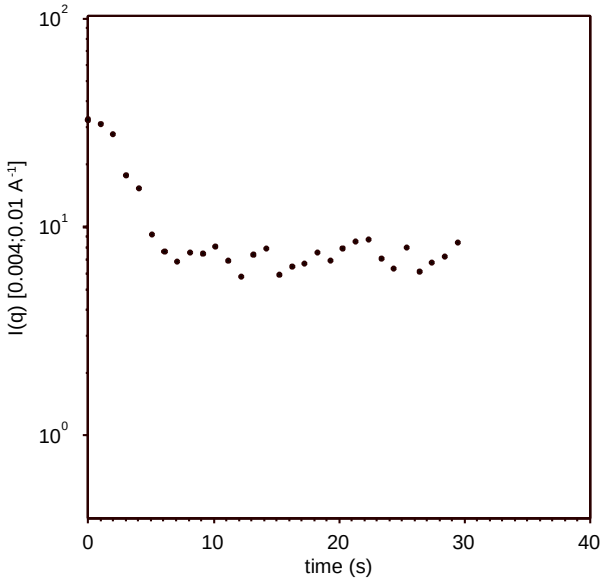


Figure A.23 $I(q)$ of static native silk as a function of time under constant X-ray exposure.

As shown in Figure A.23, the intensity at low q starts to decrease a few seconds after the beginning of the irradiation for a static native silk sample. By keeping the acquisition time below one second we can thus avoid radiation damage. As the beam size is smaller than one millimetre, flowing the sample at $1s^{-1}$ or 0.7 mm/s was more than sufficient to avoid localised radiation damage on a flowing sample. Instead of making the sample flow, the second approach is the mapping of the cell. Radiation damage can also be minimised by moving the cell relative to the beam in order to probe fresh sample every time. Frames were thus collected at 0.5 mm interval and exposed for only 1 second.

SAXS Cell scanning

For the *ex situ* shear history method, the centre of the cell (stagnation point) was first located to align to with the beam. This was done by measuring the transmission value across the whole cell until the beam hits both cell walls. The centre of gravity of the

transmission was then used to align the cell horizontally and vertically using the motorised xyz stage.

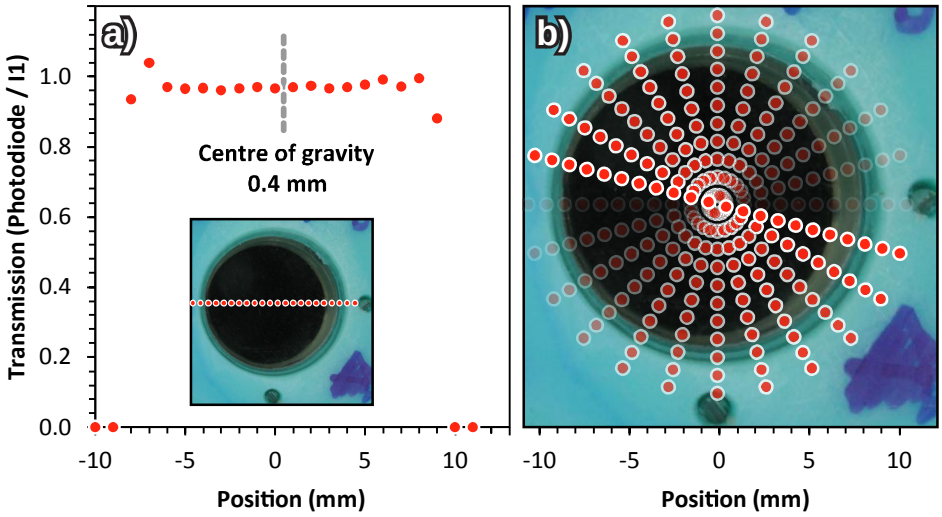


Figure A.24 a) Transmission of an empty cell as a function of the horizontal position, b) Cell mapping scattering acquisition sequence.

As plotted in Figure A.24a, the transmission drops to zero when the beam hits the cell's frame. Even if the interval between each point was 1 mm, the centre of the cell could be determined to 100 μm accuracy using the centre of gravity. The motor's zero position along x and z was then set to the centre of the cell to ensure scattering pattern were symmetrical on each side of the stagnation point. Scattering patterns were acquired along a line from one edge to the other at 0.5 mm intervals. Once the first line is completed, another line for points is acquired but rotated of 15° from the centre. Since the stagnation point at the centre of the cell was probed repeatedly using this mapping mode, this point was rejected from the analysis. As illustrated in Figure A.24b, successive lines are acquired all around the cell until the last line superimposed the first one at 180°. Although more complex to program than a simple Cartesian mapping, this acquisition method kept a regular time interval between each shear history profile. Consequently, this method allowed the study of the spontaneous conversion kinetics as well as the measurement of the shear rate profile.

As the acquisition time was set to one second per point, the main limiting factor became the motor speed as it took much more time to move the cell to the required position than to perform the measurement. The fast shutter ensured that the cell was not exposed between each stage repositioning.

Appendix 5 Thesis finding summary

The observation and subsequent interpretation which have led to the thesis's main findings are summarised in Table A.2, Table A.3 and Table A.4 below.

	Observations	Interpretations
Figure 3.5	If put on a relative scale, the IR absorption band at 1617 and 1700 cm^{-1} components are assigned to β-sheets, as well as the 1547 and 1642 cm^{-1}.	Shear-induced β-sheets are aligned in the flow direction.
Figure 3.6	The peak at ν_1= 1642 / ν_2= 1512 cm^{-1} starts to decrease before the earliest β-sheets bands. The weak ψ peak at ν_1= 1700 / ν_2= 1617 cm^{-1} suggests that 1617 cm^{-1} is affected slightly before 1700 cm^{-1}.	Unordered structures are affected before the β-sheets' vibration modes parallel to the strands, followed by the perpendicular vibration modes and the β-turns.
Figure 3.7	Addition of alcohol generated many more β-sheets than shear.	Shearing forces applied by our setup is less effective than alcohol at converting standard RSF.
	Conversion is far from being completed when 20 kPa of normal force is reached for RSF.	Better gap control is required. And / Or RSF is not a suitable analogue.
Figure 3.8	Standard RSF conversion could only be triggered above ~50% concentration.	Standard RSF requires higher concentration than native to become shear sensitive.
Figure 3.9	Orientation increases before the rapid growth of β-sheet content for RSF.	The protein pre-aligned along the flow direction before the rapid conversion is triggered.
Figure 4.4	Small angle scattering changes are only observed for q < 0.09 $Å^{-1}$	Silk has persistent length scales between 8 to 70 Å.
Figure 4.5	For NSF, $I(q)$ varies as a function of the azimuthal angle, peaking at 90 and 270°.	NSF nanoscale domains align along the shearing direction.
Figure 4.6	The $\langle P_2 \rangle$ increased only at q < 0.05 $Å^{-1}$.	Only structures larger than 126 Å aligned under shear (~3 beads of 4 nm).
Figure 4.7	Getting the equivalent level of orientation at 5 and 10 s^{-1} requires more strains than 100 s^{-1}.	Silk's alignment is a rate-dependent process unlike conventional polymers.
Figure 4.10	I_{iso} was only 7 ± 1% of the final value after 10 seconds at 70 s^{-1}.	The nanoscale changes are far from being completed when shearing force becomes ineffective.
	The half process time $t_{1/2}$ was determined to be 13600 seconds.	The spontaneous conversion process takes many hours to complete at room temperature.
	The instability shear rate for triggering the conversion was evaluated to be 26.3 s^{-1}.	The stress required for triggering conversion is more than the silk's relaxation time.

Table A.2 The main findings from Chapter 3 and 4 with their associated observation and interpretation. I_{iso} is the isotropic scattering intensity. RSF is the abbreviation for reconstituted silk feedstock

	Observations	Interpretations
Figure 5.3	G_N for NSF samples was 13 ± 3 kPa, in contrast with 0.008 ± 0.006 kPa for standard RSF. RSF never showed a cross-over point.	The gap revealed the distinct levels at which native silk and artificial feedstocks can store and dissipate mechanical energy.
Figure 5.4	NSF and RSF static IR spectra are indistinguishable, but only NSF converted under shear flow at 22 ± 3%.	IR is not sensitive to the structures responsible for the flow properties' differences. Flow stress is required for discriminating RSF and NSF.
Figure 5.5	NSF η_0 was 1.2 ± 0.4 kPa·s whilst it was only 0.09 ± 0.05 kPa·s for standard RSF.	The difference in η_0 between the NSF and standard RSF can be due to their different intermolecular interactions.
	Only the COG of the amide II band for NSF started to shift slightly during the shear thinning.	Thus the shear thinning response of NSF is likely to be due to greater molecular alignment and a subsequent reduction in internal friction.
	Shear rates above a critical value ($\dot{\gamma}_i$ = 50 ± 20 s^{-1}) led to shear thickening and to the shift of both amide I and II bands.	The start of the protein aggregation is responsible for the shear thickening.
	Shortly after the shear thickening, wall slippage occurs; well before the completion of the conversion. Spontaneous conversion follows once stress is stopped.	Shearing forces alone cannot drive the β-sheet conversion to completion. Spontaneous conversion can complete the process.
Figure 5.6	Most changes are revealed by s polarisation.	If neither polarisation can be collected, aligning the polarisation with the velocity vector is preferable.
Figure 5.8	The meta-structures were quantified to 30% by MCR-ALS.	Most of the structures are permanent in *Bombyx mori* silk.
Figure 5.8	Decrease of the measured alignment by MCR-ALS.	The orientation relaxes after shear. And / Or The β-sheets formed spontaneously are not as aligned as the first formed under stress.

Table A.3 The main findings from Chapter 5 with their associated observation and interpretation. NSF is the abbreviation for native silk feedstock. $\dot{\gamma}_i$ represents the instability shear rate whilst G_N is the plateau modulus and η_0 is the zero shear viscosity. MCR-ALS is the abbreviation of self-Modelling Curve Resolution Alternating Least Square.

	Observations	Interpretations
Figure 6.3	Silk secreted by *Bombyx mori* single still has ~68% of its water content.	Most of the feedstock's water evaporates after secretion *ex vivo*.
	The β-sheet peaks are very weak after secretion.	Secreted silk is not completely processed.
Figure 6.4	The β-sheet conversion continues *ex vivo* as long as the fibres are not dried.	Drying silk quickly after secretion can be used to interrupt silk's conversion and obtain lower-crystallinity fibres.
Figure 6.5	Increasing the water content will progressively decrease the glass transition $(T, RH)_g$ until room temperature is reached, resuming the conversion at RH =~76% relative humidity.	Dry-spun silk's conversion can be resumed if stored under wet and/or warm conditions.
Figure 6.7 & Figure 6.8	Tanned *Saturnia pavonia* silk cocoons have higher β-sheet content than paler silks. The darker silk feedstock portion found in an *Attacus Atlas* gland had more β-sheets than clear feedstocks.	The molecules responsible for wild silk's tanning can only change the coloration of aggregated or converted silk.
		And / Or
		β-sheets are required for wild silk's tanning and cross-linking.
Figure 6.9	In contact with the LiBr, the amide II band area stabilised after 5 minutes at 25 °C.	Dry-spun fibres are soluble in 9M LiBr at room temperature, making them easier to solubilise than aged fibres.
Figure 6.10	Hi-Fi RSF has a cross-over point at 2.5 ± 0.9 Hz. Hi-Fi RSF G_N is 7 ± 1 kPa whilst NSF is 13 ± 3 kPa.	NSF and Hi-Fi RSF made of lower-crystallinity fibres have very similar dynamic flow properties.
Figure 6.11	Hi-Fi RSF 1.0 ± 0.5 kPa·s compared with 1.3 ± 0.6 kPa·s for NSF. They both present shear thinning followed by thickening behaviours with rising normal force.	NSF and Hi-Fi RSF made of lower-crystallinity fibres have undistinguishable viscosity and recoverable elastic strain.
Figure 6.12	Like NSF, Hi-Fi RSF amide bands shift abruptly once the instability shear rate is reached.	Capable of forming β-sheets under equivalent stress, Hi-Fi RSF is as shear sensitive as native silk.
Figure 7.3	Saturnid wild silk feedstocks have a distinct marker at 1308 cm^{-1}.	This component is an indicator of a distinctive precursor secondary structure.
		Or
		This component is an indicator of tanning and maybe cross-linking.
Figure 7.5	Cocoon infrared spectra have distinctive IR spectra features.	IR spectra can inform on the crystallinity, sericin, calcium oxalate and the polyphenol content of the cocoon surface measured.
Figure 7.7	The canonical values provide the relative dissimilarity between cocoons from different species.	*Epiphora bauhiniae* and *Samia* silks are found to be the most similar measured silks to spider dragline.
	Bombyx mori silk is relatively dissimilar to all wild species measured.	*Bombyx mori* might not represent well the large diversity of silks.
Figure 7.9	The ultrametric tree built from IR spectra is remarkably similar to the phylogenetic tree made from protein expressing nuclear genes.	As IR spectra are phylogenetically informative, they could complement gene-based species classifications.

Table A.4 The main findings from Chapter 6 and 7 with their associated observation and interpretation. RSF stands for reconstituted silk feedstock whilst Hi-Fi stands for High Fidelity. RH stands for relative humidity. IR is the abbreviation for infrared.

Appendix 6 Lo-Fi RSF protocol

Reconstituted silk feedstocks preparation protocol for the sample measured in Chapter 3 and Chapter 5.

Degumming

- ❑ Prepare 1L of 70°C Na_2CO_3 solution (5 g/L).
- ❑ Weigh 20g of dry cocoon to degum.
- ❑ Add 500mL of Elix type II purified water into the food processor with the blades in.
- ❑ Turn on the food processor at maximum speed and pour in the cocoons one by on leave for 15 minutes. It is necessary to cut roughly the cocoons before doing the degumming otherwise fibres can entangle the blender's shaft.
- ❑ Using gloves, take the blade out before taking the fibres out. Filter the blender's content using a coarse mesh to recover most of the fibres before cleaning the food processor with Elix water. Filter the washing water to recover most of the fibres. Wash the fibres by pouring Elix water in the filter. Wring the fibres and put them in a clean plastic box.
- ❑ Repeat 2 times.
  - Fill the food processor again with 500 mL of 70°C Na_2CO_3 solution (5g/L).
  - Turn on the food processor at minimum speed and gradually pour in the wrung fibres little by little and leave for 60 minutes.
  - Using gloves take the blade out before taking the fibres out. Filter the blender's content using a coarse mesh to recover most of the fibres before cleaning the food processor with Elix water. Filter the washing water to recover most of the fibres. Wash the fibres by pouring Elix water in the filter. Wring the fibres and put them in a clean plastic box.
- ❑ Repeat 3 times.
  - Fill the food processor with 500 mL of Elix type II water.
  - Turn on the food processor at minimum speed and gradually pour in the wrung fibres little by little and leave for 15 minutes (use timers).
  - Using gloves take the blade out before taking the fibres out. Filter the blender's content using coarse mesh to recover most of the fibres before cleaning the food processor with Elix water. Filter the washing water to recover most of the fibres. Wash the fibres by pouring helix water in the filter. Wring the fibres and put then in a clean plastic box.
- ❑ Replace the food processor steel blade by the mixing plastic blade.
- ❑ Place the fibres in the blender and blend for 5 minutes until they become small bits.
- ❑ Put the fibres in the Mini Oven (blue, under the freeze dryer) at 50°C for drying overnight and label/date the batch.
- ❑ Replace the food processor steel blade by the mixing plastic blade.

- ❑ Place the fibres in the blender and blend for 5 minutes until they become very small fluffy bits.
- ❑ Put the fibres in the vacuum oven overnight and label/date the batch.
- ❑ Replace the food processor steel blade by the mixing plastic blade.
- ❑ Place the fibres in the blender and blend for 5 minutes until they become a fluffy mass.
- ❑ Store the fibres in a clean plastic box with desiccant packs and leave at 5°C.
- ❑ Fill in the XP Metadata spreadsheet (degumming section).

Dialysis tube preparation

- ❑ Cut a 25cm long dialysis tube and immerge in Elix water of few minutes.
- ❑ Put tie a strings at the tube base and attach an Eppendorf.
- ❑ Rinse the tube twice with Elix water and test its permeability.
- ❑ Keep the tube in Elix water.
- ❑ Drying tube preparation:
- ❑ Cut a 30cm long dialysis tube and immerge in Elix water of few minutes.
- ❑ Cut the tip of a 10 mL at its 2 mL mark.
- ❑ Cut and seal a needle that fit the syringe.
- ❑ Insert the syringe tip inside the dialysis tube and tie with three strings, one at the tip, on the base and one just after the syringe.
- ❑ Seal the bottom with parafilm.
- ❑ Rinse the tube twice and test its permeability.
- ❑ Keep the tube in Elix water.

Dissolving the silk

- ❑ Prepare 9M LiBr solution (100ml -> 80g LiBr). Place a large beaker and on the balance weigh the desired volume of solution (1g = 1mL)
  Draw a line on the beaker, remove half of the water. Add the required amount of LiBr slowly. Attention! Exothermic reaction! Complete the volume to the marked line. Store in a glass bottle for further use.
- ❑ Weigh no more than 25% (w/w) of dried and degummed silk. Note the fibre on LiBr ratio (the standard concentration is 250mg/mL)
- ❑ Finely cut the fibres using scissors or an herb chopper to obtain fibre less than 1 mm long. The fibre should not have enough entanglement to flow freely through a liquid funnel. The fibres that do not pass through the funnel must be cut again.
- ❑ Heat a water bath to 70°C (or less, note the temperature) with a smaller 40 mL beaker containing 20mL of LiBr solution. Make sure the water of the bath is stirred and that the bottom of the beaker is not touching the bath to prevent any local heating. The goal is to uniformly heat the beaker.
- ❑ Mount the dialysis bag at the end of the funnel while keeping the bag immersed in tall container filled with Elix water.
- ❑ Pour the silk fibers in the funnel and stir gently with a glass rod.
- ❑ Soak the silk as quickly as possible (2-3 min) to ensure that the whole batch has a similar exposition to the LiBr solution.

- ❑ Let the fibres solubilise without stirring for 20 min (note the duration, between the first fibre is soaked and the moment the solution is poured in the funnel).
- ❑ Once solubilised pour the silk solution in the funnel into the dialysis bag.
- ❑ Once the dialysis bag is filled, seal the top end with a string and a clamp. Close the tall container.

Dialysis

- ❑ Leave the dialysis container in the cold room (~5°C).
- ❑ Change the water after 2h, 4 times and leave overnight for a 4th dialysis.
- ❑ Test for remaining traces of LiBr by adding silver nitrate to the bottom fraction of the washing water.

Drying concentration step

- ❑ Attach the drying bag to a funnel with a filter. Note the type of filter used. Pierce the dialysis bag and transfer the RSF to the drying bag.
- ❑ Hang the dialysis bag in the cold room in front a spinning fan.
- ❑ Silver nitrate test for LiBr:
- ❑ Test wash water by taking 1ml in an eppendorf an adding one-two grains of silver nitrate, If it turns black after some time (exposure to light) there is still LiBr in there.

Appendix 7 Hi-Fi RSF protocol

This protocol detailed the method for the high fidelity reconstituted silk feedstock preparation used in Chapter 6.

- 5^{th} instar silkworms just starting to spin are stored at 9°C for 2 days to slow this process until we were ready. When ready to use, the worms need to be stored for spinning at room temperature (22± 2°C) in a compartmented and punctured cardboard box.
- Each compartment of the box is 2 cm wide, 2 cm deep and 4 cm tall allowing silkworms to construct cocoons vertically. Absorbent material is placed at the bottom of the box preventing increased local humidity and contamination of other cocoons. The box is placed in a larger nearly sealed container constantly purged with dry air from a compressed air dryer. The maintained positive pressure ensures that the relative humidity level in the cardboard box was very close to zero %.
- The worms need to be left alone for spinning for at least 5 days, but no more than 10 days.
- After this time the cocoons are removed from the box. Cocoons are rotated upside down to let the pupae fall in the top of the cocoons. A circular opening is then cut from the top (originally the bottom). The cocoon is then rotated again to let the pupae fall outside the cocoon, which is discarded along with the cocoon's lid. The pupae must not be punctured to prevent contamination from internal fluid. Any contaminated portion of the cocoon needs to be removed.
- The dry-spun raw silk needs to be stored under dry air purge at room temperature (22 ± 2°C) before degumming. One by one, the cocoons were blended in demineralised water at room temperature (22 ± 2°C).
- In the blender, 500 mL of water (type II, >2MΩcm) is used for 10 g of raw cocoons. Cocoons are first blended for 15 minutes before filtering the mixture with a 50µm pore size filter to remove the water and keep the fibres. The blending step is repeated two more times.
- Afterward, the degummed fibres are wringed and dried at room temperature for 24 hours under partial vacuum (~800 mBar). The dried and degummed fibres are then stored under dry air purge at room temperature (22 ± 2°C). A 9.5M lithium bromide solution (0.8 g/mL), 20mL is first heated to 70 ± 2°C in a glass container in a water bath. 5g of degummed dried silk is then added rapidly to the solution to make a 0.25 g/mL solution. The solubilising silk was stirred gently with a glass rod to homogenise the solution. 10 minutes after the fibres were added to the LiBr solution, the mixture is poured in a 20 cm long dialysis bag equipped with a closable nozzle.
- Once filled, the dialysis bag was sealed by attaching a string to the end whilst making sure that no air is trapped inside the completely filled bag. Nozzle up, the dialysis bag is then put into a long and narrow container filled with demineralised type II water. The LiBr is then removed by dialysis over 12 hours.
- The water is replaced every 2 hours in the container to maintain the osmotic pressure gradient. Using a conductivity meter, the resistivity of the container's water

is measured after 12h. If the resistance is still lower than 2 MΩcm (0.5 μScm^{-1}), the dialysis is repeated.

- ❑ The reconstituted silk dialysis bag is hung nozzle down in a cold room (4 ± 2°C) to dry under a constant air current provided by a fan situated 20 cm away from the bag.
- ❑ The concentration is monitored by comparing to a concentration curve produced by Fourier transform infrared spectroscopy until desired concentration is reached. Afterwards, the sample is sealed to prevent it from drying further and stored at (4 ± 2°C) until used.

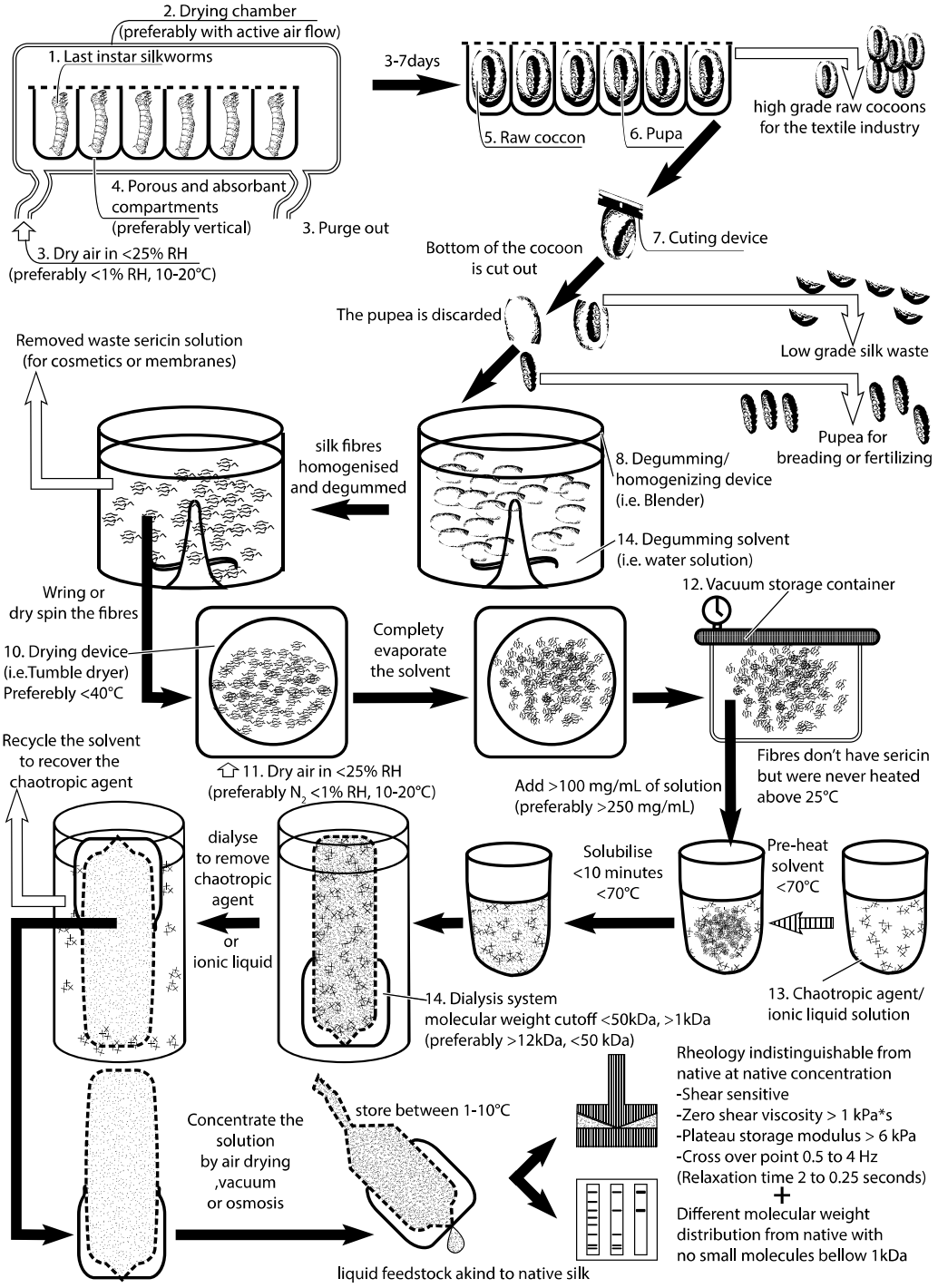


Figure A.25 Schematic of the Hi-Fi RSF process.

Appendix 8 Published manuscripts

Cite this: *Phys. Chem. Chem. Phys.*, 2011, **13**, 3979–3984

www.rsc.org/pccp **PAPER**

Rheo-attenuated total reflectance infrared spectroscopy: a new tool to study biopolymers

Maxime Boulet-Audet,* Fritz Vollrath and Chris Holland

Received 19th November 2010, Accepted 22nd December 2010
DOI: 10.1039/c0cp02599b

Whilst rheology is the reference technique to study the mechanical properties of unspun silk, we know little of the structure and the dynamics that generate them. By coupling infrared spectroscopy and shearing forces to study silk fibroin conversion, we are introducing a novel tool to address this gap in our knowledge. Here the silk conversion process has been studied dynamically using polarized attenuated total reflectance Fourier transform infrared spectroscopy whilst applying shear, thus revealing silk protein conformation and molecular orientation *in situ*. Our results show that the silk conversion process starts with a pre-alignment of the proteins followed by a rapid growth of the β-sheet formation and then a subsequent deceleration of the growth. We propose that this tool will provide further insight into not only silk but any biopolymer solution, opening a new window into biological materials.

Introduction

The cocoon of the Chinese silkworm, *Bombyx mori*, is a complex biological composite consisting of two silk fibres, surrounded by a glue-like sericin matrix. The fibres consist of two structural proteins, heavy and light chain fibroins of 391 and 26 kDa, respectively.[1–3] These proteins possess highly repetitive amino acid motifs $(GAGAGS)_8$, which enables them to adopt anti-parallel β-sheet structures containing an extended network of hydrogen bonds[4] which are responsible for silk's toughness.[5–7] Even though silk has evolved to perform truly *ex vivo*, its biocompatibility allows its use *in vivo* as well. This combination of properties makes silk highly suitable for numerous biomedical applications, from suture threads to bone scaffold.[8] However, to create such devices, the silk needs to be first resolubilised in order to allow it to be shaped and formed into foams, fibres, meshes or films.

Unfortunately, the network of hydrogen bonds responsible for its impressive toughness is also responsible for making silk regeneration, or reconstitution, such a challenge.[9] Indeed, the reconstitution of silk is known to have a major effect on the mechanical properties, making it much stiffer and more brittle that its natural counterpart.[10] Silks are typically reconstituted using strong chaotropic agents that are known to disrupt the proteins.[10] Even if it might be impossible to "unspin" silk completely,[11] we should still be able to optimise this process, provided that we have the appropriate tools to determine the quality of a reconstituted silk fibroin (RSF) solutions.

University of Oxford, Department of Zoology, Tinbergen building, Oxford, OX1 3PS, UK. E-mail: maxime.boulet-audet@zoo.ox.ac.uk; Tel: +44(0)1865271216

It is well established that mechanical forces trigger the conversion of silk.[12,13] Thus, rheology became one of the leading techniques to study RSF[10,14–18] and a very useful tool to evaluate the "spinnability" of RSF solutions.[10] Nonetheless, with the improvement of the reconstitution process, a finer discrimination of RSF from native silk dopes is becoming necessary, requiring a multidimensional approach to "spinnability indicators".

The shear-induced crystallization of polymers has been the object of many rheo-optics studies including small angle X-ray scattering (SAXS),[19–21] neutron (SANS),[20] light (SALS)[22] and wide angle X-ray scattering (WAXS).[21] Despite being a model biopolymer,[23] silk has been investigated in very few rheo-optical studies using a couette cell by SAXS[24] or NMR spectrometry.[25] These studies were limited by either having to use dilute solutions, long acquisition times, or both. Since time resolved Fourier Transform Infrared (FTIR) spectroscopy is a well established technique to determine silk protein secondary structure,[14,15,26–30] and has an exceptionally fast acquisition speed (50 ms down to 2 ns in step-scan mode), it is perfectly suited to combine with shearing devices.

FTIR has been previously combined with parallel plates[31] and extensional shearing devices using an attenuated total reflectance (ATR) accessory,[32] however these approaches are best applied to large sample volumes and/or dilute samples. The use of a cone and plate shearing device presents a suitable alternative; allowing small and highly concentrated samples to be studied with minimal shear history caused by the loading.[33]

We evaluated Rheo-ATR-FTIR as a method to provide deep physiochemical insights into the shear sensitivity of silk macromolecules by monitoring *in situ* their molecular structure during controlled shear induced transitions. Specifically, we

This journal is © the Owner Societies 2011

set out to verify whether this approach would allow us to study the complexity of the spinning process of silk. More generally, we also set out to evaluate Rheo-ATR-FTIR as a method to determine the "quality" of RSF by providing a new set of "spinnability" indicators.

Materials and methods

Reconstituted silk fibroin (RSF)

Bombyx mori cocoons were degummed according to standard methods and solubilised in 9 M lithium bromide solution (< 70 °C).[10] After solubilisation, silk solutions were dialyzed at 4 °C in dialysis tubing (VISKING® MWCO 12000–14000; pore diameter *ca.* 25 Å) against stirred demineralized water changed four times over 12 h. A subsequent concentration step was performed by hanging the dialysis bags at 4 °C in a gentle air stream. A wide nozzle was used at the end of the dialysis bag to facilitate loading onto the ATR crystal. Completely converted samples were obtained by placing a fibroin sample onto the ATR crystal surrounded by an environment cuff containing methanol vapour.

Spectral acquisition

A Nicolet 6700 Fourier transform infrared spectrometer equipped with a liquid nitrogen cooled MCT-A detector was used with a single bounce diamond attenuated total reflectance (ATR) sampling accessory (Thermo Electron Corp., Madison, WI). The diamond's internal reflectance element (IRE) has a refractive index of 2.417 with an angle of incidence of 45°. The penetration depth of the evanescent wave for diamond is 1.2 μm at 1650 cm^{-1} and varies with the wavelength.[34] For molecular orientation measurements, the electric field of the infrared beam was polarized perpendicular (*s*) or parallel (*p*) to the plane of incidence with a motorized (~10° s^{-1}) ZnSe holographic wire grid polarizer with 2700 grooves/mm (Thermo Scientific, Madison, WI). For fast kinetic experiments, only the *s* polarization was used. A large aperture was selected to probe a ~2 mm^2 area whilst keeping a well defined beam spot. Spectra were acquired at a 4 cm^{-1} resolution from 500 to 6000 cm^{-1} using a Happ-Genzel apodization, a Metz phase correction and no zero filling. Static spectra were obtained from the average of 32 scans as kinetics were recorded using 5.05 s time frames of 22 scans at a 5.0632 cm s^{-1} mirror speed. All spectral operations were executed using the Omnic 7.3 (Thermo Scientific, Madison, WI). The only applied correction was an offset at 4000 cm^{-1}. The absorbance variation profiles were plotted by using the average absorbance of 10 cm^{-1} region. The centre of gravity of the amide I band was plotted using the 20% upper portion of the 1594–1700 cm^{-1} region for a more sensitive monitoring of the conformation. The point at which the first detectable changes occurred (take-off point) was calculated using the detection limit of the amide I band centre of gravity, three times the standard deviation of the blank average for two consecutive time frames. The growth point was defined as the absolute maximum of the second differential determined by a partial least square linear regression over a 70 s mobile average.

Dry weight quantification

An additional drying step was performed once the RSF was placed onto the ATR crystal. The samples were dried using a gentle dry air stream as spectra were recorded to determine the concentration using a calibration curve built using TQ analyst edition 7.2 (Thermo Electron Corp. Madison, WI). The dry weight (DW) of the 94 standards was measured from 0.05 to 0.30 grams of RSF dried under vacuum for at least 12 h. The method used was the partial least square (PLS) with three factors (representing 94% of the variance) on the 2500–3900 cm^{-1} and 500–1430 cm^{-1} regions. The predicted concentration values were calculated using the multiplicative parameters (Eigen vectors) of three factors. The performance index of the method was 86.6, the curve correlation coefficient was 0.987 and the average uncertainty of the dry weight was 3%.

Experimental setup

The Rheo-ATR-FTIR setup consists of a purpose built shear flow cell mounted on the single bounce diamond ATR accessory preceded by the polarizer. The geometry used for all shearing experiments was a 10 mm tungsten cone with a 1° angle (CP1/10). The ATR accessory's stainless steel plate served as the bottom plate of the geometry as the rotating cone (0.0874 rad s^{-1}) provided a constant shear rate of 5 s^{-1}. The strain was calculated by multiplying the time by the shear rate. The weight of the shaft ensured a constant normal force of 20 kPa on the sample to maintain the gap during the conversion process. To ensure the sample did not dry during shear, the system was sealed with an environment cuff.

As illustrated in Fig. 1, the infrared beam propagates along the *x* axis. The *s*-polarized light only probes along the *y* whilst *p*-polarized light probes along both *x* and *z* axes. Thus, the theoretical ratio of *p* on *s* polarized spectra (R^{ATR}) is 2 for non-oriented (isotropic) samples with a 45° angle of incidence.[34]

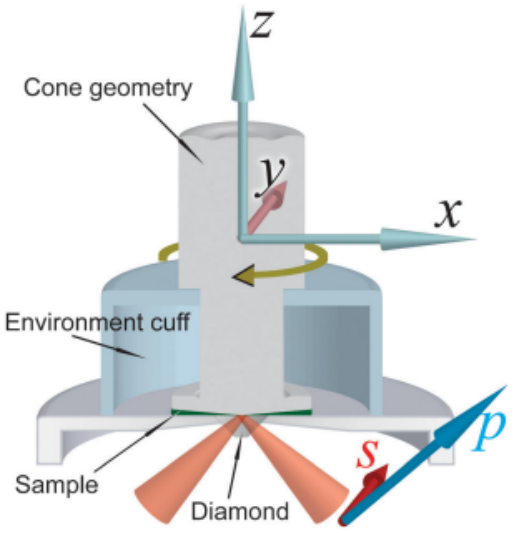


Fig. 1 Experimental setup used for the Rheo-ATR-FTIR measurements.

This journal is © the Owner Societies 2011

A R^{ATR} lower than 2 means a preferential orientation in the plane of the ATR crystal and a R^{ATR} higher than 2 is out of the plane. The geometry is concentric to the beam spot evenly distributing the strain around the z axis. The quantification of the orientation along the z axis would be theoretically possible by assuming a cylindrical symmetry and decomposing the spectra into their components.[35] However, R^{ATR} was used directly to qualify the orientation since the interfering H_2O content makes the spectral decomposition challenging.

Results and discussion

Fig. 2 shows the typical conversion kinetics of a concentrated RSF sample under shear (5 s^{-1}) after subtraction of the initial unsheared sample spectrum. Shearing the material faster than its relaxation time, typically 2 to 5 s^{-1},[33] triggers a change in conformation from disordered structures to β-sheets.[36] After the start of shearing, the subtle variations in the signal are due to changes in the local concentration whilst the sample is homogenised. By probing only the bottom layer of the sample (1.2 μm at 1650 cm^{-1}),[34] ATR spectroscopy is sensitive to the local concentration and can detect precipitation or phase separation. The exponential growth of the β-sheets occurs a few hundreds of seconds later. Once a notable proportion of β-sheets were generated, the samples started to become solid, increasing the normal force drastically and lifting the cone geometry.[33] As a result, the sample either stuck to the bottom plate or started to roll between the cone and plate. As the sample became detached from the geometry, the β-sheet growth rate slowed rapidly. Importantly, the observed three-phase conversion kinetics induced by the mechanical stresses is in agreement with the results obtained using other types of stress.[36,37]

FTIR spectroscopy is very sensitive to protein conformations.[38] As shown in Fig. 3, the difference spectra at the beginning of the fast growth (blue) and at the end of the kinetic (red) are nearly identical, once put on a relative scale. Both show gained β-sheet peaks at 1512, 1614 and 1700 cm^{-1} as well as negative peaks due to unordered structures lost at 1547 and 1642 cm^{-1} (see Table 1 for assignment). The stacked curves indicate that gained and lost structures in the early stage of the conversion process are similar to those formed later.

The conversion kinetics can be easily visualised by directly plotting the absorbance difference of vibrational modes.

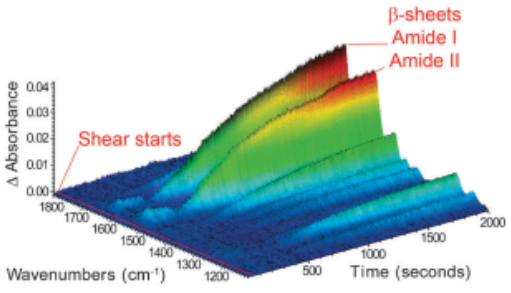


Fig. 2 Difference spectra of a 68 ± 3% RSF sample under 5 s^{-1} shear rate as a function of time.

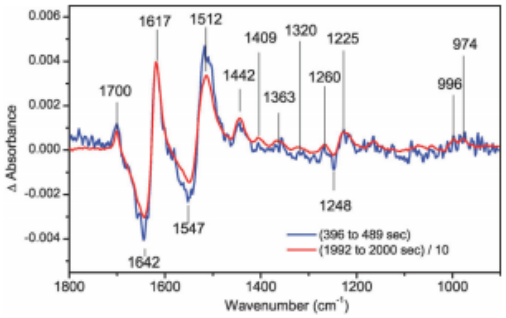


Fig. 3 Difference spectra at the beginning of the growth (red) and after the gelation divided by a factor of 10 (blue).

However, if the sample starts to roll between the upper and lower plates, the absolute absorbance will decrease proportionally to the contact surface. To overcome this potential issue, the centre of gravity of the amide I band's upper part can be used as a monovariable conversion indicator independent of the surface contact. The point at which the first variation in the infrared signal is detected (take off point) and the point at which the β-sheet content starts to increase rapidly (growth point) can be measured accurately with the second differential of the centre of gravity.

It is possible to distinguish in Fig. 4 the three steps of the conversion process by plotting the components that varied the most. If put on a relative scale, the 1617 and 1700 cm^{-1} components assigned to the β-sheets, as well as the 1547 and 1642 cm^{-1} assigned to unordered structures, have very similar kinetics confirming that these components are associated with the same or joined structures. Since the spectra were *s*-polarized, the contrasting kinetics observed in Fig. 4 for the 1512 and 1617 cm^{-1} components could be explained by their different orientations relative to the protein's backbone (see Table 1).[30,39,51]

To estimate the relative amount of β-sheets formed by controlled shearing, a sample with the same concentration was converted using methanol vapour. As shown in Fig. 5, the peaks associated with β-sheets are much more prominent in the sample converted by alcohol. The difference between the amide I and II ratio could be explained by the lack of molecular orientation of the MeOH converted sample. After subtraction of the static spectrum, the difference obtained with methanol is several folds greater in the amide I region. This result suggests that the conversion process is far from completed when the sample gels by shearing. According to this observation, it is likely that the shearing forces trigger the silk conversion in this system, but are not driving it to completion. *In vivo*, we predict that extensional flow and changes to the pH and ionic concentrations[52] can contribute to complete the conversion.

Sample concentration is one of the critical parameters governing a silk solution's rheological behaviour.[10] As displayed in Fig. 6, the amount of strain required to initiate the fast growth of β-sheets (growth point) varied according to the concentration, comparable to the rheology-only "spinnability indicators". The variability can be explained by the tolerances

BBB

Table 1 Assignment of the main fibroin bands

Position (cm^{-1})	Assignment	Preferential orientation[a]	References
1700	Amide I, β-sheets	∥	39–42
1642	Amide I, unordered	⊥	43–46
1617	Amide I, β-sheets	⊥	30,39,40,47,48
1547	Amide II, unordered	∥	44,45,49,50
1512	Amide II, β-sheets	∥	30,43–45,47,49,50

[a] Relative to the protein backbone.

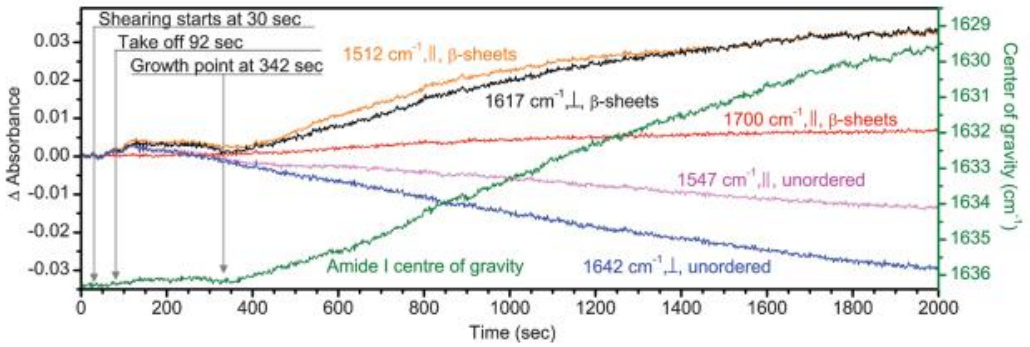


Fig. 4 Difference absorbance and centre of gravity of the major bands of a 68 ± 3% RSF sample under 5 s^{-1} shear rate as a function of time.

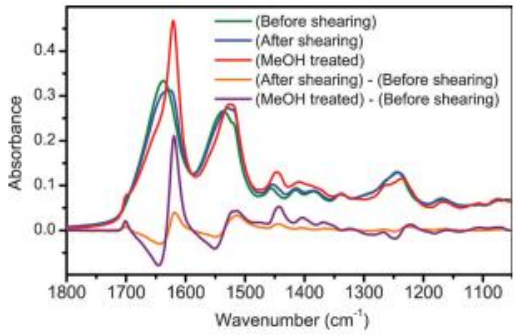


Fig. 5 ATR FTIR spectra before, after 2000 s of shearing at 5 s^{-1}, after MeOH vapour treatment and their difference.

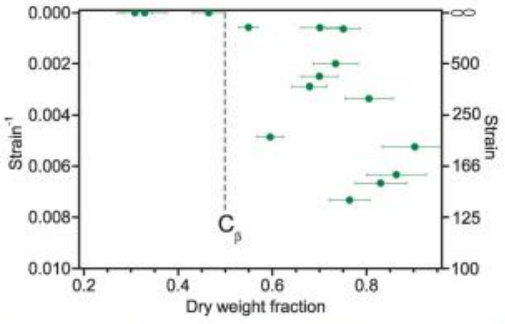


Fig. 6 Strain (time * shear rate) at the growth point as a function of the dry weight fraction.

of the purpose built rheometer or the sample loading. For a given RSF lot, the growth point indicated that the conversion requires the concentration to be over a certain threshold C_β of ~50%. As a result, the growth point could be used as a complementary indicator of the RSF quality since previous experiments investigating the rheological spinnability indicators did not exceed the C_β (reaching only 36% DW).[10] Three out of the 15 kinetics recorded never converted under a 5 s^{-1} shear ($strain^{-1} = 0$). Over the concentration range, the growth point varied by more than an order of magnitude, from 133 to 2745 strains.

As shown in Fig. 4, the 1512 cm^{-1} component has a slightly faster conversion kinetic than the 1617 cm^{-1} component before one thousand seconds and slows down afterwards. This observation implies that they do not have the same molecular orientation or they are part of different structures with different kinetics.

To determine the molecular orientation, both polarizations must be recorded so that the dichroic ratio ($R^{ATR} = p/s$) can be calculated. Unfortunately, this comes at the price of acquisition speed. By using a RSF sample of slightly lower concentration (60 ± 3% instead of 68 ± 3%), the conversion occurs over a longer time scale. While staying above the C_β threshold, it permits a suitable acquisition time for both polarizations to be recorded.

As shown in Fig. 7, the dichroic ratio of the 1512 and 1700 cm^{-1} components decreased during the conversion process, suggesting a certain degree of molecular orientation of these vibrational modes. The dichroic ratio measured for these two vibrational modes (particularly the weak 1700 cm^{-1} component) would have decreased even faster if the interfering bending mode of water present in the Amide I region was subtracted. The orientation of the 1512 cm^{-1} mode also

 This journal is © the Owner Societies 2011

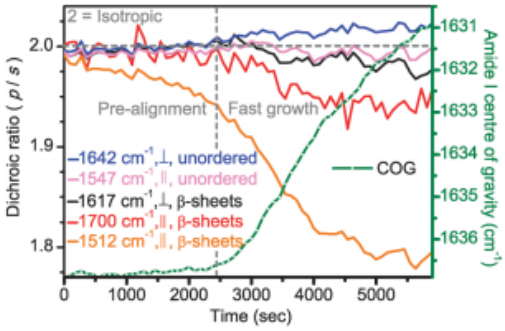


Fig. 7 Dichroic ratio of several bands and amide I band ratio as a function of time for a 60 ± 3% RSF sample.

explains the difference in kinetics compared to the 1617 cm^{-1} component shown in the Fig. 4.

The full determination of the biaxial orientation of the β-sheets requires two orthogonal components. However, the orientation of the strands constituting the sheets (β-strands) can be qualified by using only the Amide II mode which is parallel to the backbone.[51] The decrease of the dichroic ratio of the 1512 cm^{-1} component measured suggests that the β-strands align in the plane of the ATR crystal, along the shearing direction (illustrated in Fig. 8). This observation is in agreement with previous studies claiming that the β-sheets formed under mechanical stress are oriented parallel to the direction of the deformation and the resulting fibre axis.[4,30,53–55] Furthermore, the dichroic ratio of the 1512 cm^{-1} component shows a decrease before the growth point observed around 2500 s. This observation supports the hypothesis that the silk has to pass through a pre-alignment step prior to the formation of the β-sheets and the gelation.[54]

The vibrational modes perpendicular to the β-strands[39,51] at 1547 and 1617 cm^{-1} displayed a R^{ATR} close to 2. As illustrated in Fig. 8, this result suggests that the planes of the β-sheets are randomly distributed around the β-strands and the backbone of the protein.

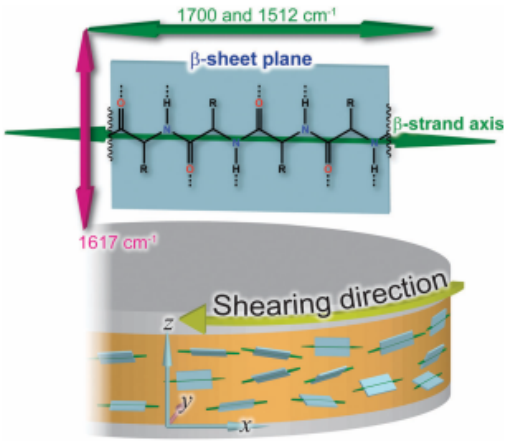


Fig. 8 Schematics of the sheets' orientation relative to the setup referential.

Conclusions

This work demonstrated for the first time the coupling of a shear flow cell and polarized ATR-FTIR spectroscopy to study shear sensitive biological materials. This powerful new tool allowed the study of RSF conversion *in situ* for various concentrations, deepening our knowledge of the spinning process. Importantly, this technique also proved to be a very useful indicator of RSF "quality" *i.e.* spinnability. Our experiments showed that the silk conversion passes through three phases; pre-alignment, fast β-sheet growth and a deceleration of the growth rate. The polarization measurements allowed the identification of a pre-alignment step occurring before the rapid growth of the β-sheets. This result suggests that the protein chains must already be partially aligned to a certain extent to lead to the formation of well orientated crystallites present in the fibers.[30,55,56] The β-strands were found to be aligned along the shearing direction. However, the β-sheet planes did not show any preferential rotational orientation around the β-strands' axis. This observation supports the hypothesis of the formation of oriented nano-fibrils as a "string of beads"[57] rather than a structure of pleated stacks of β-sheets.

We further observed that the amount of β-sheets induced by shearing was only a small fraction of what could ultimately be formed by the material. Thus, shearing forces cannot be held entirely responsible for the silk conversion as the sample becomes solid well before gaining its full crystalline content. Consequently, the extensional forces occurring after the gelation must complete the orientation of the chains and the conversion process. Finally, we observed that the conversion kinetics were strongly dependent on the concentration once a threshold concentration is surpassed. For the RSF samples, this threshold C_β is around 50% w/w, which is much higher than the native unspun silk concentration of ~26%.[58,59] As each technique tells us a different story, combining them all together will, eventually, be essential to link all parts of the silk spinning jigsaw. Once fully understood, this complex and fascinating natural material has an immense potential to inspire novel polymers to meet the challenges of the 21st century.

Acknowledgements

The authors wish to thank David Porter and Ann Terry for their critical comments on the manuscript. Maxime Boulet-Audet is supported by an EPSRC studentship (EP/G068224/1) and a NSERC scholarship (PGS-3D). Chris Holland is a Fellow by Examination (Magdalen College, Oxford). Fritz Vollrath acknowledges support from the US-AFOSR (F49620-03-1-0111) and the European Research Council (SP2-GA-2008-233409).

Notes and references

1 K. Mita, S. Ichimura and T. C. James, *J. Mol. Evo.*, 1994, **38**, 583–592.
2 C.-Z. Zhou, F. Confalonieri, N. Medina, Y. Zivanovic, C. Esnault, T. Yang, M. Jacquet, J. Janin, M. Duguet, R. Perasso and Z.-G. Li, *Nucleic Acids Res.*, 2000, **28**, 2413–2419.

3 F. Takei, Y. Kikuchi, A. Kikuchi, S. Mizuno and K. Shimura, *J. Cell Biol.*, 1987, **105**, 175–180.
4 R. E. Marsh, R. B. Corey and L. Pauling, *Biochim. Biophys. Acta.*, 1955, **16**, 1–34.
5 D. Porter and F. Vollrath, *Adv. Mater.*, 2009, **21**, 487–492.
6 F. Vollrath and D. Porter, *Polymer*, 2009, **50**, 5623–5632.
7 M. F. Ashby, L. J. Gibson, U. Wegst and R. Olive, *Proc. R. Soc. London, Ser. A*, 1995, **450**, 123–140.
8 G. H. Altman, F. Diaz, C. Jakuba, T. Calabro, R. L. Horan, J. S. Chen, H. Lu, J. Richmond and D. L. Kaplan, *Biomaterials*, 2003, **24**, 401–416.
9 H. Yamada, H. Nakao, Y. Takasu and K. Tsubouchi, *Mater. Sci. Eng., C*, 2001, **14**, 41–46.
10 C. Holland, A. E. Terry, D. Porter and F. Vollrath, *Polymer*, 2007, **48**, 3388–3392.
11 D. Porter and F. Vollrath, *Soft Matter*, 2008, **4**, 328–336.
12 O. Liivak, A. Blye, N. Shah and L. W. Jelinski, *Macromolecules*, 1998, **31**, 2947–2951.
13 D. P. Knight, M. M. Knight and F. Vollrath, *Int. J. Biol. Macromol.*, 2000, **27**, 205–210.
14 C. L. Mo, C. Holland, D. Porter, Z. Z. Shao and F. Vollrath, *Biomacromolecules*, 2009, **10**, 2724–2728.
15 X. Chen, D. P. Knight, Z. Z. Shao and F. Vollrath, *Polymer*, 2001, **42**, 9969–9974.
16 Zainuddin, T. T. Le, Y. Park, T. V. Chirila, P. J. Halley and A. K. Whittaker, *Biomaterials*, 2008, **29**, 4268–4274.
17 K. Hossain, E. Ohyama, A. Ochi, J. Magoshi and N. Nemoto, *J. Phys. Chem. B*, 2003, **107**, 8066–80733.
18 S. Nagarkara, A. Lele, C. Chassenieux, T. Nicolai, D. Durand, *Xvth International Congress on Rheology—the Society of Rheology 80th Annual Meeting*, 2008, **1027**, 573–575.
19 L. Scelsi and M. R. Mackley, *Rheol. Acta*, 2008, **47**, 895–908.
20 T. Kanaya, G. Matsuba, Y. Ogino, K. Nishida, H. M. Shimizu, T. Shinohara, T. Oku, J. Suzuki and T. Otomo, *Macromolecules*, 2007, **40**, 3650–3654.
21 G. Kumaraswamy, R. K. Verma, J. A. Kornfield, F. J. Yeh and B. S. Hsiao, *Macromolecules*, 2004, **37**, 9005–9017.
22 N. V. Pogodina, V. P. Lavrenko, S. Srinivas and H. H. Winter, *Polymer*, 2001, **42**, 9031–9043.
23 F. Vollrath and D. Porter, *Appl. Phys. A: Mater. Sci. Process.*, 2006, **82**, 205–212.
24 M. Roessle, P. Panine, V. S. Urban and C. Riekel, *Biopolymers*, 2004, **74**, 316–327.
25 K. Ohgo, F. Bagusat, T. Asakura and U. Scheler, *J. Am. Chem. Soc.*, 2008, **130**, 4182–4186.
26 X.-G. Li, L.-Y. Wu, M.-R. Huang, H.-L. Shao and X.-C. Hu, *Biopolymers*, 2008, **89**, 497–505.
27 X. Chen, L. Zhou, Z. Z. Shao, P. Zhou, D. P. Knight and F. Vollrath, *Acta Chim. Sin.*, 2003, **61**, 625–629.
28 X. Chen, D. P. Knight and Z. Z. Shao, *Soft Matter*, 2009, **5**, 2777–2781.
29 M. Rossle, P. Panine, V. S. Urban and C. Riekel, *Biopolymers*, 2004, **74**, 316–327.
30 M. Boulet-Audet, T. Lefèvre, T. Buffeteau and M. Pézolet, *Appl. Spectrosc.*, 2008, **62**, 956–962.
31 J. A. Kornfield, G. G. Fuller and D. S. Pearson, *Macromolecules*, 1989, **22**, 1334–1345.
32 G. M. Wise, M. M. Denn and A. T. Bell, *AIChE J.*, 1998, **44**, 701–710.
33 C. Holland, A. E. Terry, D. Porter and F. Vollrath, *Nat. Mater.*, 2006, **5**, 870–874.
34 N. J. Harrick, *Internal Reflection Spectroscopy*, John Wiley & Sons, New York, 1967.
35 U. P. Fringeli, *Chimia*, 1992, **46**, 200–214.
36 G. Y. Li, P. Zhou, Z. Z. Shao, X. Xie, X. Chen, H. H. Wang, L. J. Chunyu and T. Y. Yu, *Eur. J. Biochem.*, 2001, **268**, 6600–6606.
37 S. Nagarkar, T. Nicolai, C. Chassenieux and A. Lele, *Phys. Chem. Chem. Phys.*, 2010, **12**, 3834–3844.
38 A. Barth, *Biochim. Biophys. Acta, Bioenerg.*, 2007, **1767**, 1073–1101.
39 W. H. Moore and S. Krimm, *Biopolymers*, 1976, **15**, 2465–2483.
40 P. Garside, S. Lahlil and P. Wyeth, *Appl. Spectrosc.*, 2005, **59**, 1242–1247.
41 H. Teramoto and M. Miyazawa, *Biomacromolecules*, 2005, **6**, 2049–2057.
42 T. Miyazawa and E. R. Blout, *J. Am. Chem. Soc.*, 1961, **83**, 712–719.
43 S. Y. Venyaminov and N. N. Kalnin, *Biopolymers*, 1990, **30**, 1259–1271.
44 L. Jeong, K. Y. Lee, J. W. Liu and W. H. Park, *Int. J. Biol. Macromol.*, 2006, **38**, 140–144.
45 M. Sonoyama and T. Nakano, *Appl. Spectrosc.*, 2000, **54**, 968–973.
46 E. Goormaghtigh, V. Cabiaux and J. M. Ruysschaert, in *Physicochemical Methods in the Study of Biomembranes*, ed. H. J. Hilderson and G. R. Ralston, Plenum Press, New York, 1994, vol. 23, pp. 363–403.
47 W. S. Muller, L. A. Samuelson, S. A. Fossey and D. L. Kaplan, *Langmuir*, 1993, **9**, 1857–1861.
48 P. Taddei and P. Monti, *Biopolymers*, 2005, **78**, 249–258.
49 Q. Lv, C. B. Cao, Y. Zhang, X. L. Ma and H. S. Zhu, *J. Appl. Polym. Sci.*, 2005, **96**, 2168–2173.
50 H. Yoshimizu and T. Asakura, *J. Appl. Polym. Sci.*, 1990, **40**, 1745–1756.
51 D. Marsh, *Biophys. J.*, 1997, **72**, 2710–2718.
52 J. Magoshi, Y. Magoshi and S. Nakamura, in *Silk Polymers: Materials Science and Biotechnology*, 1994, vol. 544, pp. 292–310.
53 F. Vollrath and D. P. Knight, *Nature*, 2001, **410**, 541–548.
54 F. Vollrath and D. P. Knight, *Int. J. Biol. Macromol.*, 1999, **24**, 243–249.
55 A. H. Simmons, C. A. Michal and L. W. Jelinski, *Science*, 1996, **271**, 84–87.
56 M.-È. Rousseau, L. Beaulieu, T. Lefèvre, J. Paradis, T. Asakura and M. Pézolet, *Biomacromolecules*, 2006, **7**, 2512–2521.
57 F. Vollrath and D. Porter, *Soft Matter*, 2006, **2**, 377–385.
58 A. Terry, D. Knight, D. Porter and F. Vollrath, *Biomacromolecules*, 2004, **5**, 768–772.
59 L. Zhou, X. Chen, Z. Z. Shao, Y. F. Huang and D. P. Knight, *J. Phys. Chem. B*, 2005, **109**, 16937–16945.

 This journal is © the Owner Societies 2011

10 Wainwright, S. A., Biggs, W. D., Currey, J. D. & Gosline, J. M. 1982 *Mechanical design in organisms.* New York, NY: John Wiley and Sons.
11 Arnaud, M. 1888 Sur la mattiere cristallisee active de fleches empoisonnee des somalis extradite du bois d'Ovabio. *C. R. Hebd. Seances l'Acad. Sci. Paris* **106/107**, 1011–1162.
12 Schmelzer, G. H. & Gurib-Fakim, A. 2008 *Medical plants 1. PROTA foundation.* Wageningen, The Netherlands: Backhuys Publishers.
13 Jacobs, W. A. & Bigelow, N. M. 1932 Ouabain or g-Strophantin. *J. Biol. Chem.* **96**, 647–658.
14 Ruegg, U. T. 1992 Ouabain: a link in the genesis of high blood pressure. *Experientia* **48**, 1102–1106. (doi:10.1007/BF01947997)
15 Vorontsov, N. N. 1979 *Evolution of the alimentary system in myomorph rodents.* New Delhi, India: The Indian National Scientific Documentation Centre.
16 Naumova, E. I. & Zharova, G. K. 2003 Structure and functions of the digestive tract in the maned hamster *Lophiomys imhausi*. *Zool. J.* **82**, 1368–1374.
17 Bennick, A. 2002 Interaction of plant polyphenols with salivary proteins. *Crit. Rev. Oral Biol. Med.* **13**, 184–196. (doi:10.1177/154411130201300208)
18 Rosenthal, G. & Berenbaum, M. 1992 *Herbivores: their interactions with secondary plant metabolites.* San Diego, CA: Academic Press.
19 Labeyrie, E. & Dobler, S. 2004 Molecular adaptation of *Chrysochus* leaf beetles to toxic compounds in their food plants. *Mol. Biol. Evol.* **21**, 218–221. (doi:10.1093/molbev/msg240)
20 Torrie, L. S., Radford, J. C., Southall, T. D., Kean, L., Dinsmore, A. J., Davies, S. A. & Dow, J. A. T. 2004 Resolution of the insect ouabain paradox. *Proc. Natl Acad. Sci. USA* **101**, 13 689–13 693. (doi:10.1073/pnas.0403087101)
21 Jansa, S. A. & Weksler, M. 2004 Phylogeny of muroid rodents: relationships within and among major lineages as determined by IRBP gene sequences. *Mol. Phylogenet. Evol.* **31**, 256–276. (doi:10.1016/j.ympev.2003.07.002)
22 Pagel, M. 1997 Inferring evolutionary processes from phylogenies. *Zool. Scr.* **26**, 331–348. (doi:10.1111/j.1463-6409.1997.tb00423.x)
23 Payne, R. J. H. & Pagel, M. 1997 Why do animals repeat displays? *Anim. Behav.* **54**, 109–119. (doi:10.1006/anbe.1996.0391)

FFF

A poisonous surprise under the coat of the African crested rat

Jonathan Kingdon[1], Bernard Agwanda[2], Margaret Kinnaird[3], Timothy O'Brien[4], Christopher Holland[1], Thomas Gheysens[1], Maxime Boulet-Audet[1] and Fritz Vollrath[1,*]

[1]*Department of Zoology, University of Oxford, South Parks Road, Oxford OX1 3PS, UK*
[2]*National Museums of Kenya, PO Box 40658, Nairobi, Kenya*
[3]*Mpala Research Station, Laikipia, PO Box 555, Nanyuki 10400, Kenya*
[4]*Wildlife Conservation Society, 2300 Southern Boulevard, Bronx, NY 10460, USA*

Plant toxins are sequestered by many animals and the toxicity is frequently advertised by aposematic displays to deter potential predators. Such 'unpalatability by appropriation' is common in many invertebrate groups and also found in a few vertebrate groups. However, potentially lethal toxicity by acquisition has so far never been reported for a placental mammal. Here, we describe complex morphological structures and behaviours whereby the African crested rat, *Lophiomys imhausi*, acquires, dispenses and advertises deterrent toxin. Roots and bark of *Acokanthera schimperi* (Apocynaceae) trees are gnawed, masticated and slavered onto highly specialized hairs that wick up the compound, to be delivered whenever the animal is bitten or mouthed by a predator. The poison is a cardenolide, closely resembling ouabain, one of the active components in a traditional African arrow poison long celebrated for its power to kill elephants.

Keywords: *Lophiomys*; *Acokanthera*; ouabain; toxicity; aposematic; mammal

1. INTRODUCTION

Since the discovery of the African crested rat, *Lophiomys imhausi* [1], the adaptive significance of the rodent's specializations, notably its peculiar coloration and generally sluggish behaviour, has escaped satisfactory explanation [2]. The ability to expose a bold black and white fur pattern has invited speculation about mimicry of spiny porcupines Hystricidae [3] or skunk-like zorillas *Ictonyx striatus* (Mustelidae). Indeed, *Lophiomys* has been held to exemplify a rare example of Batesian mimicry among mammals with the zorilla as a model [4]. While it is possible that a piebald face and flank stripes might have sufficient resemblance to the zorilla's pattern to deter some predators, *Lophiomys* is probably too poor a copy of the zorilla to qualify as its mimic. Furthermore, it is commonly overlooked that the crested rat is normally inconspicuous and that its long grey-tipped fur envelops its body completely (figure 1). Its black and white flanks are only exposed when the animal is disturbed or excited.

The belief that *Lophiomys* is poisonous has long been current in Kenya [2,5,6]. Of particular interest is a tract of hairs that are of unique structure. We have confirmed the suggestion that this tract of hairs can acquire toxic properties and we assert here that they, together with other specialized behavioural, morphological and anatomical adaptations, have led to a powerful defence, highly unusual for a mammal. Flaring of the fur is triggered by external interference or attack on the animal, whereupon white and black banding of the longer hairs on either side of the lateral line effects outlines of the tract in a bold white and black 'target' design. An aggravated rat pulls its head back into its shoulders and turns its flared tract towards its adversary as if actively soliciting an attack. This display may or may not be accompanied by vocalizations.

A complex of defensive traits in the crested rat would have evolved against natural predators; however, most reliable observations about their efficiency and effectiveness have come from numerous reports of encounters with domestic dogs. One dog, on seeing a crested rat after the former had survived a putative near-death encounter, displayed every sign of fearful aversion (P. Bengough 2010, unpublished observation). Several descriptions of symptoms exhibited by dogs that have bitten *Lophiomys* range from mild lack of coordination, mouth-frothing and signs of general distress to collapse and rapid death, apparently from heart failure (M. Coverdale 2008, unpublished observations). One autopsy of a poisoned dog described pale mucous membranes and white blood cells with toxic granules, defective blood-clotting and associated generalized bleeding (S. Ghalay 2009, unpublished observation). In two cases, dogs that were seen to have attacked a crested rat took weeks to recover from severe and disabling symptoms (M. Coverdale & T. Hobbs 2008, unpublished observations).

These reports and anecdotes all demonstrate that although there is little or no evidence of the rat physically piercing any tissue, its defence is surprisingly effective against larger mammalian predators. The adaptations that enforce deterrence and details of the mechanisms involved are equally surprising.

The closest equivalent to this phenomenon reported to date concerns hedgehogs (*Erinaceus europeus*) chewing the

*Author of correspondence (fritz.vollrath@zoo.ox.ac.uk).

Electronic supplementary material is available at http://dx.doi.org/10.1098/rspb.2011.1169 or via http://rspb.royalsocietypublishing.org.

Received 3 June 2011
Accepted 13 July 2011

This journal is © 2011 The Royal Society

GGG

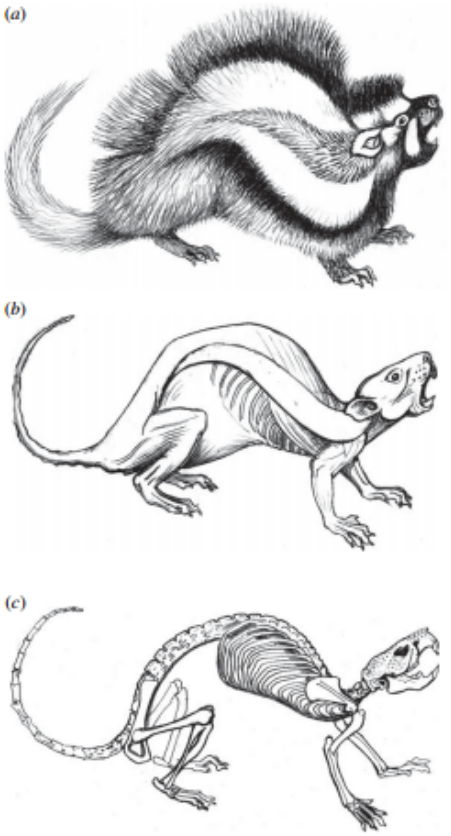


Figure 1. (*a*) *Lophiomys imhausi* warning display; note lateral hair tract at visual centre of signal design. (*b*) Outline of skinned specimen in same position with lateral-line tract outlined; note how long hair transforms visual appearance. (*c*) Skeleton; note robust and elongated vertebral column, and possible role of scapulae as protective shields above vital centres. For a view of the animal's routine state, see the figure of electronic supplementary material, video S1.

parotid glands of toads *Bufo* and slathering the resultant mixture of saliva and toad venom onto its spines [7]. While this self-annointing is known among hedgehogs to make pricks from hedgehog spines more painful and irritating, there is, as yet, no evidence for lethal/terminal effects on the predator. The primary effect of such behaviour and use of substances seems to be to augment the pain and discomfort inflicted by the spines. In the case of *Lophiomys*, there is no evidence that a response to the toxins is dependent on any kind of wound. Mere contact between the mucous membranes of the predator's mouth and toxin in the rat's hairs would seem sufficient to precipitate symptoms of acute poisoning. Further research may reveal a pathology whereby mucous membrane cells are permeated directly without the need to actually wound an aggressor. For example, the possibility that *Lophiomys* saliva might introduce facilitating agents such as non-polar cardenolides deserves investigation. Unlike the hedgehog, which relies on its spines for both deterrent and punitive effects, the exposure of *Lophiomys* to damaging bites would seem to have selected for a suite of mitigating structures. These include an armoured skull, enlarged vertebrae, and dense and thick skin, in addition to fearless behaviour, all of which imply reliance upon a form of deterrence that must be extremely fast-acting in order not to be consistently more costly and dangerous to the prey than to the predator.

Although the gross structure of flank hairs has been described under low-power microscopy, and its possible function discussed [2], some more detailed features of the microstructure of these hairs under scanning electron microscope (SEM) were first described by Stoddart [8], who, like Kingdon [2], suggested that the hairs might be adapted to absorb secretions from an apparent 'belt of glandular tissue fringed both above and below by short stiff hairs' that lie 'at the base of the crest and extend the whole of its length' (p. 552 in [8]). General characterization of the dorsal hair above the flank hair tracts as a 'crest' is misleading inasmuch as dense, long hair grows over most of the body. An excited *Lophiomys* is more aptly described as 'parting' the fur along its flanks, rather than 'raising its crest'. Furthermore, the specialized flank hairs do not 'fringe' a supposed glandular area but are, instead, densely but loosely rooted in a leaf-shaped tract of apparently differentiated skin that tapers away from behind the ears to end over the pelvic–femoral angle. Noting the uniquely complex structure of *Lophiomys* flank hairs, Stoddart suggested that pungent odours might serve to protect the animal from predators. To the human nose, *Lophiomys* does not smell strongly and dogs have been reported to show no sign of being deterred until actual oral contact with the rat has been made. This implies that an absence of olfactory cues and the deterrence must be learned by the predator from direct contact with the rat or from individuals observing the reactions of other predators.

2. HAIR MORPHOLOGY

While glandular structures underlying the flank tract have yet to be demonstrated, a more exact and detailed description of the hairs is needed, especially in the light of their now-known toxin-holding function. We have investigated the structure and function of the crested rat's highly specialized hairs in this context. Rather than growing at the ill-defined base of a 'crest', the hairs grow along two lateral lines that run across the flanks (figure 1*a*). The animal exposes these tracts of somewhat shorter hair (mean 28 mm, range 18–32 mm) by means of specially modified dermal muscles (figure 1*b*). These muscles erect the animal's long (mean 46 mm, range 38–52 mm and externally grey) fur upwards above the lateral line, while simultaneously deflecting fur downwards below the lateral line.

Hair is parted not only in response to disturbance, but also to allow the animal to apply poison to the specialized flank hairs. When presented with pieces of *Acokanthera* branch and root, we observed a living wild-caught crested rat to gnaw and masticate the bark and selectively 'slaver' the lateral-line fur between repeated bouts of gnawing and chewing. Such mastication appears to liberate the ouabain from the bark and mix it with saliva to form a coarse colloid, which is then specifically applied *only* to

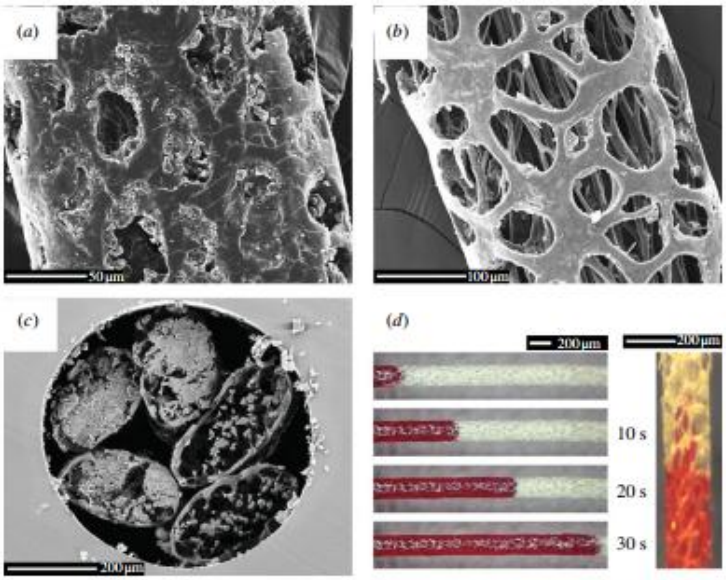


Figure 2. Microscopy images of the uniquely adapted poison-delivery hairs growing in a tract along the lateral lines of the African crested rat *Lophiomys imhausi*. (*a–c*) Scanning electron microscopy images of the hair indicating (*a*) a section near the tip fully loaded with poison, (*b*) detail of the microfibres running up the centre of a washed hair from a section near the root, and (*c*) cross-sections of five hairs to show internal microfibres and how the saliva is stored. (*d*) Light microscopy of the 'wicking' effect using red ink over 30 s. See also the electronic supplementary material, video S1.

the lateral-line hairs. Fragments of bark that drop to the ground while applying the colloid are carefully picked up and chewed again. Over a period of 5 days, three separate short bouts of bark-chewing, followed by application of the colloid, were observed. This individual ignored leaves and raw green fruit of *Acokanthera* both as food and as material for mastication. Other individuals have been seen to carefully 'groom' their flank hair tracts, but in the absence of any plant material and without any obvious stimulus.

When relaxed, long grey fur covers the lateral-line tracts, and, to a large degree, screens the tracts from the light and repels moderate rain. If toxins in the lateral-line hairs are at all light-sensitive or soluble in water, as seems likely, then insulation from both elements may be just as important a role for the long hair as keeping the rodent warm or making it less conspicuous.

We examined the structure of the lateral-line hairs under both light electron microscope and SEM, and have discovered that the hair exemplifies unique, exceptional optimization and economy of structure for sequestration and delivery of toxins [9,10]. The central portion of each main shaft develops a thin but strong outer cylinder perforated by abundant vacuoles (figure 2). This perforated cylinder encloses fibrillar strands that remain mostly separate, but can adhere to each other or to the outer cylinder along short stretches. These long fibrils are numerous and cumulatively act as a 'wick', as we have demonstrated (figure 2*d*) and observed with our captive specimen. Indeed, as the colloid is applied to the hair, one can observe an almost instantaneous flip from reflective gloss to opaque invisibility, which suggests rapid absorption. In the electronic supplementary material, a short film demonstrates such absorption through capillary action along the interior of each hair cylinder (electronic supplementary material, video S1). Once a hair has become saturated, the colloid appears to dry as a semi-viscous secretion (figure 2*a*). The hairs' open lattice ensures that processed or 'groomed' hairs cannot be touched without contacting the poisonous colloid/secretion.

Over 120 years ago, Arnaud [11] extracted and isolated ouabain, a crystalline glycoside from the bark and roots of the *Acokanthera* tree. Used for poisoning arrows in Somaliland [11], it has become famous as the weapon of choice by East African elephant hunters [12]. For more than two centuries, the bark extract also found use as a clinical treatment against congestive heart failure [13]. Ouabain's activity, as for all cardiac glycosides, comes from its capacity to inhibit the Na^+/K^+-ATPase, thus greatly increasing the force of cardiac muscle contractions [14].

3. HAIR CONTENTS

Our Fourier transform infrared (FT-IR) spectroscopy pilot study of the compounds found inside the hairs strongly suggests the presence of ouabain (figure 3). Specifically, ouabain seems to be the active ingredient transferred from the bark to the hair as our spectra had strong peaks at 1530, 916, 880 and 796 cm^{-1} and lacked peaks more typical for acovenoside, which is another toxic compound sometimes found in *Acokanthera* bark. In addition, our spectra showed signatures indicative of additional compounds such as lignins or tannins, suggesting that more detailed investigation is likely to elucidate a selective natural extraction system driven by the

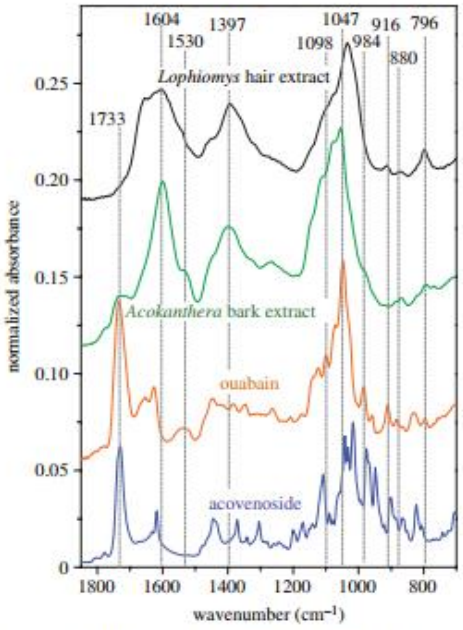


Figure 3. ATR FT-IR spectra of pure acovenoside, ouabain and extract from the *Acokanthera* bark and *Lophiomys* hairs.

rats' masticatory behaviour and salivary chemistry. Importantly, the FT-IR spectra of the *Acokanthera* bark and of the compounds in the active part of the *Lophiomys* hair are very similar. This confirms our assertion that the compounds slathered onto the rat's lateral-line fur derived from the bark of *Acokanthera*.

While key to its unique toxicity, the highly modified lateral-line hairs of the crested rat are not its only interesting morphological modification. For example, a study of the animal's skull suggests that direct contact with predators has selected for extra shielding of the brain (figure 4). The skull has invited a comparison with the armoured head of a turtle [2] and earned one supposed subspecies the name *L. i. testudo*. Margins of the frontal, squamosal and parietal have extended around the orbit and over the cranium to create a 'cranial helmet', while dense bony 'pimples' (rugose osteoblasts) extend over the bridge of the nose and most of the external surfaces of the occiput. These cranial features are unique among rodents. Superficially similar elaboration occurs in the zygomatic region of the paca *Agouti paca*, where a position around the buccal cavity supports the hypothesis that this has more of an acoustic than protective function. By contrast, bony elaboration in *Lophiomys* skulls covers or surrounds solid tissues, the brain, nasal passages, eyes and temporal muscles.

4. OTHER ADAPTATIONS

Moreover, there are other interesting macro-morphological modifications associated with the rat's toxicity. For example, the animal has an unusually dense, tough and close-textured dermis, which can be interpreted as predator-selected. The skin is resistant to all but the



Figure 4. Skull of *Lophiomys imhausi* showing extensions of jugal, squamosal, frontal and parietal bones, and their granulated surfaces. Temporal fossae are completely roofed over, as are parts of the orbital fossae.

sharpest of teeth, claws or beaks. The fresh skin of one *Lophiomys* specimen showed bruising consistent with the rat having been previously savaged by dogs, but the dogs' teeth were either unable to penetrate the tough dermis or the dogs desisted before their teeth could tear through. Species-specific specializations include an elongated vertebral column with three extra thoracic vertebrae and one extra lumbar vertebra forming a backbone that is exceptionally robust and flexible. All vertebrae have enlarged the bodies and short spines (figure 1*c*). The clavicle is highly atrophied, allowing the broad scapulae exceptional mobility, possibly enhancing the protection of the neck and anterior thorax. An exceptionally large, weakly sacculated stomach is unique among rodents [15], implying a complex physiology for processing plant material [16], resembling that of a fibre-digesting forestomach fermenter. Yet such a conclusion would be vitiated by the fact that easily digested plant parts are the main source of nutrition [16]. The observation that non-fibrous foods are the norm has been confirmed from extensive analysis of faeces in the wild (J. Kingdon 2010, unpublished observation). This could imply other, as yet unknown, functions for the digestive tract of *Lophiomys*. Given that substantial quantities of very poisonous material frequently enter the rodent's mouth, albeit temporarily, it is plausible that detoxification might be among the specializations of the *Lophiomys* digestive tract.

Possibly, a key to future studies of the animal's ability to deal with the toxicity of *Acokanthera* bark to its own health is the salivary glands of crested rats, which are unusually large for their taxon. Because some mammals' saliva produces proteins that bind to plant polyphenols [17,18], it is possible that *Lophiomys* salivary secretions are adapted to augment or process ouabain (and possibly other plant toxins) in significant but currently unknown ways, among them enhancement of the toxin's capacity to permeate cells. Among some ouabain-insensitive invertebrates, the location of an ouabain-binding site on the DNA sequence has been narrowed to a single amino acid substitution (asparagine for histidine) at position 122 of Na^+/K^+-ATPase α-subunit gene [19,20]. Possibly, some similar adaptation prevents ouabain from damaging the rat's cellular functions. Ingestion of ouabain into the mouth presents no visible risk to the rat, but what role

the salivary glands (or digestive tract) play in this immunity remains to be elucidated. Once the physiological and genetic foundations of *Lophiomys* immunity are fully understood, there could be implications for molecular or pharmacological applications in human medical therapies.

In terms of understanding the long-term evolution of specialized hair, a recent phylogeny [21] identified four major muroid subdivisions, and allocated *Lophiomys* its own lineage close to the divergence between Gerbillinae and Murinae. Among the former is a distinct radiation of proto-gerbillines with modified hair: the spiny mice (*Acomys*), link rats (*Deomys*) and brush-furred mice (*Lophuromys*). While no very close affinity between these genera and *Lophiomys* can be envisaged, it raises the possibility that incremental elaboration of dorsal or flank hair might have very ancient evolutionary origins [22], particularly if selective advantage in relation to predators can be shown, as we do here for *Lophiomys*.

5. CONCLUSIONS

Our confirmation of toxicity by acquisition in *Lophiomys* suggests that the superficially random suite of peculiarities that we have listed can all be explained as adaptations connected by the evolutionary thread of predator selection. Without regular augmentation of toxins to the flanks, a canopied skull, dense dermis and reinforced skeleton would all be insufficient to deter predators. For both rat and predator, the bold (and memorable) flank pattern represents a costly signal [23]. Significant costs to *Lophiomys* would suggest that the survival of the rat will continue to rely on readily available supplies of ouabain within the range of northeast African Apocynacae species.

While the details of this extraordinary relationship between mammal and plant require further field and laboratory work, our observations exemplify the power of predation to select for very unusual defences in prey species and, in this instance, astonishing integration of a large suite of behaviours with complex structures. The rat's behaviour in the presence of a predator directs the latter's attention and attack towards a well-advertised specific area, where a painful and poisonous surprise awaits. Micro-structural modification of the hairs growing within this specific area (presumably evolved by small increments) allows them to serve as exceptionally efficient receptacles for self-applied poison. Likewise, chemical adaptation of saliva and tissues probably maximizes deterrence to the predator, while avoiding or minimizing self-harm from the toxins. Finally, macro-structural modifications of separate elements of whole-body anatomy (skin and skeleton) have evolved to make survival more likely by attracting and then 'managing' the bites of a predator.

6. METHODS SUMMARY

Microscopy was performed using an Olympus SZ40 dissection microscope with a Canon A640 digital camera. Samples for SEM studies were coated using an AuPd target for 180 s (resulting in a 6–10 nm layer) and imaged using a Jeol Neoscope (Nikon, UK) under high vacuum at either 10 or 15 keV.

For spectra acquisition, we used a Nicolet 6700 Fourier transform infrared spectrometer equipped with a liquid-nitrogen-cooled MCT-A detector together with a single bounce diamond attenuated total reflectance (ATR) accessory (Thermo Electron Corp., Madison, WI, USA). Spectra were acquired at 4 cm^{-1} resolution from 6000 to 500 cm^{-1} using a Happ-Genzel apodization, a Metz phase correction and no zero filling. Spectra were obtained from an average of 64 scans at 5.0632 cm s^{-1} mirror speed. All spectral operations were performed using Omnic 7.3 (Thermo Scientific, Madison, WI, USA). Spectra were neither deconvolved nor smoothed; the only applied correction was an offset at 4000 cm^{-1} and a normalization of the intensity. The ouabain and acovenoside spectra were recorded from a thin film cast from an aqueous solution on the ATR crystal. We obtained the *Acokanthera* bark extract spectrum by immersing the bark in 70°C demineralized water for 10 h before casting the solution on the ATR crystal. *Lophiomys imhausi* hair extract was prepared by washing several hairs with demineralized water. Both extracts were purified by using 0.2 µm pore size filters under vacuum. Unwashed and washed hair spectra were acquired by directly pressing different parts of specimen hairs with an anvil on the ATR crystal.

Hairs were taken from National Museums of Kenya skin Catalogue number NMK 180396 Coll Sept 2010 Field No D. 1.

J.K. initiated the study and wrote the first draft; B.A. provided hairs and background information; J.K., T.O. and M.K. documented poison-slathering behaviour; F.V. and C.H. performed scanning electron microscopy and structural analyses of the hairs; T.G. and M.B.-A. analysed the compounds within the hairs and are indebted to Cedric Dicko for pilot studies. All authors contributed throughout the analysis and writing process. Thanks to Philippa Bengough, Chris Thouless, Miles and Elizabeth Coverdale, Tennai, Susanna Rouse, Richard Mwenda, Surita Ghalay, Darcy Ogada, Tony Archer, Fumi Mizutani Wells, Ian Hardy, Henk Beentje, and John Michael Lock.

REFERENCES

1 Milne-Edwards, H. 1867 Memoires c, iii. *Arch. Mus. Hist. Nat. Paris.*
2 Kingdon, J. 1974 *East African mammals. An atlas of evolution in Africa, vol. 2, part B (hares and rodents).* New York, NY: Academic Press Inc.
3 Hollister, N. 1919 East African mammals in the United States National Museum. II. Rodentia, Lagomorpha, and Tubulidentata. *United States National Museum Bulletin* **99**. Washington, DC: Smithsonian Institution.
4 Fogden, M. & Fogden, P. 1974 *Animals and their colours.* London, UK: Eurobook.
5 Euw, J. V., Fishelson, L., Parsons, J. A., Reichstein, T. & Rothschild, M. 1967 Cardenolides (heart poisons) in a grasshopper feeding on milkweeds. *Nature* **214**, 35–39. (doi:10.1038/214035a0)
6 Goldfinch, G. H. 1923 Notes on the African Crested Rat (*Lophiomys imhausi*). *Proc. Zool. Soc. Lond.* **93**, 1091.
7 Brodie, E. D. 1977 Hedgehogs use toad venom in their own defence. *Nature* **268**, 627–628. (doi:10.1038/268627a0)
8 Stoddart, D. M. 1979 Specialised scent releasing hair in the crested rat *Lophiomys imhausi*. *J. Zool.* **189**, 551–553. (doi:10.1111/j.1469-7998.1979.tb03986.x)
9 Wainwright, S. A. 1988 *Axis and circumference: the cylindrical shape of plants and animals.* Cambridge, UK: Harvard University Press.

Acta Biomaterialia 10 (2014) 776–784

Contents lists available at ScienceDirect

Acta Biomaterialia

journal homepage: www.elsevier.com/locate/actabiomat

Silk protein aggregation kinetics revealed by Rheo-IR

Maxime Boulet-Audet [a,*], Ann E. Terry [a,b], Fritz Vollrath [a], Chris Holland [c]

[a] Department of Zoology, University of Oxford, South Parks Road, Oxford OX1 3PS, UK
[b] ISIS Facility, Science and Technology Facilities Council, Rutherford Appleton Laboratory, Harwell Science and Innovation Campus, Didcot, UK
[c] University of Sheffield, Department of Materials Science and Engineering, Sheffield, UK

ARTICLE INFO

Article history:
Received 11 June 2013
Received in revised form 23 October 2013
Accepted 28 October 2013
Available online 5 November 2013

Keywords:
Native silk
Attenuated Total Reflectance Fourier Transform Infrared Spectroscopy
Rheology
Bombyx mori
Reconstituted silk fibroin

ABSTRACT

The remarkable mechanical properties of silk fibres stem from a multi-scale hierarchical structure created when an aqueous protein "melt" is converted to an insoluble solid via flow. To directly relate a silk protein's structure and function in response to flow, we present the first application of a Rheo-IR platform, which couples cone and plate rheology with attenuated total reflectance infrared spectroscopy. This technique provides a new window into silk processing by linking shear thinning to an increase in molecular alignment, with shear thickening affecting changes in the silk protein's secondary structure. Additionally, compared to other static characterization methods for silk, Rheo-IR proved particularly useful at revealing the intrinsic difference between natural (native) and reconstituted silk feedstocks. Hence Rheo-IR offers important novel insights into natural silk processing. This has intrinsic academic merit, but it might also be useful when designing reconstituted silk analogues alongside other polymeric systems, whether natural or synthetic.

© 2013 Acta Materialia Inc. Published by Elsevier Ltd. All rights reserved.

1. Introduction

The conversion of an aqueous silk protein solution into a solid may be achieved through the use of a wide range of external stresses, including heat [1], acoustic waves [2], electric current [3], solvent interactions [4–7], pH [8,9] and metallic ion concentration [10]. However, within the animal, be it spider or silkworm, native silk feedstocks appear to have been selected primarily to respond to flow, resulting in rapid but controlled protein denaturation and aggregation [11–16]. Thus, to gain a better understanding of what is assumed to be a highly optimized pultrusion spinning process [17], the flow properties of native silk feedstocks (dope) have attracted substantial attention [16,18–22]. Here the study of flow, i.e. rheology, has proven very valuable for revealing the close similarities between native silkworm and spider feedstocks [15]. Combined with direct visualization, rheology has also revealed that native silk feedstocks behave like conventional polymer melts, but at much lower temperatures and requiring substantially less energy to solidify [14]. Despite much progress, the kinetics and mechanism of flow-induced structural changes in silk proteins are still poorly understood beyond macroscopic observations.

Several techniques have been employed to investigate the structural features present in silk's hydrated state, including X-ray scattering [23], neutron scattering [24], birefringence [25], dynamic light scattering [22] nuclear magnetic resonance spectroscopy [26–31], circular dichroism [24,32,33], Raman spectroscopy [23,34,35] and infrared spectroscopy [6,36,37]. These stand-alone techniques have proved helpful at determining silk's protein conformation and nanoscale structure. Furthermore silk's solid, denatured and semi-crystalline states are revealed when a feedstock has been converted by an external stress source [1–5,8–10]. However, few studies have achieved this conversion through the application of the most biologically relevant stress type, which is flow [7,38]. A rheo-optical platform will allow us not only to apply such stress/strain but also to monitor it. Whilst rheo-spectrometry has often been used to study conventional polymer melts [39–42], only a single study coupled rheological to structural measurements of silk and only for a reconstituted silk feedstock (RSF) [43]. Reconstituted silks can be an economic source of large quantities of spinning feedstock, yet RSF preparation requires strong chaotropic agents to disrupt the β-sheets' secondary structure present in silk fibres during resolubilization [44] and their quality varies enormously alongside their flow properties [19,24,45,46]. In addition, once these feedstocks are dehydrated and processed, the resulting fibres and films have yet to exhibit the same strain hardening behaviour combined with high toughness seen in their natural counterparts [47–54].

In order to fill the gap in our knowledge concerning the structural response of native silk feedstock (NSF) and RSF to flow, we have coupled infrared spectroscopy to rheology (Rheo-IR). Infrared spectroscopy is sensitive to most molecular vibration bonds and

* Corresponding author.
E-mail address: maxime.boulet.audet@gmail.com (M. Boulet-Audet).

1742-7061/$ - see front matter © 2013 Acta Materialia Inc. Published by Elsevier Ltd. All rights reserved.
http://dx.doi.org/10.1016/j.actbio.2013.10.032

can probe the molecular orientation of any polymer melt when the infrared beam is polarized. More specifically, IR is sensitive to protein concentration, conformation and alignment [5,6,55–60]. Infrared spectroscopy has been coupled to parallel shearing cells in transmission [61,62] but the absorptivity cross-section of water and protein in our system would limit this configuration to a very short beam path of only a few microns. Fortunately, probing the sample with IR spectra with attenuated total reflectance (ATR) avoids the absorbance saturation of silk solution in the mid-infrared bands by only measuring the absorption of the emerging evanescent wave. Unlike dynamic light scattering or circular dichroism, ATR allows the analysis of samples "straight from the gland" and at native concentration [15,57]. This study extends our previous work on the shear-induced conversion of RSF [59] to include NSF and for the first time relate molecular alignment to conformation to changes in bulk rheology in situ.

2. Materials and methods

2.1. Reconstituted silk feedstock

Concentrated reconstituted silk fibroin solutions were prepared following the most common procedure [19,35,63]. *Bombyx mori* silkworm cocoons were degummed in a 0.1% $NaCO_3$ solution at 70 ± 1 °C for 3 h. The dried degummed fibres were cut finely and solubilized in a 9 M lithium bromide (LiBr) solution (70 ± 1 °C) for 20 min for a 250 mg ml^{-1} silk concentration. The resulting solution was poured into dialysis tubing (VISKING® molecular weight cut-off 12–14 kDa) and dialysed against demineralized water type II (ρ > 1 MΩ cm) changed every 2 h over 48 h. Once dialysed, the dialysis bags were hung for 3 days at 4 °C in a gentle air stream to concentrate the silk solution to 22 ± 3% dry weight fraction and remove air bubbles. No opaqueness was observed by visual inspection in any of the samples thus prepared.

2.2. Native silk feedstock

Fifth instar spinning *B. mori* silkworms were dissected to extract their silk glands. The glands were rinsed for a few seconds and then submerged in type II demineralized water at 22 ± 2 °C. The glands were cut between the posterior and posterior-median section, where the dope is free of sericin [64,65]. A small fraction (10 ± 5 µl) of the gland's content was expelled from the posterior division within 60 s, purely by the osmotic pressure difference between the dope and water. A fraction of the posterior section of a single gland provided enough liquid silk to completely fill the cone and plate geometry of the rheometer (2.3 µl). The NSF was carefully lifted out of the water with tweezers and blotted to remove excess water before loading into the geometry. Thirteen samples were prepared for testing. As *B. mori* silkworms are invertebrates, this study is in accordance with the Animals (Scientific Procedures) Act 1986 of the UK.

2.3. Rheo-IR set-up

The Rheo-IR experiment was made possible by coupling a Gemini 200 HR Nano Rheometer (Malvern Instruments, UK) to a Nicolet 6700 Fourier transform infrared (FTIR) spectrometer equipped with a liquid-nitrogen-cooled MCT-A detector and a Golden Gate single reflection diamond ATR accessory (Specac, UK) in a configuration similar to commercial alternatives (Resultec analytic equipment, Germany) [66]. The rheometer had a torque range sensitivity of 1×10^{-8} to 2×10^{-1} N m. In order to achieve a homogeneous shear rate across the probed area, a cone-and-plate geometry system was used. The set-up is shown schematically in Fig. 1a. The

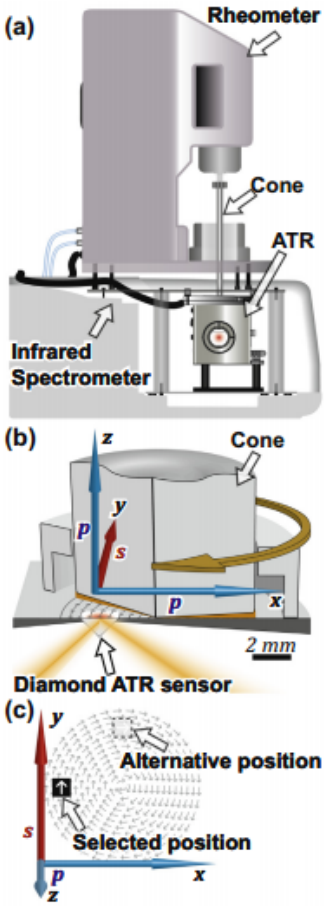


Fig. 1. (a) Schematics of the Rheo-IR setup consisting of a rheometer (Gemini 200 HR Nano, Malvern Instruments, UK) mounted onto the infrared spectrometer (Nicolet 6700, Thermo, USA) equipped with a diamond attenuated total reflectance accessory (Golden Gate, Specac, UK) The bottom plate of the geometry consisted of the spectrometer's ATR accessory made of a tungsten carbide disc with an embedded diamond prism. (b) Cross-sectional view of the Rheo-IR geometry with the laboratory coordinate system and the polarization vectors. (c) Top view of the flow field in relation to the laboratory coordinate system and the polarization vectors.

cone was formed from a custom-made 210 mm long, 10 mm diameter aluminium rod cut at a 1 ± 0.03° angle and truncated by 30 µm, and had a 41×10^{-9} g m^{-2} moment of inertia as measured by the instrument. The geometry could hold 2.3 µl of sample but was slightly overfilled before gently trimming the excess material. For native silk, a single blob of homogeneous material was used to eliminate the risk of incorporating air bubbles in the geometry. To prevent air bubbles in RSF aliquots, RSF was collected from the bottom of the dialysis bag and was constantly kept upright.

Specac's maximum roughness tolerance specification for Golden Gate's bottom plate is 200 nm. The working temperature was maintained at 25 ± 1 °C by the ATR accessory across the whole bottom plate. To prevent any drying of the sample during measurements, an environmental cuff filled with water-soaked wet tissues sealed

the geometry. The geometry's parallelism was verified using a high precision spirit level precise to 0.02°. As illustrated in Fig. 1b and c, the ATR sensor was positioned 3 mm away from the centre of geometry rotation along the beam propagation direction (x-axis) to simplify the interpretation of the orientation; it shows the shear flow field in relation to the polarization vectors. The infrared beam had an ellipsoidal footprint of ~1060 by ~750 μm along the beam path. The beam was refracted internally, at an angle of incidence of 45°, giving an evanescent wave penetration depth of ~1 μm, depending on the wavelength [67]. Thus, the ATR sensor will mostly probe the velocity profile close to the static bottom plate since the geometry is 52 μm thick at a radial distance of 3 mm.

The electric field of the infrared beam was polarized using a motorized zinc selenide holographic wire grid polarizer (Thermo Scientific, Madison, WI); s-polarized light only probed vibration modes along the y-axis, the velocity or shearing direction, whilst p-polarized light selectively probed vibration modes along the x- and z-axes, the vorticity and velocity gradient directions, respectively. One of the advantages of our custom-built rheo-IR setup is the ability to change the position of the probed area relative to the flow direction, either along the s polarization (y-axis) or the p polarization (x-axis) by simply moving the rheometer laterally with respect to the infrared sensor (see Fig. 1c). For an infrared beam at an incidence angle of 45°, the theoretical value of the dichroic ratio ($R_{ATR} = p/s$) of polarized spectra is 2 for a non-oriented (isotropic) sample [67,68]. If the refractive index of the sample is known (1.55 for silk [69]), the second Legendre orientation parameter $\langle P_2 \rangle$ can be calculated to quantify the orientation using R_{ATR} [58,68]. However, for our rapid dynamic experiments, both polarizations would have to be acquired simultaneously. This could be performed using dual channel acquisition and a photo modulator, which was unfortunately not possible with our current experimental setup. Instead, the polarization could only be changed every 30 s using the motorized polarizer. To obtain quantitative information, band decomposition would need to be performed on the amide I band. Decomposing the amide bands into their components can be subjective as many solutions can give a reasonable fit when many broad and overlapping peaks are present. The initial optimization parameters can also strongly influence the final result.

In order to avoid such confounding issues we qualitatively measured the protein orientation and conformation using the amide bands' centre of gravity (COG), which is commonly used to follow dynamic processes [59,70]. Although the COG doesn't provide direct measurement of the intensity of the underlying components, it has the advantage of being an objective metric. Due to the low noise level and precise frequency measurements of infrared spectra, the COG can be very accurately measured ($\pm 0.1\ cm^{-1}$) [71]. The COG has the additional advantage of being independent of absolute intensity variations.

2.4. Experimental procedure

After sample loading onto the ATR assembly, two types of rheological measurements were performed [19]. For NSF and RSF, amplitude sweeps were performed to determine the material's linear viscoelastic region and subsequent oscillatory tests from 623 to 0.623 rad s^{-1} were performed, with a target strain of 0.002 and $n = 13$ for NSF and $n = 13$ for RSF. Thereafter, samples were subjected to a viscosity test under either a slow exponential shear ramp, from 0.0018 to 150.6 s^{-1}, $\gamma(t) = 0.0014e^{0.0445t}$ (from 0 to 100 s^{-1} in 251 s, $n = 7$), or a fast shear rate ramp, from 0.03 to 1062 s^{-1}, $\gamma(t) = 0.0014e^{1.42t}$ (from 0 to 100 s^{-1} in 6 s, $n = 6$). The slow exponential shear ramp was chosen to be consistent with the published literature [15,19,72], whereas the faster shear rate profile follows the estimated amount of shear within a duct, as calculated by Moriya et al. [20]. In order to prevent overloading the rheometer's normal force transducer, shearing was stopped once the thrust reached 250 kPa of first normal force N_1 along the z-axis. The fast exponential shear ramp has the additional advantage of allowing higher shear rates without reaching the N_1 threshold. The apparent zero shear viscosity η_0 was calculated by averaging the five highest viscosity data points measured at near zero rates, and the plateau modulus G_N has been calculated from the average of the three highest data points, free of instrumental error, at high frequencies. As a precaution during the oscillatory tests, infrared spectra were also recorded and no variation in the infrared signal was detected, confirming that we did not reach the viscoelastic limit of native silk.

Static IR spectra were collected from the average of 64 scans (17 s). Dynamic FTIR spectra were recorded using 19 scans per time frame for slow exponential ramps (5.05 s) or 2 scans per time frame for fast exponential ramps (0.53 s). The rheology data collection consistently started 11 s after the spectroscopy. Spectra were recorded at a 4 cm^{-1} resolution from 6000 to 500 cm^{-1}. The only applied correction was a constant baseline correction, the level of which was equal to the average intensity measured from 4000 to 3950 cm^{-1}. The centre of gravity of the amide I band was calculated from the 20% upper portion of the 1700–1594 cm^{-1} region and the amide II from the 10% upper portion of the 1594–1480 cm^{-1} region. The dry weight was quantified in situ with a partial least square calibration curve using TQ Analyst 7.2 (Thermo Electron Corp., Madison, WI) as described elsewhere [59]. The average uncertainty on the dry weight is 3% (w/w).

3. Results and discussion

To test the ability of native and reconstituted silk feedstock to store and dissipate energy, an oscillatory sweep was first performed for each sample. Fig. 2 shows the storage modulus (blue lines) and loss modulus (red lines) from one representative sample of NSF (green circles) and RSF (orange diamonds) in response to an oscillatory frequency sweep. The protein concentration for every sample was 22 ± 3 wt.% for both NSF and RSF, as calculated from in situ measurements of protein/water absorbance between 1500 and 900 cm^{-1}. Although the same angular frequency range is covered for both sets of samples, the phase angle δ between strain and stress waves for RSF became too large above $\omega = 10$ rad/s for accurate calculation. As the software could not unambiguously calculate the moduli, this data range was truncated. It is clear that the response and values of the moduli of the two sets of samples are distinct. NSF shows a clear crossover point in the storage modulus G' (red line) and loss modulus G'' (blue line) where they become equal ($\tan(\delta) = 1$). This crossover appears at 10 ± 2 rad s^{-1}, giving a relaxation time $\tau_p = \omega^{-1}$ of 0.6 ± 0.1 s, with the values of the moduli and relaxation time being consistent with previous measurements [21].

As plotted in Fig. 2, the response of RSF is very different from that of NSF. Since the elastic modulus is lower than the viscous modulus over the range of frequencies measured, none of the RSF samples showed a crossover point, making the calculation of the relaxation time impossible. The absolute values of the moduli of RSF are also substantially lower than those of NSF. At high frequencies, the plateau modulus ($G_N = G'|_{\omega \to \infty}$) gives us a parameter representative of the sample's elastic energy storage potential [73]. For NSF, the average plateau modulus from all the samples measured, G_N, is 13 ± 3 kPa, in sharp contrast with only 0.008 ± 0.006 kPa for RSF. Upon comparison with the published RSF data from Holland et al. [19], the moduli measured for the RSF in our study are higher, which is most likely due to a lower degree of degradation caused by reducing exposure to high temperatures during reconstitution

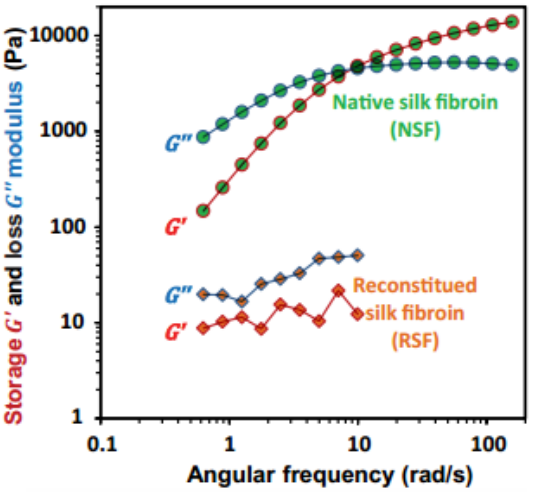


Fig. 2. Storage modulus (red lines) and loss modulus (blue lines) as a function of the angular frequency for a representative native (green circles) and reconstituted (orange diamonds) silkworm feedstock (22 ± 3 wt.%).

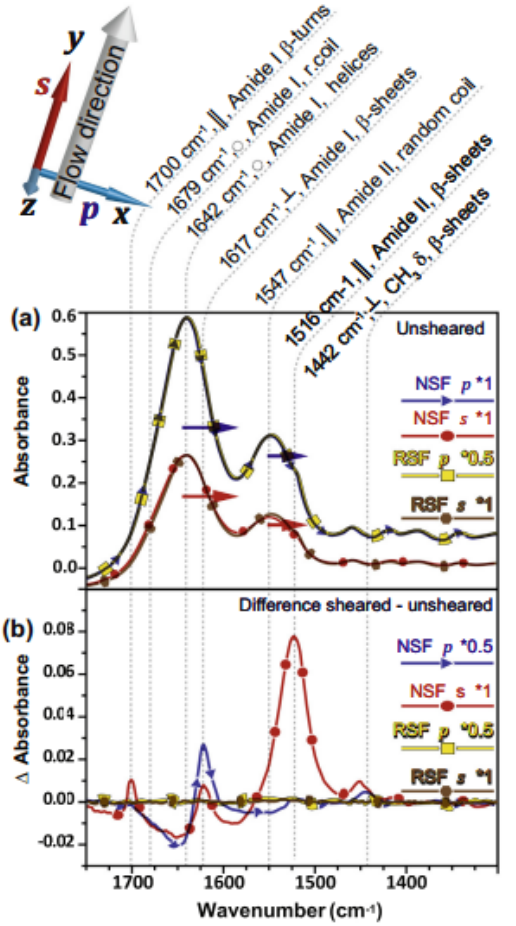


Fig. 3. (a) NSF spectrum before shearing (blue line with arrows for *p* polarization and red line with circles for *s* polarization), RSF before shearing (yellow line with squares for *p* polarization and brown line with hexagons for *s* polarization). The arrows represent the direction of the shift of the amide bands. (b) Difference between after and before the slow exponential shear ramp profile for native silk feedstock and reconstituted silk feedstock with assigned components [4,29,44,58,75–84]. The polarization difference spectrum was multiplied by 0.5 to compensate for its greater ATR absorption. The flow direction vector relative to the laboratory coordinate system is represented on top of the figure.

[46]. The three-orders-of-magnitude gap in G_N reveals the distinct levels at which native silk and artificial feedstocks can store and dissipate mechanical energy. This result suggests that NSF is different in kind, not just degree, from RSF as, whilst both behave like non-Newtonian fluids, RSF has a much weaker modulus dependency on the frequency [19,74].

Infrared spectroscopy is commonly used to assess protein secondary structure (conformation) as vibrational mode frequencies of the amide bands are dependent on hydrogen bonding and the tridimensional structures formed [85]. For non-oriented (isotropic) samples, both *s* and *p* polarized spectra give the same spectral line shape, with *p* polarization having twice the absorbance of *s* [67]. This is the case for unsheared NSF and RSF, as plotted in Fig. 3a. Such information is useful in order to determine unwanted orientation induced from sample loading. Despite their distinctly different rheologies, the mid-infrared spectra of static or unsheared samples of both native (blue line with arrows and red line with circles, respectively) and reconstituted silk (yellow line with squares and brown line with hexagons, respectively) are indistinguishable. Importantly, they both show typical protein peaks, including the amide I and II peaks at 1642 and 1547 cm^{-1}, respectively [75,85]. Furthermore, even when converted using heat, chemical or electrical stresses it is difficult to determine any differences between native and reconstituted feedstocks.

However, when flow stress was applied, the difference between the two materials became very clear. These changes can be highlighted by plotting the difference between sheared and unsheared spectra for each polarization, as shown in Fig. 3b. Overall the difference spectra revealed increases in intensity at peaks 1442, 1516, 1617 and 1700 cm^{-1} associated with anti-parallel β-sheets and β-turns [58,75,86] and decreases in intensity at 1547, 1642 and 1679 cm^{-1} assigned to random coil and helical secondary structures (α and/or 3_{10} helices) [4,29,44,58,75–84]. Whilst additional absorption components from gained and loss structures are

present in the amide III region and at lower frequencies [60], their weaker extinction coefficient limits their use as conversion markers in fast kinetics.

When considering the polarization of the spectra we work from the hypothesis that the protein chains and associated vibrational modes will be aligned along the velocity direction (y-axis) and will be probed predominantly by the s polarization (red curves) whilst any structures with modes perpendicular to the protein backbone will be probed mainly by the p polarization (blue curves). The bands at 1642 and 1679 cm^{-1}, which are associated to the random coil and helical secondary structures, have about the same intensity change in both polarizations, indicating that these structures have little orientation. Since the 1516 and 1700 cm^{-1} components appear only in s polarization for the sheared NSF, it suggests that they are aligned along the velocity direction. The intensity increase at 1617 cm^{-1} is only slightly higher for p polarization, indicating a weaker orientation perpendicular to the velocity vector. Consequently we believe that molecular alignment will have little influence on the amide I band position. The amide I COG shift is thus mostly due to the change in conformation. In contrast, the amide II 1516 cm^{-1} component is aligned along the protein backbone [75], which oriented along the shearing direction and thus the s-polarization. Hence the amide II band of s-polarized spectra will be strongly influenced by the flow alignment of the protein backbone. In contrast to the amide I band position, the position of the amide II band is therefore a good indicator of both conformational change and orientation.

Clearly it is possible to obtain key structural changes in conformation and orientation by observing the amide bands' COG. This information can then be related to changes in bulk rheological measurements obtained during a viscosity test. For both NSF and RSF, we observe shifts in the COG of the amide I and II bands alongside changes in viscosity η and first normal force difference N_1. Fig. 4 shows representative steady shear rate responses for two samples of NSF and RSF each. Fig. 4a and b represents a slow exponential ramp from 0.0018 to 150.6 s^{-1} and Fig. 4c and d a fast shear rate ramp from 0.03 to 1062 s^{-1}. For clarity, the relevant shifts of the COGs of the amide I band are plotted in the upper panes (a and c) and those of the amide II in the lower ones (b and d). Four response regions with increasing shear rates were identified and labelled from I to IV for NSF in each pane. At the bottom of Fig. 4, we illustrated our interpretation of the four regions observed for native silk feedstock with cartoons adapted from the aquamelt model presented by Holland et al. [14,72].

3.1. Region I

Both NSF (green curves) and RSF (orange curves) exhibited a plateau region at vanishing shear rates, giving the apparent zero shear viscosity $\eta_0 = \eta|_{\dot{\gamma}\to 0}$ [15,16,19,21]. This Newtonian plateau is always observed for both types of feedstocks (Fig. 4a and c) at rates below 1 s^{-1}. At 1.2 ± 0.4 kPa s, the η_0 value measured for NSF is lower than the value predicted by linear viscoelastic theory based upon our oscillatory measurements. This apparent inconsistency could be due to a transient gel structure for NSF causing higher modulus values. Such a gel structure could be removed under a steady shear experiment and thus the apparent zero-shear viscosity would become lower. However, the value of η_0 measured is perfectly consistent with previous experimental results reported by Holland et al. [15]. On the other hand, in our case the apparent zero shear viscosity η_0 or RSF was one order of magnitude lower (0.09 ± 0.05 kPa s) for the slow shear ramp despite these being for the same concentration (within the error). A similar difference was measured with the fast shear ramp, 1.3 ± 0.4 kPa s for NSF compared to 0.19 ± 0.08 kPa s for RSF. The difference in η_0 between the NSF and RSF could therefore be due to a difference in the degree of intermolecular interactions [73]. Consistent with a higher G_N and for the reasons mentioned above, the η_0 measured is higher than those of Holland et al. [19]. Within this plateau region, the rheological parameters are invariant and there are also no observable shifts in the COG of the amide I and II bands.

3.2. Region II

When the sample's linear viscoelastic limit was reached, both NSF and RSF exhibited non-Newtonian behaviour. Their viscosity started to decrease around $\dot{\gamma}_p = 3 \pm 2\ s^{-1}$ for both slow and fast shear rate ramps. This shear thinning behaviour has been previously reported [15,16,20,72]. Interestingly, FTIR spectra show no fluctuation in amide I COG for NSF and RSF, suggesting no changes in the protein conformation. On the other hand, the COG of the amide II band for NSF only (Fig. 4b) started to shift as an indicator of the molecular orientation. During this region of shear thinning behaviour, the first normal force difference N_1 for NSF becomes non-zero as the sample begins to push against the walls of the geometry, typically interpreted as the result of an increase in recoverable elastic strain of the molecules [88,89]. For RSF, even at higher shear rates, no increase in N_1 was measured. Thus the shear thinning response of NSF is likely to be due to increasing molecular alignment and a subsequent reduction in internal friction. Associating these results with birefringence measurements in the silkworm spinning apparatus, an increase in molecular orientation is also seen in the common duct after the feedstock of both glands combine [25].

Similarly to highly concentrated polymer melts, the regions I and II of NSF can be easily fitted by the Carreau–Yasuda constitutive model of $\eta = \eta_0(1 + (\dot{\gamma}\tau_p)^a)^{(n-1)/a}$, where τ_p is the relaxation time, n is the power-law exponent characteristic of the shear thinning rate and a is the rate of transmission [90]. With a fit of R^2 value > 0.99 for native silk, this relation gives us a n of 0.20 ± 0.04, a of 1.8 ± 0.3 and τ_p of 0.3 ± 0.2 s, close to other reported values [21,72]. These values are representative of a high concentration polymer with a strong shear-thinning behaviour resulting from the reduction in internal friction as protein chains are able to disentangle and align under shear rates faster than the relaxation time [73,91]. In contrast, no molecular alignment is observed for RSF, possibly due to protein degradation during the reconstitution process, creating smaller polymer chains and faster relaxation times.

3.3. Region III

For the slow shear rate ramp of NSF (Fig. 4a), shear rates above a critical value ($\dot{\gamma}_c = 50 \pm 20\ s^{-1}$) led to shear thickening, with the flow of NSF becoming unstable with an abrupt rise in the apparent viscosity. The point at which this instability occurred for our NSF is close to the value of 40 s^{-1} reported for *Samia ricini*, but higher than the 4 s^{-1} given for the middle and posterior part of *B. mori* reported by Moriya et al. [20] and the 15 s^{-1} measured by Terry et al. [16]. This difference in $\dot{\gamma}_c$ for native silk fibroin from *B. mori* could be due to (i) the different geometries used, (ii) dissimilar dissection techniques, (iii) other gland sections measured or (iv) an effect of the loading method. Coinciding with the onset of shear thickening, a rapid shift of both the COG of the amides I and II was also observed (Fig. 4a and b). Simultaneously, N_1 also increased from ~100 kPa to our self-imposed 250 kPa threshold as the sample's elastic recoverable strain continued to grow, as shown in Fig. 4b. As the amide I band shift is closely associated with the formation of β-sheet structures, the observed thickening and increase in N_1 are most likely the result of subsequent protein aggregation/shear-induced crystallization [92]. However, for the fast shear rate ramp (Fig. 4c), no clear shear thickening was observed for NSF. Instead, only the gradient decreased with increasing shear rate

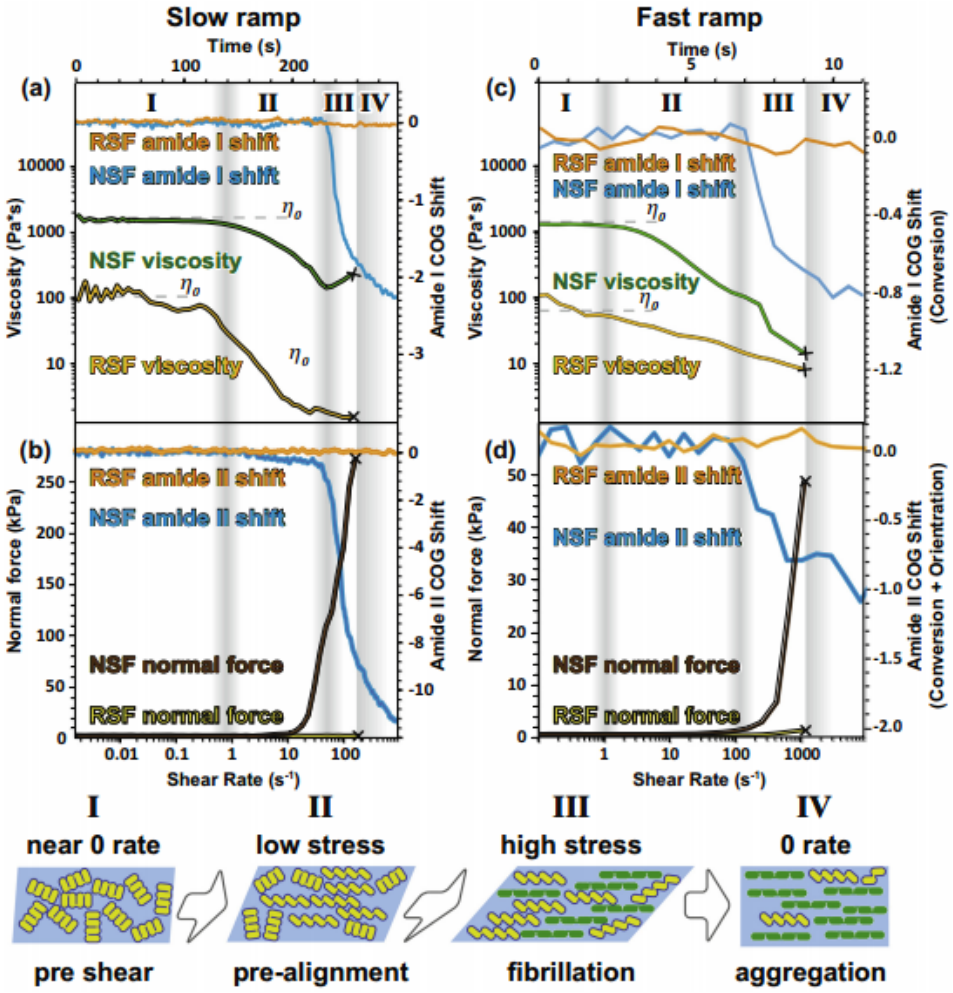


Fig. 4. Viscosity, first normal force, amide I and II centre of gravity shift as a function of the shear rate and time for NSF and RSF for two exponential shear ramps (slow ramp (a) and (b), fast ramp (c) and (d)). The black crosses represent the end of shearing after the exponential shear ramp. Bottom illustration represents individual unspun silk proteins in yellow with an outer hydration shell in dark blue followed by the converted, dehydrated silk proteins as a dark green "string of beads" on a nanometer [87].

before a drop in viscosity. At the same time, we observed a marked growth in N_1, although with lower values than for slow shear rate ramp (~50 kPa compared with ~250 kPa, Fig. 4b and d). Simultaneously, commensurate shifts to lower wavenumbers for NSF's COG of the amide I ($-2\ cm^{-1}$) and amide II bands ($-9\ cm^{-1}$) were also observed. Similar shifts were also present for the fast shear ramp, Fig. 4c and d, but to a smaller degree. Moreover, $\dot{\gamma}_c$ was higher for the fast exponential ramp, occurring at $\sim 100\ s^{-1}$. As N_1 appears to be proportional to the accumulated strain (Supplementary Fig. S.1), this may explain the higher $\dot{\gamma}_c$ observed under a faster shear rate profile. This conclusion is in agreement with spectroscopic evidence suggesting that fewer β-sheets were formed at comparable rates under a faster ramp.

As with our orientation measurements for region II, comparing our results with duct birefringence measurements, the rapid increase in N_1 and shift in the amide bands' COG may be considered analogous to the jump in birefringence observed in the silk duct [25,93]. If we assume that these events are related, as they appear to be, then shear thickening would occur just at the beginning of the silk press [20,94].

In contrast to the shear rate response of NSF, RSF did not show shear thickening for either the slow or fast shear rate ramp, Fig. 4a and c. Instead, the RSF continued to exhibit shear thinning with increasing shear rate without shifts in both COGs. N_1, too, displayed almost no change, although there was a slight increase above a shear rate of $10\ s^{-1}$ for both the slow and fast shear rate ramps, indicating a much smaller elastic recoverable strain. In previous work, shear thickening and a significant increase in thrust were only observed at very high RSF concentrations, above 50 wt.% [59]. The difference in response of NSF and RSF to high shear rates may be due to a lower molecular weight or to the removal of small compounds during the dialysis step [45]. Indeed,

QQQ

Greving et al. [24] show that there are fundamental differences in both size and shape between diluted NSF and RSF. The difference in shape could be explained by differences in the intra- and intermolecular interactions of the hydrated proteins, accounting for the lack of shear-induced interactions in RSF. As the transition to a β-sheet structure is essential for the spinning process [13], our study implies that reconstituted silk prepared in this manner would not be able to be spun at concentrations and shear rates that are comparable to native silk fibroins.

3.4. Region IV

Once shear thickening starts, a white plug surrounded by a lower viscosity fluid is quickly formed [15,19]. This normally occurs above 250 kPa of normal force and can be avoided by prematurely stopping the experiment before the end of the shear ramp. As N_1 in the fast exponential shear ramp is lower at equivalent rates, higher rates can be reached without slip and sample ejection. A shear transient with lower accumulated strains would therefore enable native silk feedstocks to be exposed to higher shear rates. Hence exposing the dope to shearing for only a brief period of time in region II would permit a longer exposure to the higher rates of region III prior to plug formation. In the animal, to prevent detrimental duct plugging, dope gelation/thickening would have to occur only once the narrowing of the duct is completed (i.e. at the silk press), as suggested by the measurement of Moriya et al. [20]. For spiders, the structure equivalent to the silk press is the draw-down taper, where β-sheet formation is observed [13,17,95].

Infrared spectroscopy also allows us to evaluate feedstock concentration during the experiment, which did not show any substantial variation for either RSF or NSF. An interesting feature of Rheo-IR is its ability to continue monitoring the conversion of the NSF by FTIR, even post shearing. Although at this stage no more mechanical energy was applied to the silk, the amide bands continued to shift towards lower frequencies, indicating a spontaneous self-assembly process and corroborating previous observations [36,72,86]. However, this process occurred very slowly and took hours to complete (the amide I could shift to lower frequencies by up to 5 ± 1 cm^{-1} and the amide II band 18 ± 1 cm^{-1}). The amide bands are far from being completely shifted before slippage or ejection occurs. Hence our methodology was unable to generate 100% conversion of NSF in the short time scale of the natural spinning process. We propose that extensional flow fields would be more effective at achieving this as they are already known to play an important role in the natural spinning process [96,97].

4. Conclusions

This study represents the first time rheological measurements have been coupled with attenuated total reflectance infrared spectroscopy (Rheo-IR). By directly correlating rheology with molecular structure, Rheo-IR is a robust and versatile tool which has the potential to be used to study not just silks but any polymeric material, from biomaterials to polymer melts [98,99]. In addition to providing information on aggregation dynamics and shear-induced crystallinity, polarized infrared spectroscopy also permits the determination of flow-induced molecular orientation. More specifically in this study, we have correlated silk protein structure to feedstock flow properties under a range of shear conditions. For native silk feedstocks our results support the hypothesis that shear thinning results from molecular alignment. We propose that this alignment occurs in the common duct of the silkworm's spinning apparatus, a hypothesis supported by birefringence measurements [25,93]. Additional support comes from the observation that, after a critical shear rate and strain threshold is surpassed, shear thickening is associated with the onset of a rapid solidification process promoted by β-sheet formation, which would coincide with the start of the silk press [13,20,93]. Additionally infrared spectroscopy allowed us to investigate the spontaneous protein conversion process post shear. This observation is in perfect agreement with a nucleation mechanism for solidification/fibrillation [72,86,100].

We also demonstrated that, whilst static spectra of NSF and RSF are indistinguishable, Rheo-IR highlights their intrinsic differences. Despite RSF undergoing shear thinning, it does not (unlike NSF) shear thicken or solidify under mechanical stress, even at very high rates. Therefore it would be imprudent to assume that traditionally prepared RSFs are representative analogues of native silk, even when they have similar spectra and comparable responses to chemical or thermal stress [7]. Importantly, the fundamental differences in the shear responses of the two materials offer the potential of an explanation to the disappointing properties of the fibres spun from such feedstocks [101].

In summary, Rheo-IR has provided a fresh perspective on the natural spinning process as well as a tool that could also be employed to investigate the processing of practically any polymer melt or solution. We envisage, moreover, that Rheo-IR will be of significant value in helping attempts to refine silk reconstitution processes, which in turn would allow the manufacture of sustainable feedstock analogues akin to native silks and with the potential to be processed in a biomimetic manner into high performance fibres.

Disclosures

The authors declare that they have no conflict of interests.

Acknowledgements

The authors thank David Porter for his critical comments on the manuscript as well as Tony Price and John Hogg for building parts necessary for coupling the instruments. M.B.-A. is supported by an EPSRC studentship (EP/G068224/1) and an NSERC scholarship (PGS 3D/6799-379132-2009). F.V. acknowledges support from the US-AFOSR (FA9550-12-1-0294) and the European Research Council (SP2-GA-2008-233409). C.H. thanks Magdalen College, Oxford and the EPSRC (EP/K005693/1) for their support.

Appendix A. Figures with essential colour discrimination

Certain figures in this article, particularly Figs. 1–4, are difficult to interpret in black and white. The full colour images can be found in the on-line version, at doi: 10.1016/j.actbio.2013.10.032.

Appendix B. Supplementary data

Supplementary data associated with this article can be found, in the online version, at http://dx.doi.org/10.1016/j.actbio.2013.10.032.

References

[1] Putthanarat S, Zarkoob S, Magoshi J, Chen JA, Eby RK, Stone M, et al. Effect of processing temperature on the morphology of silk membranes. Polymer 2002;43:3405–13.
[2] Kim UJ, Park J, Li C, Jin HJ, Valluzzi R, Kaplan DL. Structure and properties of silk hydrogels. Biomacromolecules 2004;5:786–92.
[3] Leisk GG, Lo TJ, Yucel T, Lu Q, Kaplan DL. Electrogelation for protein adhesives. Adv Mater 2010;22:711.
[4] Jeong L, Lee KY, Liu JW, Park WH. Time-resolved structural investigation of regenerated silk fibroin nanofibers treated with solvent vapor. Int J Macromol 2006;38:140–4.
[5] Chen X, Zhou L, Shao ZZ, Zhou P, Knight DP, Vollrath F. Conformation transition of silk protein membranes monitored by time-resolved FT-IR

spectroscopy – conformation transition behavior of regenerated silk fibroin membranes in alcohol solution at high concentrations. Acta Chim Sin 2003; 61:625–9.
[6] Chen X, Cai HF, Ling SJ, Shao ZZ, Huang YF. Conformation transition of *Bombyx mori* silk protein monitored by time-dependent Fourier transform infrared (FT-IR) spectroscopy: effect of organic solvent. Appl Spectrosc 2012;66: 696–9.
[7] Zhang C, Song D, Lu Q, Hu X, Kaplan DL, Zhu H. Flexibility regeneration of silk fibroin in vitro. Biomacromolecules 2012;13:2148–53.
[8] Rammensee S, Slotta U, Scheibel T, Bausch AR. Assembly mechanism of recombinant spider silk proteins. Proc Natl Acad Sci U S A 2008;105:6590–5.
[9] Dicko C, Vollrath F, Kenney JM. Spider silk protein refolding is controlled by changing pH. Biomacromolecules 2004;5:704–10.
[10] Foo CWP, Bini E, Hensman J, Knight DP, Lewis RV, Kaplan DL. Role of pH and charge on silk protein assembly in insects and spiders. Appl Phys A-Mater 2006;82:223–33.
[11] Vollrath F, Knight DP. Liquid crystalline spinning of spider silk. Nature 2001;410:541–8.
[12] Knight DP, Vollrath F. Liquid crystals and flow elongation in a spider's silk production line. Proc R Soc Lond Ser B-Biol Sci 1999;266:519–23.
[13] Knight DP, Knight MM, Vollrath F. Beta transition and stress-induced phase separation in the spinning of spider dragline silk. Int J Biol Macromol 2000;27:205–10.
[14] Holland C, Vollrath F, Ryan AJ, Mykhaylyk OO. Silk and synthetic polymers: reconciling 100 degrees of separation. Adv Mater 2012;24:105–9.
[15] Holland C, Terry AE, Porter D, Vollrath F. Comparing the rheology of native spider and silkworm spinning dope. Nat Mater 2006;5:870–4.
[16] Terry AE, Knight DP, Porter D, Vollrath F. PH induced changes in the rheology of silk fibroin solution from the middle division of *Bombyx mori* silkworm. Biomacromolecules 2004;5:768–72.
[17] Davies GJ, Knight DP, Vollrath F. Structure and function of the major ampullate spinning duct of the golden orb weaver *Nephila edulis*. Tissue Cell 2013;45:306–11.
[18] Holland C, Porter D, Vollrath F. Comparing the rheology of mulberry and "wild" silkworm spinning dopes. Biopolymers 2012;97:362–7.
[19] Holland C, Terry AE, Porter D, Vollrath F. Natural and unnatural silks. Polymer 2007;48:3388–92.
[20] Moriya M, Roschzttardtz F, Nakahara Y, Saito H, Masubuchi Y, Asakura T. Rheological properties of native silk fibroins from domestic and wild silkworms, and flow analysis in each spinneret by a finite element method. Biomacromolecules 2009;10:929–35.
[21] Kojic N, Bico J, Clasen C, McKinley GH. Ex vivo rheology of spider silk. J Exp Biol 2006;209:4355–62.
[22] Ochi A, Hossain KS, Magoshi J, Nemoto N. Rheology and dynamic light scattering of silk fibroin solution extracted from the middle division of *Bombyx mori* silkworm. Biomacromolecules 2002;3:1187–96.
[23] Martel A, Burghammer M, Davies RJ, Di Cola E, Vendrely C, Riekel C. Silk fiber assembly studied by synchrotron radiation SAXS/WAXS and Raman spectroscopy. J Am Chem Soc 2008;130:17070–4.
[24] Greving I, Dicko C, Terry A, Callow P, Vollrath F. Small angle neutron scattering of native and reconstituted silk fibroin. Soft Matter 2010;6: 4389–95.
[25] Kataoka K, Uematsu I. Studies on liquid silk. 8. Fiber formation of liquid silk in spinneret. Kobunshi Ronbunshu 1977;34:457–64.
[26] van Beek JD, Beaulieu L, Schafer H, Demura M, Asakura T, Meier BH. Solid-state NMR determination of the secondary structure of *Samia cynthia* ricini silk. Nature 2000;405:1077–9.
[27] Asakura T, Kuzuhara A, Tabeta R, Saito H. Conformation characterization of *Bombyx mori* silk fibroin in the solid-state by high-frequency C-13 cross polarization-magic angle spinning NMR, X-ray diffraction, and infrared spectroscopy. Macromolecules 1985;18:1841–5.
[28] Ishida M, Asakura T, Yokoi M, Saito H. Solvent-induced and mechanical-treatment-induced conformational transition of silk fibroins studied by high-resolution solid-state C-13 NMR spectroscopy. Macromolecules 1990;23: 88–94.
[29] Yoshimizu H, Asakura T. The structure of *Bombyx mori* silk fibroin membrane swollen by water studied with ESR, C-13-NMR, and FT-IR spectroscopies. J Appl Polym Sci 1990;40:1745–56.
[30] Simmons A, Ray E, Jelinski LW. Solid-state ^{13}C NMR of *Nephila clavipes* dragline silk establishes structure and identity of crystalline regions. Macromolecules 1994;27:5235–7.
[31] Jelinski LW, Blye A, Liivak O, Michal C, LaVerde G, Seidel A, et al. Orientation, structure, wet-spinning, and molecular basis for supercontraction of spider dragline silk. Int J Macromol 1999;24:197–201.
[32] Iizuka E, Yang JT. Optical rotatory dispersion and circular dichroism of beta-form of silk fibroin in solution. Proc Natl Acad Sci U S A 1966;55:1175–82.
[33] Dicko C, Porter D, Bond J, Kenney JM, Vollratht F. Structural disorder in silk proteins reveals the emergence of elastomericity. Biomacromolecules 2008;9:216–21.
[34] Lefevre T, Paquet-Mercier F, Rioux-Dube JF, Pezolet M. Structure of silk by Raman spectromicroscopy. From the spinning glands to the fibers. Biopolymers 2011.
[35] Hang YC, Zhang YP, Jin Y, Shao HL, Hu XC. Preparation of regenerated silk fibroin/silk sericin fibers by coaxial electrospinning. Int J Biol Macromol 2012;51:980–6.
[36] Lu Q, Zhu H, Zhang C, Zhang F, Zhang B, Kaplan DL. Silk self-assembly mechanisms and control from thermodynamics to kinetics. Biomacromolecules 2012;13:826–32.
[37] Chen X, Shao Z, Knight DP, Vollrath F. Conformation transition kinetics of *Bombyx mori* silk protein. Proteins 2007;68:223–31.
[38] Ohgo K, Bagusat F, Asakura T, Scheler U. Investigation of structural transition of regenerated silk fibroin aqueous solution by Rheo-NMR spectroscopy. J Am Chem Soc 2008;130:4182–6.
[39] Scelsi L, Mackley MR. Rheo-optic flow-induced crystallisation of polypropylene and polyethylene within confined entry-exit flow geometries. Rheol Acta 2008;47:895–908.
[40] Kanaya T, Matsuba G, Ogino Y, Nishida K, Shimizu HM, Shinohara T, et al. Hierarchic structure of shish-kebab by neutron scattering in a wide Q range. Macromolecules 2007;40:3650–4.
[41] Kumaraswamy G, Verma RK, Kornfield JA, Yeh FJ, Hsiao BS. Shear-enhanced crystallization in isotactic polypropylene. In-situ synchrotron SAXS and WAXD. Macromolecules 2004;37:9005–17.
[42] Pogodina NV, Lavrenko VP, Srinivas S, Winter HH. Rheology and structure of isotactic polypropylene near the gel point: quiescent and shear-induced crystallization. Polymer 2001;42:9031–43.
[43] Roessle M, Panine P, Urban VS, Riekel C. Structural evolution of regenerated silk fibroin under shear: combined wide- and small-angle X-ray scattering experiments using synchrotron radiation. Biopolymers 2004;74:316–27.
[44] Miyazawa T, Blout ER. Infrared spectra of polypeptides in various conformations – amide I and II bands. J Am Chem Soc 1961;83:712–9.
[45] Yamada H, Nakao H, Takasu Y, Tsubouchi K. Preparation of undegraded native molecular fibroin solution from silkworm cocoons. Mater Sci Eng C-Biomimetic Supramol Syst 2001;14:41–6.
[46] Wray LS, Hu X, Gallego J, Georgakoudi I, Omenetto FG, Schmidt D, et al. Effect of processing on silk-based biomaterials: reproducibility and biocompatibility. J Biomed Mater Res Part B 2011;998:89–101.
[47] Elices M, Guinea GV, Plaza GR, Karatzas C, Riekel C, Agullo-Rueda F, et al. Bioinspired fibers follow the track of natural spider silk. Macromolecules 2011;44:1166–76.
[48] Matsumoto K, Uejima H, Iwasaki T, Sano Y, Sumino H. Studies on regenerated protein fibers. 3. Production of regenerated silk fibroin fiber by the self-dialyzing wet spinning method. J Appl Polym Sci 1996;60:503–11.
[49] Seidel A, Liivak O, Calve S, Adaska J, Ji G, Yang Z, et al. Regenerated spider silk: processing, properties, and structure. Macromolecules 2000;33:775–80.
[50] Lazaris A, Arcidiacono S, Huang Y, Zhou JF, Duguay F, Chrétien N, et al. Spider silk fibers spun from soluble recombinant silk produced in mammalian cells. Science 2002;295:472–6.
[51] Yao J, Masuda H, Zhao C, Asakura T. Artificial spinning and characterization of silk fiber from *Bombyx mori* silk fibroin in hexafluoroacetone hydrate. Macromolecules 2002;35:6–9.
[52] Shao ZZ, Vollrath F, Yang Y, Thogersen HC. Structure and behavior of regenerated spider silk. Macromolecules 2003;36:1157–61.
[53] Zuo B, Dai L, Wu Z. Analysis of structure and properties of biodegradable regenerated silk fibroin fibers. J Mater Sci 2006;41:3357–61.
[54] Plaza GR, Corsini P, Marsano E, Perez-Rigueiro J, Biancotto L, Elices M, et al. Old silks endowed with new properties. Macromolecules 2009;42: 8977–82.
[55] Li X-G, Wu L-Y, Huang M-R, Shao H-L, Hu X-C. Conformational transition and liquid crystalline state of regenerated silk fibroin in water. Biopolymers 2008;89:497–505.
[56] Chen X, Knight DP, Shao ZZ. Beta-turn formation during the conformation transition in silk fibroin. Soft Matter 2009;5:2777–81.
[57] Mo CL, Holland C, Porter D, Shao ZZ, Vollrath F. Concentration state dependence of the rheological and structural properties of reconstituted silk. Biomacromolecules 2009;10:2724–8.
[58] Boulet-Audet M, Lefèvre T, Buffeteau T, Pézolet M. Attenuated total reflection infrared spectroscopy: an efficient technique to quantitatively determine the orientation and conformation of proteins in single silk fibers. Appl Spectrosc 2008;62:956–62.
[59] Boulet-Audet M, Vollrath F, Holland C. Rheo-attenuated total reflectance infrared spectroscopy: a new tool to study biopolymers. Phys Chem Chem Phys 2011;13:3979–84.
[60] Goormaghtigh E, Ruysschaert J-M, Raussens V. Evaluation of the information content in infrared spectra for protein secondary structure determination. Biophys J 2006;90:2946–57.
[61] Kornfield JA, Fuller GG, Pearson DS. Infrared dichroism measurements of molecular relaxation in binary blend melt rheology. Macromolecules 1989;22:1334–45.
[62] Chiou B-S, Avena-Bustillos RJ, Shey J, Yee E, Bechtel PJ, Imam SH, et al. Rheological and mechanical properties of cross-linked fish gelatins. Polymer 2006;47:6379–86.
[63] Rockwood DN, Preda RC, Yucel T, Wang XQ, Lovett ML, Kaplan DL. Materials fabrication from *Bombyx mori* silk fibroin. Nat Protoc 2011;6:1612–31.
[64] Machida J. On the secretion of the silk substances of the silkworm. Proc Imperial Acad 1926;2:421–2.
[65] Akai H. The structure and ultrastructure of the silk gland. Experientia 1983;39:443–9.
[66] **Feustel M. Apparatus for determining rheological properties. G01N11/14 ed. United State 2006.**
[67] Harrick NJ. Internal Reflection Spectroscopy. New York: Wiley; 1967.

[68] Fringeli UP, Günthard HH. Infrared membrane spectroscopy. In: Grell E, editor. Molecular Biology, Biochemistry and Biophysics. Berlin: Springer; 1980. p. 270–332.
[69] Tsukada M, Nagura M, Ishikawa H, Shiozaki H. Structural characteristics of silk fibers treated with epoxides. J Appl Polym Sci 1991;43:643–9.
[70] Stuart B. Infrared Spectroscopy Fundamentals and Applications. Chichester UK/Hoboken: NJ. Wiley; 2004.
[71] Griffiths PR, De Haseth JA. Fourier Transform Infrared Spectrometry. New York: Wiley; 1986.
[72] Holland C, Urbach JS, Blair DL. Direct visualization of shear dependent silk fibrillogenesis. Soft Matter 2012;8:2590–4.
[73] Ferry JD. Viscoelastic Properties of Polymers. 3rd ed. New York: Wiley VCH; 1980.
[74] Rössle M, Panine P, Urban VS, Riekel C. Structural evolution of regenerated silk fibroin under shear: combined wide- and small-angle X-ray scattering experiments using synchrotron radiation. Biopolymers 2004;74:316–27.
[75] Moore WH, Krimm S. Vibrational analysis of peptides, polypeptides, and proteins. 2. Beta-poly(L-alanine) and beta-poly(L-alanylglycine). Biopolymers 1976;15:2465–83.
[76] Teramoto H, Miyazawa M. Molecular orientation behavior of silk sericin film as revealed by ATR infrared spectroscopy. Biomacromolecules 2005;6: 2049–57.
[77] Venyaminov SY, Kalnin NN. Quantitative IR spectrophotometry of peptide compounds in water (H_2O) solutions. 2. Amide absorption-bands of polypeptides and fibrous proteins in alpha-coil, beta-coil, and random coil conformations. Biopolymers 1990;30:1259–71.
[78] Sonoyama M, Nakano T. Infrared rheo-optics of *Bombyx mori* fibroin film by dynamic step-scan FT-IR spectroscopy combined with digital signal processing. Appl Spectrosc 2000;54:968–73.
[79] Goormaghtigh E, Cabiaux V, Ruysschaert JM. Determination of soluble and membranes protein structure by Fourier transform infrared spectroscopy. II. Experimental aspects, side chain structure, and H/D exchange. In: Hilderson HJ, Ralston GR, editors. Physicochemical Methods in the Study of Biomembranes. New York: Plenum; 1994. p. 363–403.
[80] Garside P, Lahlil S, Wyeth P. Characterization of historic silk by polarized attenuated total reflectance Fourier transform infrared spectroscopy for informed conservation. Appl Spectrosc 2005;59:1242–7.
[81] Muller WS, Samuelson LA, Fossey SA, Kaplan DL. Formation and characterization of Langmuir silk films. Langmuir 1993;9:1857–61.
[82] Taddei P, Monti P. Vibrational infrared conformational studies of model peptides representing the semicrystalline domains of *Bombyx mori* silk fibroin. Biopolymers 2005;78:249–58.
[83] Lv Q, Cao CB, Zhang Y, Ma XL, Zhu HS. Preparation of insoluble fibroin films without methanol treatment. J Appl Polym Sci 2005;96:2168–73.
[84] Sonoyama M, Miyazawa M, Katagiri G, Ishida H. Dynamic FT-IR spectroscopic studies of silk fibroin films. Appl Spectrosc 1997;51:545–7.
[85] Goormaghtigh E, Cabiaux V, Ruysschaert JM. Determination of soluble and membranes protein structure by Fourier transform infrared spectroscopy. III. Secondary structures. In: Hilderson HJ, Ralston GR, editors. Physicochemical Methods in the Study of Biomembranes. New York: Plenum; 1994. p. 404–50.
[86] Li GY, Zhou P, Shao ZZ, Xie X, Chen X, Wang HH, et al. The natural silk spinning process – a nucleation-dependent aggregation mechanism? Eur J Biochem 2001;268:6600–6.
[87] Vollrath F, Porter D. Spider silk as archetypal protein elastomer. Soft Matter 2006;2:377–85.
[88] Rivlin RS. Large elastic deformations of isotropic materials. 4. Further developments of the general theory. Philos Trans R Soc London A 1948; 241:379–97.
[89] Porter D. Group Interaction Modelling of Polymer Properties. New York: Dekker; 1995.
[90] Yasuda K, Armstrong RC, Cohen RE. Shear-flow properties of concentrated-solutions of linear and star branched polystyrenes. Rheol Acta 1981;20: 163–78.
[91] Graessley W. Viscosity of entangling polydisperse polymers. J Chem Phys 1967;47:1942–53.
[92] Vrahopoulou EP, McHugh AJ. Shear-thickening and structure formation in polymer-solutions. J Non-Newton Fluid Mech 1987;25:157–75.
[93] Asakura T, Umemura K, Nakazawa Y, Hirose H, Higham J, Knight D. Some observations on the structure and function of the spinning apparatus in the silkworm *Bombyx mori*. Biomacromolecules 2007;8:175–81.
[94] Moriya M, Ohgo K, Masubuchi Y, Knight DP, Asakura T. Micro-computerized tomographic observation of the spinning apparatus in *Bombyx mori* silkworms. Polymer 2008;49:5665–9.
[95] Lefèvre T, Boudreault S, Cloutier C, Pézolet M. Conformational and orientational transformation of silk proteins in the major ampullate gland of *Nephila clavipes* spiders. Biomacromolecules 2008;9:2399–407.
[96] Smith DE, Chu S. Response of flexible polymers to a sudden elongational flow. Science 1998;281:1335–40.
[97] Crowley DG, Frank FC, Mackley MR, Stephenson RG. Localized flow birefringence of polyethylene oxide solutions in a 4 roll mill. J Polym Sci Pol Phys 1976;14:1111–9.
[98] Storm C, Pastore JJ, MacKintosh FC, Lubensky TC, Janmey PA. Nonlinear elasticity in biological gels. Nature 2005;435:191–4.
[99] Mykhaylyk OO. Time-resolved polarized light imaging of sheared materials: application to polymer crystallization. Soft Matter 2010;6:4430–40.
[100] Chen X, Knight DP, Shao ZZ, Vollrath F. Conformation transition in silk protein films monitored by time-resolved Fourier transform infrared spectroscopy: effect of potassium ions on *Nephila spidroin* films. Biochemistry 2002;41: 14944–50.
[101] Vollrath F, Porter D, Holland C. There are many more lessons still to be learned from spider silks. Soft Matter 2011;7:9595–600.